

**Copyright**  
**by**  
**Ehab Mohamed Ali Hussein Hassan**  
**2015**

The Dissertation Committee for Ehab Mohamed Ali Hussein Hassan certifies that this is the approved version of the following dissertation:

**Plasma Turbulence in the Equatorial Electrojet  
Observations, Theories, Models, and Simulations**

Committee:

---

**Philip Morrison, Supervisor**

---

**C. Wendell Horton, Co-Supervisor**

---

**Richard Fitzpatrick**

---

**Roger Bengtson**

---

**Todd Humphreys**

**Plasma Turbulence in the Equatorial Electrojet  
Observations, Theories, Models, and Simulations**

by

**Ehab Mohamed Ali Hussein Hassan, B.S., M.S.**

**Dissertation**

Presented to the Faculty of the Graduate School of  
The University of Texas at Austin  
in Partial Fulfillment  
of the Requirements  
for the degree of  
**Doctor of Philosophy**

The University of Texas at Austin  
December, 2015

## Dedication

I dedicate the work I have done and reported in this dissertation to my parents Faten and Mohamed for their great support and continuous prayers for me and my family; my wife Marwa for her patience, advice, and postponement of her own future career plans for the sake of mine; and finally my kids Eyad, Mariam, and Mohamed, Jr., whom I forever wish to make proud.

# Acknowledgements

First and foremost, I want to praise my Lord, Allah, for his continuous support and guidance. I have always felt that I am not alone while he is watching, protecting, and guiding me and my family, even in the days of difficulty and hardship.

I need to thank my research co-adviser Prof. Wendell Horton for enthusiastically guiding me every step along the way, and for helping me refocus my attention whenever I became too distracted by side research projects. Prof. Wendell Horton gave me complete freedom to choose my research topics and to find my way through them with his close supervising, mentoring, and encouraging at every step.

I wish to thank my research adviser Prof. Phil Morrison for his never failing direction over my progress in research and for generously providing his time and knowledge in guiding me through the hard times we face during our Ph.D. journey. I also wish to thank him for all he has taught me in the classroom through many amazing courses, such as the nonlinear dynamics and fluid mechanics.

Many thanks to Dr. David Hatch who selflessly took time to advance my computing skills. Dr. David Hatch was willing to examine every detail of my work, and who always exhibited a fervor for collaborating with me in the field of ionosphere plasma physics. His perspective as a scientist who manages multiple professional and personal responsibilities was invaluable.

I would like to thank Dr. Steven Morley and Dr. John Steinberg for their valuable discussions about various statistical methods for solar wind data and for their mentoring during the Los Alamos Space Weather Summer School.

I would love to thank Dr. John Keto, Dr. Richard Fitzpatrick, Dr. Roger Bengtson, and Dr. Francois Waelbroeck for having their offices open to me every time I needed scientific or personal advice.

Thanks have to be given to Dr. Todd Humphreys for the fruitful discussions we had about the GPS systems and ionospheric scintillations before, during, and after the two classes he taught over these topics.

My thanks go out to Ioannis Keramidas Charidakos for his valuable feedback and profitable conversations about the non-canonical Hamiltonian systems.

I want to thank my group mates Cynthia Correa, Dmitry Meyerson, Xiangrong Fu, and Jingfei Ma, for their ever cordial and valuable discussions about my simulation code and research activities in the Department of Physics.

I also would like to thank Cathy Rapinett and James Haligan in the Institute of Fusion, and Lisa Gentry, Matt Ervin, and Olga Vorloou in the Department of Physics for taking care of all the needed administrative work, which saved me much time and trouble.

Last but not least, I would love to thank my wife Marwa Al-Badry for taking care of me and my kids, for making my life away from home bearable, and for bringing so much joy and happiness to our little house.

Finally, I would like to thank the Muslim Community at Nueces Mosque in Austin for always being there to help us with difficulties, and more importantly, to maintain our faith.

# **Plasma Turbulence in the Equatorial Electrojet Observations, Theories, Models, and Simulations**

Ehab Mohamed Ali Hussein Hassan, Ph.D.  
The University of Texas at Austin, 2015

Supervisor: Philip Morrison

The plasma turbulence in the equatorial electrojet due to the presence of two different plasma instability mechanisms has been observed and studied for more than seven decades. The sharp density-gradient and large conductivity give rise to gradient-drift and Farley-Buneman instabilities, respectively, of different scale-lengths. A new 2-D fluid model is derived by modifying the standard two-stream fluid model with the ion viscosity tensor and electron polarization drift, and is capable of describing both instabilities in a unified system. Numerical solution of the model in the linear regime demonstrates the capacity of the model to capture the salient characteristics of the two instabilities. Nonlinear simulations of the unified model of the equatorial electrojet instabilities reproduce many of the features that are found in radar observations and sounding rocket measurements under multiple solar and ionospheric conditions. The linear and nonlinear numerical results of the 2-D unified fluid model are found to be comparable to the fully kinetic and hybrid models which have high computational cost and small coverage area of the ionosphere. This gives the unified fluid model a superiority over those models.

The distribution of the energy content in the system is studied and the rate of change of the energy content in the evolving fields obeys the law of energy conservation. The dynamics of the ions were found to have the largest portion of energy in their

kinetic and internal thermal energy components. The redistribution of energy is characterized by a forward cascade generating small-scale structures. The bracket of the system dynamics in the nonlinear partial differential equation was proved to be a non-canonical Hamiltonian system as that bracket satisfies the Jacobi identity.

The penetration of the variations in the interplanetary magnetic and electric fields in the solar winds to the dip equator is observed as a perfect match with the variations in the horizontal components of the geomagnetic and electric fields at the magnetic equator. Three years of concurrent measurements of the solar wind parameters at Advanced Composition Explorer (ACE) and Interplanetary Monitoring Platform (IMP) space missions used to establish a Kernel Density Estimation (KDE) functions for these parameters at the IMP-8 location. The KDE functions can be used to generate an ensemble of the solar wind parameters which has many applications in space weather forecasting and data-driven simulations. Also, categorized KDE functions were established for the solar wind categories that have different origin from the Sun.

# Contents

List of Figures . . . . .	xii
List of Tables . . . . .	xx
Chapter One: Aeronomy and Space Weather . . . . .	1
1.1 Solar Activities . . . . .	3
1.2 Ionosphere . . . . .	4
Chapter Two: An Introduction to the Turbulence in the Equatorial Electrojet . . . . .	8
2.1 Discovering the Equatorial Electrojet . . . . .	8
2.2 Physics of the Equatorial Electrojet . . . . .	10
2.3 The Equatorial Electrojet Instabilities . . . . .	12
2.3.1 Radar Observations . . . . .	12
2.3.2 Sounding Rocket Observations . . . . .	19
2.3.3 Theoretical Interpretation . . . . .	25
Chapter Three: Modeling the Equatorial Electrojet Instabilities . . . . .	27
3.1 Past and Present Models . . . . .	28
3.2 Basic Fluid Model . . . . .	29
3.3 Unified Fluid Model . . . . .	35
3.3.1 Plasma Dynamic Equations . . . . .	35
3.3.2 Linear Dynamical Equations . . . . .	38
3.3.3 Numerical Solution of Linear System . . . . .	39
3.3.4 Basic versus Unified Fluid Models . . . . .	42
3.3.5 Altitude Dependent Growth Rate . . . . .	44
3.3.6 Type-I and Type-II Instabilities . . . . .	46
3.4 Ion Thermal Flux and Farley-Buneman Instability . . . . .	46
Chapter Four: Simulation Results of the Equatorial Electrojet Instabilities . . . . .	51
4.1 Simulation Results for Basic Fluid Model . . . . .	51
4.2 Simulation Results for Unified Fluid Model . . . . .	52

4.2.1	Nonlinear System Initialization . . . . .	52
4.2.2	Spectral Analysis of Electron Density . . . . .	55
4.2.3	Instabilities Evolution, Coupling, and Saturation . . . . .	57
4.2.4	Turbulence in Electron Density . . . . .	63
4.2.5	Perturbed Electric Fields . . . . .	65
4.2.6	Asymmetries in Plasma Fluxes . . . . .	66
4.2.7	Phase Velocity of Plasma Irregularities . . . . .	68
Chapter Five: Dynamic System Hamiltonian and Energy Cascades . . . . .		72
5.1	Energy in the Equatorial Electrojet Model . . . . .	72
5.1.1	System Energy Equation . . . . .	74
5.1.2	Energy Conservation in System Dynamics . . . . .	76
5.1.3	Total Energy in Simulation Results . . . . .	79
5.1.4	Energy Sources and Dissipations . . . . .	82
5.1.5	Energy Transfer Mechanisms . . . . .	86
5.1.6	Energy Cascades . . . . .	88
5.2	Non-Canonical Hamiltonian System . . . . .	93
5.2.1	The System Hamiltonian Bracket . . . . .	93
5.2.2	Casimir's Invariant . . . . .	96
Chapter Six: Impacts of the Solar Wind on the Equatorial Electrojet . . . . .		99
6.1	Introduction . . . . .	99
6.2	Solar Wind 4-Categorization Scheme . . . . .	103
6.3	Solar Wind Advection . . . . .	106
6.4	Data Sources, Limitations, and Conditioning . . . . .	110
6.5	Advectioned Solar Wind Parameters . . . . .	112
6.6	Solar Wind Ensemble . . . . .	114
6.7	Conclusions . . . . .	119
Chapter Seven: Summary and Conclusions . . . . .		121
Appendices . . . . .		127
.1	Appendix A: Vector Identities . . . . .	127
.2	Appendix B: Functional Derivative for the Electric Potential . . . . .	128
.3	Appendix C: Verifying Jacobi Identity For Hamiltonian Bracket . . . . .	130

Bibliography . . . . . 134

# List of Figures

1.1	A cartoon for the areas of study in the Aeronomy system and the coupling in atmosphere-ionosphere-magnetosphere (AIM) system. Reprinted from the Solar and Space Physics: A Science for a Technological Society report, figure source courtesy of Joe Grebowsky, NASA GSFC . . . . .	2
1.2	The 11 year solar cycles are identified by the number of sunspots that gradually increases from solar minimum to solar maximum cycles (top and bottom) and migrate towards the equator of the Sun as the solar cycle progresses (top), credit to NASA/MSFC. . . . .	3
1.3	The electron density profile in the ionosphere for altitude range 70 - 1070 km at the midnight (green) and noon (blue) times using International Reference Ionosphere (IRI) empirical model. . . . .	5
1.4	The altitude profile of ions and electrons parameters in the ionosphere for altitude range 70 - 1070 km using NMSIS2000, IRI, and IGRF12 models. . . . .	6
2.1	A daytime vertical profiles for: (a) the ionosphere plasma density and ion composition, (b) the parallel ( $\sigma_o$ ), Pedersen ( $\sigma_P$ ), and Hall ( $\sigma_H$ ) electric conductivities under average solar conditions [from Forbes and Lindzen [29]]. . . . .	10
2.2	The equatorial electrojet current generation mechanism as a dynamo process followed by combination of Pedersen and Hall electric fields [from Kelley [46]]. . . . .	11
2.3	The spectrum of Type-I fluctuations as measured at at 50 MHz at different elevation angles in both sides of the vertical line. The spectra are normalized to the peak value and measured as a shift from the radar central frequency. [From Cohen and Bowles [16]] . . . . .	13
2.4	The spectrum of Type-II fluctuations as measured simultaneously at 50 MHz by antennas at different zenith angles. The spectra are normalized to the peak value. [From Balsley [6]] . . . . .	14

2.5	Snapshots of the spectrum in the radar echoes of the scattering regions before (top) and after (bottom) the phase reversal of the electrojet. [From Fejer [25]] . . . . .	16
2.6	A comparison between the spectra of a scattering region taken simultaneously at three different frequencies for two successive days show the dominance of type-I spectrum and the dependence of the Doppler shift on the operating frequency of the radar. [From Balsley and Farley [4]] . . .	17
2.7	Spectrogram for the backscattered echoes from the AMISR prototype radar at Jicamarca at different zenith angles ( $-32^\circ, -24^\circ, -12^\circ, 0^\circ$ ) to show the east-west symmetry in the equatorial electrojet plasma flux. [From Hysell <i>et al.</i> [43]] . . . . .	18
2.8	The vertical profile of the electron density and the sizes of the irregularities as a function of altitude in the daytime (left-panel) and nighttime (right-panel). [From Prakash <i>et al.</i> [84]] . . . . .	20
2.9	The vertical profile of the plasma density (left) and spectrum of the electric field wave (right) measured at the upleg. [From Pfaff <i>et al.</i> [80]] . . . . .	21
2.10	The perturbed electric field wave in the east-west direction with amplitude variation of $\pm 10 - 15$ mV/m (up) and the normalized fluctuations in the electron density (bottom) as measured at the upleg. [From Pfaff <i>et al.</i> [81]]	23
2.11	The variations in the vertical (up) and horizontal (bottom) electric field waves as measured at the upleg. [From Pfaff <i>et al.</i> [81]] . . . . .	23
2.12	The horizontal DC electric field (a) changes its direction from eastward to westward around 105 km and its peak value is ranged in $\pm 1 - 3$ mV/m. The vertical DC electric field (b) is directed upward and has a maximum value of 10 mV/m. The peak value of the calculated electron current density (c) is at altitude 105 km. The profile of the fluctuation in the electron density (d) shows a large fluctuation in the region of large density-gradient scale-length. [From Pfaff <i>et al.</i> [83]] . . . . .	24
3.1	The growth rates for different electron density scale-lengths $L_n = 1, 4, 6$ km and at opposite limits of $E \times B$ drift velocity at (a) $v_E = 200$ m/s (below type-I instability threshold) and (b) $v_E = 400$ m/s (above type-I instability threshold). . . . .	33

3.2	The dependence of the unified model instabilities growth rates on the $\mathbf{E} \times \mathbf{B}$ drift, $v_E$ , and electron density scale-lengths, $L_n$ , in the east-west (left) and vertical (right) directions at 105 km altitude. . . . .	41
3.3	A comparison between the growth-rate, $\gamma_k(k_y)$ , in the standard two-stream model (dashed-green) and the unified model with including both the ions viscosity and the electrons inertia (solid-black), absence of ions viscosity (dashed-blue), and absence of electrons inertia (dashed-red). [From Hassan <i>et al.</i> [36]] . . . . .	42
3.4	A comparison between the real-frequency, $\omega_k(k_y)$ , profile of the standard two-stream model (dashed-green) and the unified model with including both the ions viscosity and the electrons inertia (solid-black). The unified model gives smaller phase velocity than the standard two-stream model. [From Hassan <i>et al.</i> [36]] . . . . .	43
3.5	The growth-rate profile of the unified model as a function of altitude and horizontal wavenumber ( $k_y$ ). It shows the dominance of Type-II instability at low altitudes up to the coupling region between Type-I and Type-II instabilities between 100-110 km. Above 110 km, Type-I instability dominates and Type-II instability disappears as a result of the reverse of the electron density scale length sign to be negative at that region. [From Hassan <i>et al.</i> [36]] . . . . .	45
3.6	The growth rate (top) and the real frequency (bottom) for the ions dynamics including both the viscosity and thermal flux in the fluid model using the corresponding moments in the Vlasov equation. [From Litt <i>et al.</i> [55]] . . . . .	49
4.1	The initial condition and evolution of the unstable modes of electrons density for the basic fluid model. It shows the upward (downward) drifting of the low-density (high-density) plasma structures due to the cross-field instability. [From Hassan <i>et al.</i> ] [35] . . . . .	53

4.2	The Energy Spectrum of the Perturbed Electron Carrier Density at different states of the simulation. The top panel shows that the energy spectrum of the available modes accumulates at two peaks for two types of instabilities at low- and high-k values. The second panel shows the transition of the energy to the modes of higher wavenumbers. These modes decay as they enter the region of negative growth-rates as long as they are in the region where the linear terms dominate. The third panel shows the distribution of energy over the available modes right before the transition region between the linear and the nonlinear regimes which has different distribution of the energy spectrum as shown in the fourth panel. The fourth and the fifth panels show the distribution of the energy over modes at all wavenumbers. This verifies the coupling between the two types of instabilities and the cascade transition of the energy from small wavenumbers to large wavenumbers that makes the system has electron density structures of all sizes. [From Hassan <i>et al.</i> [36]] . . . . .	56
4.3	The evolution of the pertubed electron carrier density ( $t = 500ms$ ) during the dominance of the linear terms on the simulation. It shows the downward drifts of the high-density plasma and the upward drifts of the low-density plasma as a result of the dominance of the Gradient-Drift (Type-II) instability at this phase of the simulation. [From Hassan <i>et al.</i> [36]] . . . . .	58
4.4	The pertubed electron carrier density ( $t = 600ms$ ) during the transition from the dominance of linear terms to the dominance of nonlinear terms in the saturation state of the simulation. It shows the expected large size structures of plasma densities that are drifting straight downward before the effect of the Farley-Buneman (Type-I) instability effectively shows up and break these large structures into smaller ones. [From Hassan <i>et al.</i> [36]]	59
4.5	The pertubed electron carrier density ( $t = 1000ms$ ) during the dominance of the nonlinear terms at the saturation state of the system reaches 8% relative to the background electron density. It shows the very small structures of sizes less than a meter embedded in larger structures that are seen before as a result of the coupling between Type-I and Type-II instabilities in the saturation state. [From Hassan <i>et al.</i> [36]] . . . . .	60

4.6	A close view of the large-scale structures formed during the transition phase (left-panel) and the small-scale structures formed during the saturation phase of the simulation under the solar maximum (1987) conditions. [From Hassan <i>et al.</i> [36]] . . . . .	61
4.7	A comparison between the the perturbed density maxima (lower panel) and its stadard deviations (upper panel) at the solar maximum (blue-line) and solar minimum (red-line) year. The standard deviations in the lower panel also defines clearly the growing, transion, and saturation phases during the simulation under two different solar conditions. [From Hassan <i>et al.</i> [36]] . . . . .	62
4.8	A comparison between the perturbed density maxima for different density scale-lengths, $L_n = 1, 4, 6$ km that shows different growing rate of the unstable modes and different levels of saturation. [From Hassan <i>et al.</i> [37]]	64
4.9	A comparison between the maximum perturbed electric field components in the horizontal (top panel) and vertical (bottom panel) directions at the solar maximum (red-line) and solar minimum (blue-line) years shows the effect of solar activity on the magnitude of the electric field components. [From Hassan <i>et al.</i> [36]] . . . . .	65
4.10	A comparison between the root-mean-square of the perturbed electric field components in the horizontal (top panel) and vertical (bottom panel) directions at the solar maximum (blue-line) and solar minimum (red-line) year. The dotted (dashed) lines show the root-mean-square of the positive (negative) component of the electric field. [From Hassan <i>et al.</i> [36]] . . .	67
4.11	The inverse fourier transform of the particle density spectrum of all $k_y$ values at $k_z=0$ ( $m^{-1}$ ) for each time step during the saturation region. A phase velocity of 330 (m/s) can be estimated from the slope as a drift speed of the particle density to be approximately equal to the ion-acoustic speed at 105 m altitude. [From Hassan <i>et al.</i> [36]] . . . . .	69
4.12	The calculated $\delta \mathbf{E} \times \mathbf{B}$ drift velocity for the electrons (top) using the perturbed electric field ( $\delta E$ ) and the corresponding drift velocity for the collisional ions (bottom) in the zonal (red) and vertical (blue) directions.	70

5.1	The total energy in the evolving fields $\{\delta n, \delta\phi, \delta\chi\}$ (top-panel) and the ratio between the energy in each evolving field and the total energy (bottom-panel) for a case of $L_n = 6$ km and $v_E = 400$ m/s. . . . .	79
5.2	A comparison between the total energy (the sum of the ions and electrons kinetic energy and the plasma internal energy) for different magnitudes of density scale-length ( $L_n$ ) and the $v_E$ drifts. . . . .	81
5.3	The time-average of the total energy in the evolving fields $\{\delta n, \delta\phi, \delta\chi\}$ over the saturation state of the simulation for a case of $L_n = 6$ km and $v_E = 400$ m/s as a function of the horizontal wavenumber. . . . .	82
5.4	The time-average of the rate of energy transfer in the evolving fields $\{\delta n, \delta\phi, \delta\chi\}$ over the saturation state of the simulation for a case of $L_n = 6$ km and $v_E = 400$ m/s as a function of the horizontal wavenumber. . . . .	83
5.5	Various terms in the energy equation of the evolving fields over the transition and saturation phases of the simulation for a case of $L_n = 6$ km and $v_E = 400$ m/s. The rate of variations in the energy content of the density is too small to be represented in this plot. . . . .	84
5.6	Various terms in the energy equation of the evolving fields over the transition and saturation phases of the simulation for $L_n = 1$ km and $v_E = 400$ m/s (Top), $L_n = \infty$ km and $v_E = 400$ m/s (Middle), and $L_n = 6$ km and $v_E = 425$ m/s (Bottom). . . . .	85
5.7	The energy transfer mechanisms and physics between the source (pink) and dissipation (cyan) terms in addition to the coupling (green) terms between the saturated evolving fields for the case of $L_n = 6$ km and $v_E = 400$ m/s. . . . .	87
5.8	Forward energy cascade over the saturation state of the simulation for a case of $L_n = 6$ km and $v_E = 400$ m/s. The top panel shows the term $\dot{E}_\phi = \frac{en_o}{B} \delta\tilde{\phi}[\delta\tilde{\phi}, \delta\tilde{n}]$ over the saturation phase of the simulation and integrated in the vertical direction. The bottom panel shows the time-average of the rate of change in energy over the saturation phase. (The color bar has removed and the bottom panel can be use as a reference for the energy level in the color coded on) . . . . .	89

5.9	Dual energy cascades over the saturation state of the simulation for a case of $L_n = 6$ km and $v_E = 400$ m/s. The top panel shows the temporal variations of energy in $\dot{E}_\phi = \frac{en_p}{B} \delta\tilde{\phi}[\delta\tilde{\phi}, \nabla^2\delta\tilde{\phi}]$ over the saturation phase of the simulation and integrated in the vertical direction. The bottom panel shows the time-average of the rate of energy variations over the saturation phase. (The color bar has been removed and the bottom panel can be used as a reference for the energy level in the color coded on) . . . . .	91
5.10	Forward (top-panel) and Dual (bottom-panel) energy cascading mechanisms over the saturation state of the simulation for different cases of density-gradient scale-length, $L_n = 1, 6$ km, and cross-field drift velocities, $v_E = 400, 425$ m/s. . . . .	92
6.1	The enhancement of the horizontal component of the geomagnetic field (H) in the lower panel as a result of the tangential discontinuity of the interplanetary magnetic field (IMF) from southward to northward in the upper panel [adapted from Ohtani <i>et al.</i> [67]]. . . . .	101
6.2	The horizontal component of the perturbed electric field measured at the magnetic equator is comparable to the east-west component of the interplanetary electric field measured at ACE spacecraft [adapted from Kelley <i>et al.</i> [47]] . . . . .	102
6.3	Four categories of solar wind origins in the Solar Corona. Adapted after Xu and Borovsky [124] . . . . .	103
6.4	Separation of four solar wind categories in (a) 3-D plot of $S_p$ , $v_A$ , and $T_{exp}/T_p$ and (b) 2-D plot of $S_p$ and $v_A$ . The blue points are the ejecta, the red points are the coronal hole wind, the green points are the streamer-belt wind, and the purple points are the regions around sector reversals. Adapted after Xu and Borovsky [2015]. . . . .	105
6.5	Testing the solar wind data in OMNI dataset against 4-categorization scheme during (a) solar maximum and (b) solar minimum conditions. . .	106
6.6	(a) Parker spiral model for the advection of magnetized plasma parcels in the solar wind, and (b) the probability distribution function of the solar wind speed dependence on arrival angle at 1 AU. . . . .	108

6.7	A comparison of the error in the arrival time between different methods (flat delay, MVAB, and MVAB-0) for calculating the solar wind time delay [adapted from Mailyan <i>et al.</i> [59]]. . . . .	109
6.8	Comparison of the location of ACE and IMP8 in the heliosphere to other spacecraft such as WIND and Geotail. ACE stays in its halo orbit at the first Lagrangian point and IMP8 orbits the Earth and stays outside the nominal bow shock location most of its orbital time. [Adapted after Haggerty <i>et al.</i> [33]] . . . . .	111
6.9	Two comparisons between the solar wind speed (first-panel), density (second-panel), and magnetic field (third-panel) measured at IMP8 spacecraft to those measured at ACE spacecraft and are the advected to IMP8 location. The calculated pointwise advection time (time-lag) is shown in the fourth-panel. The comparisons are made between these solar wind parameters that are measured in Summer 1998 (a) and Summer 2000 (b) that show different solar wind status. . . . .	113
6.10	Uncategorized Kernel Density Estimation (KDE) functions of solar wind wind that are measured at IMP8 spacecraft based on three years of advected measurements from ACE spacecraft to the IMP8 location using the flat-delay method. The vertical blue lines represent the interval of solar wind speeds measured at ACE. . . . .	115
6.11	Categorized Kernel Density Estimation (KDE) functions (streamer-belt-origin in green and coronal-hole-origin in red) of solar wind speed at IMP8 spacecraft based on three years of advected measurements from ACE spacecraft, compared to the uncategorized KDE functions (solid black line). The vertical blue lines represent the corresponding interval of solar wind speed at ACE. . . . .	116
6.12	An ensemble of solar wind speed at IMP8 location based on one-point of measurements at ACE spacecraft on Jan-Mar 2003 by using the KDE functions generated for the solar wind data in 1998 - 2000. . . . .	118

## List of Tables

3.1	Ionosphere background parameters based on IRI07, NMSIS00, and IGRF12 empirical models for the ionosphere and neutral atmosphere compositions densities and the geomagnetic field components. . . . .	39
6.1	Average solar wind parameters at 1 AU during a solar minimum [105]. . . . .	104

# Chapter One: Aeronomy and Space Weather

Aeronomy is an interdisciplinary field of space science that studies the interaction between our neighbor star, the *Sun*, and the upper regions of the atmosphere, such as the thermosphere, ionosphere, magnetosphere. In addition, aeronomy is interested in studying the coupling between different components in space between the Earth and the Sun, such as 1) coupling between the solar wind and the magnetosphere, 2) the upper and lower atmosphere regions, and 3) the thermosphere and ionosphere. Sidney Chapman introduced the term *Aeronomy* during the General Assembly of the International Union of Geodesy and Geophysics held in Rome in 1954. This was a few years before the launch of Sputnik-1 to orbit the Earth in 1957.

The birth of the space weather field of research started after Carrington [1859] reported the largest solar storm recorded in the history of space science in September 1859. The next day when the storm reached the Earth it was strong enough to power the telegraph lines with no external power sources, where the telegraph stations were able to communicate and send messages to each other without powering the telegraph lines. Since then, the impact of space weather on daily human technological activities has been considered comparable to that of terrestrial weather. This has been demonstrated in multiple recent incidents, such as the major blackouts in some big cities and Global Navigation Satellite System (GNSS) receiver impairment during severe solar storms and some magnetic sub-storms [17].

The status of the Earth's ionosphere reflects the current conditions of space weather either directly by the precipitation of energetic particles or indirectly by the coupling with the magnetosphere and solar winds. The plasma turbulence, especially at the low- and high-latitudes, has a strong effect on the availability of navigation systems, which are central to many modern-day applications and aerospace activities [50].

Inside the Earth system, the absorption of the solar radiation in the upper atmosphere creates layers of different levels of ionization that are collectively called the *Ionosphere*. The solar heating flux drives planetary waves, tides, and gravity waves that propagate upward and deposit momentum in the ionosphere global circulation

system. Also, the dynamo mechanisms arising from the neutral atmosphere kinematics generate electric fields in the lower ionosphere that affect its dynamics. Figure(1.1) illustrates the coupling processes that govern the dynamics in the aeronomy system [7].

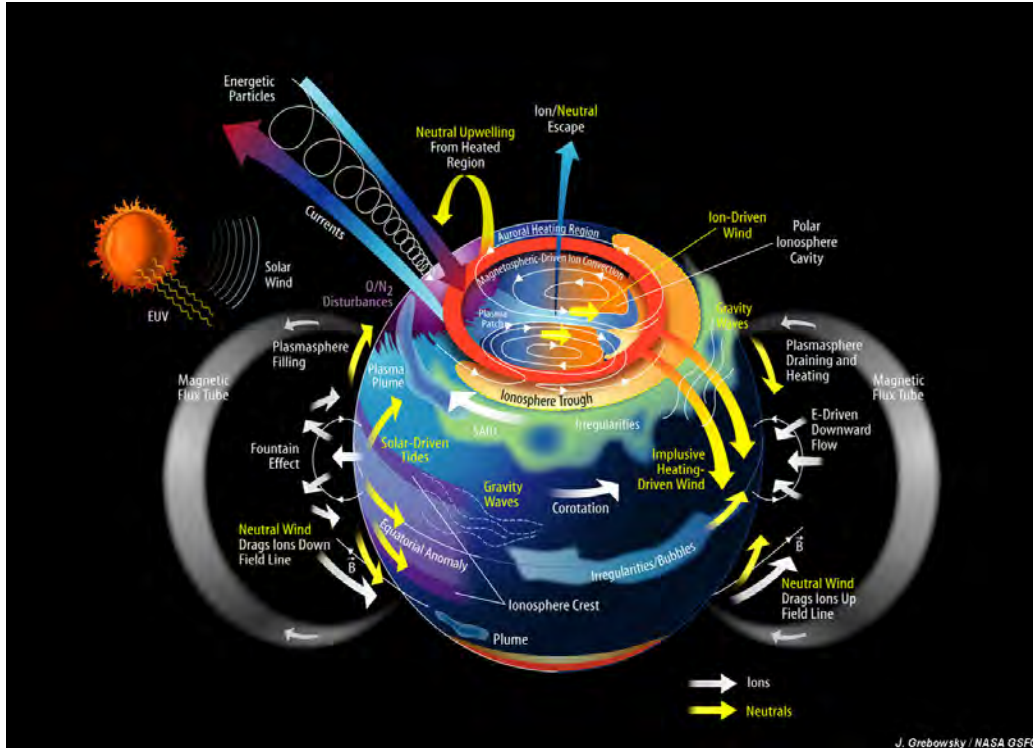


Figure 1.1: A cartoon for the areas of study in the Aeronomy system and the coupling in atmosphere-ionosphere-magnetosphere (AIM) system. Reprinted from the Solar and Space Physics: A Science for a Technological Society report, figure source courtesy of Joe Grebowsky, NASA GSFC

All of these external and internal sources of free energy deposited in the Earth system result in the excitation of different types of plasma instabilities at all regions of the ionosphere. The motivation of this work is to study the turbulence in the ionosphere plasma due to different types of instabilities that can be excited locally in the ionosphere equatorial E-region [27] using a 2-D fluid model that has less computational cost and produce numerical simulation results that are comparable to the corresponding hybrid and fully-kinetic models that has large computational cost.

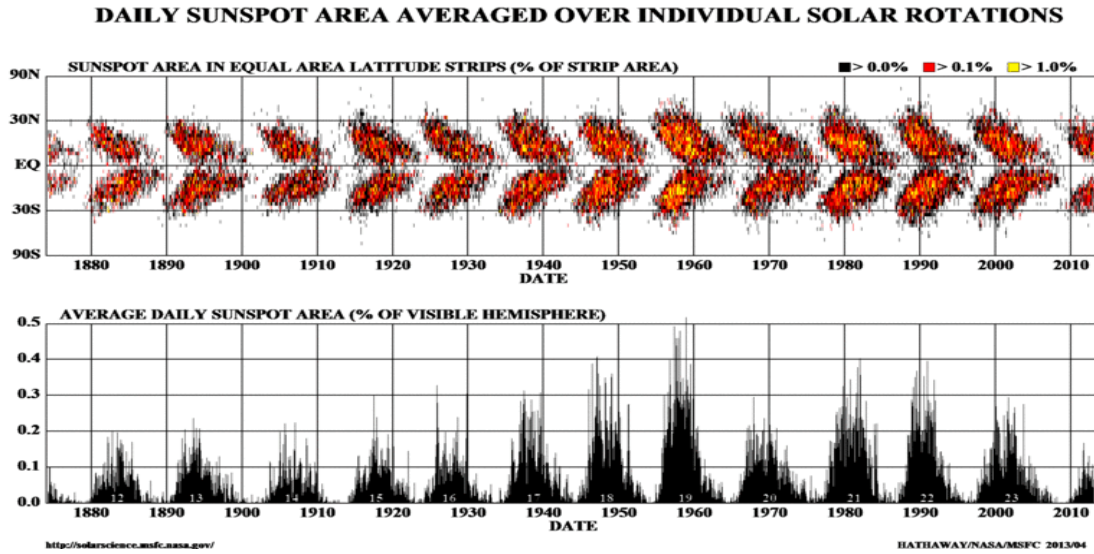


Figure 1.2: The 11 year solar cycles are identified by the number of sunspots that gradually increases from solar minimum to solar maximum cycles (top and bottom) and migrate towards the equator of the Sun as the solar cycle progresses (top), credit to NASA/MSFC.

## 1.1 Solar Activities

The activity on the surface of the Sun has 11 year cycles that are defined by the number of sunspots recorded on the surface of the Sun. In figure (1.2) the location of the sunspots over the solar cycle is shown in the top-panel, and the lower-panel show the variation in the number of these sunspots over the solar cycle. When the surface of the Sun has no or very few sunspots the Sun is said to be in its solar minimum mode, while a large number of sunspots defines the solar maximum. The sunspots are magnetically active areas on the surface of the Sun and because their temperature is less than the surrounding area, they look dimmer in the infrared imaging of the solar corona [51].

Sunspots have polarities and each pair forms a magnetic dipole. The configuration of the magnetic field between the sunspots is very complex. The twists in these magnetic field lines may give rise to magnetic reconnection that releases massive amounts of dense magnetized plasma from the solar corona to the heliosphere. This process is called Coronal Mass Ejection (CME). There are different proposed mechanisms for

the eruption of the CMEs from the surface of the Sun depending on the magnetic field configurations [95].

The solar winds flow from the surface of the Sun into areas of open magnetic field lines. The fast solar winds emerge from the top and bottom solar coronal holes where the magnetic field lines are open. The origin of the slow solar winds on the surface of the Sun is controversial, and there are various arguments about the possibility that they emerge from the area between the closed magnetic loops and open ones [74]. The characteristics of the solar winds are covered in more depth in chapter (6).

## 1.2 Ionosphere

The transmission of the first radio signal across the Atlantic by Marconi in December 12, 1901 triggered the process of discovering the presence of a conducting layer in the upper atmosphere, which was called later the “*Ionosphere*”. After the early work by Stewart[109] and Schuster[102, 103], Kennelly[49] suggested in a short article published in March 1902 that: “*There is well-known evidence that the waves of wireless telegraph, propagated through the ether and atmosphere over the surface of the ocean are reflected by that electrical conducting surface.*” Three months later, Heaviside[38] came to the same conclusion and he stated: “*There may possibly be a sufficient conducting layer in the upper air. If so, the waves will, so to speak, catch on it more or less. Then the guidance will be by the sea on one side and the upper layer on the other side.*” The conducting layer that Kennelly and Heaviside discovered in the upper atmosphere was named originally after their names “*Kennelly-Heaviside Layer,*” and it is known now as “*the E-Layer.*”

The reflection of electromagnetic waves of frequencies equal to or below the characteristic frequency of the plasma, which depends on the local electron density, opened the gates to use ionosonde radars to discover the ionospheric layers of different densities and their corresponding heights. The ionosphere is divided during the daytime into three layers (D, E, and F) according to their different in plasma density, conductivity, and dynamics.

The electron density vertical-profile in the ionosphere during the daytime is different

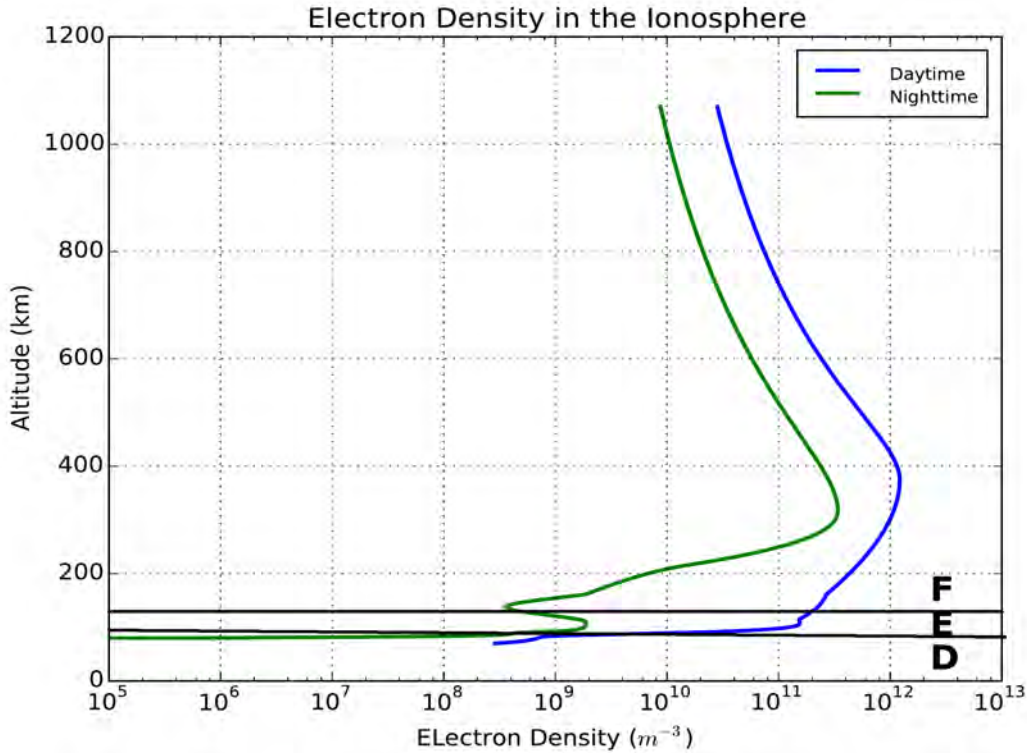
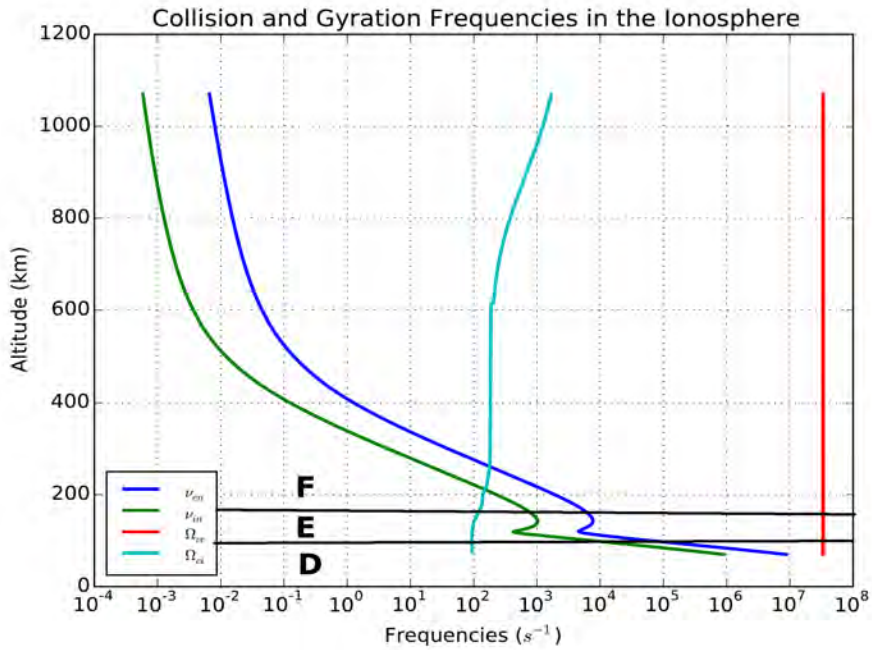


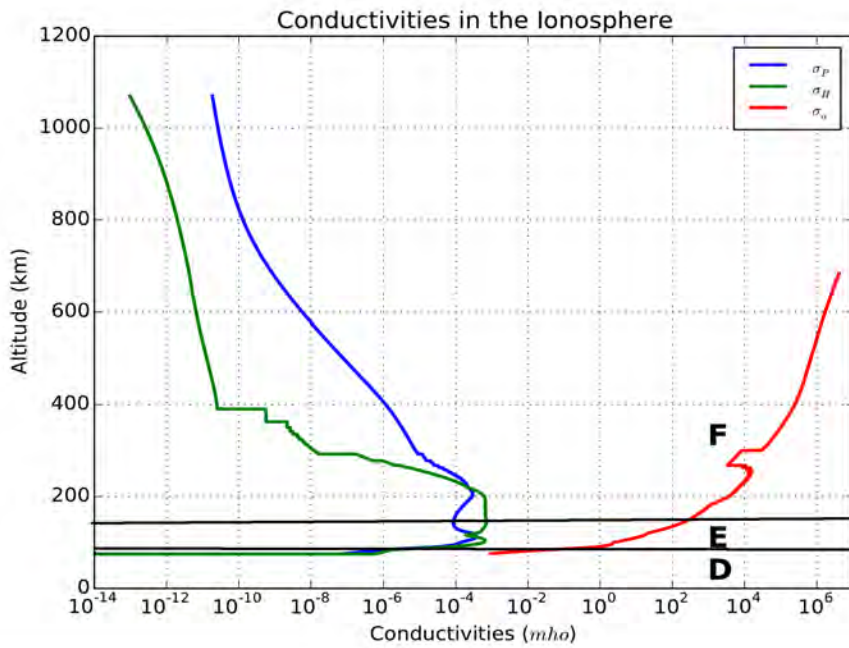
Figure 1.3: The electron density profile in the ionosphere for altitude range 70 - 1070 km at the midnight (green) and noon (blue) times using International Reference Ionosphere (IRI) empirical model.

from its vertical-profile during the nighttime. The large electron density in the daytime is attributed to the large solar flux, which is the main source of ionization. The dominance of the recombination processes between the ions and electrons during the nighttime in the absence of the solar flux causes a drastic decrease in the ionization level [46]. The International Reference Ionosphere (IRI) empirical model is used to plot the electron density profile in the ionosphere as a function of altitude in the range of 70 to 1070 km during the daytime and nighttime, as shown in figure(1.3).

The D-layer is situated at the bottom of the daytime ionosphere and extends over a range of altitudes at 75 - 90 km. The D-layer is characterized by its low electrical conductivity, as shown in figure (1.4-b), due to the large collision frequency of the ions and electrons with the background neutrals compared to their corresponding gyration frequencies (see figure (1.4-a)). In the absence of the solar flux during the



(a) The altitude profile of the Collision and Gyration frequencies for the electrons and ions



(b) The altitude profile of the Parallel, Pedersen, and Hall conductivities

Figure 1.4: The altitude profile of ions and electrons parameters in the ionosphere for altitude range 70 - 1070 km using NMSIS2000, IRI, and IGRF12 models.

nighttime, the D-layer completely disappears due to the fast rate of recombination processes and different chemical reactions [101].

The top layer in the ionosphere is characterized by its high electron density and is subdivided into two layers during the daytime, called  $F_1$ - and  $F_2$ -layer. However, during the night, due to the dominance of the recombination mechanism these two layers are merged into one layer called the F-layer. The average height of the largest density layer is at 350 - 400 km while the layer extends between 200 - 1000 km, as shown in figure(1.3). In the F-layer the ions and electrons are magnetized and they experience cross-field ( $\mathbf{E} \times \mathbf{B}$ ) drifts [46]. This gives rise to a low electrical conductivity in the F-layer, as shown in figure (1.4-b).

The E-layer is characterized by magnetized electrons and collisional ions where  $\Omega_{ce} \gg \nu_{en}$  and  $\Omega_{ci} \ll \nu_{in}$ , respectively, as shown in figure (1.4-a). This makes the E-layer in the ionosphere have the largest Pedersen and Hall conductivities as indicated in figure (1.4-b). The magnitude of net electrical conductivity in the E-region is called the Cowling conductivity. The Cowling conductivity is proportional to the ratio between the Pedersen and Hall conductivities which has its largest value in the E-region around 105 km altitude [46]. This very large electrical conductivity results in a very large current called the electrojet in the equatorial and high-latitude regions. During the daytime, the E-layer extends in 90 - 190 km but it shrinks in altitude during the nighttime.

The density-gradient, temperature-gradient, and gradients in magnetic field excite different types of instabilities in all ionospheric regions. The turbulence in the plasma density due to these instabilities influences the transionospheric radio wave communications and in some cases gives rise to ionospheric scintillation [50]. Ionospheric scintillations make random variations in the amplitude and phase of the propagating radio waves and can cause a loss-of-lock especially in the GPS receivers [41]. Moreover, the presence of a dispersive medium in the upper atmosphere due to its ionization causes a large delay in the radio waves passing the ionosphere which has to be considered while finding the location in GPS receivers [63].

# Chapter Two: An Introduction to the Turbulence in the Equatorial Electrojet

The equatorial electrojet was discovered earlier than the ionosphere in the upper atmosphere. The historical record for the variations in the geomagnetic field aided space scientists in discovering the presence of a strong current in the upper atmosphere, which was called later the “Equatorial Electrojet”. Since that date, the equatorial electrojet has been studied using ionosondes, radars, sounding rockets, and satellites to understand its characteristics and the properties of different types of plasma instabilities initiated in that region. Many theories have been proposed for understanding the physics of the equatorial electrojet and for the different mechanisms driving its instabilities. In this chapter we will give an introduction to the discovery of the equatorial electrojet and a physics model for the generation of its large current density. Then we present the characteristics of the plasma instabilities as determined from radar observations and sounding rocket measurements. Finally, we provide an overview of the theoretical models used to describe the physical mechanisms for driving of and coupling between these instabilities.

## 2.1 Discovering the Equatorial Electrojet

The compass was the first man-made navigation tool used before the development of modern navigation technology. Modern technology consists of, notably, Global Navigation Satellite System (GNSS), especially its first and mature constellation called the Global Positioning System (GPS). Chinese scholars (220 BCE) discovered that a small needle from a lodestone always points to the geographic North in a process they called it “a maternal principle.” They also had found that heating a needle to a very high temperature and then allowing it to cool down while it is oriented parallel to north-south direction will turn this material into a magnet. This idea was used early in the 20<sup>th</sup> century by a Japanese geophysicist named Motonori Matuyama [60] who found that some volcanic rocks from the Pleistocene age or older have their magnetic dipoles of reversed orientations compared to the current orientation of the

geomagnetic field. He attributed that to a reversal process of the geomagnetic field orientation, which requires the disappearance of the magnetic field that shields the Earth from the solar winds and coronal mass ejections from the Sun during the time of reorientation of the geomagnetic field.

Beside its use as a navigation tool, the magnetic compass has been used since its invention for many scientific purposes and in many experiments. For example, the magnetic compass has been used to estimate the inclination and declination of the Earth's magnetic field which explains that the magnetic north pole wanders around the geographic north.

In 1724, Graham [32] reported his experimental results of using a three-needle compass with needles of different lengths to measure the daily variation of the Earth's magnetic field. Graham discovered that the daily variation happens in the mid afternoon and early evening, and he could not give any explanation for these variations in the Earth's magnetic field. More than a century later, Stewart [109] proposed that a transverse current across the magnetic field causes these daily variations in the geomagnetic field. The recorded fluctuations in the measured pressure at the ground was an indicator of the role that the semidiurnal tidal winds play in providing the electromotive force required to generate a current of conducting air in the upper atmosphere [102, 103, 13]. The generation of an electric current due to a thermal motion of the neutral atmosphere is called "dynamo," which is a process of converting the kinetic energy into electrical energy.

Egedal [19] studied the variations in the Earth's magnetic field measured in the geomagnetic observatories located at different latitudes and longitudes, and he reported the presence of a belt of enhanced east-west current centered at the magnetic dip equator and extended in the north-south direction for a distance about 600 km. Finally, Chapman [15] considered the presence of this electric current an abnormal phenomenon and he called it the "*Equatorial Electrojet*."

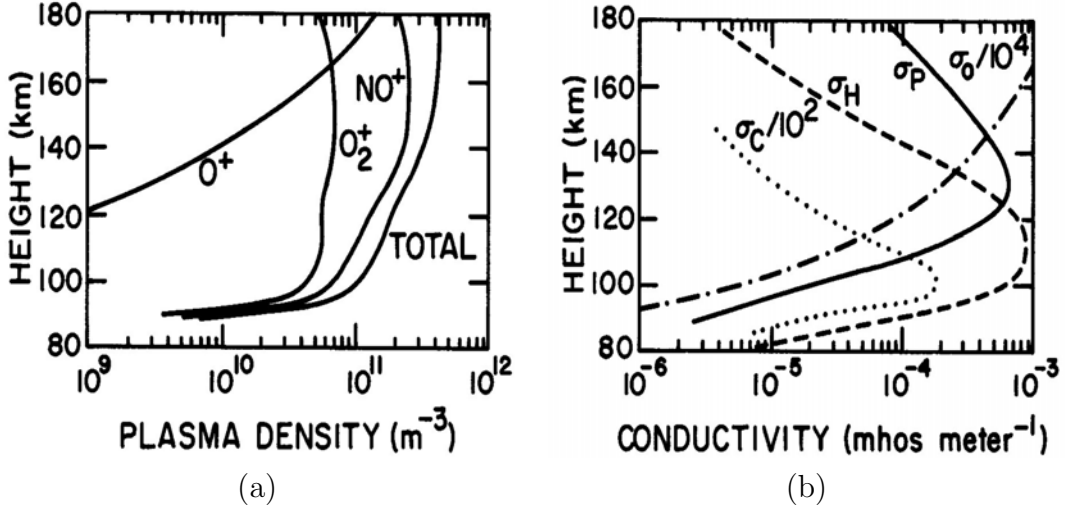


Figure 2.1: A daytime vertical profiles for: (a) the ionosphere plasma density and ion composition, (b) the parallel ( $\sigma_o$ ), Pedersen ( $\sigma_P$ ), and Hall ( $\sigma_H$ ) electric conductivities under average solar conditions [from Forbes and Lindzen [29]].

## 2.2 Physics of the Equatorial Electrojet

The large current found in the equatorial E-region at 103-105 km in altitude is called the “Equatorial Electrojet” and is a result of a dynamo process in the E-region driven by the tidal oscillations of the atmosphere [14]. The Earth rotation and the solar heating cause the diurnal and semidiurnal tides, which are considered the largest atmospheric tides, to be driven in the daytime side of the E-region [21].

The propagation of the diurnal tides perpendicular to the geomagnetic field between  $\pm 30^\circ$  latitudes [46] gives rise to different drifting mechanisms for ions and electrons in that region. The heavy ions, such as  $O_2$  and  $NO$ , which dominate the equatorial E-region, figure(2.1-a), have high collision rates with the neutral background and thus they drift with the diurnal tides speed,  $\mathbf{U}$ . On the other hand, the light electrons are tied to the geomagnetic field and drift with speed  $-\frac{\mathbf{U} \times \mathbf{B}}{B^2}$  in the westward direction. These different electron and ion drifts give rise to a zonal electric field,  $E_y$ , of order 0.5-1.0 mV/m [21]. This magnitude of the zonal electric can not by itself explain the large equatorial current in the E-region, and we need to find another driving factors.

In the E-region, the Hall,  $\sigma_H$  and Pedersen,  $\sigma_P$ , electrical conductivities have their largest magnitudes around an altitude of 110 km, figure(2.1-b). A vertical downward

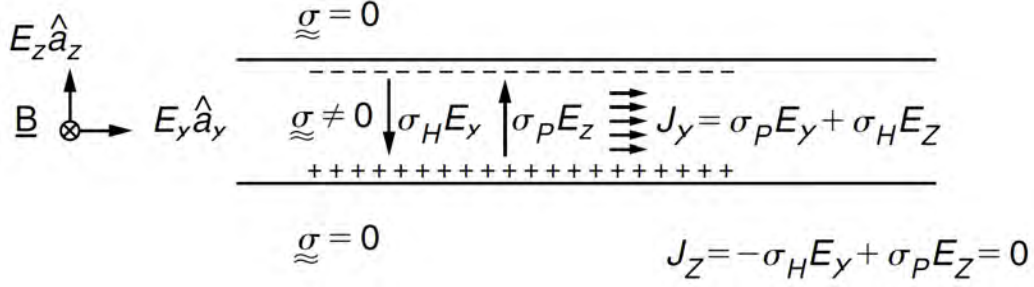


Figure 2.2: The equatorial electrojet current generation mechanism as a dynamo process followed by combination of Pedersen and Hall electric fields [from Kelley [46]].

Hall current,  $\sigma_H E_y$ , is generated from the zonal electric field,  $E_y$ . However, because the current is divergence free,  $\nabla \cdot \mathbf{J} = 0$ , a polarization electric field is established due to the accumulation of the positive ions and electrons at the bottom and top sides of the layer, respectively, see figure(2.2), and a Pedersen current is generated,  $\sigma_P E_z$ . The presence of (almost) nonconducting layers around the E-region helps this polarization electric field to persist<sup>1</sup> and to keep inhibiting the downward Hall current. Therefore, the net vertical current in this region is zero and it is given by:

$$J_z = -\sigma_H E_y + \sigma_P E_z \approx 0$$

$$E_z \approx \frac{\sigma_H}{\sigma_P} E_y \quad (2.1)$$

The large ratio between the Hall and Pedersen conductivities at 105-110 km altitude ( $\sigma_H/\sigma_P = 15 - 20$ ) [46, 21] gives rise to a large vertical electric field,  $E_z$ , which contributes to the electrojet current. Then, the total horizontal current is given by sum of the Pedersen and Hall currents as:

$$J_z = \sigma_P E_y + \sigma_H E_z \quad (2.2)$$

Using equation(2.1) into equation(2.2), we get:

$$J_z = \sigma_C E_y \quad (2.3)$$

---

<sup>1</sup>The plasma in the D-region is highly collisional which reduces the conductivity of this layer, however, the very low collision rates of ions and electrons in the F-region make both of them tied to the geomagnetic field and drift with the same  $\mathbf{E} \times \mathbf{B}$  speed which also reduces the layer conductivity.

where,  $\sigma_C$  is called *Cowling* conductivity, which is the effective conductivity in the equatorial electrojet region, and it is given by:

$$\sigma_C = \frac{\sigma_H^2}{\sigma_P} + \sigma_P \quad (2.4)$$

Showing that the horizontal electrojet current is dominated by the Hall conductivity and the vertical electric field, the coupling between the E-region dynamo driven by the diurnal and semidiurnal tides and the large Cowling conductivity in that region causes the generation of that large horizontal electrojet current due to a relative drift between the ions and electrons that reaches 800 m/s in some cases.

## 2.3 The Equatorial Electrojet Instabilities

The instabilities of the equatorial electrojet have been studied for more than seven decades. It was found from radar observations and rocket in-situ measurements that there are two main types of instabilities in the equatorial E-region; the Farley-Buneman and Gradient-Drift instabilities. In the following subsections we are going to describe in brief detail the observations and measurements of the equatorial electrojet instabilities and the theories that arise to explain the physics of these instabilities.

### 2.3.1 Radar Observations

Radar scattering technique has been used for decades to *continuously* observe the plasma irregularities in a certain region of the ionosphere, which is not possible with other techniques such as sounding rockets and satellites (except geosynchronous satellites). The radar is used in studying the dispersive media that have a wavelength dependent refractive index which is the case in the ionosphere.

There are three mechanisms for observing the ionosphere using radar technique depending on the radar operational frequency. The HF-radars (or ionosondes) operate at the *local* characteristic frequency of the ionosphere plasmas which causes total or partial reflection of the transmitting signal. This technique can be used to examine the variation of the ionosphere density in different layers and find regions of maximum electron density. When the transmitted wave frequency is much larger than the characteristic frequency of the plasma, the thermal motion of the electrons in

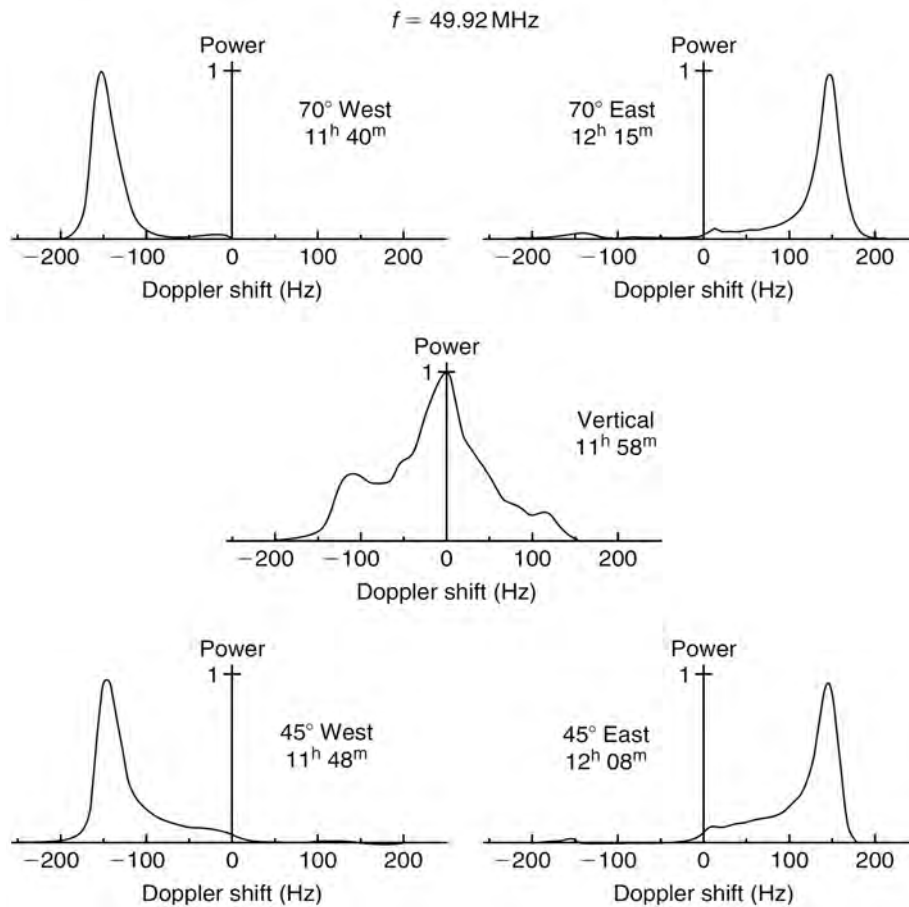


Figure 2.3: The spectrum of Type-I fluctuations as measured at at 50 MHz at different elevation angles in both sides of the vertical line. The spectra are normalized to the peak value and measured as a shift from the radar central frequency. [From Cohen and Bowles [16]]

the ionosphere plasma causes an incoherent scattering to the transmitted signal and incoherent scattering radars should be used. However, the turbulence in the electron density due to different mechanisms of plasma instabilities gives rise to a coherent scattering. The name “*coherent scattering*” comes from the spatial and temporal coherency of the ionosphere irregularities on the Bragg scale in the radar echoes.

In 1963, Bowles *et al.* [9] used the radar backscattering experiment at 50 MHz at Jicamarca, Peru to study the echoes of the field-aligned irregularities in the equatorial electrojet (EEJ). Between 1967 and 1978, the experiment was repeated for different

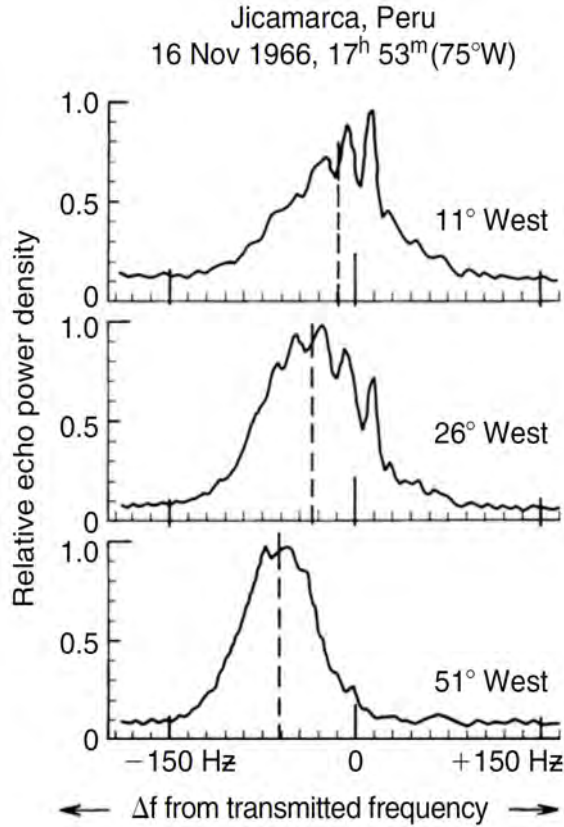


Figure 2.4: The spectrum of Type-II fluctuations as measured simultaneously at 50 MHz by antennas at different zenith angles. The spectra are normalized to the peak value. [From Balsley [6]]

case studies by Cohen *et al.* [16], Balsley [6], Balsley and Farley [4], Farley and Balsley [22], Balsley *et al.* [5], and Fejer *et al.* [25, 26, 23] in order to examine the characteristics of the backscattered echoes with the goal of understanding the mechanisms of the E-layer plasma irregularities at the equatorial region and high-latitudes.

When the electron drift velocity in the equatorial electrojet exceeds the ion-acoustic speed<sup>2</sup>, an echo spectrum appears simultaneously at all elevations and its Doppler shift always equals the ion-acoustic speed to a good approximation. In figure(2.3), the Doppler shift is the same for different elevation angles in either the east or west to the radar location. Also, the Doppler echoes show a westward drift of the plasma

<sup>2</sup>The ion-acoustic speed in the plasma is close to the sound speed of the neutral atmosphere in the E-region.

irregularities (during the day) with speed of 450 m/s. The spectrum of the radar echoes is characterized by a spectral width narrower than the echoes' Doppler shift. The Doppler shift of the echoes is isotropic in the angle between the horizontal plane and the wave propagation wavevector,  $\theta$ . The instability with these characteristics is called the Type-I instability [9, 6, 25].

However, as the electron drift speed falls below the ion-acoustic speed, the backscattered radar echoes exhibit different spectral characteristics and we have now what is called the Type-II instability. Despite the increase of the spectral width of Type-II echoes with the wavenumber, it does not change appreciably with the elevation angle as shown in figure(2.4). The Doppler shift of the Type-II instability varies as the cosine of the angle between the horizontal plane and the wave propagation wavevector ( $\theta$ ) and varies linearly with the wavenumber at constant angle  $\theta$  [9, 6, 25, 34]. The type-II instability is always easily excited in the presence of a density-gradient [107, 39, 58, 52, 86, 91, 4] and owing to the absence of a real electron drift threshold [22], the type-II instability is difficult to observe in the presence of the type-I instability which is excited in a strong turbulence mechanism [113, 111].

The echoes for the type-I and type-II instabilities can be seen both during the daytime and nighttime. The strong damping of the instabilities above 115 km, as a result of the carrier's recombination processes and the negative density scale-length, limits these echoes in the daytime to the altitude region between 93 and 113 km. However, the irregularity in the electron density profile during the nighttime, which gives rise to irregularity in the density gradient, extends the instabilities beyond 113 km and the echoes can be seen up to 130 km as reported by Kudeki *et al.* [54].

Shortly after sunset the radar backscattered data of the electrojet shows an inverse of the sign of its phase velocity. The change of the sign in the phase velocity is a primary evidence for the reversal of the flowing direction of the electrons and ions in the equatorial electrojet, where the electrons reverse the daytime westward flow to an eastward flow during the nighttime. Figure(2.5) shows that the electrojet reversal is accompanied by a disappearance of the instabilities echoes [25]. Also, the structure of the electrojet is different before and after sunset, where we can see two layers of echoes in the daytime; one below 103 km and the other above 113 km, figure(2.5-top),

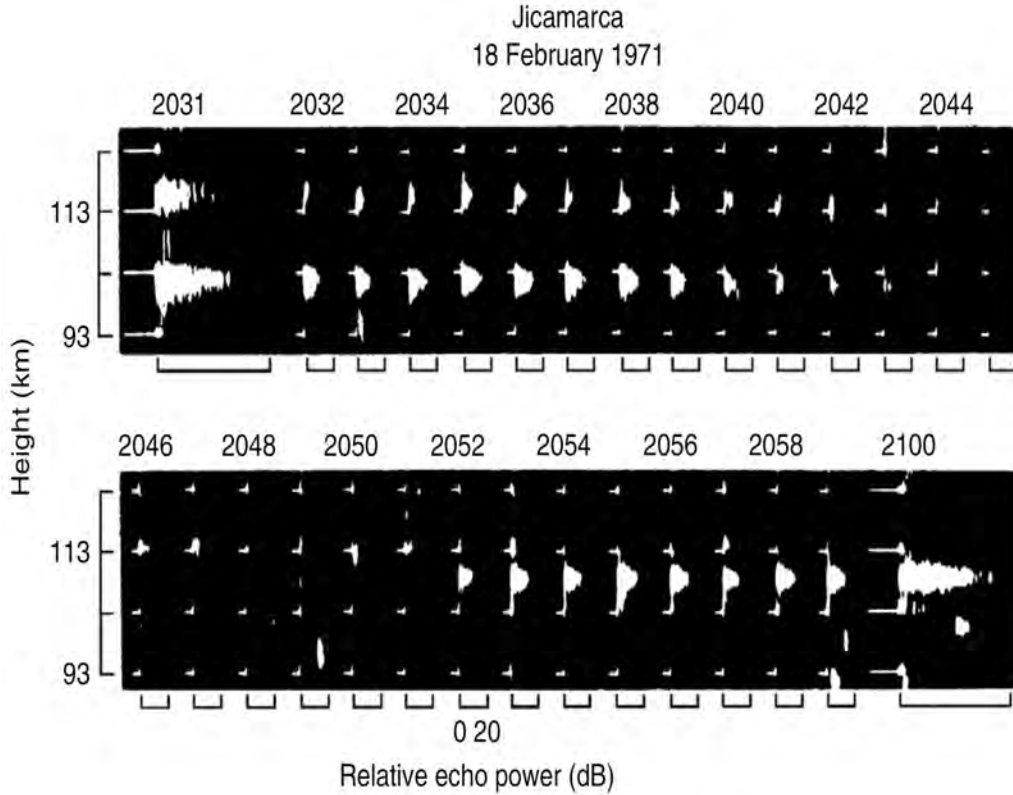


Figure 2.5: Snapshots of the spectrum in the radar echoes of the scattering regions before (top) and after (bottom) the phase reversal of the electrojet. [From Fejer [25]]

whereas there is only one echoing layer centered at 110 km after the sunset, as shown in figure(2.5-bottom).

Balsley and Farley [4] shows the radar data at 50 MHz and 146-MHz frequencies that emphasize the dominance of the type-I instability in the spectrum of the radar echoes at both frequencies when the electron drifts reach the threshold of the type-I instability as their speed go beyond the ion-acoustic speed ( $v_E \geq C_s$ ). There is, however, no practical threshold for the type-II instability, as discussed earlier, that can be detected at the HF radar echoes (50-MHz) but the type-II echoes can not be seen at the VHF radar echoes (150-MHz). This means that the type-I instability dominates at this higher radar frequency with structure sizes of order 2 meters.

In figure(2.6), the three peaks show the dependence of the phase velocity on the operating frequency of the radar, which reflects the smallest size of irregularities that

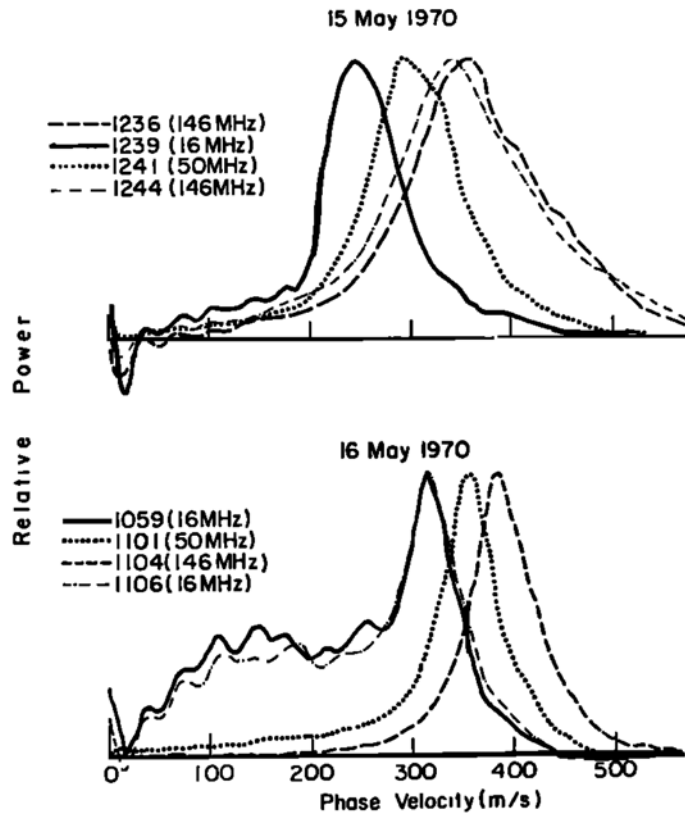


Figure 2.6: A comparison between the spectra of a scattering region taken simultaneously at three different frequencies for two successive days show the dominance of type-I spectrum and the dependence of the Doppler shift on the operating frequency of the radar. [From Balsley and Farley [4]]

can be detected<sup>3</sup>. These measurements indicate the presence of irregularities of different scale lengths that range from a kilometer or tens of meters scales due to pure type-II instability down to a sub-meter scale size due to the pure type-I instability. In addition, the small temporal variations of the echoes are illustrated by taking measurements at the same frequency in different times and measurements in different days, (146 MHz in May 15, 1970 at the top panel and 16 MHz in May 16, 1970 at the bottom panel).

Recently, a combined system of five radars was used at Jicamarca on July 26, 2006

<sup>3</sup>The smallest size of ionosphere irregularity that can be detected by a radar equals half of the wavelength of the radar transmitted signal,  $\omega_{echo} = k_{plasma} \cdot v_{drift}$ .

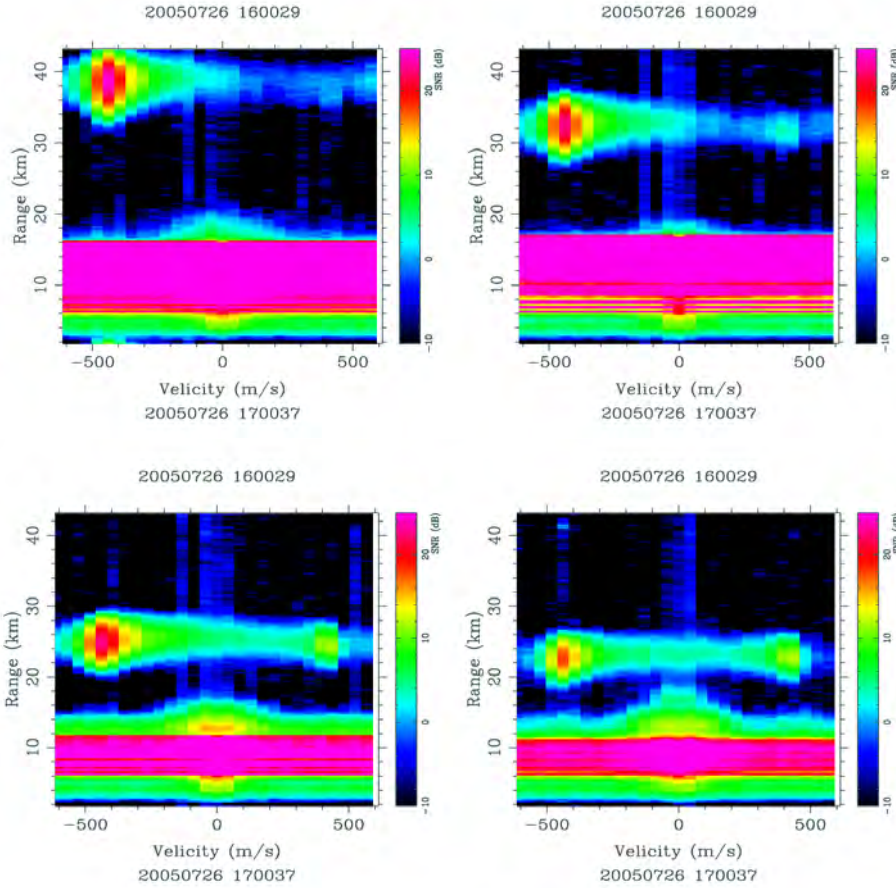


Figure 2.7: Spectrogram for the backscattered echoes from the AMISR prototype radar at Jicamarca at different zenith angles ( $-32^\circ$ ,  $-24^\circ$ ,  $-12^\circ$ ,  $0^\circ$ ) to show the east-west symmetry in the equatorial electrojet plasma flux. [From Hysell *et al.* [43]]

to monitor the equatorial electrojet, including range-time-intensity (RTI) mapping, radar imaging, radar oblique scattering, Faraday rotation, and multiple frequency scattering using AMISR prototype UHF radar [43]. Radar imaging data shows narrow type-I echoes excited from the vertically polarized electric field of the large-scale waves which is different from the type-I echoes excited directly by the background electrojet current. Hysell *et al.* [43] found stronger echoes come from the upward flux at the spectrograms from the AMISR prototype radar at Jicamarca, when he compared the red-shifted spectral lines to the blue-shifted spectral lines in figure(2.7). Hysell *et al.* [43] considered that difference in the echoes is a primary evidence for the “up-down” asymmetry in the vertical particle fluxes. In addition, another asymmetry

in the irregularity drifts is found in “east-west” direction with more westward drift during the daytime, where the stronger echoes along the westward zenith, compared to echoes along eastward zenith which can be observed in figure(2.7).

### 2.3.2 Sounding Rocket Observations

Sounding rockets are another way to study the ionosphere locally, because they provide in-situ measurements for the ionosphere irregularities that result from different instability mechanisms in plasma. The use of sounding rockets started early in the 50s using ships in the South Pacific near Peru [82], however most of the rocket missions before 1983 were flown with relatively high apogees and so they did not provide high resolution measurements of the equatorial electrojet.

In 1972, Prakash and colleagues in the India rocket group showed their measurements from a rocket mission above Thumba, India, [84]. The electron density profile during the daytime, as shown in the left-panel of figure(2.8), were found to have an upward (positive) gradient at 90 - 107 km in altitude. However, during the nighttime the electron density profile is jagged and shows regions of upward (positive) and downward (negative) gradients, as shown in the right-panel of figure(2.8). A similar density profile was shown by Pfaff and his colleagues from the measurements of a sounding rocket mission above Peru (daytime - 1975) and Kwajalein (nighttime - 1978) [78, 79]. The unstable density gradient<sup>4</sup> was found to have a scale-length between 6 - 10 km during the day and 1 - 2 km during the night.

The daytime density fluctuations in the unstable region of the ionosphere plasma are characterized by unstructured oscillations of short-wavelength (1 - 15 meters) and have a maximum amplitude of  $\delta n = 1\%$  between 103 and 105 km, see figure(2.8-left). Stronger irregularities are observed during the nighttime due to the east-west switching of the ambient vertical electric field along with the jagged vertical profile of the zero-order electron density. The strong negative gradient between 120 and 130 km during the nighttime drives large irregularities of wavelength of order 300 meters and up to 30% amplitude in the fluctuating density [21]. The formation of these large scale irregularities at the top part of the electrojet shows the role that the downward

---

<sup>4</sup>The zero-order density gradient is considered unstable when it points in a direction parallel to the vertical component of the ambient electric field [21].

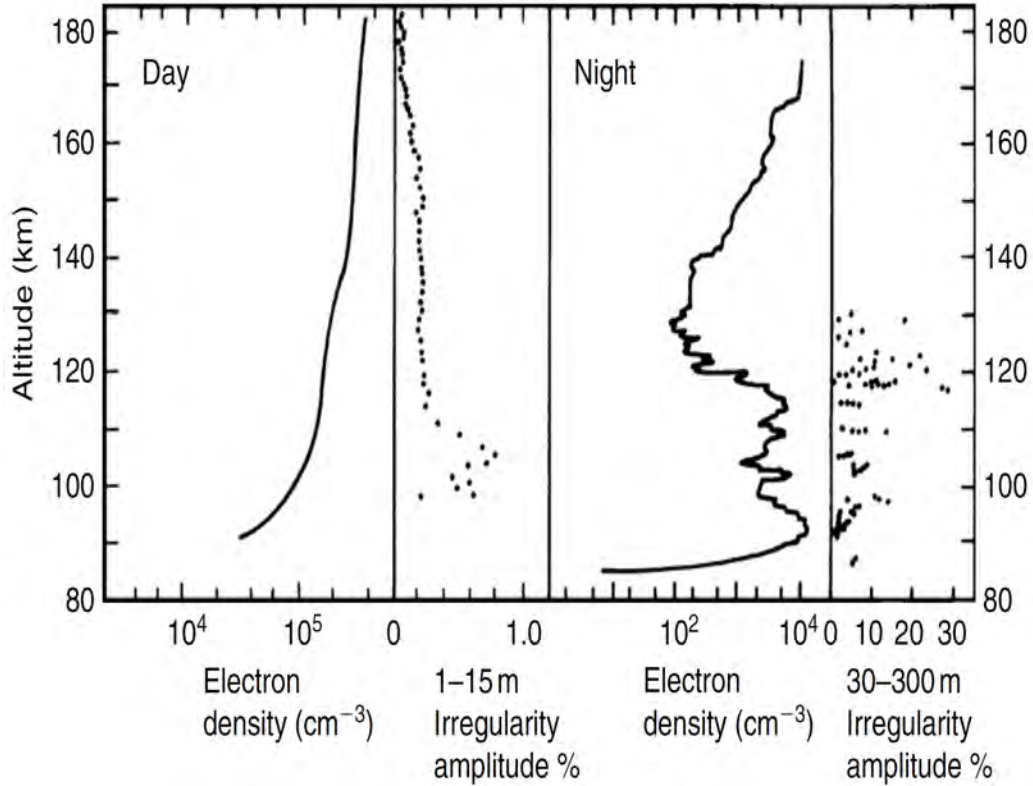


Figure 2.8: The vertical profile of the electron density and the sizes of the irregularities as a function of altitude in the daytime (left-panel) and nighttime (right-panel). [From Prakash *et al.* [84]]

gradient-drift instability along with a downward ambient vertical electric field play to generate them during the nighttime.

Pfaff *et al.* [80, 81] showed the data collected from a sounding rocket launched from Punta, Lobos, Peru in order to quantify the plasma instabilities by detecting the turbulence in the daytime plasma density and electric field in the equatorial electrojet. A simultaneous measurement taken by the Jicamarca radar showed strong type-I echoes of 3 m wavelength accompanied by long-scale horizontally propagating waves with phase velocity equal to the ion-acoustic speed [54].

The data in the frequency-altitude sonogram in figure(2.9) shows a maximum spectral density below 100 Hz. This strong spectral feature is attributed to the long-wavelength irregularities excited in the region of positive (unstable) density-gradient

33.027 - Punta Lobos, Peru  
March 12, 1983  
10:35 L.T.

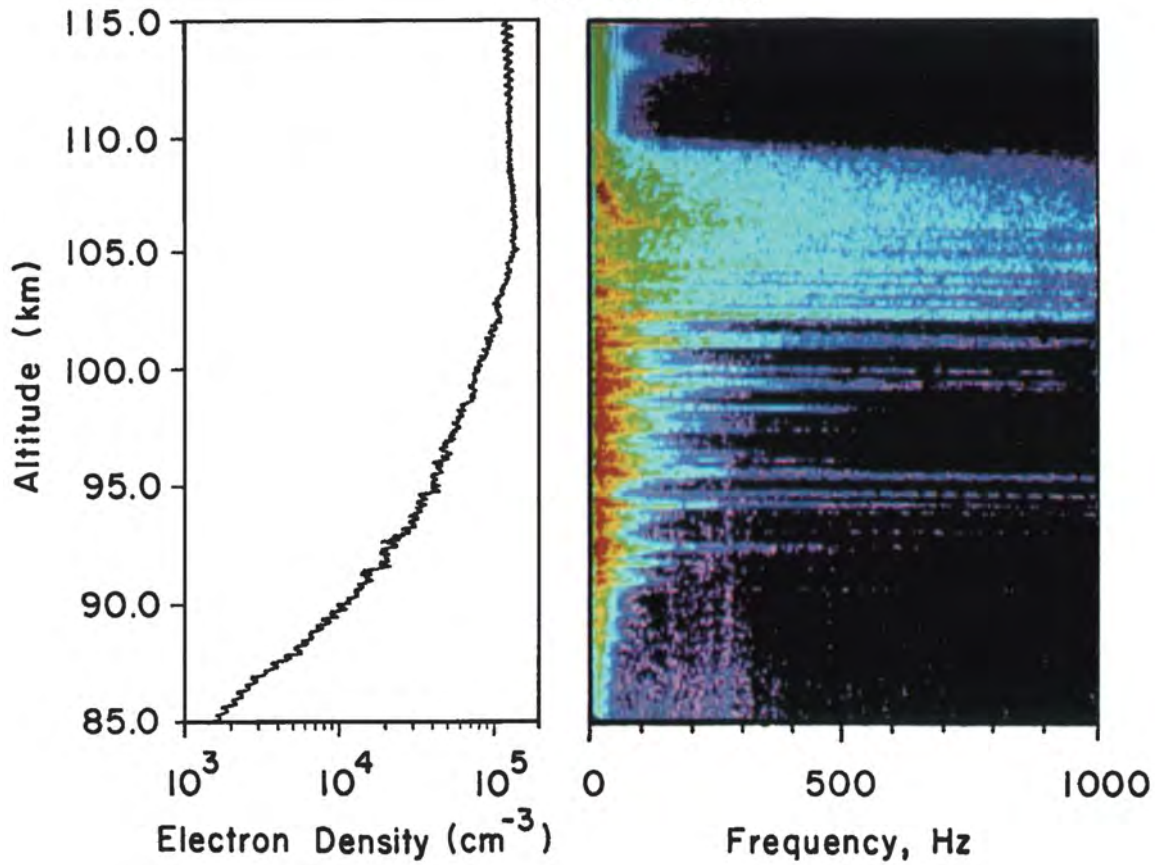


Figure 2.9: The vertical profile of the plasma density (left) and spectrum of the electric field wave (right) measured at the upleg. [From Pfaff *et al.* [80]]

between 90 - 107 km altitude. However, short-wavelength irregularities are characterized by their high-frequency (100 - 1000 Hz) in spectral density of the electric field in the range between 103 - 113 km altitude as a result of the collisional two-stream instability.

Pfaff *et al.* [81] used the frequency-altitude sonogram to divide the backscattering echoes into three regions of different instability mechanisms: region-1 between 90 and 103 km with a dominance of gradient-drift (type-II) instability where the spectrum peaks at low-frequencies, region-2 between 103 and 108 km where a coupling between two-stream (type-I) and gradient-drift (type-II) instabilities is taking place, and region-3 between 107 and 113 km with the dominance of pure two-stream (type-I) instabilities with a strong spectrum at high-frequencies. The region above 107 km has no gradient-drift instability due to the coincidence of a negative zero-order vertical density-gradient and upward electric field. In addition, the electron density scale-length calculated from the left-panel of figure(2.9) is roughly around 7 - 10 km and it increases as we go higher in altitude.

Figure(2.10) shows waves of long-wavelength ( $\approx 1.6km$ ) propagating in the east-west direction for both the electric field and electron density. The fluctuating electric field ( $\delta E$ ) and the normalized electron density ( $\delta n/n$ ) are found to be in phase as indicated by the vertical lines in Figure(2.10), where the regions of density enhancements (depletions) were observed coincident with regions of westward (eastward) electric fields. Also, these waves were found to have large amplitudes of order 10 - 15 mV/m for the electric field that corresponds to a 10 - 15% amplitude of the electron density fluctuations. The propagation of these waves in the horizontal direction (perpendicular to the magnetic field ) elucidates the electrostatic nature of these waves, which was also found in the observation of the fluctuating electric field.

In the region of stable plasma density-gradient ( $\geq 107$  km), there are two different types of primary two-stream waves propagating perpendicular to each other. The vertically propagating 3 meters waves have a measured amplitude of 1 mV/m rms, however, the horizontally propagating waves have wavelength less than 10 meters. The measured amplitude of the east-west propagating two-stream waves was roughly 2 mV/m with density fluctuations of 1 - 2% rms. In contrary to the phase relation

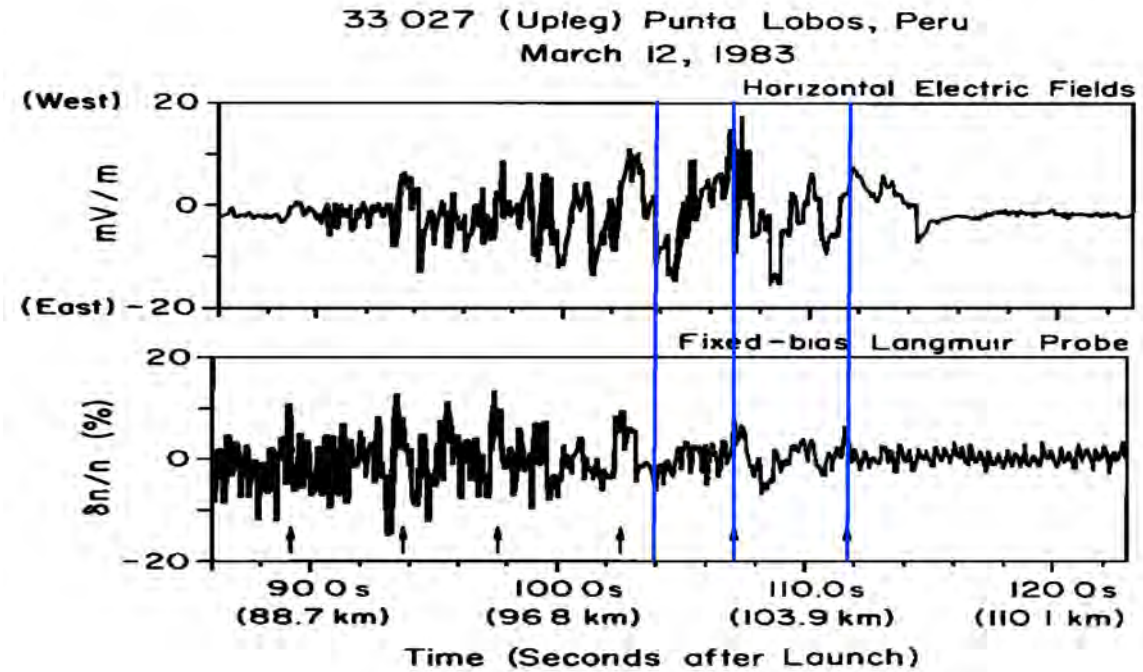


Figure 2.10: The perturbed electric field wave in the east-west direction with amplitude variation of  $\pm 10 - 15$  mV/m (up) and the normalized fluctuations in the electron density (bottom) as measured at the upleg. [From Pfaff *et al.* [81]]

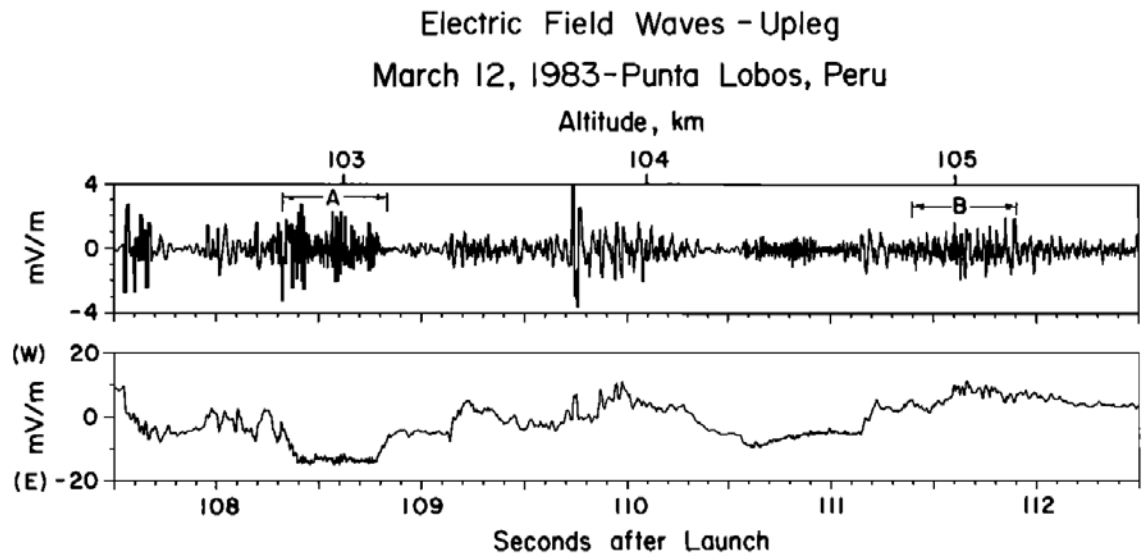


Figure 2.11: The variations in the vertical (up) and horizontal (bottom) electric field waves as measured at the upleg. [From Pfaff *et al.* [81]]

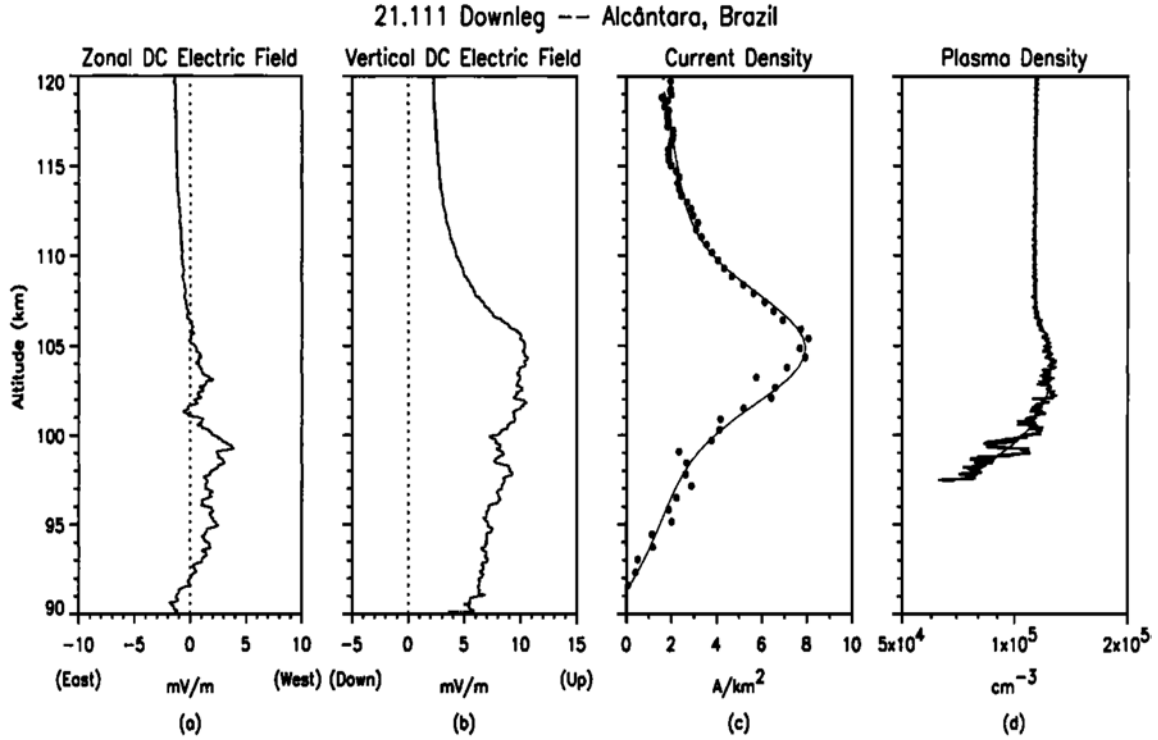


Figure 2.12: The horizontal DC electric field (a) changes its direction from eastward to westward around 105 km and its peak value is ranged in  $\pm 1 - 3$  mV/m. The vertical DC electric field (b) is directed upward and has a maximum value of 10 mV/m. The peak value of the calculated electron current density (c) is at altitude 105 km. The profile of the fluctuation in the electron density (d) shows a large fluctuation in the region of large density-gradient scale-length. [From Pfaff *et al.* [83]]

between the horizontal fluctuating electric field and density, the vertical fluctuating electric field was found to have a 180 phase difference with the fluctuating plasma density waves.

The electric field components in figure(2.11) shows a slowly varying horizontal perturbed electric field that fluctuates between  $\pm 10 - 15$  mV/m, which is of the same order of magnitude as the vertical DC polarized electric field and an order of magnitude larger than its zonal component. This large strength of the horizontal component of the electric field drives secondary two-stream and gradient-drift vertically propagating waves. However the vertical, rapidly oscillating, component of the electric field has a maximum amplitude between  $\pm 4$  mV/m [81] and is characterized by its

wave-packet structure. This wave-packet structure of the secondary two-stream waves elucidates the influence of kilometer-scale irregularities of the horizontally propagating electric field fluctuations on the small structures for type-I instability.

Later in 1997, Pfaff *et al.* [83] described the measurements gathered from the in-situ sounding rocket that was launched from *Alântara*, Brazil in 1994. Pfaff and his colleagues found a maximum daytime vertical electric field of about 9 - 10 mV/m near 105 km altitude coincident with a maximum current density of magnitude  $8.0\mu A/m^2$ , figure(2.12). The maximum vertical electric field corresponds to 360 - 400 m/s westward electron drift, which is about the ion-acoustic speed calculated at the same altitude. These measurements agree with the estimated large electrojet Hall current and Cowling conductivity estimated at about the same altitude.

### 2.3.3 Theoretical Interpretation

In 1973, Sudan *et al.* [113] uses the two-step mechanism to explain the generation of the meter scale Type-II irregularities detected by 50-MHz incoherent scattering radar at electron drifts of order 100 m/s. The gradient-drift instability is excited in the daytime with positive density gradient and westward drift of the electron. When the amplitude of large-scale instability reaches a certain level, the energy starts to transfer from that primary long-wavelength waves to the secondary short-wavelength waves. This energy transfer takes place due to the strong perturbations of the electrojet local parameters, where the horizontal density gradient becomes greater than the background vertical gradients and the magnitude of the vertically perturbed drifts increases to the order of magnitude of the horizontal electron drift [22]. However, the excitation of vertical irregularities of wavelength of the order of meters or sub-meter is a pure type-I nonlinear mechanism that takes place only when the electron drifts exceed the ion-acoustic speed [113].

On the other hand, the dependence of the phase velocity of type-I instability on the cosine of the angle between the horizontal plane and the wave propagation wavevector,  $\theta$ , in the linear theory is not supported by the observations [111]. The phase velocity which equals the Doppler shift is independent of the angle  $\theta$  and has a constant value that equals the ion-acoustic speed [6, 22, 34], and various mechanisms have been suggested to explain these observations. Kamanetskaya [44], Rogister [90],

and Sato [98] used quasilinear theory to limit the electron drifts to the ion-acoustic speed, but they assumed a uniform horizontal drift for the electrons, which is not consistent with the radar observations for long-scale irregularities of type-I instability.

Kaw [45] suggested the convection of the waves by refraction in a horizontally stratified electrojet. Considering electrojet stabilization by the convection mechanism, the radar observations should show a signature for (only) negative Doppler shifts coming from the top of the electrojet and (only) positive echoes coming from bottom the part as a result of the corresponding reflection and refractions, but no negative Doppler shifts can be found in the observations. Also, this mechanism does not account for the simultaneous appearance of type-I echoes at different zenith angles which can be seen in the radar observations in figure (2.3).

The nonlinear orbital diffusion mechanisms of ions and electrons were proposed by Skadron and Weinstock [108] and Weinstock and Sleeper [120], respectively. This mechanism depends on the random perturbation of the ion and electron orbits with the large amplitude of short-wavelength electric field waves. Thus, a stabilization in the growing modes at the ion-acoustic speed due to the increase of the electron collision frequency with the amplitude of the growing waves (which enhances the electrons diffusion) will take place. This mechanism gives rise to a phase velocity that is dependent on the electron  $E \times B$  drift speed, which does explain the ion-acoustic speed limit of the phase velocity found in the radar observations.

Sudan *et al.* [111, 112] has also treated this problem differently by considering the coexistence of the two types of instabilities and the effect of the developed type-II strong turbulence on the evolution and development of type-I instability. Sudan *et al.* [112] suggested that the nonlinear process modifies the electron-neutral collision frequency  $\nu_{en}$  by a wave-amplitude dependent value that causes the growth rate to vanish in the saturation region.

# Chapter Three: Modeling the Equatorial Electrojet Instabilities

<sup>1</sup>After the coherent backscattering radar observations of type-I<sup>2</sup> and type-II<sup>3</sup> instabilities at Jicamarca by Bowles *et al.* [9], the mechanism of type-I instability was studied by Farley [20] and Buneman [10], however, the mechanism of type-II instability was interpreted by Simon [107] and Hoh [39]. Later, many self-consistent models have studied the turbulence in the equatorial electrojet region that arise from the gradient-drift and Farley-Buneman instabilities. Each model aims to provide a physics-based theory to interpret most of the radar observations and rocket measurements.

The large difference between the effective scale-length of these instabilities makes this multi-scale turbulence problem very challenging to be simulated due to the large computation resources required. Also, the common drawback of fluid equations is the absence of the finite mean free-path-effect due to thermal motion, however with strong collisional closures for viscosity and/or heat flux, which are only valid in regimes with short mean-free-path,  $v_{ti}/\nu_{in} < \omega$ , we can retrieve some the thermal properties.

In this chapter, we introduce our effort to have a unified model for both types of instabilities in the equatorial electrojet. We have developed a self-consistent fluid model that unifies both types of instabilities and study the spatial and spectral coupling between them [36]. In this fluid model we include the ion viscosity in the ion's equation of motion with the electrons polarization drift in a model and the ions heat flux in the other model. Both models show linear results that interpret most of the

---

<sup>1</sup>The work in this chapter is based on a collaboration with coauthors in Hassan, E., Horton, W., Smolyakov, A.I., Hatch, D.R., Litt, S.K., Multiscale equatorial electrojet turbulence: Baseline 2-D model, Journal of Geophysical Research, doi: 10.1002/2014JA020387, 2015. The theoretical model has been done in collaboration with Horton and Smolyakov, the simulation code optimization and computational techniques have been discussed with Hatch, and the linear and nonlinear results have been discussed with Litt, Smolyakov, Hatch, and Horton.

<sup>2</sup>Historically called type-I instability for its strong echoes that dominate the coherent backscattering spectrum and it is excited as a result of the ion-acoustic instability.

<sup>3</sup>Historically called type-II instability because its echoes appear in the coherent backscattering spectrum in the absence of type-I instability and it is excited as a result of the gradient-drift instability.

features of the plasma turbulence in the equatorial electrojet.

### 3.1 Past and Present Models

The one-dimensional simulations have been done by Sato and Tsuda [99] and Rogister [90] to study the gradient-drift (Type-II) instability. However, the use of only one-dimension to model type-II instability ignores the coupling between the waves propagate horizontally and vertically in the equatorial electrojet region, which is the principle reason for Sudan et al. [113] to criticize the works that had done by Sato and Tsuda [99] and Rogister [90] in one-dimensional model.

In 1990, Ronchi *et al.* [93] proposed a two-fluid model based on the nonlocal theory of the gradient-drift instability to study the coupling between the short-scale and large-scale irregularities in the equatorial electrojet. Ronchi *et al.* [93] had shown the role that the nonlocal turbulent mobility and diffusion plays in the inverse energy cascade between the short-scale and the large-scale irregularities. A numerical simulation that was done by Ronchi *et al.* [94] in 1991 shows that during the weak electrojet conditions the electric field of the large-scale irregularities influence the dynamics of the small-scale structures. This shows the role of forward energy-cascade in transferring the energy to the unstable small-scale structures.

The saturation of Farley-Buneman (type-I) instability has also been studied in different types of simulations. Newman and Ott [65] ran a fluid nonlinear simulation that shows the dominant wave propagates in a direction that is different from the direction of the electron drift. A particle-in-cell (PIC) code was used by Machida and Goertz [57] to model the dominant wave in a plane parallel to the geomagnetic field. This geometry ignores the nonlinear term,  $\hat{b} \cdot \nabla \phi \times \nabla n$  where  $\hat{b}$  is in the direction of the magnetic field, that is important for the saturation of type-I instability.

Oppenheim et al. [69] presented two-dimensional hybrid simulations that treat the electrons in the fluid regime and the ions kinetically to model the effects of Landau damping. The agreement between the radar/rocket spectra and the simulation spectra was presented by Oppenheim and Otani [68]. The hybrid simulation is able to reproduce the phase velocity during the saturated state similar to the drift velocity

of the observed irregularities and its independence from the elevation angle. Also, the hybrid simulation shows the presence of a secondary type-II instability in the absence of the electron density gradient as a result of the mode coupling. Otani and Oppenheim presented the mechanism of the saturation of Farley-Buneman (type-I) instability in a series of papers [72, 73]. Otani and Oppenheim [72, 73] attributed the saturation mechanism to the interaction between three modes in the system and used a fluid model to reproduce some observed features from the echoes of the irregularities.

In 2008, Oppenheim et al. [70] presented the results from a fully kinetic high-resolution two-dimension simulation that covers (160 m  $\times$  160 m) space. The simulation showed the coupling between the linearly growing modes and the damping modes while including the electron and ion thermal effects. This simulation reproduced most of the measurements and features of Farley-Buneman turbulence with a phase velocity larger than the ion-acoustic speed. Later, Oppenheim and Dimant [71] presented the first fully kinetic 3-D simulation results for the Farley-Buneman instability with the ionospheric condition at the aurora region. The simulation was able to resolve the 1 - 5 m waves during the transition region and the formation of a large-scale structure at the saturation region. Also, it shows the role of the anomalous electron heating in reducing the phase velocity of the short waves to a value very close to the local ion-acoustic speed compared to the previous 2-D simulation. Although the hybrid and kinetic simulators can retrieve most of the physics and characteristics of the equatorial electrojet instabilities, it still has very high computation cost and does not cover large area in the ionosphere, e.g. over 8000 processors are used in a fully kinetic model to cover 160 m  $\times$  160 m area in the ionosphere for studying Farley-Buneman instability by Oppenheim and Dimant [71].

## 3.2 Basic Fluid Model

In this section we present the Basic (or standard two-stream) fluid model for the equatorial electrojet instabilities. The basic plasma dynamic equations for electrons and ions in the frame-of-reference of the neutrals are given by:

$$\partial_t n_s = -\nabla \cdot (n \mathbf{v}_s) \quad (3.1)$$

$$m_s n_s (\partial_t + \mathbf{v}_s \cdot \nabla) \mathbf{v}_s = q_s n_s (\mathbf{E} + \mathbf{v}_s \times \mathbf{B}) - T_s \nabla n_s - m_s n_s \nu_{sn} \mathbf{v}_s \quad (3.2)$$

where,  $s = \{e, i\}$  and  $q_s = \{-e, e\}$  for electrons and ions, respectively.

Using the diffusion approximation<sup>4</sup>, we can ignore the electrons inertia term (the convective derivative on the left-hand-side of the electrons equation of motion). Also, because the ionosphere in the E-region is characterized by its *low*  $\beta$  plasma (where  $\beta = \frac{p_i + p_e}{B^2/2\mu_0} \sim 10^{-6}$ ) due to the low thermal pressure and the small variations in the geomagnetic field under solar quiet conditions, the fluctuations in plasma can be considered electrostatic with the electric field is defined as:  $E = -\nabla\phi$ . Therefore, the electrons equation of motion can be written as:

$$0 = en(\nabla\phi - v_e \times \mathbf{B}) - T\nabla n - m_e n \nu_{en} v_e \quad (3.3)$$

With some algebraic manipulation of equation(3.3) the drift velocity of electrons is given by:

$$\bar{v}_e = \frac{1}{B_o} \hat{e}_z \times \nabla(\varphi - \frac{T_e}{e} \ln(\frac{n}{n_o})) + \frac{\nu_{en}}{B_o \Omega_e} \nabla(\varphi - \frac{T_e}{e} \ln(\frac{n}{n_o})) \quad (3.4)$$

By substituting electrons velocity in its continuity equation we get the first dynamic equation in the system which can be written as:

$$\frac{\partial n}{\partial t} - \frac{1}{B_o} [n, \phi] = D_e \nabla^2 n - \frac{\nu_{en}}{B_o \Omega_{ce}} (\nabla n \cdot \nabla \phi + n \nabla^2 \phi) \quad (3.5)$$

Notice that in equation (3.3) and (3.5), we used the quasi-neutrality condition  $n_i \approx n_e$ , which is a good approximation according to the ionosphere dynamics in the E-region. That shows that the  $NO^+$  ions are dominating the equatorial electrojet region, and  $O_2^+$  comes second in the rank.

On the other hand, the ions are heavy and their collision frequency with the neutral atoms in the background is much greater than their gyro-frequency. So, the ions can not gyrate a complete cycle because of their high collisionality. Therefore, the ions in the E-region are considered unmagnetized, and we can drop the magnetic part in Lorentz force from the ions equation of motion. However, as an approximation,

---

<sup>4</sup>The diffusion-approximation is valid for a slowly varying, subsonic flow of plasma species. We can check it by comparing the nonlinear convective term ( $\mathbf{v}_s \cdot \nabla \mathbf{v}_s$ ) and time-varying term ( $\partial_t \mathbf{v}_s$ ) on the left-hand side of the equation of motion to the pressure term ( $\nabla p_s$ ) on the right-hand side of that equation. This is related to the Mach number  $M$  which is the ratio of the species drift velocity  $v_s$  to the species thermal velocity  $v_{th} \sqrt{T_s/m_s}$ . ( $M \ll 1$  for subsonic flow.)

and for the sake of computation, we keep the magnetic force in the ions equation of motion which can be written now in the following form:

$$m_i n (\partial_t + \mathbf{v}_i \cdot \nabla) \mathbf{v}_i = -en(\nabla\phi - \mathbf{v}_i \times \mathbf{B}) - T\nabla n - m_i n \nu_{in} \mathbf{v}_i \quad (3.6)$$

Solving for the zeroth-order approximation of the ions velocity, we get:

$$\bar{v}_i = \frac{1}{B_o} \hat{e}_z \times \nabla \left( \varphi - \frac{T_i}{e} \ln\left(\frac{n}{n_o}\right) \right) - \frac{e}{m_i \nu_{in}} \nabla \left( \varphi + \frac{T_i}{e} \ln\left(\frac{n}{n_o}\right) \right) \quad (3.7)$$

By substituting the ions velocity in the ions equation of motion and then taking the Curl of both sides we left with the second partial differential equation for our dynamic system in the following form:

$$\partial_t \nabla^2 \phi + \frac{1}{B_o} [\phi, \nabla^2 \phi] = -\nu_{in} \nabla^2 \phi \quad (3.8)$$

Equation (3.8) shows the evolution of the electrostatic vorticities in the dynamic system and their effect on the fluctuation of the plasma density and instability.

For collisionless ion-acoustic waves we can introduce a set of normalized variables,  $\hat{n} = \frac{n}{n_o}$ ,  $\hat{\varphi} = \frac{e\varphi}{m_i C_s^2}$ ,  $\hat{t} = \Omega_{ci} t$ ,  $\hat{x} = \rho_i x$ , to be used in equation (3.5) and (3.8), and the normalized set of dynamic equations are now have the following form:

$$\frac{\partial \hat{n}}{\partial \hat{t}} - \frac{C_s^2}{\Omega_{ci}^2} [\hat{n}, \hat{\phi}] = \frac{D_e}{\Omega_{ci}} \hat{\nabla}^2 \hat{n} - \frac{\nu_{en}}{\Omega_{ce}} \frac{C_s^2}{\Omega_{ci}^2} (\hat{\nabla} \hat{n} \cdot \hat{\nabla} \hat{\phi} + \hat{n} \hat{\nabla}^2 \hat{\phi}) \quad (3.9)$$

$$\frac{\partial}{\partial \hat{t}} \hat{\nabla}^2 \hat{\phi} + \frac{C_s^2}{\Omega_{ci}^2} [\hat{\phi}, \hat{\nabla}^2 \hat{\phi}] = -\frac{\nu_{in}}{\Omega_{ci}} \hat{\nabla}^2 \hat{\phi} \quad (3.10)$$

where,  $D_e$  is the electrons transverse diffusion coefficient,  $\Omega_{ce(ci)}$  is the gyro-frequency of electrons (ions),  $\nu_{en(in)}$  is the electrons (ions) collision frequency with the background neutral atoms, and  $C_s$  is the ions acoustic speed.

Now, to study the system dynamics for the linear waves in the E-region, we need to linearize the basic set of partial differential equations that describes our system. We separate the quasi-static background from the fluctuating part for each field in the dynamic system, e.g.  $f = f_o + \delta f$ . Then we substitute these fields in our dynamic equations and drop all the zero-order and higher-order (terms of order equal or greater than the second order) terms. Employing this technique on the basic set of equations, we can rewrite the dynamic system equation in a matrix form as following:

$$\begin{bmatrix} \omega - k_x v_E & -k_x & -(k_y + iL_n^{-1}) & 0 & 0 & 0 \\ \omega & 0 & 0 & -k_x & -k_y & 0 \\ ik_x v_{te}^2 + \nu_{en} v_E & \nu_{en} & \Omega_{ce} & 0 & 0 & -ik_x \frac{\Omega_{ci}}{B_o} \\ ik_y v_{te}^2 & -\Omega_e & \nu_{en} & 0 & 0 & -ik_y \frac{\Omega_{ce}}{B_o} \\ ik_x v_{ti}^2 & 0 & 0 & -i\omega + \nu_{in} & 0 & ik_x \frac{\Omega_{ci}}{B_o} \\ ik_y v_{ti}^2 & 0 & 0 & 0 & -i\omega + \nu_{in} & ik_y \frac{\Omega_{ci}}{B_o} \end{bmatrix} \begin{bmatrix} \delta n \\ \delta v_{ex} \\ \delta v_{ey} \\ \delta v_{ix} \\ \delta v_{iy} \\ \delta \varphi \end{bmatrix} = \begin{bmatrix} 0 \\ 0 \\ 0 \\ 0 \\ 0 \\ 0 \end{bmatrix}$$

To find the dispersion relation for the dynamic system from this matrix format, we need to evaluate the determinant of this matrix and put it equal to zero. Thus, the *dispersion relation* can be found from the determinant of the square matrix on the left-hand side of the previous equation and is written in the following form:

$$\omega = \frac{\mathbf{k} \cdot \mathbf{v}_E}{1 + \psi} + i \frac{\psi}{1 + \psi} \left( \frac{\Omega_{ce} v_E \cos^2 \theta}{\nu_{en} L_n} - \frac{k^2 C_s^2}{\nu_{in}} \right) \quad (3.11)$$

where,  $v_E = -\partial_z \phi / B_o$  is the  $\mathbf{E} \times \mathbf{B}$  drift,  $v_{te}$  and  $v_{ti}$  are the thermal speeds for electrons and ions, respectively,  $L_n^{-1} = n_o \partial_z^{-1} n_o$  is the electron density scale-length,  $\psi = \frac{\nu_{en} \nu_{in}}{\Omega_{ce} \Omega_{ci}}$  is the ratio between the ions and electrons transverse mobilities, and  $\cos \theta = k_y / k_\perp$  is the angle of the propagating modes.

Employing the linear approximation of marginal instability<sup>5</sup>,  $\omega_r \gg \gamma$ , to the dispersion relation where  $\omega = \omega_r + i\gamma$ , we found the phase velocity,  $v_p = \omega / k_y$ , of the propagating plasma waves to have the following form:

$$v_p = \frac{v_E \cos \theta}{1 + \psi}, \quad (3.12)$$

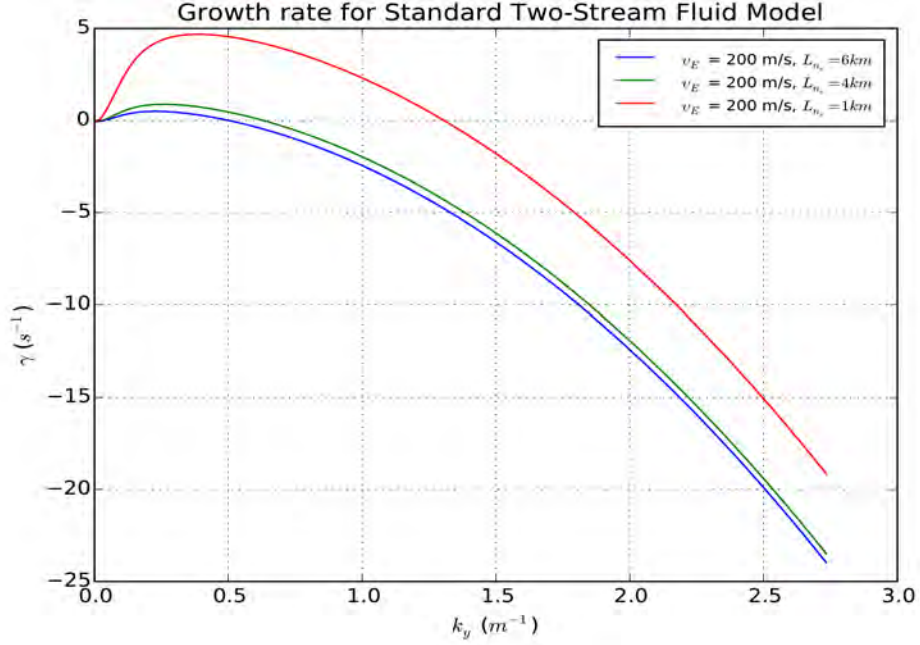
and the growth rate is to be given by:

$$\gamma = \frac{k_\perp^2 \psi}{(1 + \psi) \nu_{in}} (v_E^2 - C_s^2) + \frac{\nu_{in}}{\Omega_{ci}} \frac{1}{L_n} v_E \cos \theta \quad (3.13)$$

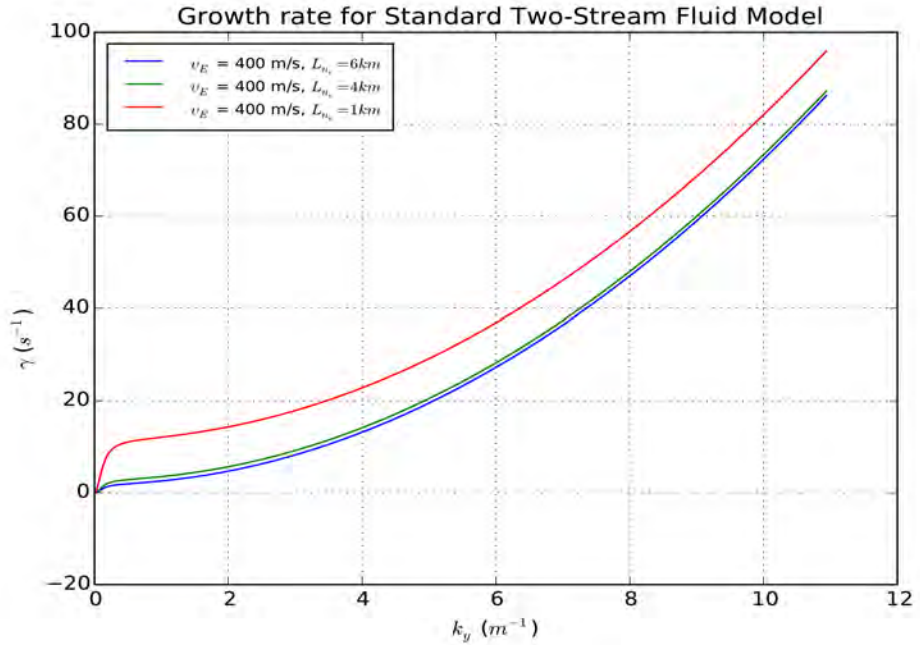
where,  $\cos \theta = k_y / k_\perp$ .

Equation(3.12) shows a linear relation between the phase velocity and the  $\mathbf{E} \times \mathbf{B}$  drift velocity for the electrons which points westward. Also, the ratio between the ion and electron mobilities decreases with altitude, which gives rise to an increase

<sup>5</sup>In marginal instability the amplitude of plasma fluctuations is small enough that the nonlinear terms do not dominate the dynamics in the system.



(a) Different density-gradient scale-length.



(a) Different  $\mathbf{E} \times \mathbf{B}$  electron drifts.

Figure 3.1: The growth rates for different electron density scale-lengths  $L_n = 1, 4, 6$  km and at opposite limits of  $\mathbf{E} \times \mathbf{B}$  drift velocity at (a)  $v_E = 200$  m/s (below type-I instability threshold) and (b)  $v_E = 400$  m/s (above type-I instability threshold).

in the phase velocity with altitude. However, the observed phase velocity always matches the ion-acoustic speed in the local ionosphere. So, the linear theory of the phase velocity can not explain the observation of an upper limit for the phase velocity.

The density-gradient, which is a destabilization effect and is responsible for the gradient-drift instability, manifests itself in the second term in equation(3.13) through the electron density scale-length  $L_n$ . In the equatorial electrojet region, the density scale-length is always positive during the daytime and that seeds any perturbation in the plasma in the horizontal direction and gives rise to large-scale structures. However, during the nighttime the electron density scale-length is small and has positive and negative magnitudes depending on the electron density profile and shown in the rocket measurements over Thumba, India in figure (2.8).

The first term in equation(3.13) has a destabilization term,  $v_E \cos \theta$ , due to the ions inertia, however, the other destabilization term,  $v_E^2 - C_s^2$ , is attributed to the ions diffusivity,  $C_s$ . When the drift velocity,  $v_E$ , of the plasma waves exceeds the ion acoustic speed, the perturbations in plasma density grow as a result of Farley-Buneman instability. However, a weak eastward electric field in the equatorial electrojet region gives rise to a drift speed smaller than the ion acoustic speed which inhibits that instability.

The growth rate profiles for different values of electron density scale-length and  $E \times B$  drifts is shown in figure(3.1). The shorter density scale-length is strongly driving the gradient drift instability at small wavenumbers compared to the longer one. However, the  $E \times B$  drift of values smaller than the ion-acoustic speed such as the case in figure(3.1-a) can not drive Farley-Buneman instability at large wavenumbers. For  $E \times B$  drift of 400 m/s, which is larger than the local value of the ion-acoustic speed drives Farley-Buneman instability as shown in figure(3.1-b). But it is clear that there is no stabilization mechanism that stops the growing of the unstable modes at the appropriate wavenumbers. Type-I instability was studied using the kinetic theory by Schmidt and Gary [100] and they found a stabilization of unstable modes at large wavenumber their model considers the structures of the order of the mean-free-path.

On the other hand, the gradient-drift instability always stabilizes for plasma fluctuations of wavelength of order of 10 meters for density-gradient scale-length ( $L_n$ ) of 6 - 10 km which is typical in the daytime. A density scale-length of order 1 km, which is

typical during the nighttime gives rise to plasma waves of wavelength of order 5 meters. It appears in figure(3.1-b) that the level of growth rate due to type-II instability controls the level of the corresponding instability for type-I. This might give us an idea about the coupling between type-I and type-II instabilities and the probability of having energy cascade between them.

### 3.3 Unified Fluid Model

In section(3.1), we reviewed the work that had been done to retrieve the spatial and spectral characteristics of the Equatorial Electrojet instabilities, and in section(3.2) we reviewed the linear theory of the standard or basic fluid model for both the gradient-drift and Farley-Buneman instabilities. The fluid models up-to-date have not shown any saturation for Farley-Buneman instability because of the ion Landau damping effect, which requires higher moments of Vlasov equation to be included in the fluid model, or a long runtime beyond the acceptable cost for computations. This explains the need for a fully kinetic or hybrid code with the ions treated kinetically to include that effect.

The fluid model we propose in this work shows a stabilization of the growth rates in the vertical and east-west directions in the linear regime. In the nonlinear regime, the simulation reaches a saturation state for all the evolving fields as shown in chapter(4). In addition, in chapter(5) we show that the dynamic system we propose to conserve energy in all (growing, transition, and saturation) phases of the simulation. Studying the coupling between the gradient-drift and Farley-Buneman instabilities in our dynamical system shows a strong evidence for dual energy cascading mechanisms depending on the dominant modes in the Hamiltonian system.

#### 3.3.1 Plasma Dynamic Equations

The large collision frequency of the ions with the background neutrals compared to their cyclotron frequency drops the rotational part of its vector representation, and the ions velocity can be written as:

$$\bar{\mathbf{v}}_i = -\nabla\chi \tag{3.14}$$

where,  $\chi$  is the ions velocity potential. Hence, we can write the continuity equation of the ions in the following form:

$$\begin{aligned}\partial_t n &= \nabla \cdot (n \nabla \chi) \\ \partial_t n &= n \nabla^2 \chi + \nabla n \cdot \nabla \chi\end{aligned}\quad (3.15)$$

The equation of motion for the unmagnetized ions is given by:

$$m_i n \Delta_t \bar{\mathbf{v}}_i = en \bar{\mathbf{E}} - T_i \nabla n - \nabla \cdot \bar{\boldsymbol{\pi}} - m_i n \nu_{in} \bar{\mathbf{v}}_i \quad (3.16)$$

where,  $\Delta_t = \partial_t + \bar{\mathbf{v}}_i \cdot \nabla$  is the convective derivative for the ions and  $\bar{\boldsymbol{\pi}}$  is the ion momentum stress tensor.

The third term in the right-hand-side,  $\bar{\boldsymbol{\pi}}$ , is the ions viscosity stress tensor and it is given from Braginskii equations [28]:

$$\pi_{\alpha\beta} = -\frac{nT_i}{\nu_{in}} \left( \partial_\beta v_\alpha + \partial_\alpha v_\beta - \frac{2}{3} \nabla \cdot \bar{\mathbf{v}} \delta_{\alpha\beta} \right) \quad (3.17)$$

which gives rise to force on the ion fluid by:

$$\nabla \cdot \bar{\boldsymbol{\pi}} = -\frac{nT_i}{\nu_{in}} \nabla (\nabla^2 \chi) \quad (3.18)$$

The difference between the ions momentum equation in the unified fluid model (3.16) and its corresponding form in (3.6) is the ions viscosity tensor ( $\bar{\boldsymbol{\pi}}$ ) in the later one. This term plays an important role in the linear and nonlinear regime as we show in section (3.3.2) and Chapter (4).

Using the electrostatic approach for the electric field,  $\bar{\mathbf{E}} = -\nabla \phi$ , due to the small variations in the background magnetic field under the solar quiet conditions, the ions equation of motion can be rewritten as:

$$\partial_t \nabla \chi = v_{t_i}^2 \nabla \ell n n + \mu_{iH} \Omega_{c_i} \nabla \phi - \nu_{in} \nabla \chi + \frac{4}{3} \frac{v_{t_i}^2}{\nu_{in}} \nabla \nabla^2 \chi + \frac{1}{2} \nabla (\nabla \chi \cdot \nabla \chi) \quad (3.19)$$

where,  $\phi$  is the electrostatic potential,  $\mu_{iH}$  is the ions Hall mobility,  $v_{t_i}$  is the ions thermal velocity,  $\Omega_{c_i}$  is the ions cyclotron frequency, and  $\nu_{in}$  is the collision frequency between the ions and the neutral background.

Then, taking the divergence of both sides in equation(3.19), we get:

$$\partial_t \nabla^2 \chi = v_{ti}^2 \nabla^2 \ell n n + \mu_{iH} \Omega_{ci} \nabla^2 \phi - \nu_{in} \nabla^2 \chi + \frac{4}{3} \frac{v_{ti}^2}{\nu_{in}} \nabla^4 \chi + \frac{1}{2} \nabla^2 (\nabla \chi \cdot \nabla \chi) \quad (3.20)$$

where the viscosity terms in equation (3.20) describe the steepening on the amplitude of the ions sound waves, and the fourth term on the right-hand side represents the divergence of ions viscosity stress tensor.

For electrons dynamics, we keep the electron inertia while not employing the diffusion approximation in this model, and the equation of motion for the magnetized electrons is given by:

$$m_e n \Delta_t \mathbf{v}_e = -en(\mathbf{E} + \mathbf{v}_e \times \mathbf{B}) - T_e \nabla n - m_e n \nu_{en} \mathbf{v}_e \quad (3.21)$$

By crossing equation(3.21) from the left with the magnetic field ( $\mathbf{B}$ ) and the electrostatic approach for the electric field we get:

$$\mathbf{v}_{e\perp} = \frac{1}{B^2} (\mathbf{B} \times \nabla \phi) - \frac{T_e}{eB^2} (\mathbf{B} \times \nabla \ell n n) - \frac{m_e}{eB^2} [\Delta_t + \nu_{en}] (\mathbf{B} \times \mathbf{v}_e) \quad (3.22)$$

Also, by rearranging the terms in equation (3.21) we can get:

$$\mathbf{B} \times \mathbf{v}_e = \frac{m_e}{e} [\Delta_t + \nu_{en}] \mathbf{v}_e - \nabla \left[ \phi - \frac{T_e}{e} \ell n n \right] \quad (3.23)$$

Then substituting equation(3.23) into equation(3.22) gives the first-order approximation of the electrons drift velocity in the following form:

$$\mathbf{v}_{e\perp} = \frac{\hat{\mathbf{b}}}{B} \times \nabla \left[ \phi - \frac{T_e}{e} \ell n n \right] + \frac{[\Delta_t + \nu_{en}]}{\Omega_{ce}^2} \nabla \left[ \phi - \frac{T_e}{e} \ell n n \right] \quad (3.24)$$

or

$$\mathbf{v}_{e\perp} = \mathbf{v}_E + \mathbf{v}_{d_e} + \mathbf{v}_{p_e} + \mathbf{v}_{\nu_{en}} \quad (3.25)$$

where  $\mathbf{v}_E$  is the  $\mathbf{E} \times \mathbf{B}$  drift velocity,  $\mathbf{v}_{d_e}$  is the diamagnetic drift velocity,  $\mathbf{v}_{p_e}$  is the polarization drift velocity, and  $\mathbf{v}_{\nu_{en}}$  is the drift velocity due to the frictional force between the electrons and the neutral background.

Now we derive the dynamical equation for  $\nabla^2 \phi$  by substituting the ions drift velocity in equation(3.14) and the electrons drift velocity in equation (3.24) into the plasma

quasineutrality condition,  $\nabla \cdot (\mathbf{J}_e + \mathbf{J}_i) = 0$ . After some algebraic manipulation we can close our system with the following dynamic equation:

$$\begin{aligned} \partial_t \nabla^2 \phi &= \nu_{en} \nabla \ell n n \cdot \nabla \ell n n - \nu_{en} \nabla \ell n n \cdot \nabla \phi + \rho_e^{-2} \nabla \ell n n \cdot \nabla \chi \\ &+ \nu_{en} \nabla^2 \ell n n - \nu_{en} \nabla^2 \phi - \rho_e^{-2} \nabla^2 \chi \\ &- \Omega_{ce} [\phi, \ell n n] - \rho_e^2 \Omega_{ce} [\phi, \nabla^2 \phi] \end{aligned} \quad (3.26)$$

where,  $[f, g]$  is the Poisson (*Jacobian*) bracket which is defined as  $[f, g] = \partial_x f \partial_y g - \partial_x g \partial_y f$ , or  $[f, g] = \hat{\mathbf{a}} \cdot \nabla f \times \nabla g$ , and it is responsible for the coupling between the perturbations in the horizontal and vertical directions in a plane perpendicular to the unit vector  $\hat{\mathbf{a}}$ .

Hence, we have derived a closed dynamic system consists of a set of three first-order nonlinear partial differential equations(3.15, 3.20, 3.26). These three equations govern the plasma dynamics during the early evolution (growing), transition, and saturation phases of the plasma dynamical simulations. In section(3.3.2) we study the plasma dynamics in the equatorial electrojet in the linear regime. In Chapter(4) we discuss the numerical simulation results for different ionospheric conditions, and finally in Chapter(5) we study energy conservation and energy cascade in this dynamic system.

### 3.3.2 Linear Dynamical Equations

To study the linear characteristics of the dynamical system,  $n, \phi, \chi$ , we need to linearize the dynamic equations (3.20, 3.15, 3.26). The linearized equation for the density  $n$ , electric potential  $\phi$ , and ions velocity potential  $\chi$ , with the assumption of a stationary background plasma  $v_{io} = \nabla \chi_o = 0$ , can be written as:

$$n = n_o + \delta n, \quad \phi = \phi_o + \delta \phi, \quad \chi = \delta \chi$$

where the general spectral representation of the fluctuations of the perturbed parts of those three fields in space and time is given by:

$$\delta \zeta (i = 1, 2, 3) = \sum_{k_x, k_y} \zeta_i \exp [i(\mathbf{k} \cdot \mathbf{x} - \omega t)]$$

with a condition for real values giving  $\zeta_n(-k, -\omega^*) = \zeta_n^*(k, \omega)$ . where  $(\delta \zeta_1, \delta \zeta_2, \delta \zeta_3)$  are equivalent to  $(\delta n, \delta \phi, \delta \chi)$ , respectively.

Table 3.1: Ionosphere background parameters based on IRI07, NMSIS00, and IGRF12 empirical models for the ionosphere and neutral atmosphere compositions densities and the geomagnetic field components.

Quantity	Symbol	Unit	Solar Maximum	Solar Minimum
Electron Density	$N_e$	$m^3$	$1.52 \times 10^{11}$	$1.60 \times 10^9$
Electron Temperature	$T_e$	$^{\circ}K$	192.1	191.1
Ion Temperature	$T_i$	$^{\circ}K$	192.1	191.1
Magnetic Field	$B_o$	T	$3.7 \times 10^{-5}$	$3.5 \times 10^{-5}$
Ion Acoustic Speed	$C_s$	m/s	360.0	330.0
Electron Thermal Speed	$v_{te}$	m/s	$5.4 \times 10^4$	$5.4 \times 10^4$
Ion Thermal Speed	$v_{ti}$	m/s	225.2	228.5
Electron Collision Frequency	$\nu_{en}$	rad/s	$2.3 \times 10^4$	$2.4 \times 10^4$
Ion Collision Frequency	$\nu_{in}$	rad/s	$3.2 \times 10^3$	$2.8 \times 10^3$
Electron Gyro-Frequency	$\omega_{ce}$	rad/s	$6.5 \times 10^6$	$6.1 \times 10^6$
Ion Gyo-Frequency	$\omega_{ci}$	rad/s	113	110
Electron Larmor Radius	$\rho_e$	m	$8.3 \times 10^{-3}$	$8.8 \times 10^{-3}$
Ion Larmor Radius	$\rho_i$	m	2	2

With employing these reductions we have the set of linear dynamic equations of the normalized quantities ( $\tilde{n} = \frac{\delta n}{n_o}$ ,  $\tilde{\phi} = \frac{e\phi}{k_B T_i}$ ,  $\tilde{\chi} = \frac{\chi}{1}$ ) as shown below:

$$\partial_t \delta \tilde{n} = \left( \nabla^2 + \frac{\partial_z}{L_n} \right) \delta \tilde{\chi} \quad (3.27)$$

$$\begin{aligned} \partial_t \nabla^2 \delta \tilde{\phi} = & \left( \nu_{en} \nabla^2 + 2\nu_{en} \frac{\partial_z}{L_n} + \frac{v_E \nu_{en}}{\rho_e^2 \Omega_{ce}} \partial_z - \frac{v_E}{\rho_e^2} \partial_y + v_E \partial_y \nabla^2 \right) \delta \tilde{n} + \\ & \left( -\nu_{en} \nabla^2 - \frac{\nu_{en}}{L_n} \partial_z - \frac{\Omega_{ce}}{L_n} \partial_y - v_E \partial_y \nabla^2 - \frac{1}{L_n} \partial_y \nabla^2 \right) \delta \tilde{\phi} + \\ & \left( -\frac{1}{\rho_e^2} \nabla^2 - \frac{1}{\rho_e^2 L_n} \partial_z \right) \delta \tilde{\chi} \end{aligned} \quad (3.28)$$

$$\partial_t \nabla^2 \delta \tilde{\chi} = v_{ti}^2 \nabla^2 \delta \tilde{n} + v_{ti}^2 \nabla^2 \delta \tilde{\phi} + \left( \frac{4}{3} \frac{v_{ti}^2}{\nu_{in}} \nabla^4 - \nu_{in} \nabla^2 \right) \delta \tilde{\chi} \quad (3.29)$$

where,  $\rho_e$  is the electron gyro-radius.

### 3.3.3 Numerical Solution of Linear System

The local and the nonlocal approximations have been used to model plasma instabilities in the E-region depending on the relation between the density scale-length,

$L_n$  and the fluctuation wavenumber,  $k$  [92]. We use the local approximation, valid in the case of  $|kL_n| \gg 1$  (or  $L_n \gg \lambda$ , where  $k = 2\pi/\lambda$ ), which is the condition that is satisfied in this study for the length of the type-II irregularities much smaller than a kilometer ( $\sim 100 - 200$  meters).

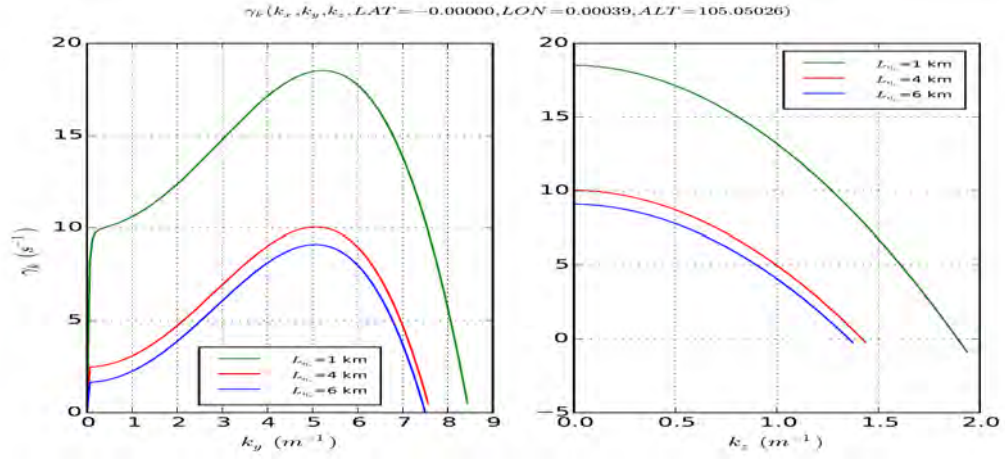
To study the plasma dynamics in the linear domain we solve the linearized equations (3.27, 3.28, 3.29) numerically for the eigenvalues, thus we find the phase velocity and growth rate of the unstable modes of the plasma fluctuations in the real and imaginary parts of those eigenvalues, respectively.

We employ the International Reference Ionosphere (IRI2007), Naval Research Laboratory Mass Spectrometer and Incoherent Scatter Radar Exosphere (NRLMSIS00), and International Geomagnetic Reference Field (IGRF12) empirical models under different solar and ionospheric conditions to get the altitude-dependent values of the collision frequencies, gyrofrequencies, and gyroradii for ions and electrons, as shown in table(3.1) for the solar-maximum and solar-minimum conditions, as an example.

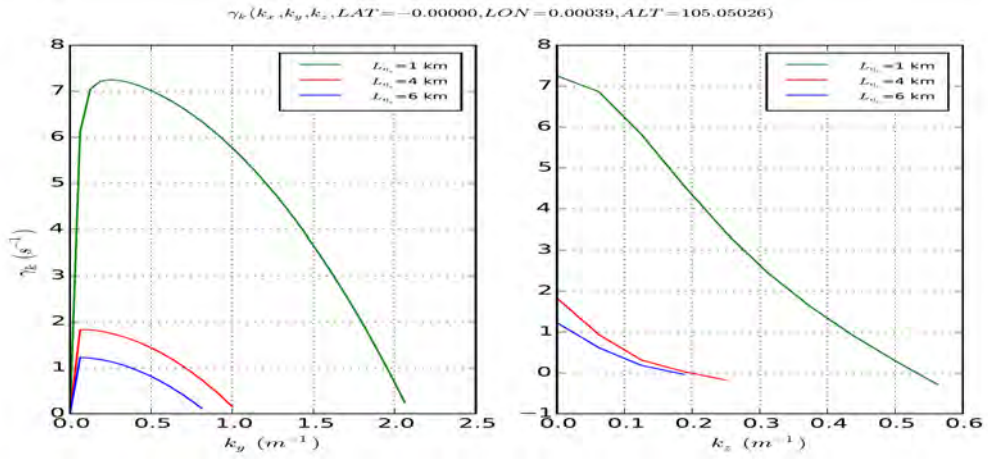
Figure(3.2) shows the growth rate profiles for different values of the  $\mathbf{E} \times \mathbf{B}$  drifts,  $v_E$ , and electron density scale-lengths,  $L_n$  at both the horizontal wavenumber ( $k_y$ ) and vertical wavenumber ( $k_z$ ) directions. In figure(3.2-a,c) we can see two peaks in the horizontal direction with the shorter one at the wavenumber that corresponds to the large-structures as a result of gradient-drift instability, however the higher peak is found at the wavenumber that corresponds to the small-structures which confirms the presence of Farley-Buneman instability.

The small density-gradient scale-length gives rise to a strongly driven gradient-drift instability at small wavenumbers, which in turn affect the level of the peak at the region of large wavenumbers where Farley-Buneman instability dominates with no change in the  $\mathbf{E} \times \mathbf{B}$  drift as shown in green-solid-line in figure(3.2-a). As the density-gradient scale-length gets larger the driver of type-II instability gets weaker but it still presents and drives the instability as long as it has a positive magnitude.

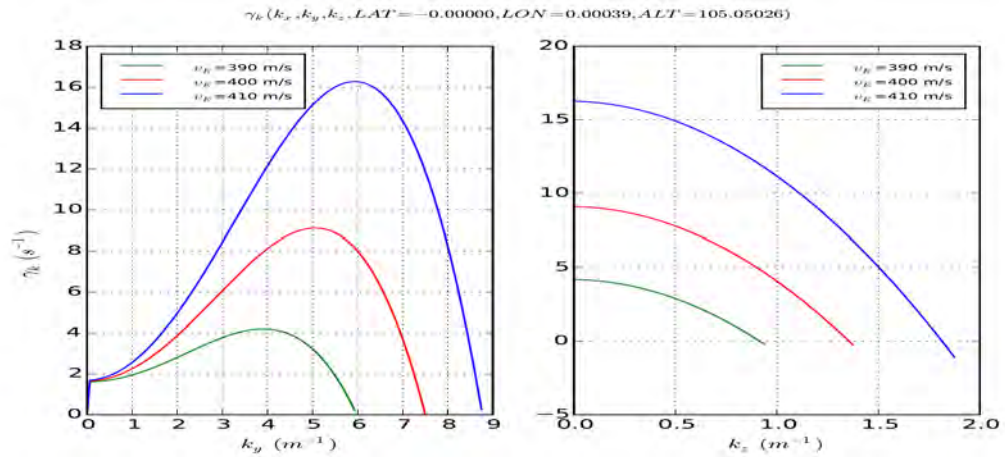
In contrast, the increase in the cross-field drift velocity as shown in figure(3.2-c) does not have any influence on the large plasma irregularities at small-wavenumbers, however, it strongly drives the unstable waves of shorter wavelength as a result of



(a) Growth rate profile for different values of  $L_n$  at  $v_E = 400$  m/s.



(a) Growth rate profile for different values of  $L_n$  at  $v_E = 300$  m/s.



(a) Growth rate profile for different values of  $v_E$  at  $L_n = 6$  km.

Figure 3.2: The dependence of the unified model instabilities growth rates on the  $\mathbf{E} \times \mathbf{B}$  drift,  $v_E$ , and electron density scale-lengths,  $L_n$ , in the east-west (left) and vertical (right) directions at 105 km altitude.

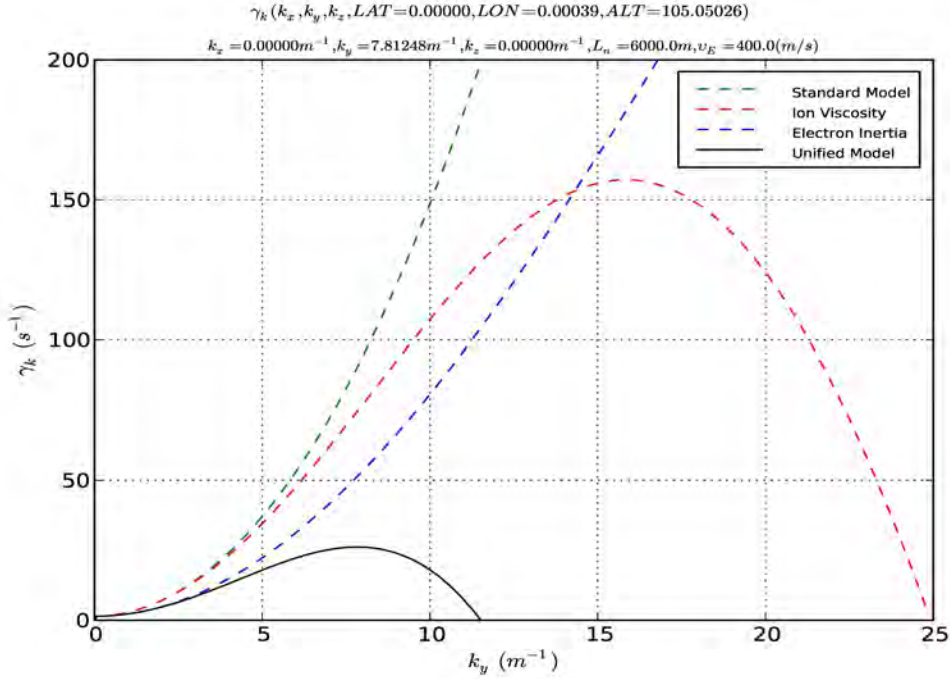


Figure 3.3: A comparison between the growth-rate,  $\gamma_k(k_y)$ , in the standard two-stream model (dashed-green) and the unified model with including both the ions viscosity and the electrons inertia (solid-black), absence of ions viscosity (dashed-blue), and absence of electrons inertia (dashed-red). [From Hassan *et al.* [36]]

Farley-Buneman instability. When the  $\mathbf{E} \times \mathbf{B}$  drift velocity goes below the local value of the ion-acoustic velocity in the ionosphere, the driver of the Farley-Buneman instability ceases completely and the peak at the large-wavenumbers disappears but we still can see the presence of the gradient-drift instability at small-wavenumbers, as shown in figure(3.2-b).

### 3.3.4 Basic versus Unified Fluid Models

In figure(3.3) we demonstrate the effect of the ion viscosity term,  $\nabla^4 \chi$ , and the electron polarization drift term that comes from the electrons inertia,  $\partial_y \nabla^2 \varphi$ , which both are stabilizing at high wavenumbers for a reference case at 105 km altitude. When the electron inertia is ignored but the ion viscosity is retained (dashed-red), we find the instabilities are suppressed at high wavenumber ( $k_y \approx 25 m^{-1}$ ). However, the stabilization of the growing modes is found at  $k_y \approx 81 m^{-1}$  when we only consider the

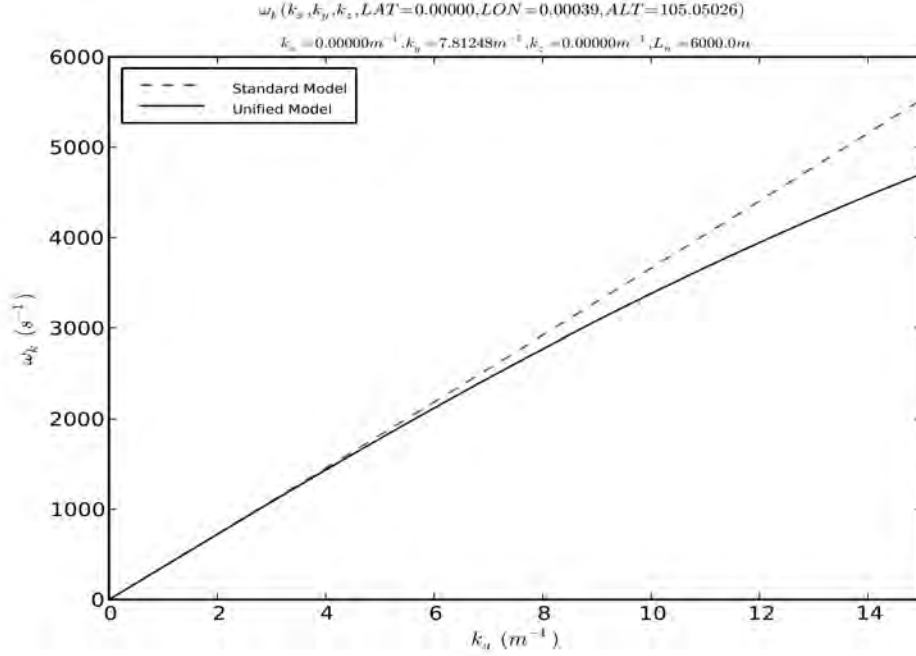


Figure 3.4: A comparison between the real-frequency,  $\omega_k(k_y)$ , profile of the standard two-stream model (dashed-green) and the unified model with including both the ions viscosity and the electrons inertia (solid-black). The unified model gives smaller phase velocity than the standard two-stream model. [From Hassan *et al.* [36]]

electron inertia term and drop the term coming from the ion viscosity. The electron inertia is not relevant at these length-scales in the linear regime, however, it is important in saturating the growing modes of large amplitudes in the nonlinear regime.

A monotonic increase of the growth rate with the wavenumber (dashed-green) can be seen when we drop both the ion viscosity and the electron inertia terms. This case is similar to the basic or standard two-stream fluid model [25] that shows no cut-off for the type-I instability. However, the solid black line shows stabilization at large wavenumbers around  $k_y = 11.5(m^{-1})$  when both the ion viscosity and electron inertia are included in the model. This comparison shows the importance of the ions viscosity in stabilizing the growing unstable modes due to the Farley-Buneman instability in the equatorial electrojet which is missing in the standard fluid model.

A maximum growing mode at  $k_y = 7.8 (m^{-1})$  is equivalent to an irregularity of scale size less than a meter in the zonal direction. In the vertical direction we have the

maximum growing mode at  $k_z = 0$ , and there are modes of positive growth rate at  $k_z = 2.1 \text{ (m}^{-1}\text{)}$ , which is equivalent to 3 meters wavelength. Farley and Balsley [22] found that the excitation of 3 meters wavelength waves requires a very large drift speed which is not possible in the equatorial electrojet region and they referred to Sudan *et al.* [113] theory, which attributed the generation of vertical structures of wavelength 3-meters or less in the equatorial electrojet to the cascade of energy to small scales.

The linear growth-rate for both types of instabilities that is derived in the standard fluid model by Fejer [1975] increase monotonically in contrast with the growth rate calculated numerically from our unified fluid model that includes both the ion viscosity and electron inertia terms. Our unified model produces a cut-off at high wavenumbers. The growth rate profile of the unified fluid model is similar to that of the kinetic model of type-I instability studied by Schmidt and Gary [100] and Oppenheim *et al.* [69], which was compared to the linear growth rate of the standard fluid model by Fejer *et al.* [25].

On the other hand, there is a decrease in the phase velocity found in our unified fluid model compared to that which was estimated by the standard linear fluid model [25] as shown in figure(3.4). This decrease in the phase velocity at high wavenumbers is in agreement with the radar observations that show the phase velocity is limited to the acoustic speed of ions inside the equatorial electrojet.

### 3.3.5 Altitude Dependent Growth Rate

The altitude-dependence of the growth rates of the gradient-drift and Farley-Buneman instabilities for our unified fluid model were calculated by solving the eigenvalue problem for the linearized set of partial differential equations (3.27, 3.28, 3.29) between 90 - 120 km at each altitude. We use  $\Delta k_z = 0.03 \text{ m}^{-1}$  resolution in k-space and  $\Delta z = 0.25 \text{ km}$  resolution along the altitude, z-axis, and the background parameters are calculated based on IRI07, NMSIS00, and IGRF12 empirical models.

The growth rate profile as a function of altitude is shown in figure(3.5) and divides the E-layer into three regions. The lower region below 103 km shows a dominance of the pure gradient-drift (type-II) instability over the small wavenumbers with the

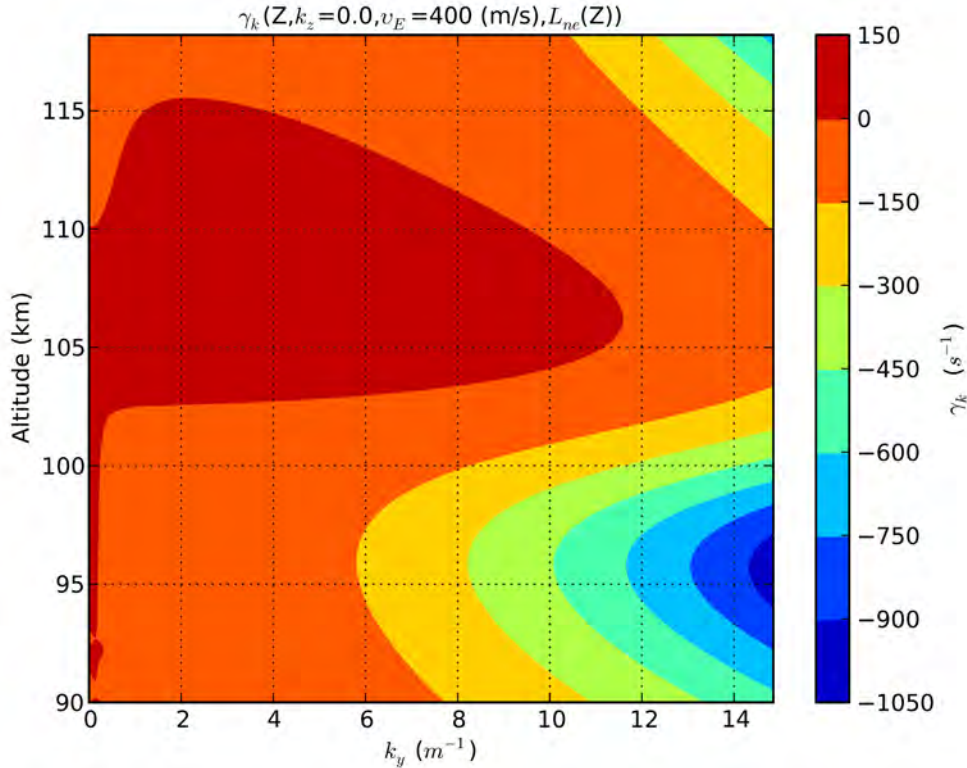


Figure 3.5: The growth-rate profile of the unified model as a function of altitude and horizontal wavenumber ( $k_y$ ). It shows the dominance of Type-II instability at low altitudes up to the coupling region between Type-I and Type-II instabilities between 100-110 km. Above 110 km, Type-I instability dominates and Type-II instability disappears as a result of the reverse of the electron density scale length sign to be negative at that region. [From Hassan *et al.* [36]]

absence of the Farley-Buneman instability at the intermediate and large wavenumbers due to the large collision rates of plasma species with the ionosphere neutral background and the small relative speed between the electrons and ions. The region extends between 110 - 115 km does not have instabilities at small wavenumbers which reflects the absence of gradient-drift instability as a result of the negative scale-length of the plasma density in this region. The growing modes in this region are found in the intermediate and large wavenumbers where the pure Farley-Buneman (type-I) instability dominates. The coupling between type-I and type-II instabilities can be seen at the core of the electrojet region between 103 - 110 km, where the maximum positive growth rate extends over all wavelength scales from hundreds or tens of me-

ters and down to sub-meter scales.

Thus, the altitude-dependent growth rate profile is in a good agreement with the rocket observations that divides the instabilities in the equatorial electrojet region into three regions as we described with the peak of the electrojet turbulence between 103 - 108 km [80], and the linear dynamics in our unified fluid model reflect the interchanging role between type-I and type-II instabilities and the coupling between them.

### 3.3.6 Type-I and Type-II Instabilities

The linear growth rate profile shows the presence of a transition from the type-II instability at small wavenumber ( $< 0.1 m^{-1}$ ) to type-I instability at large wavenumbers. For electron cross-field drift velocity of magnitude less than the ion-acoustic speed we find that the growth rate maximum is located at the transition wavenumber ( $\sim 0.1 m^{-1}$ ) with a peak value that depends on the electron density scale length ( $L_n$ ). Also, the level of the growth rate peak at the large wavenumbers, where the type-I instability dominates, depends on both the electron drift speed ( $v_E$ ) and the electron density scale length ( $L_n$ ). Therefore, to model the dynamics of and coupling between type-I and type-II instabilities in our simulation we need a large simulation box of high-resolution in k-space to include all the linear and nonlinear unstable modes that can possibly being excited in the system.

## 3.4 Ion Thermal Flux and Farley-Buneman Instability

The kinetic effect of Landau damping limits the ability to describe the ions in the fluid domain, and drove some researchers to model the ion dynamics in the kinetic domain to study the Farley-Buneman instability. In this section we show another approach to model the ions in the fluid domain and include the ion thermal flux moment from Vlasov equation to compensate the absence of Landau damping term in the fluid representation of the ions dynamics [55].

The Vlasov equation of unmagnetized ions are given by:

$$\partial_t f + \mathbf{v}_i \cdot \nabla f + \frac{\Omega_{ci}}{B_o} \mathbf{E} \cdot \frac{\partial f}{\partial \mathbf{v}_i} = C(f) \quad (3.30)$$

where,  $C(f)$  is BGK collision operator which is defined as:

$$C(f) = -\nu_{in} \left( \delta f - \frac{\delta n}{n_o} \frac{m_i}{2\pi T_i} e^{-\frac{v^2}{v_i^2}} \right)$$

The continuity, momentum, and heat flux equations for the ions dynamics are given in (3.31, 3.32, and 3.33), respectively, where:

$$\partial_t n_i + \nabla \cdot (n_i \mathbf{v}_i) = 0 \quad (3.31)$$

$$m_i \frac{d\mathbf{v}_i}{dt} = e\mathbf{E} - \frac{\nabla p_i}{n_i} - \frac{\nabla \cdot \boldsymbol{\pi}}{n_i} - m_i \nu_{in} (\mathbf{v}_i - \mathbf{v}_n) \quad (3.32)$$

$$\frac{3}{2} n_i \frac{dT_i}{dt} + p_i \nabla \cdot \mathbf{v}_i + \nabla \cdot \mathbf{q} = -\frac{3}{2} \nu_{in} n_i (T_i - T_n) \quad (3.33)$$

Assuming a Maxwellian distribution for the ions, we can find the moments in Vlasov equation for the ions viscosity tensor and heat flux as following:

$$\frac{d\mathbf{q}_i}{dt} + \frac{5}{2} \frac{p_i}{m_i} \nabla T_i + \frac{T_i}{m_i} \nabla \cdot \bar{\boldsymbol{\pi}}_i = -\nu_{in} \mathbf{q}_i \quad (3.34)$$

$$\frac{d\bar{\boldsymbol{\pi}}_i}{dt} + p_i \left( \nabla \mathbf{v}_i + (\nabla \mathbf{v}_i)^{Tr} - \frac{2}{3} \mathbf{I} \nabla \cdot \mathbf{v}_i \right) + \frac{2}{5} \left( \nabla \mathbf{q}_i + (\nabla \mathbf{q}_i)^{Tr} - \frac{2}{3} \mathbf{I} \nabla \cdot \mathbf{q}_i \right) = -\nu_{in} \bar{\boldsymbol{\pi}}_i \quad (3.35)$$

Using the Fourier representation of the evolving quantities in equations(3.34 and 3.35) we can their closure in the following form:

$$\mathbf{q}_i = \frac{1}{i\omega - \nu_{in}} \left( \frac{5}{2} \frac{p_i}{m_i} \nabla T_i + \frac{T_i}{m_i} \nabla \cdot \bar{\boldsymbol{\pi}}_i \right) \quad (3.36)$$

$$\bar{\boldsymbol{\pi}}_i = \frac{p_i}{i\omega - \nu_{in}} \left( \nabla \mathbf{v}_i + (\nabla \mathbf{v}_i)^{Tr} - \frac{2}{3} \mathbf{I} \nabla \cdot \mathbf{v}_i + \frac{2}{5 p_i} \left( \nabla \mathbf{q}_i + (\nabla \mathbf{q}_i)^{Tr} - \frac{2}{3} \mathbf{I} \nabla \cdot \mathbf{q}_i \right) \right) \quad (3.37)$$

Thus, the ions viscosity and heat flux tensors can be written as:

$$\mathbf{q}_i = \frac{1}{i\omega - \nu_{in}} \frac{5}{2} \frac{p_i}{m_i} \nabla T_i + \frac{1}{(i\omega - \nu_{in})^2} \frac{4}{3} \frac{p_i T_i}{m_i} \nabla (\nabla \cdot \mathbf{v}_i) \quad (3.38)$$

$$\bar{\boldsymbol{\pi}}_i = \frac{p_i}{i\omega - \nu_{in}} \left( \nabla \mathbf{v}_i + (\nabla \mathbf{v}_i)^{Tr} - \frac{2}{3} \mathbf{I} \nabla \cdot \mathbf{v}_i \right) + \frac{4}{3} \frac{p_i}{m_i} \nabla^2 T_i \quad (3.39)$$

The large collision frequency for the ions compared to the fluctuation frequency in the system allows us to make further simplification for the ions viscosity tensor,  $\bar{\bar{\pi}}_i$ , and heat flux tensor,  $\mathbf{q}_i$ , and to have them in the following form:

$$\mathbf{q}_i = -\frac{5}{2\nu_{in}} \frac{p_i}{m_i} \nabla T_i \quad (3.40)$$

$$\bar{\bar{\pi}}_i = -\frac{p_i}{\nu_{in}} \left( \nabla \mathbf{v}_i + (\nabla \mathbf{v}_i)^{Tr} - \frac{2}{3} \mathbf{I} \nabla \cdot \mathbf{v}_i \right) \quad (3.41)$$

On the other hand, the electron dynamics do not include the electrons inertia in this model and have the following form:

$$\partial_t n + \nabla \cdot (n \mathbf{v}_e) = 0 \quad (3.42)$$

$$-e(\mathbf{E} + \mathbf{v}_e \times \mathbf{B}) - \frac{\nabla p_e}{n_e} - m_e \nu_{en} \mathbf{v}_e = 0 \quad (3.43)$$

Now, using the quasi-neutrality assumption for the E-region plasma and the second-order terms in the closure the dispersion relation, which is a fifth-order polynomial of  $\omega$ , can be written in the following form:

$$\begin{aligned} & (\omega + i\nu_{in})(6s^2 - 5) \left( \omega - \mathbf{k} \cdot \mathbf{v}_{e0} + i\nu_{en} \frac{k^2 v_{Te}^2}{2\omega_{ce}} \right) = \\ & \frac{i\psi}{n\nu_{in}} \left( (\omega + i\nu_{in})(6s^2 - 5) \left( \omega(\omega + i\nu_{in}) - \frac{k^2 v_{Ti}^2}{2} \right) - \frac{4}{3} \omega \frac{k^2 v_{Ti}^2}{2} (9s^2 - 3) \right) \end{aligned} \quad (3.44)$$

where,  $s = (\omega + i\nu_{in})/k\nu_{Ti}$

For small  $k$ , the dominant modes fall in the collisional domain where  $\omega < \nu_{in}$ , and hence the phase velocity and growth-rate are given by:

$$v_{ph} = \frac{\hat{\mathbf{k}} \cdot \mathbf{v}_{e0}}{1 + \psi} \left( 1 - \frac{k^2 v_{Ti}^2}{\Omega_{ce} \Omega_{ci}} \frac{\nu_{en}/\nu_{in}}{1 + \psi} \right) \quad (3.45)$$

$$\gamma = \frac{i\nu_{en}}{(1 + \psi)(\Omega_{ce} \Omega_{ci})} \left( \omega^2 - \frac{3}{2} k^2 v_{Ti}^2 - k^2 C_s^2 \right) \quad (3.46)$$

The growth rate profile in the top-panel of figure(3.6) shows strong stabilization for the growing modes at shorter wavenumber compared to the Unified fluid model that includes the ions viscosity and electrons polarization drift. The mode of maximum growth rate centered around 3.14 meters which is equivalent to 1 meter scale irregularity, which agrees with type-II observations.

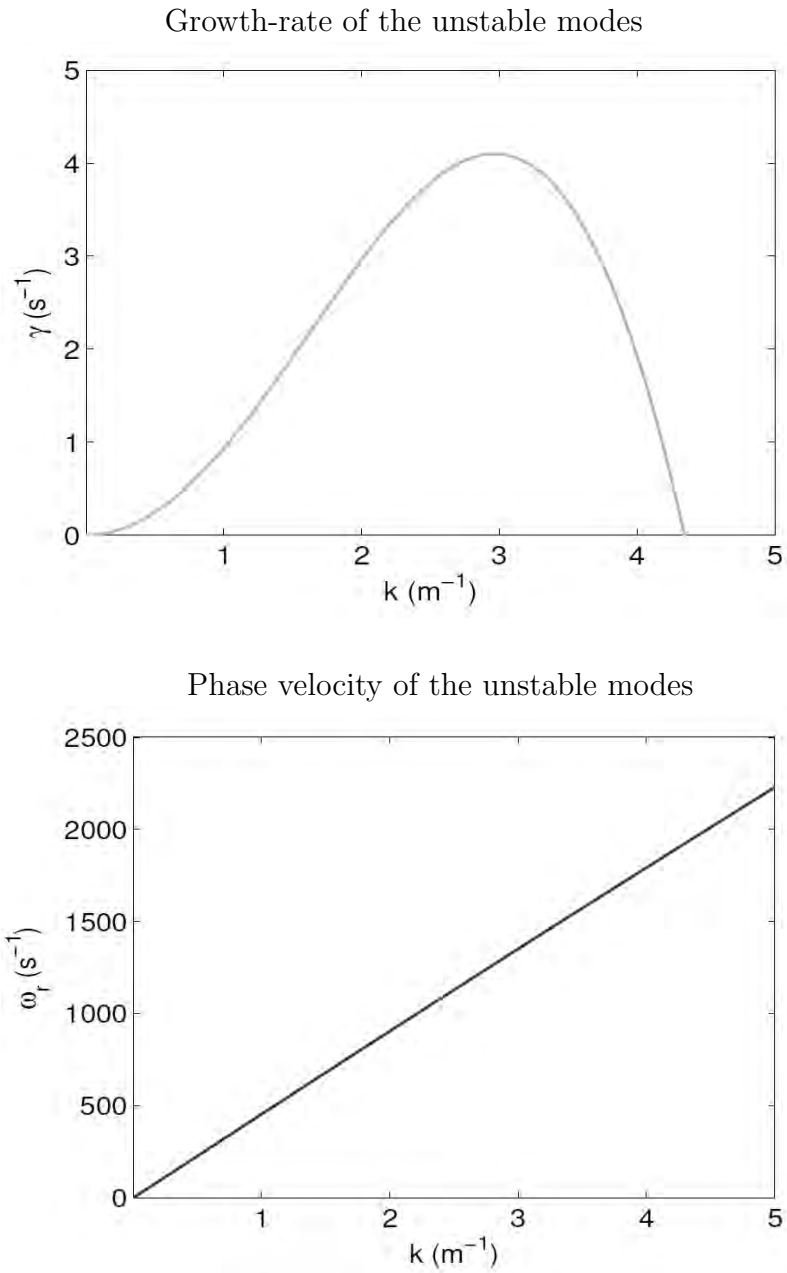


Figure 3.6: The growth rate (top) and the real frequency (bottom) for the ions dynamics including both the viscosity and thermal flux in the fluid model using the corresponding moments in the Vlasov equation. [From Litt *et al.* [55]]

On the other hand, the phase velocity in the bottom-panel of figure(3.6) has smaller magnitude compared to the standard two-stream Farley-Buneman instability fluid model at the same  $\mathbf{E} \times \mathbf{B}$  drift velocity for the electrons stream. But the phase velocity magnitude still larger than the local ion-acoustic speed which represents the maximum observed speed in the equatorial electrojet.

Thus, adding the ion thermal flux term to the equation of motion of the ions (3.32) enhances the dynamics of the ions in the linear domain and shows a promising results in stabilizing the evolving fields.

# Chapter Four: Simulation Results of the Equatorial Electrojet Instabilities

<sup>1</sup>The solution of the system of partial differential equations for the dynamics of plasma instabilities in the equatorial electrojet in the linear regime are presented and discussed in chapter(3). These results are promising and reflect some of the features of the type-I and type-II instabilities, such as the scale-length of the plasma irregularities of type-I and type-II instabilities, the smaller value of the horizontal plasma structures compared to the electrons cross-field drift velocity, etc. Other features, such as the electron maximum perturbed density, flux asymmetry, limitation of phase-front drift speed to the ion-acoustic speed, etc., require the solution of the dynamic equations in the nonlinear domain to manifest themselves in accordance with the coupling between the unstable modes and the redistribution of their energy content. Thus, in this chapter we present the nonlinear simulation results under different ionospheric conditions, and compare them to the radar observations and sounding rocket measurements presented in chapter (2).

## 4.1 Simulation Results for Basic Fluid Model

The basic fluid model is discussed in section (3.2), and this model is considered an acceptable two-stream model for the equatorial electrojet instabilities for a long time cause of its success to reflect some characteristics of these instabilities in the linear regime. Because of the failure of this model to saturate in the nonlinear simulation, its success is limited to the linear domain results. However, the physics in basic fluid model is the base for all further advances in solving this problem in the fluid domain. For example our unified fluid model is based on this model but it adds more moments from Vlasov equation (the ion viscosity stress tensor) to include more damping effect

---

<sup>1</sup>The work in this chapter is based on a collaboration with coauthors in Hassan, E., Horton, W., Smolyakov, A.I., Hatch, D.R., Litt, S.K., Multiscale equatorial electrojet turbulence: Baseline 2-D model, *Journal of Geophysical Research*, doi: 10.1002/2014JA020387, 2015. The theoretical model has been done in collaboration with Horton and Smolyakov, the simulation code optimization and computational techniques have been discussed with Hatch, and the linear and nonlinear results have been discussed with Litt, Smolyakov, Hatch, and Horton.

for the short-scale structures and to play the same role of the ions Landau damping effect which can only be retrieved in the kinetic domain.

Before we derived the unified fluid model we had run a simulation of the basic fluid model that only retrieves the large structures in the instabilities. In the simulation results in figure (4.1) we show the initial condition and evolution of large structures in the electron density of order hundreds to tens of meters.

The simulation box is  $300 \times 300$  meters with resolution  $256 \times 256$ . So, it does not resolve the Farley-Buneman (type-I) instability at the large wavenumbers, and only the gradient-drift (type-II) instability is included in this larger domain simulation. The simulation shows only the upward drifts of low-density plasma which encountered by the downward drift of the high-density plasma. Only the large structure of plasma irregularities of order 10 meters can be seen in the simulation box because the structures of smaller scales can not be generated in the simulation box due to its low-resolution.

We had this simulation as a preliminary step for two reasons: (1) to check the ability of the basic two-stream fluid model to simulate the plasma instability in the equatorial electrojet before running the large simulation of the unified fluid model which resolves both types of instabilities, (2) to verify our simulation code results by comparing them with another simulation of the same problem that had done by Sudan *et al.* [114].

## 4.2 Simulation Results for Unified Fluid Model

### 4.2.1 Nonlinear System Initialization

For the nonlinear simulation of the dynamic equations we use the Pseudospectral method to find the spatial derivatives of the fields in spectral-domain (k-space) and then integrate the three partial differential equations in the time-domain using a fifth-order and sixth-order Runge-Kutta (RK6) method with periodic boundary conditions at all boundaries for all the evolving fields. We solve our nonlinear system in a simulation box of size  $100 \text{ m} \times 100 \text{ m}$  in the real-space (r-space) with grid resolution  $1024 \times 1024$ . This r-space grid is equivalent to  $22 \text{ m}^{-1} \times 22 \text{ m}^{-1}$  in k-space

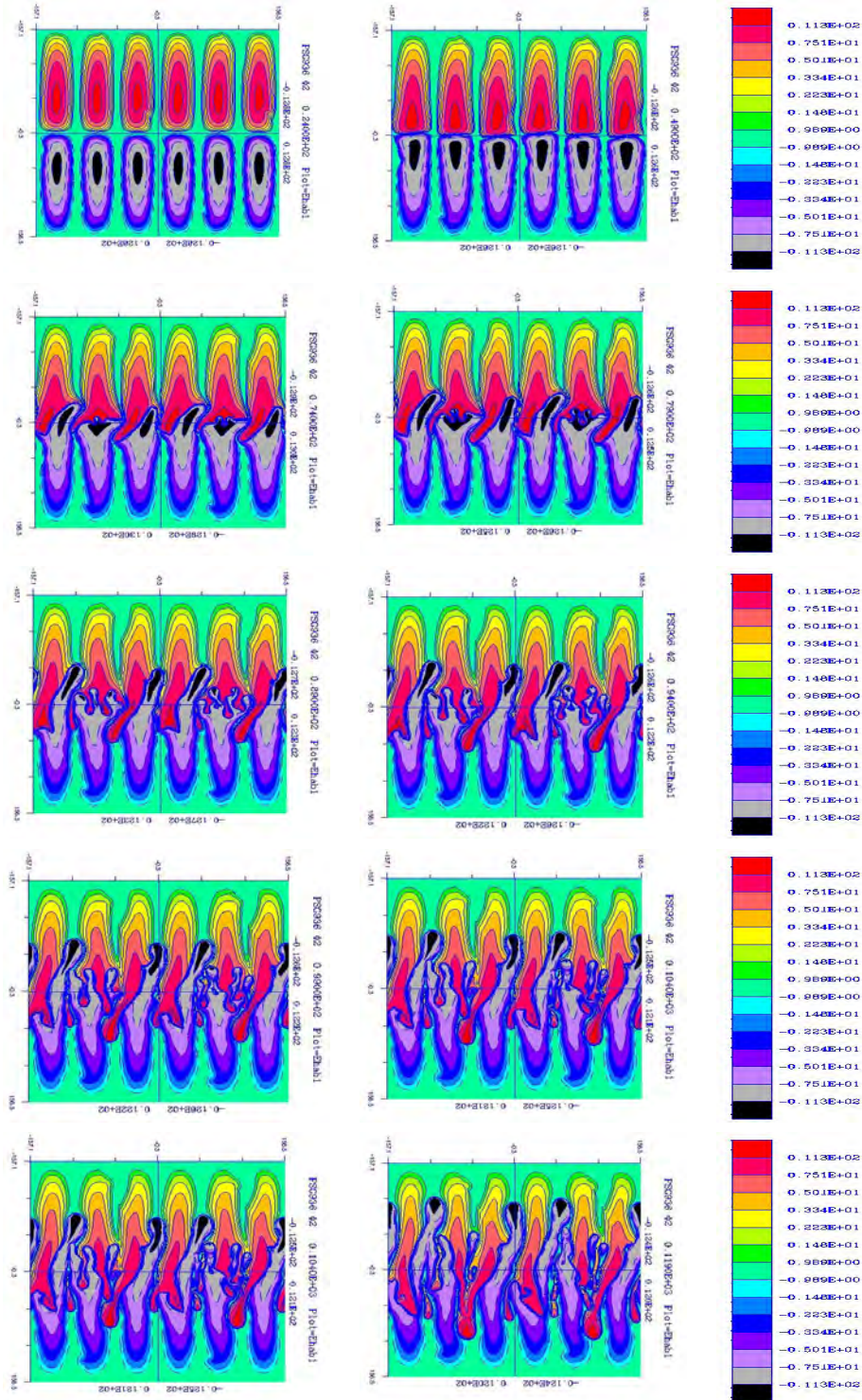


Figure 4.1: The initial condition and evolution of the unstable modes of electrons density for the basic fluid model. It shows the upward (downward) drifting of the low-density (high-density) plasma structures due to the cross-field instability. [From Hassan *et al.*] [35]

(after removing the dealiasing region that is required by the nonlinear terms for spectral methods). We use  $1024 \times 1024$  resolution to be able to include both types of instabilities (type-II at  $k_y \approx 0.1 \text{ m}^{-1}$  and type-I at  $k_y \approx 12.0 \text{ m}^{-1}$ ) in the simulation box of our dynamical system as we indicated earlier in chapter(3) when discussed the linear results and show them in figure (3.3). The rest of the k-space are considered guard cells for the excitation of nonlinear unstable modes and the dissipation of the energy in the damping modes.

The local values (where,  $|kL_n \gg 1|$ ) around 105 km altitude for the physical quantities on March 2008; which is coincident with the deep solar minimum and a solar quiet (Sq) time of the last and unusual solar minimum conditions as reported by Benevolenskaya and Kostuchenko [8], with setting  $v_E = 400 \text{ m/s}$  and  $L_n = 6 \text{ km}$  are employed in the coefficients of the dynamical system equations. Woods *et al.* [123] found the total solar irradiance in 2008 is much smaller than its value in the previous solar minimum in 1996, and the value of the solar radio flux index at this day is F10.7=69.9. Then we used the different values of  $L_n$  and  $v_E$  under the solar maximum conditions in March 1987 to run many simulations and compare them with those of solar minimum conditions.

We initialize the perturbed part of the plasma density, electric potential, and the ion velocity potential in the k-space using the values of the eigenvectors calculated numerically while solving the eigenvalue problem. In the system initialization we used all the modes those correspond to positive growth-rates at all the  $k_y$  and  $k_z$  values. This insures the availability of a very large number of unstable modes that can couple together in the nonlinear regime.

On the other hand, the time integrator uses adaptive time step based on a tolerance value for the maximum error accepted in the system. The time integrator solves the set of dynamical equations using the Runge-Kutta method in its fifth-order and six-order domains and compare the difference between them to have it less than the tolerance. If the difference is more than the tolerance, the time integrator divides the time-step into halves and find another answer and it proceed in this process until it gets the most accurate answer. We set the initial time-step to be  $10 \mu s$  but as we explained the integrator adapts this value by integrating over its half seeking smaller

error in the integration if the error was found to be larger than the tolerance.

The simulation code has used one processor of 16 cores at Stampede *High Performance Computing (HPC)* machine at the *Advanced Texas Computing Center (TACC)*. The wall-time of the simulation is very dependent on the parameters we are using and the phase of the simulation but on average we found that every 40,000 - 70,000 time steps take 48 hours computation wall-time.

## 4.2.2 Spectral Analysis of Electron Density

In the nonlinear run we evolve the perturbed normalized quantities  $(\delta\tilde{n}, \delta\tilde{\phi}, \delta\tilde{\chi})$  in the k-space over time to check the transition from the region of linear dominance to the region of nonlinear dominance and end in the saturated state of the simulation where the time-average of the perturbed quantity integrated over the k-space is almost zero.

Snapshots of the energy spectrum of the plasma density are shown in figure(4.2) at different stages of the simulation. For context, the reader is also referred to figure(3.3) (which shows the range of linear instability), and figures(4.3 - 4.5) (which show the time evolution of the density perturbations).

The first panel in figure(4.2) shows the energy spectrum of the plasma density in the linear growth phase with more energy content at small k-values in the horizontal and vertical directions. In the second panel, the energy is concentrated at low  $k_z$  and shifts to higher  $k_y$  to damp linearly after generating waves of sub-meter wavelengths. Panels three through five demonstrate the transition from initial nonlinear stabilization to fully saturated turbulence. The third panel ( $t = 0.53$  s) represents a point of transient saturation, as can be seen in figure(4.7). At this point, the energy is largely concentrated in the small type-I scale range. In panel four, the dominant scales are reversed during the transition to the final saturated state. Here the energy is concentrated at large type-II scales, with comparatively less energy at small scales. In the fifth panel, the final nonlinear balance is achieved with two distinct scales having energy apportioned quite evenly between them. These two dominant scales, however, are embedded in broadband turbulence, as can be seen from the significant energy observed over the entire instability range (e.g., in the intermediate  $k_y = 2.0 - 7.0 m^{-1}$  range).

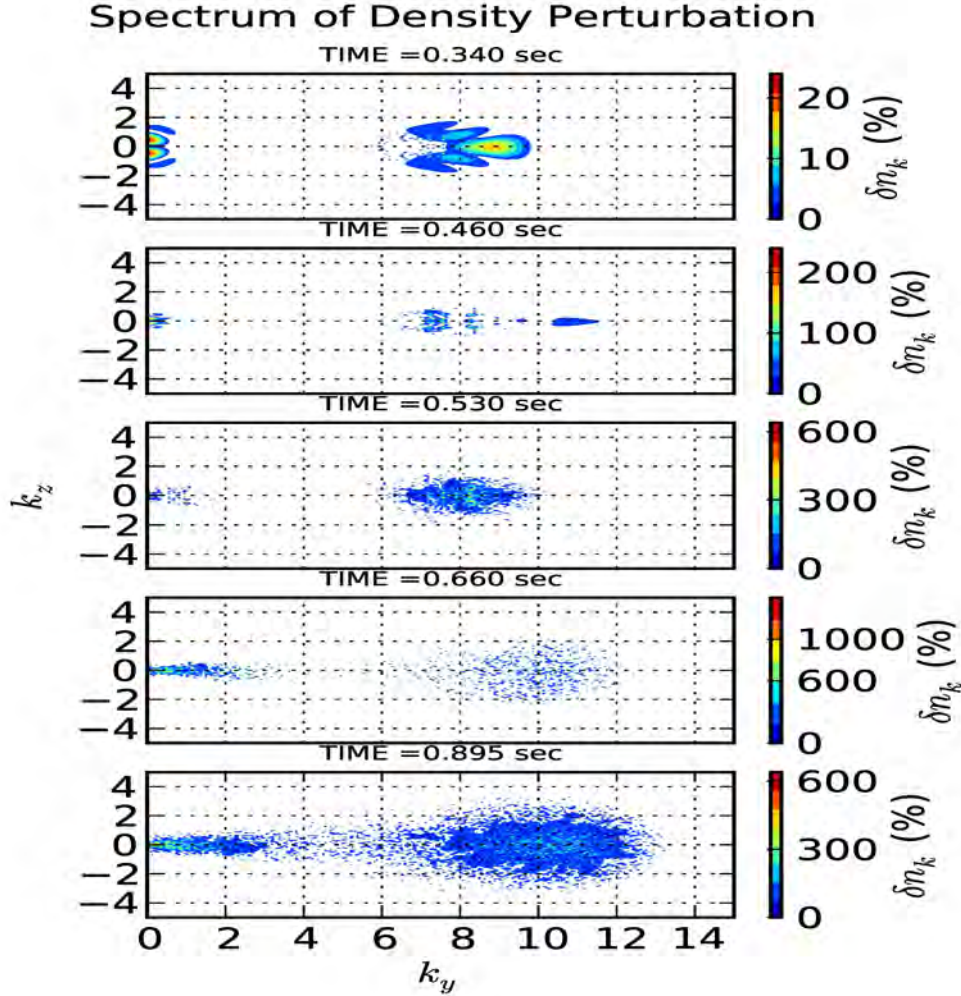


Figure 4.2: The Energy Spectrum of the Perturbed Electron Carrier Density at different states of the simulation. The top panel shows that the energy spectrum of the available modes accumulates at two peaks for two types of instabilities at low- and high- $k$  values. The second panel shows the transition of the energy to the modes of higher wavenumbers. These modes decay as they enter the region of negative growth-rates as long as they are in the region where the linear terms dominate. The third panel shows the distribution of energy over the available modes right before the transition region between the linear and the nonlinear regimes which has different distribution of the energy spectrum as shown in the fourth panel. The fourth and the fifth panels show the distribution of the energy over modes at all wavenumbers. This verifies the coupling between the two types of instabilities and the cascade transition of the energy from small wavenumbers to large wavenumbers that makes the system has electron density structures of all sizes. [From Hassan *et al.* [36]]

The onset of the nonlinearity dominance in the transition region is coincident with the generation of long structures of the plasma irregularities in the vertical direction with scale-length of 40 meters, see figure (4.4). In addition, we attribute the generation of the 3 meter scale waves in the vertical direction to the cascade energy transfer from the long structures at small wavenumbers to the short irregularities at the large wavenumbers which is consistent with the theory of Sudan *et al.* [1973] for the generation of small-scale irregularities in the equatorial electrojet.

This complex nonlinear interplay between the different scales of instabilities and the forward and reverse cascading of energy between these plasma structures is studied and presented in detail in chapter (5) using the nonlinear energy transfer functions for a non-canonical Hamiltonian system.

### 4.2.3 Instabilities Evolution, Coupling, and Saturation

Many of the features described in the previous section can also be directly observed in the contour plots of the perturbed density in the real space. The upward (downward) drift of the low-density (high-density) plasma is shown in figure(4.3) during the linearly growing phase of the simulation. The vertical drift velocity is found from successive frames to be around 50-70 m/s which is consistent with the observation of type-II instability. The plasma waves in horizontal direction have small-scale of order 1 - 5 meters in wavelength.

Figures(4.4 and 4.5) show snapshots of the plasma density fluctuations at  $t = 0.6$  seconds (during the initial saturation phase) and  $t = 1.0$  s (during the final saturated phase), respectively. The multi-scale nature of the turbulence is evident in the East-West direction in both figures, with prominent features visible at  $\sim 1$  meter that are embedded in structures with  $\sim 10$  meters in scale. In the vertical direction, the fluctuations exhibit a stark change during this transition to fully developed turbulence. The vertical structures are very large scale  $\sim 20 - 40$  meters at  $t = 0.6$  seconds, but are reduced to  $\sim 1 - 3$  meters at  $t = 1.0$  seconds. At this point, the simulation box is filled with small-scale structures embedded both vertically and horizontally in the long-scale irregularities of Type-II instabilities. The small-scale vertical structures can be considered as the formation of the secondary type-I instabilities in the vertical direction and is consistent with the energy cascade theory [113] to small vertical

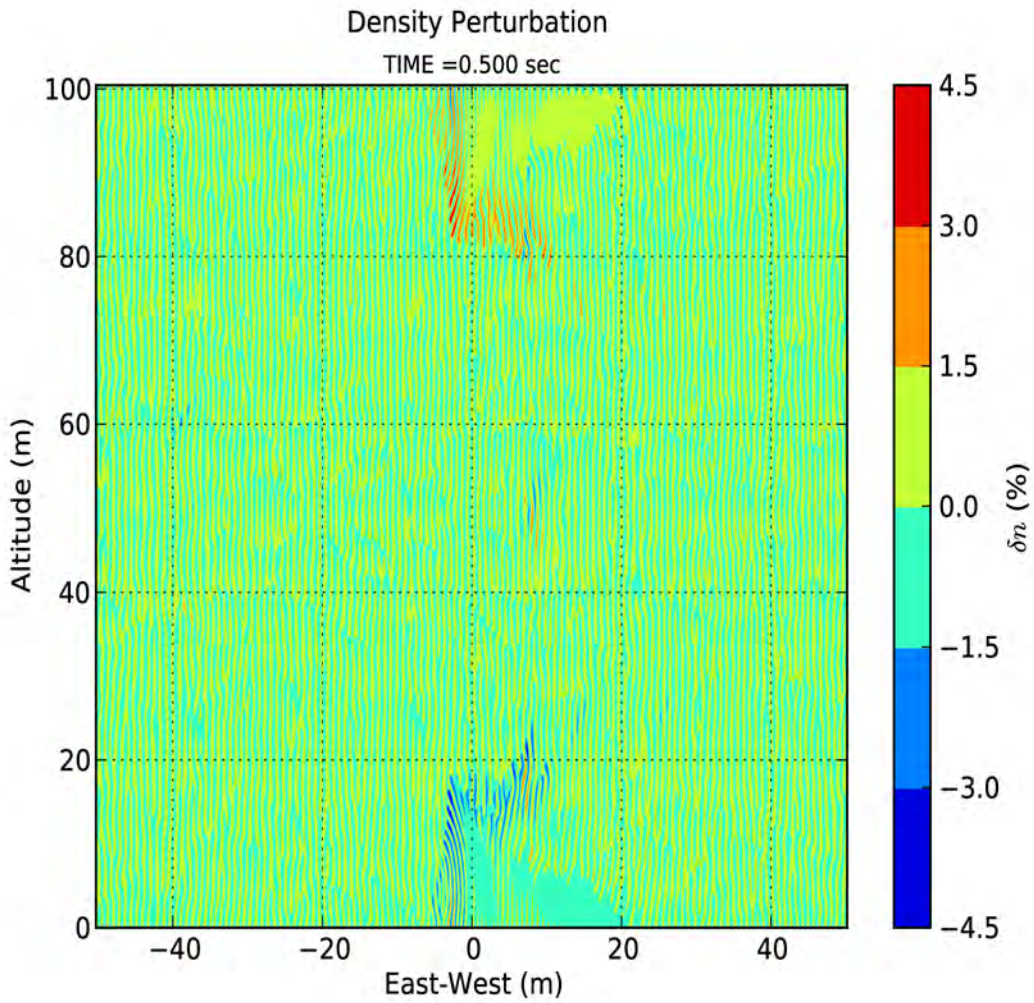


Figure 4.3: The evolution of the perturbed electron carrier density ( $t = 500ms$ ) during the dominance of the linear terms on the simulation. It shows the downward drifts of the high-density plasma and the upward drifts of the low-density plasma as a result of the dominance of the Gradient-Drift (Type-II) instability at this phase of the simulation. [From Hassan *et al.* [36]]

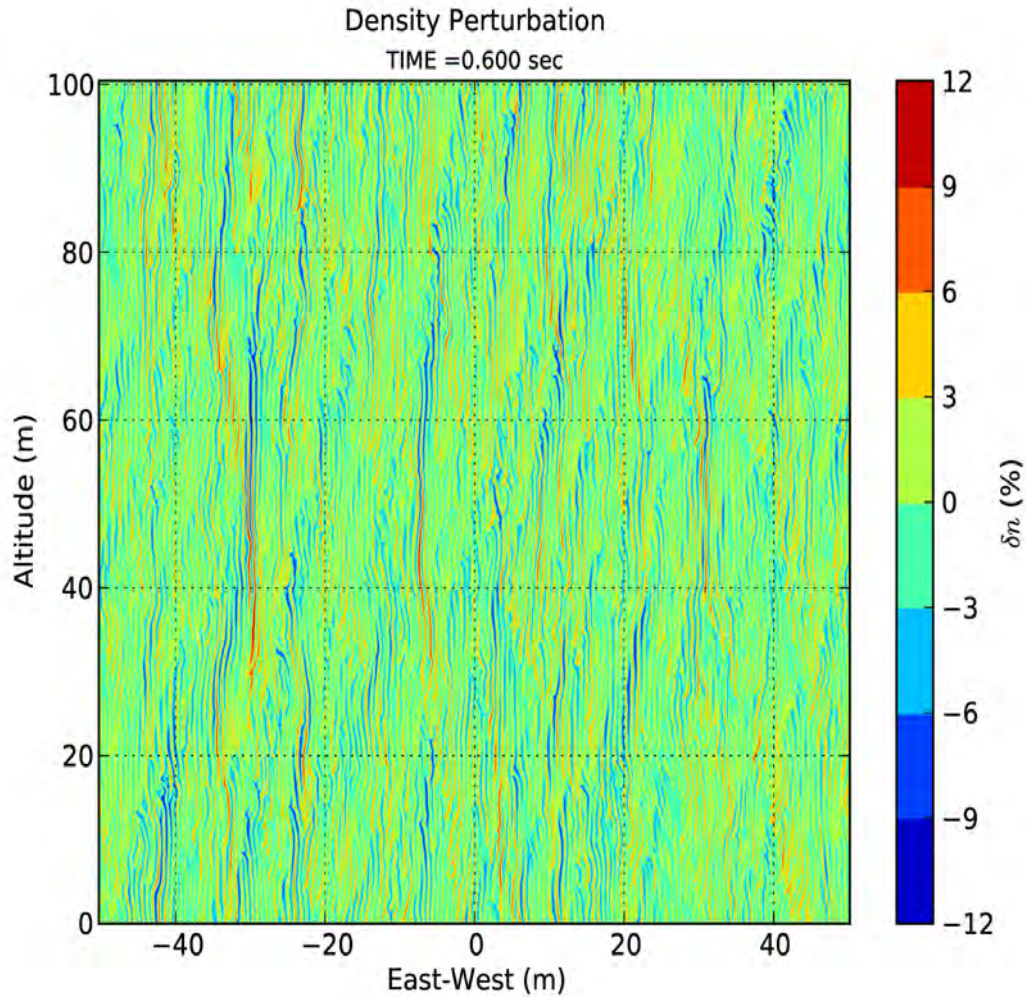


Figure 4.4: The perturbed electron carrier density ( $t = 600ms$ ) during the transition from the dominance of linear terms to the dominance of nonlinear terms in the saturation state of the simulation. It shows the expected large size structures of plasma densities that are drifting straight downward before the effect of the Farley-Buneman (Type-I) instability effectively shows up and break these large structures into smaller ones. [From Hassan *et al.* [36]]

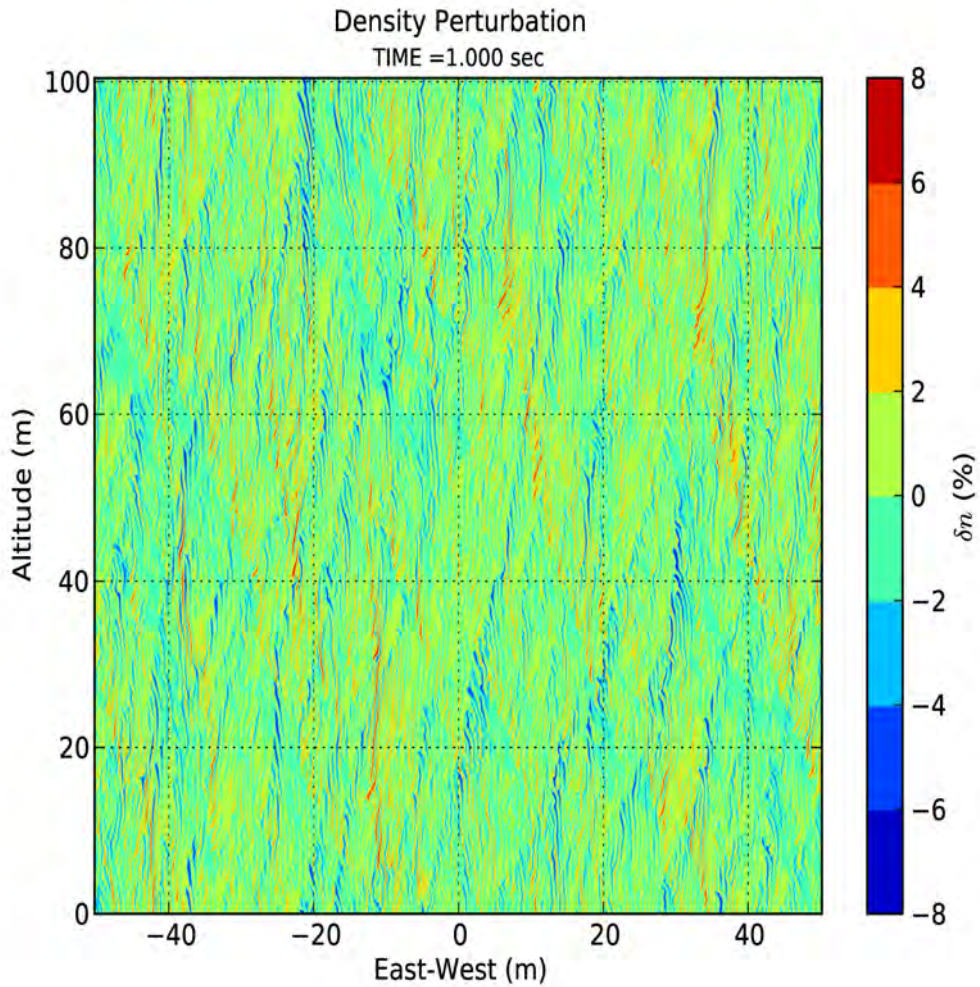


Figure 4.5: The perturbed electron carrier density ( $t = 1000ms$ ) during the dominance of the nonlinear terms at the saturation state of the system reaches 8% relative to the background electron density. It shows the very small structures of sizes less than a meter embedded in larger structures that are seen before as a result of the coupling between Type-I and Type-II instabilities in the saturation state. [From Hassan *et al.* [36]]

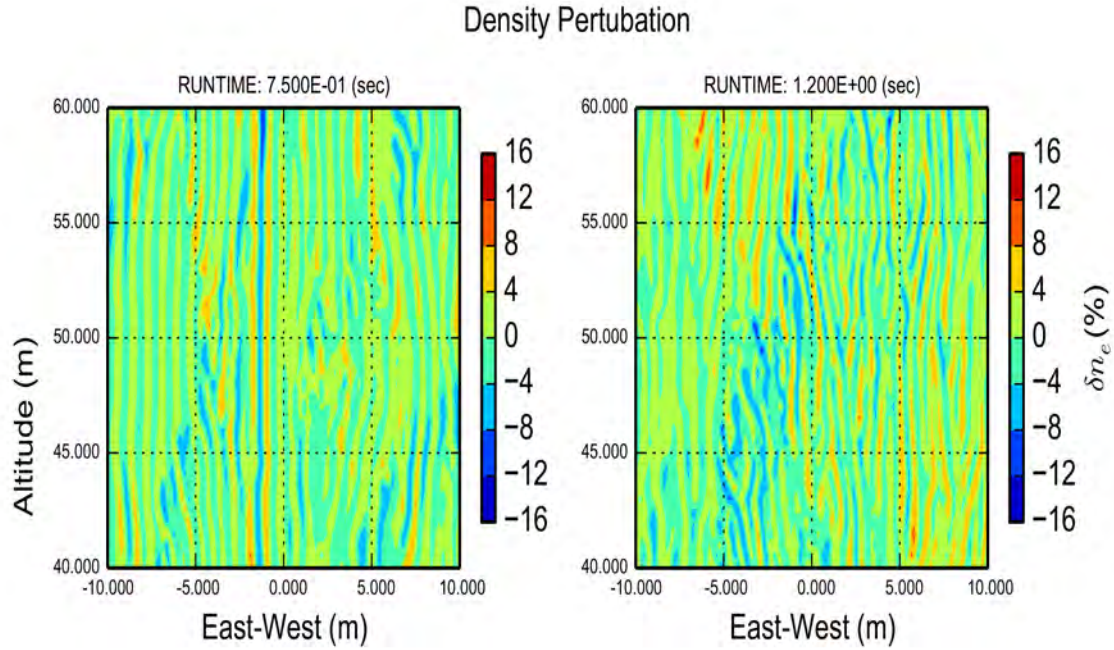


Figure 4.6: A close view of the large-scale structures formed during the transition phase (left-panel) and the small-scale structures formed during the saturation phase of the simulation under the solar maximum (1987) conditions. [From Hassan *et al.* [36]]

scales.

A closer look at the turbulence in the plasma density under the solar-maximum condition (March 1987) is shown in figure(4.6). The left-panel shows the long-structures at  $t = 0.75$  seconds which is right-shifted in time with respect to the transition region under the solar-minimum condition as we discussed in section (4.2.4). These long-structures fill the box with a few small-scale structures. At  $t = 1.2$  s, the perturbation in density is saturated and we see in the right-panel of figure(4.6) many small-structures of 1 - 3 meters scale-length. The structure of the plasma density during the growing-, transition-, and saturation-phases of the simulation is identical under different solar conditions and only the saturation levels of the perturbed quantities are different.

Watching successive frames of the density evolution during the saturation states shows

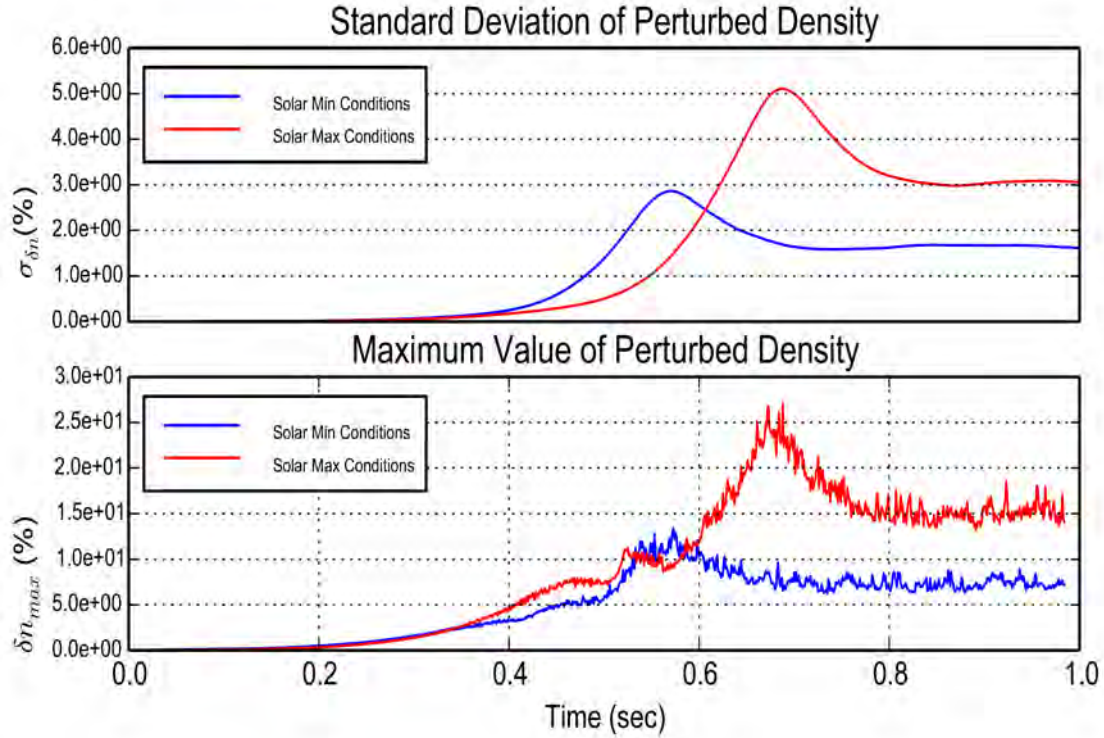


Figure 4.7: A comparison between the the perturbed density maxima (lower panel) and its stadard deviations (upper panel) at the solar maximum (blue-line) and solar minimum (red-line) year. The standard deviations in the lower panel also defines clearly the growing, transion, and saturation phases during the simulation under two different solar conditions. [From Hassan *et al.* [36]]

that the downward and upward drifts are not in a straight vertical direction, but they drift with an inclination to the horizontal direction which is parallel to the direction of  $\mathbf{E} \times \mathbf{B}$  plasma drifts. Oppenheim and Otani [68] called this motion toward the corners of the simulation box “a bent of the primary waves,” and they attributed it to the decrease in the linear growth-rate for the primary waves of  $k_z \neq 0$  to a value that is below its value at  $k_z = 0$  in the linear regime of the simulation. This feature can be seen from the vertical profile of the growth rate.

#### 4.2.4 Turbulence in Electron Density

A comparison between the time variations in the plasma density during the condition of solar maximum on March 1987 (red-line) and solar-minimum on March 2008 (blue-line) is shown in figure(4.7). The top-panel shows the standard-deviation of the perturbed density, however the bottom-panel shows the maximum perturbation in the plasma density as a function of time.

The standard-deviation shows the three distinct domains of the simulation, e.g. linear, transition and saturation phases. The evolution time required in the simulations in the growing phase under the solar-maximum conditions is longer than the corresponding time under the solar-minimum conditions. Also, the level of the standard-deviation of the saturated perturbed plasma density, which reaches a fluctuation level of 15% relative to the plasma density in the background, is higher under the solar-maximum conditions ( $\sigma_{\delta n} = 3.0\%$ ) than the solar-minimum conditions ( $\sigma_{\delta n} = 1.7\%$ ) with a  $\Delta t = 0.1$  seconds difference between their start of the saturation region in the simulation.

Under the solar-minimum condition, the perturbation in the electron density increases to 12% of the background density during the transition region before it goes back to 7% in the saturation region as a result of the strong coupling between the primary and secondary waves in the nonlinear saturation regime. This is below the expected 10 - 12% perturbations found in both the Rocket and the Radar Observations [4, 54, 83, 43]. Our interpretation of the low level of plasma density perturbations is the result of the low solar radio flux accompanied by the unusual solar minimum conditions and the solar quiet condition employed in this simulation [8, 123].

When we examined the dynamical system under the solar-maximum condition we found that the time variations in the perturbed density during the saturation region shows a maximum which is much higher than the 7% found during the solar-minimum conditions. The perturbation in the electron density increases to 25% of the background density during the transition region before it goes back to 15% in the saturation phase. So the level of the plasma density under the solar maximum condition is very close to the measured density in the CONDOR campaign [54, 80, 81].

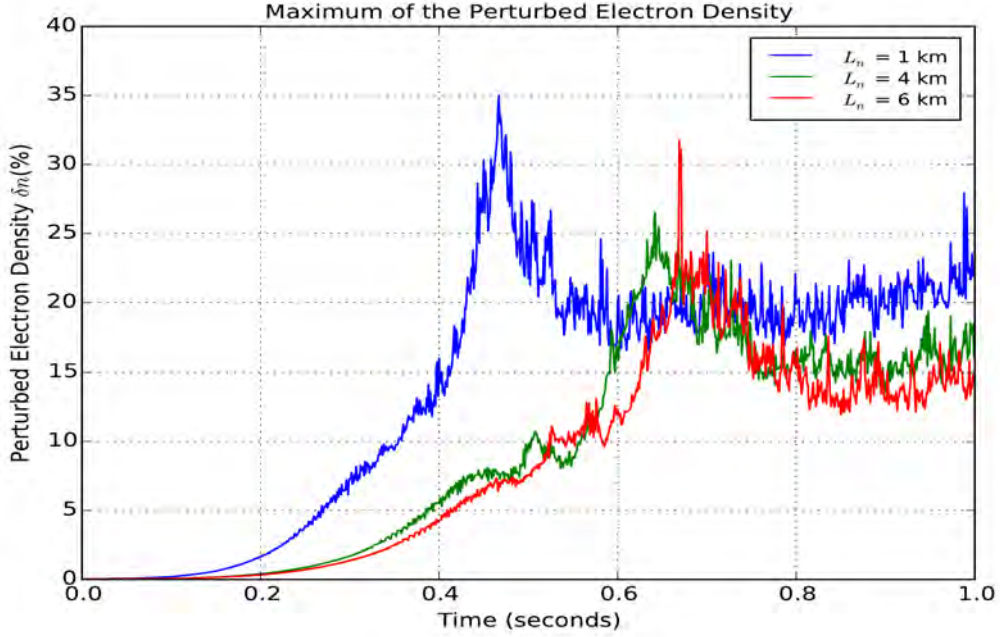


Figure 4.8: A comparison between the perturbed density maxima for different density scale-lengths,  $L_n = 1, 4, 6$  km that shows different growing rate of the unstable modes and different levels of saturation. [From Hassan *et al.* [37]]

A comparison between the maximum perturbed electron density for different density-gradient scale-length is shown in figure (4.8) where we can see that the time of the plasma density evolution in the linearly growing domain of the simulation is faster with shorter density-gradient scale-length. Although they have a very small difference in their corresponding growing modes, the difference between the evolution of the plasma density during the early stage of the simulation in the cases of  $L_n = 4$  km and 6 km does not show a big difference in the saturated state of the simulation and they come along with very little difference. In contrary, a short scale-length of 1 km makes a big difference both in its linear growing mode of the fluctuating density. In the saturation state, the perturbed density in case of  $L_n = 1$  km shows a 5% more in the maximum fluctuation of the plasma density compared to the other cases.

Therefore, these simulation results show the importance of the density-gradient scale-length in driving the plasma instabilities and gives rise to density fluctuations of different scales in the equatorial electrojet region.

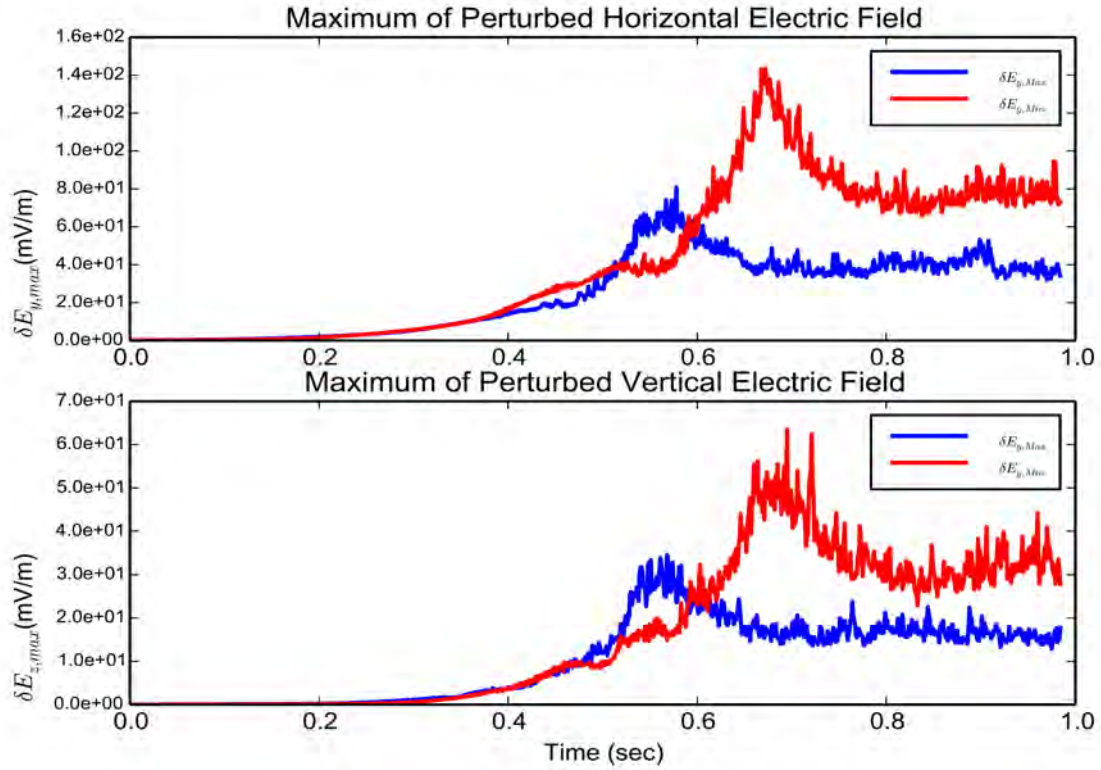


Figure 4.9: A comparison between the maximum perturbed electric field components in the horizontal (top panel) and vertical (bottom panel) directions at the solar maximum (red-line) and solar minimum (blue-line) years shows the effect of solar activity on the magnitude of the electric field components. [From Hassan *et al.* [36]]

#### 4.2.5 Perturbed Electric Fields

The maximum perturbed electric field in the zonal and vertical directions are shown in the upper and lower panels of figure (4.9), respectively. The zonal component of the perturbed electric field grows to 140 mV/m before it saturates at 80 mV/m under the solar-maximum conditions which is double its saturation value under the solar-minimum conditions. Similarly, the vertical electric field saturates at a larger value (35 mV/m) compared to the solar minimum saturation value (15 mV/m). The difference in the perturbed field between the solar maximum and solar minimum is directly related to the level of the perturbed density under these different conditions which is discussed in subsection (4.2.4).

The root-mean-squares (rms) of the perturbed electric fields (which are the measurable quantities by the sounding rockets) in the zonal (solid-lines in upper-panel) and vertical (solid-lines in lower-panel) directions are shown in figure (4.10). While the magnitude of the rms of the zonal perturbed electric field in the saturation regime reaches 15 mV/m during the solar maximum conditions, it does not exceed 8 mV/m under the solar minimum conditions. On the other hand, the rms value ( $\delta E_z = 3.0$  mV/m) of the perturbed vertical electric field during the solar-maximum conditions is almost double its value ( $\delta E_z = 1.7$  mV/m) under the solar-minimum conditions.

Comparing these results with the sounding rocket measurements of the vertical and horizontal electric field components that are presented in chapter (2), we find that the simulation results of the magnitude of the zonal and vertical perturbed fields under the ionosphere conditions in March 1987 (solar maximum) are in a very good agreement with that CONDOR campaign measurements.

Unfortunately, we could not find any sounding rocket results for the fluctuating electric field components during a solar minimum conditions to compare our results to them, but the agreement of the results under the solar maximum conditions puts results of the perturbed electric field during the solar minimum conditions in a good standing for any future sounding rocket missions.

#### 4.2.6 Asymmetries in Plasma Fluxes

The "east-west" zonal and "up-down" vertical components of the perturbed electric field are shown in the upper and lower panels of figure(4.10), respectively, during the solar-maximum (red) and solar-minimum (blue) conditions. While the solid lines represent the rms of *total* perturbed electric fields, the dotted and dashed lines represent the rms of the westward (upward) and eastward (downward) perturbed components in the zonal (vertical) directions, respectively.

These zonal and vertical components of the electric field give rise to both the Pedersen current along the direction of the electric field component and Hall current in a direction perpendicular to the plane containing both the electric field component and the magnetic field as a result of the  $\mathbf{E} \times \mathbf{B}$  electron drifts. The large ratio between the Hall and Pedersen conductivities ( $\frac{\sigma_H}{\sigma_P} \approx 10 - 20$ ); which gives rise to the Cowling

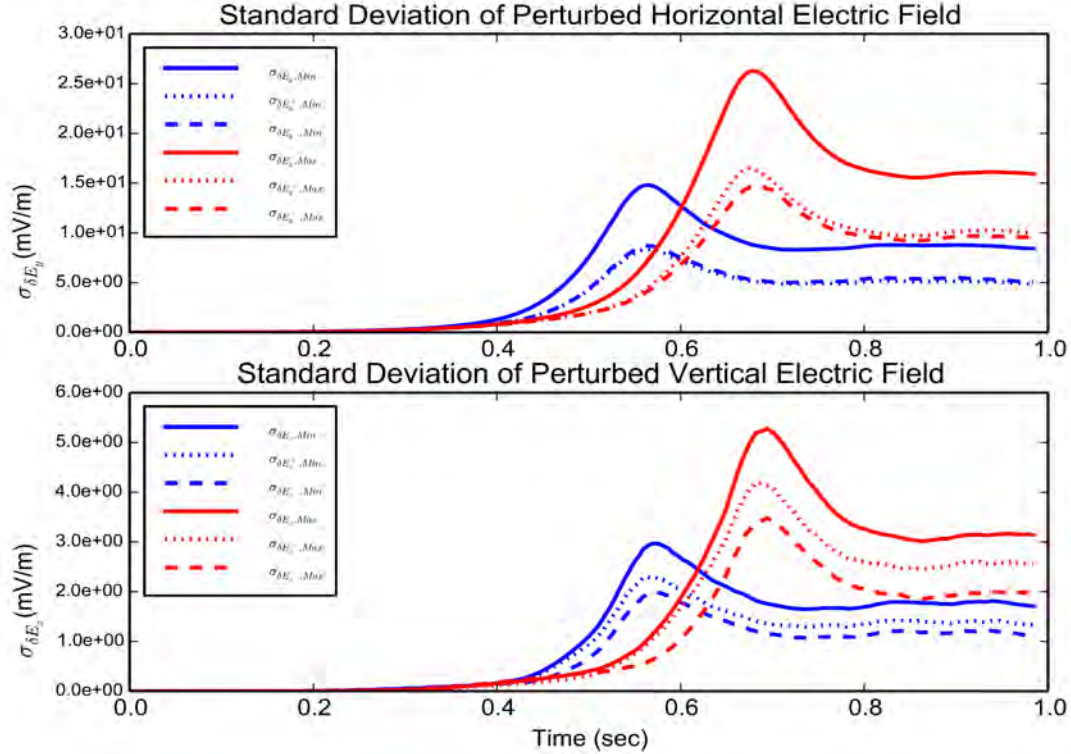


Figure 4.10: A comparison between the root-mean-square of the perturbed electric field components in the horizontal (top panel) and vertical (bottom panel) directions at the solar maximum (blue-line) and solar minimum (red-line) year. The dotted (dashed) lines show the root-mean-square of the positive (negative) component of the electric field. [From Hassan *et al.* [36]]

conductivity, makes the effect of the Hall current more important in the equatorial electrojet region. In turn, the difference in the Hall currents in the zonal and vertical directions gives rise to an asymmetry in the drift velocities and density fluxes in both directions which is reflected on the flux of the plasma density in these directions.

There is a large difference between the upward and the downward components of the perturbed electric field which is found common in all phases of simulation and causes an "east-west" asymmetry in the drift velocity. In 2005, Patra *et al.* [76] reported the first observations verifying the "east-west" velocity asymmetry found in Type-II echoes using a 18 MHz radar located at Thumba Equatorial Rocket launching Station (TERLS), Trivandrum, India. Patra *et al.* [76] attributed the "east-west" velocity

asymmetry to the large-scale primary waves that give rise to a large upward plasma drift. However, we find the "east-west" asymmetry exists even after the breaking-up of the large-scale vertical waves into smaller-scale structures. Thus, we consider the "up-down" asymmetry of vertically perturbed electric field, which is responsible of the zonal Hall drifts, to be the cause of the "east-west" velocity asymmetry.

On the other hand, the asymmetry in the vertical fluxes produces echoes of different strengths in the spectrograms from the AMISR prototype radar at Jicamarca as studied by Hysell *et al.* [43] and reported by Fejer *et al.* [26], Farley *et al.* [23], and Kudeki *et al.* [53]. The Hall drifts in the vertical direction do not show large asymmetry because of the very small difference between the zonal components of the perturbed field as shown in the upper panel of figure(4.10). The large difference between the zonal components can only be found in the presence of large-scale structures during the transition phase of the simulation, under the condition of solar maximum, and then decreases as it goes deep in the saturation phase with the "break-up" of the large-scale irregularities into small-scale structures. However, the large difference in the Pedersen drifts may play a role in causing the asymmetry in the density flux along the vertical direction.

#### 4.2.7 Phase Velocity of Plasma Irregularities

The plasma density in the zonal direction as a function of time is shown in figure(4.11). The inverse Fourier transform of the density spectrum is taken for all  $k_y$  wavenumber values of  $k_z = 0$  ( $m^{-1}$ ) for all time steps in the saturation state of the simulation. We can see small-scale waves of type-I that is superimposed on the large-scale waves of type-II instability. The phase velocity of the small-scale waves has a magnitude of 350 (m/s) and drifts westward. This value of phase velocity is about the same for the ion-acoustic speed (330-360 m/s) calculated from the ionosphere background data and shown in table(3.1). So, the phase velocity of the irregularity waves is limited to the ion-acoustic speed at the core of the electrojet at 105 km altitude. This result shows a good agreement with the radar observations that limit the speed of the plasma irregularities in the ionosphere E-region to the acoustic speed of ions and show them propagating in the westward direction [22, 54].

Another method to estimate the electron drifts in the zonal and vertical directions

### Phase Velocity of Particle Drifts

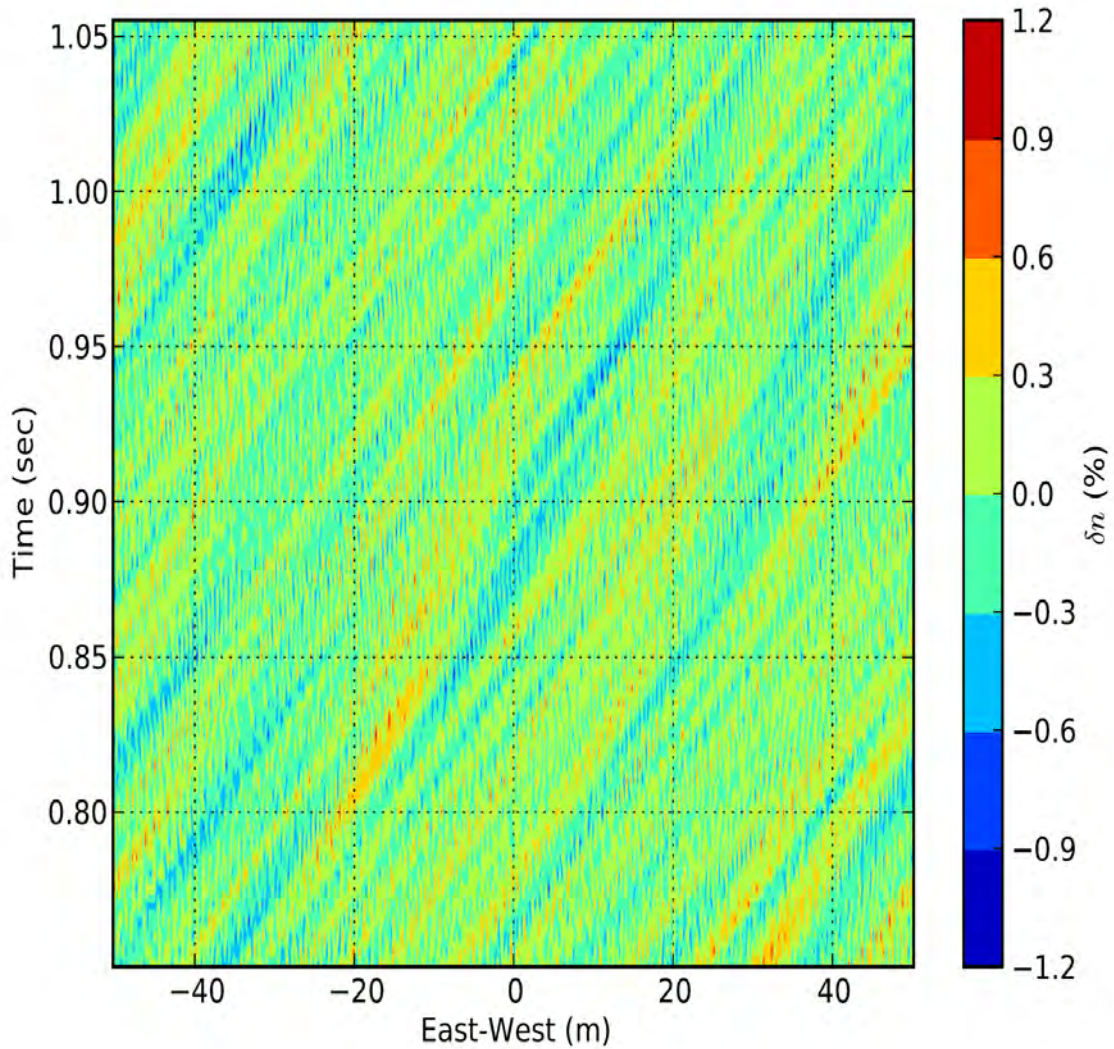


Figure 4.11: The inverse fourier transform of the particle density spectrum of all  $k_y$  values at  $k_z=0$  ( $m^{-1}$ ) for each time step during the saturation region. A phase velocity of 330 (m/s) can be estimated from the slope as a drift speed of the particle density to be approximately equal to the ion-acoustic speed at 105 m altitude. [From Hassan *et al.* [36]]

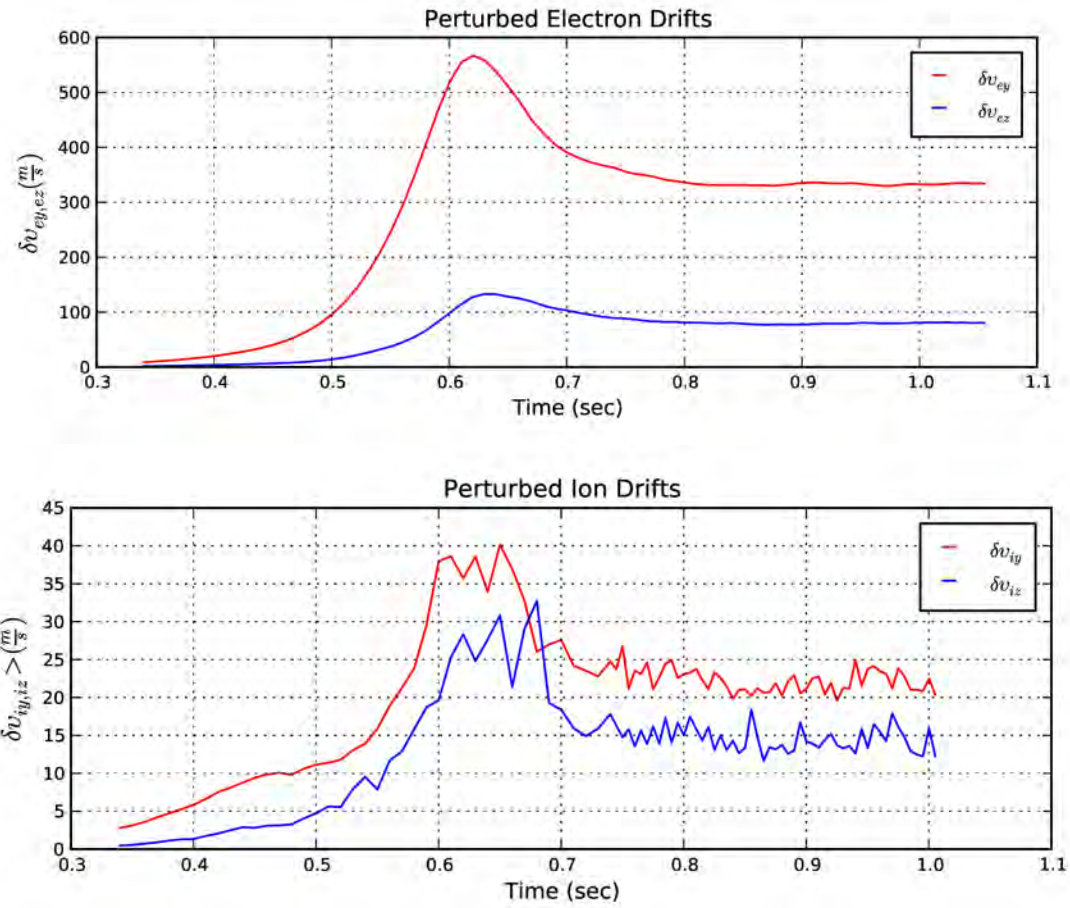


Figure 4.12: The calculated  $\delta \mathbf{E} \times \mathbf{B}$  drift velocity for the electrons (top) using the perturbed electric field ( $\delta E$ ) and the corresponding drift velocity for the collisional ions (bottom) in the zonal (red) and vertical (blue) directions.

is by calculating the  $\delta\mathbf{E} \times \mathbf{B}$  using the rms values of the fluctuating electric field components in these directions as shown in the top-panel of figure(4.12). These calculations give rise to a zonal electron  $\delta\mathbf{E} \times \mathbf{B}$  drift of magnitude 330 m/s that is similar to the drift calculated in figure (4.11). A vertical  $\delta\mathbf{E} \times \mathbf{B}$  drift for the electrons of magnitude 80 m/s is consistent with the expected up-down drift speeds of the plasma irregularities in the vertical direction due to type-II instability.

For the ions, we calculated drift velocity components in the horizontal and vertical directions as shown in the bottom-panel of figure (4.12) using the ions perturbed velocity potential ( $v_i = -\nabla\chi$ ). The large collision frequency of the ions with the background neutral particles causes that small magnitudes of the ions drift speed in both directions. The maximum value of the ions drift in the vertical direction is 15 m/s, however the maximum speed in the horizontal direction is 20 m/s where the ions are drifting eastward (opposite to the electrons direction of drift).

From the calculated measurements of the ions and electrons drifts in the zonal direction and because they drift in opposite direction to each other, the relative speed between the electrons and ions drift is  $330 - (20) = 350$  m/s which shows another proof of the supersonic nature of the equatorial electrojet plasma instability even in the saturation phase of the simulation during the solar maximum conditions.

# Chapter Five: Dynamic System Hamiltonian and Energy Cascades

Turbulence involves the injection, nonlinear redistribution between scales, and dissipation of energy. In this chapter, the details of the turbulence energetics for the unified ionosphere model are described. The two energy cascade mechanisms (*forward and reverse*) are operative in the system. The forward energy cascade is responsible for generating the small-scale structures by transferring the energy content in waves of large wavelength to these small-scale structures. However, the transfer of energy from the small-scale structures into the large-scale waves is taking place in the reverse energy cascade mechanism. The theory of energy dual-cascading mechanisms are used to explain many *in-situ* measurements and radar observations of the plasma turbulence in the equatorial electrojet.

## 5.1 Energy in the Equatorial Electrojet Model

In chapter(3) we studied different models for the plasma dynamics in the equatorial electrojet. A unified fluid model for the plasma instabilities is discussed in section(3.3) and a set of partial differential equations (3.15, 3.20, 3.26) were derived to model the role of the background density-gradient and the supersonic electron  $\mathbf{E} \times \mathbf{B}$  drifts in driving the gradient-drift and Farley-Buneman instabilities, respectively. Now we need to study the energy conservation and coupling between the evolving fields to understand the role that the nonlinear terms play to generate instabilities of different scale-lengths by cascading the energy between the unstable modes in the forward and reverse directions.

In the plasma dynamical system for the Equatorial Electrojet instabilities the energy comes into the system from the top and bottom boundaries due to the non-zero gradients of the background density and electric potential in the vertical direction which are considered as constant sources energy. However, the energy is dissipated in the electrons and ions collisions with the background neutral particles.

By separating the constant background density and electric potential from their fluctuating components, we can rewrite the dynamic equations (3.15, 3.20, 3.26) in the following form:

$$\partial_t \delta n = \nabla \cdot (\delta n \nabla \delta \chi) + \nabla \cdot (n_o \nabla \delta \chi) \quad (5.1)$$

$$\begin{aligned} \partial_t \nabla^2 \delta \chi &= \frac{\Omega_{ci}}{B} \nabla^2 \delta \phi + v_{ti}^2 \nabla^2 \delta n + \frac{1}{2} \nabla^2 |\nabla \delta \chi|^2 \\ &\quad - \nu_{in} \nabla^2 \delta \chi + \frac{4}{3} \frac{v_{ti}^2}{\nu_{in}} \nabla^4 \delta \chi \end{aligned} \quad (5.2)$$

$$\begin{aligned} \partial_t \nabla^2 \delta \phi &= -B \Omega_{ce} n_o^{-1} \nabla \cdot (\delta n \nabla \delta \chi) - B \Omega_{ce} n_o^{-1} \nabla \cdot (n_o \nabla \delta \chi) \\ &\quad - \Omega_{ce} [\phi_o, lnn_o] - \Omega_{ce} [\delta \phi, lnn_o] - \Omega_{ce} [\phi_o, \delta n] - \Omega_{ce} [\delta \phi, \delta n] \\ &\quad - \frac{1}{B} [\phi_o, \nabla^2 \delta \phi] - \frac{1}{B} [\delta \phi, \nabla^2 \delta \phi] \\ &\quad + \frac{T_e \nu_{en}}{e} \nabla^2 lnn - \nu_{en} \nabla^2 \phi + \frac{T_e \nu_{en}}{e} \nabla lnn \cdot \nabla lnn - \nu_{en} \nabla lnn \cdot \nabla \phi \end{aligned} \quad (5.3)$$

To study the system Hamiltonian we need to keep only the terms that are not sources or dissipation. So, by dropping any term that contains the gradient of the background density ( $L_n^{-1} = \partial_z lnn_o$ ) and/or background electric potential ( $v_E = -B_o^{-1} \partial_z \phi_o$ ) which are considered energy sources in the dynamic system, and any viscosity term that contains a collision frequency of the electrons and/or ions with the background neutrals we will be left with the following set of equations:

$$\partial_t \delta n = \nabla \cdot (\delta n \nabla \delta \chi) \quad (5.4)$$

$$\partial_t \nabla^2 \delta \chi = \frac{\Omega_{ci}}{B} \nabla^2 \delta \phi + v_{ti}^2 \nabla^2 \delta n + \frac{1}{2} \nabla^2 |\nabla \delta \chi|^2 \quad (5.5)$$

$$\partial_t \nabla^2 \delta \phi = -B \Omega_{ce} n_o^{-1} \nabla \cdot (\delta n \nabla \delta \chi) - \Omega_{ce} [\delta \phi, \delta n] - \frac{1}{B} [\delta \phi, \nabla^2 \delta \phi] \quad (5.6)$$

The set of equations(5.4 - 5.6) shows only the dynamics of the fluctuating quantities  $\{\delta n, \delta \phi, \delta \chi\}$  without any sources or dissipations are being considered.

### 5.1.1 System Energy Equation

For the three evolving fields  $(\delta n, \delta\phi, \delta\chi)$  we have in the plasma dynamical system for the Equatorial Electrojet instability we can expect three components of energy; the electrons kinetic energy due to the  $\delta\mathbf{E} \times \mathbf{B}$  drifts, the ions kinetic energy, and the internal thermal energy of both species. To check the way the fluctuating density is represented in the energy equation we use unknown functions of the density fluctuation  $(\delta n)$  and check the condition of zero rate of change of the system Hamiltonian. So, we may propose the system Hamiltonian equation to be as follows:

$$H = \int d^2x' \left( \frac{m_e n_o}{2B^2} |\nabla\delta\phi|^2 + f(\delta n) \frac{m_i}{2} |\nabla\delta\chi|^2 + m_i v_{t_i}^2 g(\delta n) \right) \quad (5.7)$$

where,  $f(\delta n)$  and  $g(\delta n)$  are functions depend on the density fluctuations.

Taking the time derivative of equation(5.7), we find the rate of change of the system Hamiltonian is given by:

$$\dot{H} = \int d^2x' \left( \frac{m_e n_o}{B^2} \nabla\delta\phi \partial_t \nabla\delta\phi + \dot{f}(\delta n) \frac{m_i}{2} |\nabla\delta\chi|^2 + f(\delta n) m_i \nabla\delta\chi \nabla\partial_t \delta\chi + m_i v_{t_i}^2 \dot{g}(\delta n) \right)$$

using the integration by parts in the form  $\int d^2x' \nabla\delta f \partial_t \nabla\delta g = \int d^2x' \nabla \cdot (\delta f \partial_t \nabla\delta g) - \int d^2x' \delta f \partial_t \nabla^2 \delta g = - \int d^2x' \delta f \partial_t \nabla^2 \delta g$  for the first and second terms in the previous equation we can write:

$$\dot{H} = \int d^2x' \left( -\frac{m_e n_o}{B^2} \delta\phi \partial_t \nabla^2 \delta\phi + \dot{f}(\delta n) \frac{m_i}{2} |\nabla\delta\chi|^2 - m_i \partial_t \delta\chi \nabla \cdot (f(\delta n) \nabla\delta\chi) + m_i v_{t_i}^2 \dot{g}(\delta n) \right) \quad (5.8)$$

Now substituting the equations (5.4 - 5.6) into equation(5.8), we get:

$$\begin{aligned} \dot{H} = \int d^2x' \left( e\delta\phi \nabla \cdot (\delta n \nabla\delta\chi) + \frac{en_o}{B} \delta\phi [\delta\phi, \delta n] + \frac{m_e n_o}{B^3} \delta\phi [\delta\phi, \nabla^2 \delta\phi] \right) + \\ \left( -e\delta\phi \nabla \cdot (f(\delta n) \nabla\delta\chi) - m_i v_{t_i}^2 \delta n \nabla \cdot (f(\delta n) \nabla\delta\chi) - \frac{m_i}{2} |\nabla\delta\chi|^2 \nabla \cdot (f(\delta n) \nabla\delta\chi) \right) \\ \frac{m_i}{2} |\nabla\delta\chi|^2 \dot{f}(\delta n) + m_i v_{t_i}^2 \dot{g}(\delta n) \end{aligned}$$

To have a conservation of energy in this equation (i.e. zero rate of change in H), we need to fulfill the following conditions:

$$\nabla \cdot (f(\delta n) \nabla \delta \chi) = \nabla \cdot (\delta n \nabla \delta \chi), \quad (5.9a)$$

$$\dot{f}(\delta n) = \nabla \cdot (f(\delta n) \nabla \delta \chi), \quad (5.9b)$$

$$\dot{g}(\delta n) = \delta n \nabla \cdot (f(\delta n) \nabla \delta \chi) \quad (5.9c)$$

From condition(5.9a):

$$f(\delta n) = \delta n \quad (5.10)$$

From condition(5.9b):

$$\begin{aligned} \dot{f}(\delta n) &= \nabla \cdot (f(\delta n) \nabla \delta \chi) \\ f'(\delta n) \partial_t \delta n &= \nabla \cdot (f(\delta n) \nabla \delta \chi) \\ f'(\delta n) \nabla \cdot (\delta n \nabla \delta \chi) &= \nabla \cdot (f(\delta n) \nabla \delta \chi) \\ f'(\delta n) \nabla \delta n \cdot \nabla \delta \chi + f'(\delta n) \delta n \nabla^2 \delta \chi &= \nabla f(\delta n) \cdot \nabla \delta \chi + f(\delta n) \nabla^2 \delta \chi \\ \nabla f(\delta n) \cdot \nabla \delta \chi + f'(\delta n) \delta n \nabla^2 \delta \chi &= \nabla f(\delta n) \cdot \nabla \delta \chi + f(\delta n) \nabla^2 \delta \chi \\ f'(\delta n) \delta n \nabla^2 \delta \chi &= f(\delta n) \nabla^2 \delta \chi \\ f'(\delta n) \delta n &= f(\delta n) \\ f(\delta n) &= \delta n \end{aligned} \quad (5.11)$$

Hence we can use  $f(\delta n)$  to solve for  $g(\delta n)$  in condition(5.9c) as follows:

$$\begin{aligned} \dot{g}(\delta n) &= \ln n \nabla \cdot (\delta n \nabla \delta \chi) \\ g'(\delta n) \partial_t \delta n &= \delta n \nabla \cdot (\delta n \nabla \delta \chi) \\ g'(\delta n) \nabla \cdot (\delta n \nabla \delta \chi) &= \delta n \nabla \cdot (\delta n \nabla \delta \chi) \\ g'(\delta n) &= \ln \delta n \\ g(\delta n) &= \frac{\delta n^2}{2} \end{aligned} \quad (5.12)$$

Then, the system Hamiltonian equation can be written in the following form:

$$H = \int d^2 x' \left( \frac{n_o m_e}{2B^2} |\nabla \delta \phi|^2 + \frac{m_i}{2} \delta n |\nabla \delta \chi|^2 + \frac{1}{2} m_i v_{ti}^2 \delta n^2 \right) \quad (5.13)$$

## 5.1.2 Energy Conservation in System Dynamics

The total energy in the dynamic system comes from the kinetic energy of the ions and electrons and the internal thermal energy in the system as shown in equation(5.13). Simulations can be shown to obey the energy evolution equation by demonstrating that, in the saturated steady state, the energy has zero (time-averaged) rate of change. This means that a balance has been achieved between the energy sources due to the vertical gradients of the background density and electric potential and the energy dissipated in the electrons and ions viscosity due to their corresponding collisions with the background neutrals. In addition, we have a fixed amount of energy in the system Hamiltonian which does not contain source or dissipation terms.

Thus, we can write the rate of change in the total energy in the following form:

$$\begin{aligned}\dot{E} &= S + D + \dot{H} \\ \dot{E} &= S + D + N + C \\ \dot{E} &= \{S + D + N + C\}_\phi + \{S + D + N + C\}_\chi + \{S + D + N + C\}_n\end{aligned}\tag{5.14}$$

where, S is the energy sources, D is the energy dissipations, N is energy cascading between different scales, and C is the energy coupling between the evolving fields in the system.

To study the physics in the source, dissipation, nonlinear, and coupling terms of the three evolving fields  $\{\delta n, \delta\phi, \delta\chi\}$  in equation (5.14), we need to find the rate of change of the total energy in equation (5.13) which can be found in the following equation:

$$\dot{E} = \int d^2x' \left( -\frac{m_e n_o}{B^2} \delta\phi \partial_t \nabla^2 \phi + \frac{m_i}{2} |\nabla\chi|^2 \partial_t \delta n - m_i \partial_t \delta\chi \nabla \cdot (n \nabla \delta\chi) + m_i v_{ti}^2 \delta n \partial_t \delta n \right)\tag{5.15}$$

where we used integration by parts in equation (5.17) in the first and second terms in equation (5.15).

$$\int d^2x' \nabla \delta f \partial_t \nabla \delta g = \int d^2x' \nabla \cdot (\delta f \partial_t \nabla \delta g) - \int d^2x' \delta f \partial_t \nabla^2 \delta g\tag{5.16}$$

$$\int d^2x' \nabla \delta f \partial_t \nabla \delta g = - \int d^2x' \delta f \partial_t \nabla^2 \delta g\tag{5.17}$$

In equation (5.16) we used the divergence theorem so that the first term on the right-hand-side ( $\int d^2x' \nabla \cdot (\delta f \partial_t \nabla \delta g)$ ) vanishes for the fluctuating evolving fields  $f$  and  $g$ . The divergence will not vanish if the gradients of the evolving fields are not zero at the boundaries. Both Dirichlet and periodic boundary conditions ensure the zero integration of the divergence for any evolving fields.

To study and understand the physics of energy transfer between the evolving fields we substitute the set of partial differential equations (5.1 - 5.3) that controls the plasma dynamics in the equatorial electrojet instabilities into equation (5.15). Hence, we can rewrite the rate of energy variation in the system in the following form:

$$\begin{aligned}
\dot{E} = & \int d^2x' e \delta \phi (\nabla \cdot (n_o \nabla \delta \chi) + \nabla \cdot (\delta n \nabla \delta \chi)) \\
& + \int d^2x' \frac{en_o}{B} \delta \phi [\delta \phi, \ln n_o] + [\phi_o, \delta \tilde{n}] + [\delta \phi, \delta \tilde{n}] \\
& + \int d^2x' \frac{en_o}{B^2 \Omega_{ce}} \delta \phi ([\phi_o, \nabla^2 \delta \phi] + [\delta \phi, \nabla^2 \delta \phi]) \\
& - \int d^2x' en_o \rho_e^2 \nu_{en} \delta \phi (\nabla^2 \delta \tilde{n} + 2 \nabla \ln n_o \cdot \nabla \delta \tilde{n} + \nabla \delta \tilde{n} \cdot \nabla \delta \tilde{n}) \\
& + \int d^2x' \frac{en_o \nu_{en}}{B \Omega_{ce}} \delta \phi (\nabla^2 \delta \phi + \nabla \ln n_o \cdot \nabla \delta \phi + \nabla \delta \tilde{n} \cdot \nabla \phi_o + \nabla \delta \tilde{n} \cdot \nabla \delta \phi) \quad (5.18) \\
& + \int d^2x' m_i \nu_{in} \delta \chi (\nabla \cdot (n_o \nabla \delta \chi) + \nabla \cdot (\delta n \nabla \delta \chi)) \\
& - \int d^2x' \frac{4}{3} \frac{m_i v_{ti}^2}{\nu_{in}} \nabla^2 \delta \chi (\nabla \cdot (n_o \nabla \delta \chi) + \nabla \cdot (\delta n \nabla \delta \chi)) \\
& - \int d^2x' (e \delta \phi + m_i v_{ti}^2 \delta n) (\nabla \cdot (n_o \nabla \delta \chi) + \nabla \cdot (\delta n \nabla \delta \chi)) \\
& + \int d^2x' m_i v_{ti}^2 \delta n (\nabla \cdot (n_o \nabla \delta \chi) + \nabla \cdot (\delta n \nabla \delta \chi))
\end{aligned}$$

The close look into the physics in equation(5.18) and the understanding of the contribution of each term to the rate of change of the total energy in the system allows us to categorize these terms based on their role in the system dynamics into sources (S), dissipations (D), and energy cascading (N) in each evolving field and an energy coupling (C) between the evolving fields.

We can also see that the third term in equation (5.15) plays the coupling role between the ion velocity potential and the other evolving fields (it also couples with itself).

This happens because this term represents conservation in the plasma density in addition to the quasineutrality assumption that is employed in the system.

Therefore, we can write their contributions explicitly as shown in equation(5.19):

$$\begin{aligned}
S_\phi &= \int d^2x' \frac{en_o}{B} \delta\phi \left( [\delta\phi, \ln n_o] + [\phi_o, \delta n] + \frac{1}{B\Omega_{ce}} [\phi_o, \nabla^2 \delta\phi] \right) \\
D_\phi &= \int d^2x' \frac{en_o \nu_{en}}{B\Omega_{ce}} \delta\phi \left( \nabla^2 \delta\phi + \nabla \ln n_o \cdot \nabla \delta\phi + \nabla \delta n \cdot \nabla \phi_o + \nabla \delta n \cdot \nabla \delta\phi \right) \\
&\quad - \int d^2x' en_o \rho_e^2 \nu_{en} \delta\phi \left( \nabla^2 \delta n + 2 \nabla \ln n_o \cdot \nabla \delta n + \nabla \delta n \cdot \nabla \delta n \right) \\
N_\phi &= \int d^2x' \frac{en_o}{B} \delta\phi \left( [\delta\phi, \delta n] + \frac{1}{B\Omega_{ce}} [\delta\phi, \nabla^2 \delta\phi] \right) \\
C_{\phi\chi} &= \int d^2x' e \delta\phi \left( \nabla \cdot (n_o \nabla \delta\chi) + \nabla \cdot (\delta n \nabla \delta\chi) \right) \\
D_\chi &= \int d^2x' m_i \nu_{in} \delta\chi \left( \nabla \cdot (n_o \nabla \delta\chi) + \nabla \cdot (\delta n \nabla \delta\chi) \right) \\
&\quad - \int d^2x' \frac{4 m_i v_{ti}^2}{3 \nu_{in}} \nabla^2 \delta\chi \left( \nabla \cdot (n_o \nabla \delta\chi) + \nabla \cdot (\delta n \nabla \delta\chi) \right) \\
C_{\chi\phi} &= - \int d^2x' e \delta\phi \left( \nabla \cdot (n_o \nabla \delta\chi) + \nabla \cdot (\delta n \nabla \delta\chi) \right) \\
C_{\chi n} &= - \int d^2x' m_i v_{ti}^2 \delta n \left( \nabla \cdot (n_o \nabla \delta\chi) + \nabla \cdot (\delta n \nabla \delta\chi) \right) \\
C_{n\chi} &= \int d^2x' m_i v_{ti}^2 \delta n \left( \nabla \cdot (n_o \nabla \delta\chi) + \nabla \cdot (\delta n \nabla \delta\chi) \right)
\end{aligned} \tag{5.19}$$

Thus, the energy is always injected into the system from the dynamics of the electric potential field and there is no other clear source in the dynamical equations of the ions velocity potential or plasma density fields. Part of the energy injected into the system is dissipated into the electrons viscosity, however the other part is transferred to the ions velocity potential dynamical equation through the coupling term between the fluctuating electric potential and velocity potential evolving fields to be dissipated in the collision process of the ions with the background neutral particles.

The dynamics of the ions velocity potential and density are coupled together because there is only one coupling term between them which is the only term in the continuity equation of the plasma density. This explains the close link between the total energy in the ions velocity potential and plasma density that is found in figure (5.1). Also,

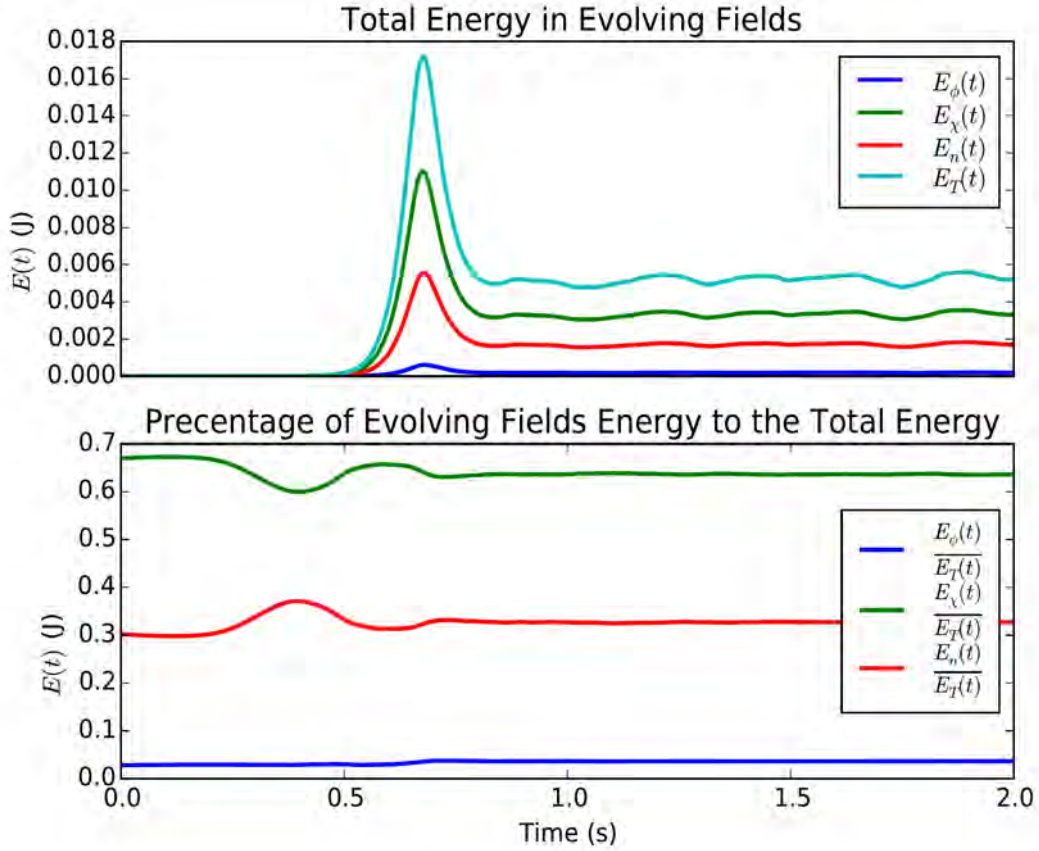


Figure 5.1: The total energy in the evolving fields  $\{\delta n, \delta\phi, \delta\chi\}$  (top-panel) and the ratio between the energy in each evolving field and the total energy (bottom-panel) for a case of  $L_n = 6$  km and  $v_E = 400$  m/s.

there is no direct coupling between the fluctuating electric potential and plasma density, however their dynamics are controlled by the ions velocity potential.

### 5.1.3 Total Energy in Simulation Results

In the total energy of the equatorial electrojet model in equation (5.13) we showed three types of energy, the kinetic energy of ions and electrons and the internal energy of the plasma. The total energy and the ratio between the energy components and the total energy in the dynamic system when  $L_n = 6$  km and  $v_E = 400$  m/s are shown in the upper and lower panels of figure (5.1), respectively. The electrons

kinetic energy due to the  $\mathbf{E} \times \mathbf{B}$  drift velocity is the smallest energy content in the system, though, it strongly controls its dynamics through the temporal variations of the electric potential. On the other hand, the energy content in the saturated ions velocity potential evolving fields are large compared to that of the electric potential. The sum of these two ion's energy components represents more than 98% of the total system energy. The ratio between the energy (bottom-panel in figure (5.1)) in the evolving fields and the total energy in the system shows that the ions internal thermal energy and ions kinetic energy are exchanging their energy contents over the evolution and transition phases of the simulation, then they have their energy content almost flatten during the saturation state with the internal energy has the larger portion of energy.

A comparison between the total energy profiles for different magnitudes of the plasma density-gradient scale-lengths ( $L_n = 1, 4, 6,$  and  $\infty$  km) and the cross-field drift velocities ( $v_E = 400, 425$  m/s) is shown in figure (5.2). For the electrons drift of magnitude  $v_E = 400$  m/s, the decrease in the density-gradient scale-length gives rise to an increase in the rate of evolution of the total energy in the growing and transition states of the simulation and different levels of the total energy at the saturation region. However, for  $v_E = 425$  m/s, the effect of the density-gradient scale-length is negligible over all phases of energy evolution in the system.

The magnitudes of total energy in the saturated evolving fields for the cases of  $L_n = 4, 6,$  and  $\infty$  km are almost the same but it takes longer to reach the saturation as the scale-length increases. The total energy at the saturation state in the simulation box almost doubles from  $\sim 7$  mW when  $L_n = 4, 6,$  and  $\infty$  km to  $\sim 14$  mW when  $L_n = 1$  km. Similarly, the energy level almost doubles when the  $\mathbf{E} \times \mathbf{B}$  drift velocity increases from  $v_E = 400$  m/s to  $v_E = 425$  m/s. This emphasizes the fact that the density-gradient scale-length ( $L_n$ ) and the cross-fields drift velocity ( $v_E$ ) are the energy sources in our dynamic system, and this energy comes from the boundary throughout the gradient of the background density and electric potential.

The time-average of the total energy and its three components as a function of the horizontal wavenumber ( $k_y$ ) during the saturation state of the simulation is shown in figure (5.3) for  $L_n = 6$  km and  $v_E = 400$  m/s. The two peaks at small- and large-

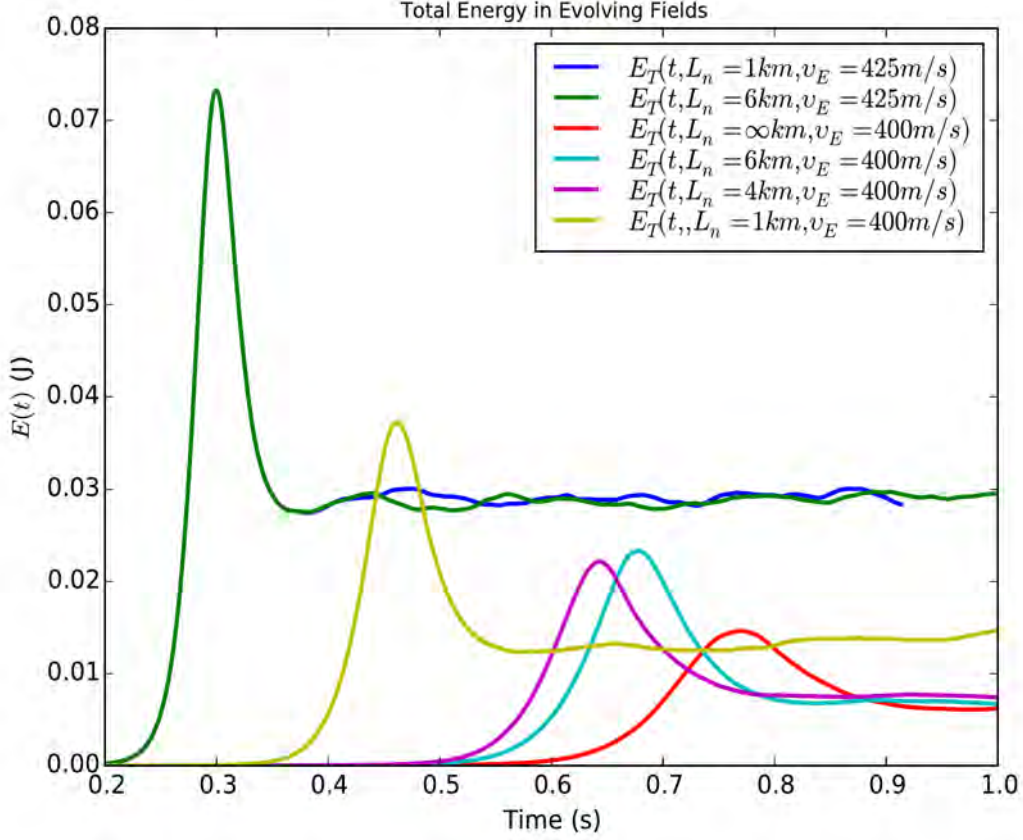


Figure 5.2: A comparison between the total energy (the sum of the ions and electrons kinetic energy and the plasma internal energy) for different magnitudes of density scale-length ( $L_n$ ) and the  $v_E$  drifts.

wavenumbers that have been seen in the linear growth-rate are still found during the saturation region in the numerical simulation of the linear and nonlinear terms. The peak at the small-wavenumber is still around  $0.1 m^{-1}$  similar to the corresponding peak in the linear growth-rate, however, the peak at the large-wavenumber shifted from  $\sim 7 - 8 m^{-1}$  to  $\sim 10 - 11 m^{-1}$ , see figure (3.3). This means that the dynamics of the system nonlinearity transferred the energy into structures of smaller wavelength, and the energy content in these small structures is larger than the longer ones which can be seen by comparing the energy peak value at the large and small structures.

The difference in energy between the small and large structures (in the favor of

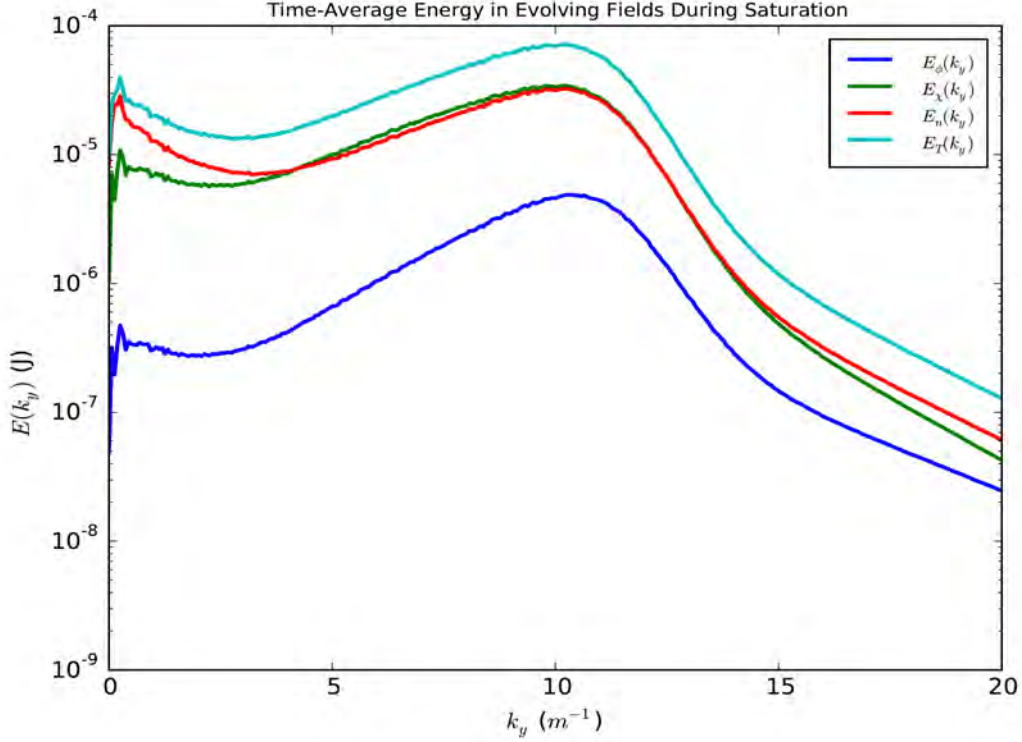


Figure 5.3: The time-average of the total energy in the evolving fields  $\{\delta n, \delta\phi, \delta\chi\}$  over the saturation state of the simulation for a case of  $L_n = 6$  km and  $v_E = 400$  m/s as a function of the horizontal wavenumber.

small-structures) explains the strong backscattering radar echoes that come from the shorter structures compared to the longer ones and the disappearance of the type-II instability in the presence of type-I instability. However, type-I instability disappears when the electron's drift velocity drops below the ion-acoustic speed [54, 81].

#### 5.1.4 Energy Sources and Dissipations

Studying the rate of energy transfer between the energy components that are shown in figure (5.4) we see that the internal energy (green-solid-line) shows very small variation over time compared to the other energy components. The rate of change of the kinetic energy of ions (blue-solid-line) shows its overall role as a sink of energy over all phases of the simulation, however, the corresponding temporal variations of the energy content in the kinetic energy of electrons (red-solid-line) shows its overall

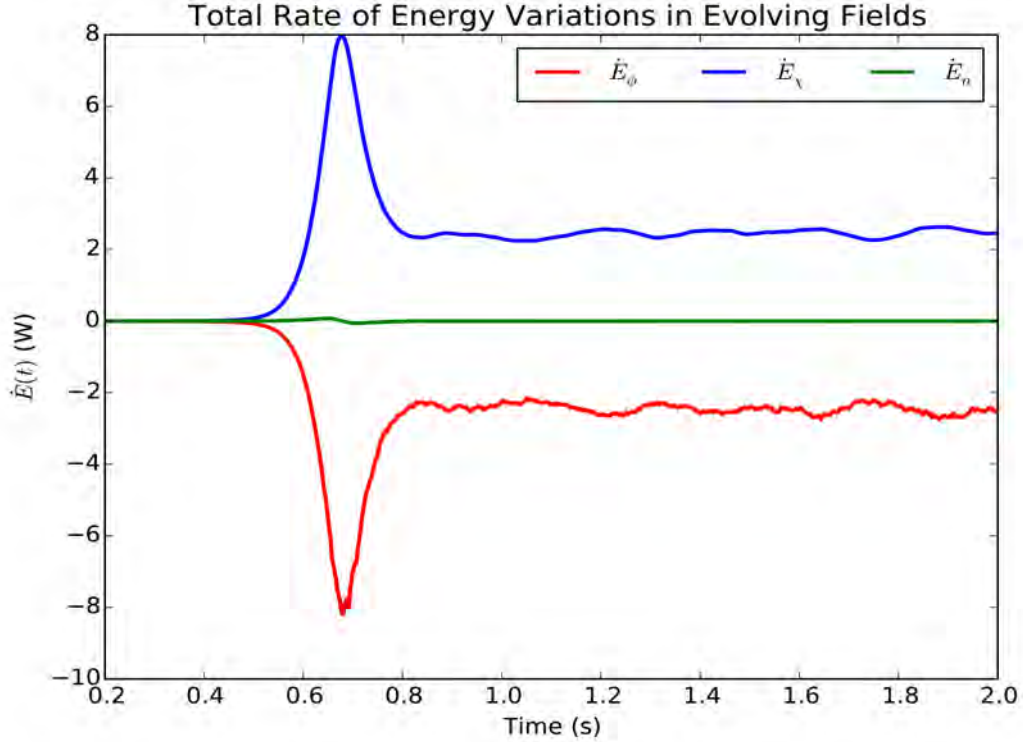


Figure 5.4: The time-average of the rate of energy transfer in the evolving fields  $\{\delta n, \delta\phi, \delta\chi\}$  over the saturation state of the simulation for a case of  $L_n = 6$  km and  $v_E = 400$  m/s as a function of the horizontal wavenumber.

role as a source of energy. This indicates that the ions viscosity dominates the dynamics of the ions and dissipate out the energy content in the system, however, the electrons inject energy in the system through the cross-field drifts. The role of the density-gradient scale-length as a source of energy is very small compared to other energy source.

The overall role of the ions and electrons kinetic energies as source and sink, respectively, does not explain the internal distribution of the energy over the different modes. In figure (5.5) we show the source and dissipation parts of the energy in the ions and electrons energies. The major source of energy in the dynamic system for the equatorial electrojet is the electrons kinetic energy in addition to a small dissipation of the energy due to the collision of the electrons with the background neutrals.

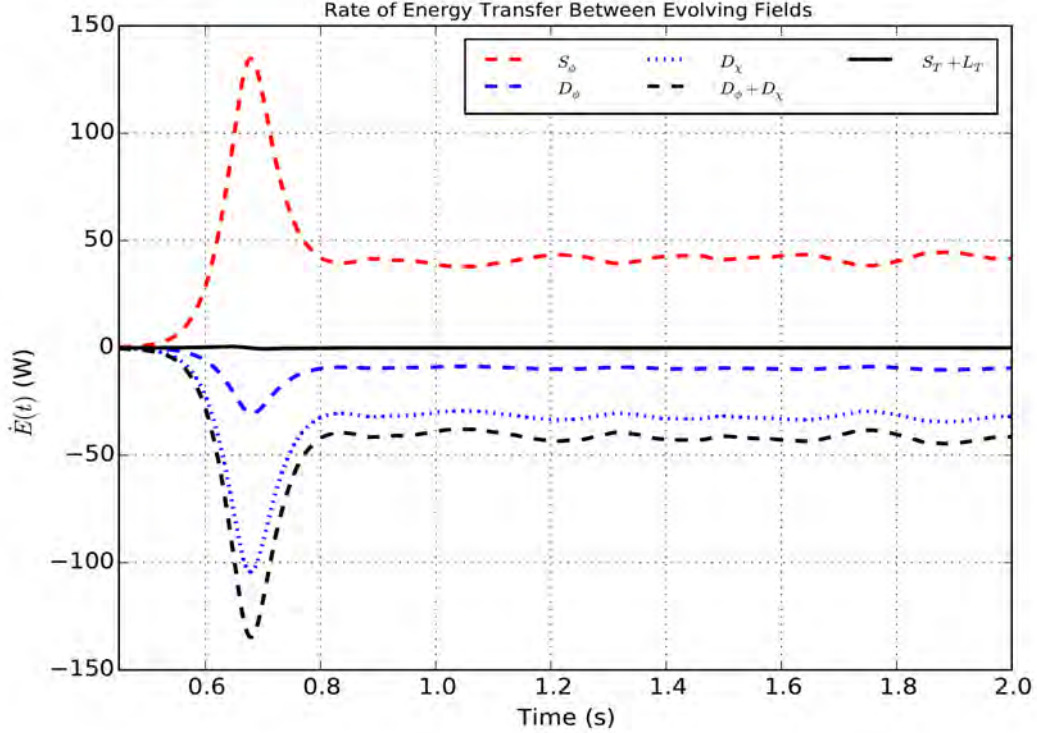


Figure 5.5: Various terms in the energy equation of the evolving fields over the transition and saturation phases of the simulation for a case of  $L_n = 6$  km and  $v_E = 400$  m/s. The rate of variations in the energy content of the density is too small to be represented in this plot.

On the other hand, the ions manifest themselves as a sink for the energy because of their large collision frequencies with the neutral particles in the background. In this representation of energy sources and dissipations we do not include the coupling terms between the two evolving fields, or the rate of energy variation in the internal thermal energy due to its smallness compared to other components.

It can be seen in figure (5.5) that the total energy dissipated in the ions and electrons collisions with the background neutral particles equal the total energy comes from the electrons dynamics as a source. So we can tell that our system satisfies the law of energy conservation between the three evolving fields. This can be indicated by the back-solid-line that passes through the x-axis at  $\dot{E} = 0$  in figure (5.5).

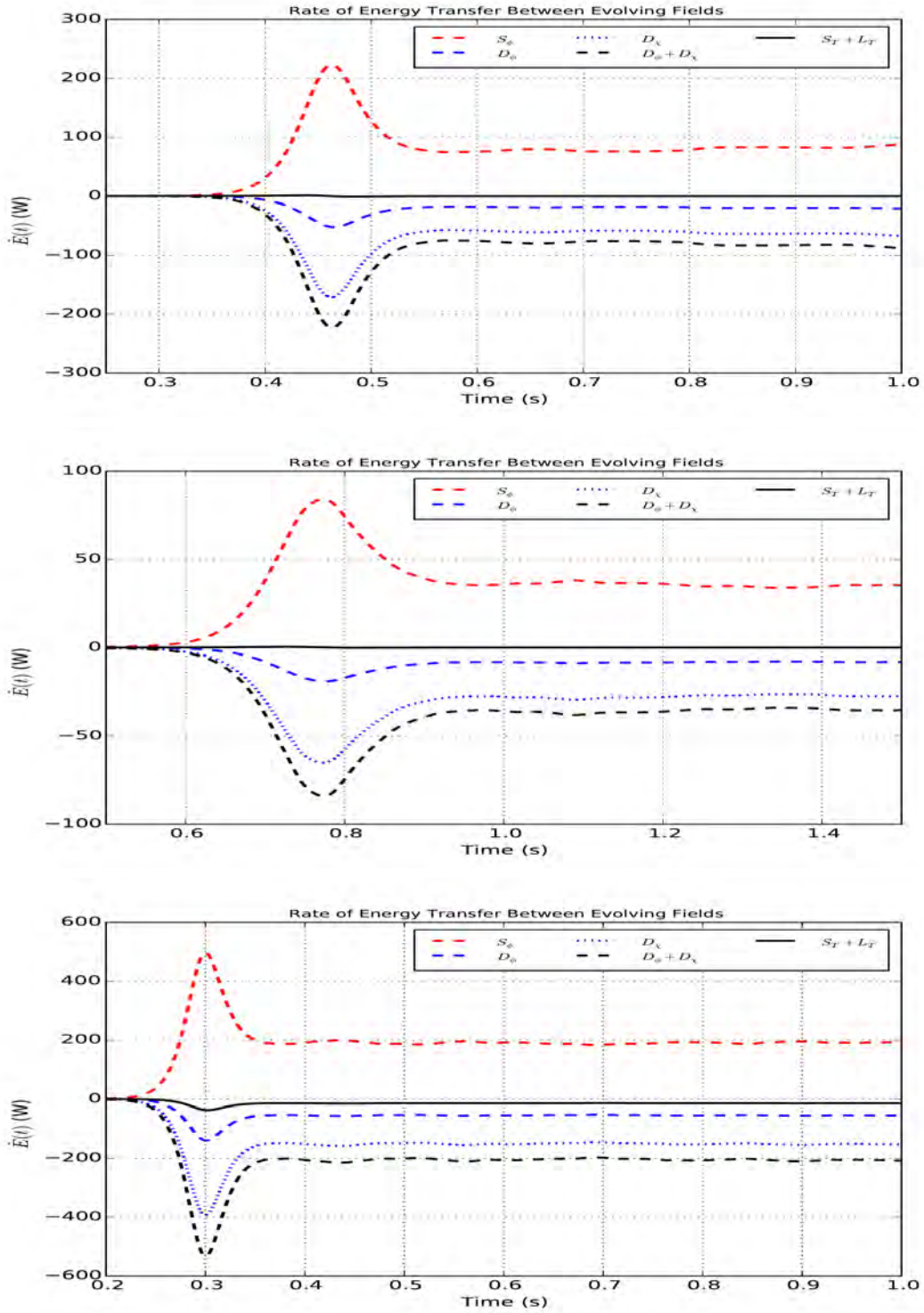


Figure 5.6: Various terms in the energy equation of the evolving fields over the transition and saturation phases of the simulation for  $L_n = 1$  km and  $v_E = 400$  m/s (Top),  $L_n = \infty$  km and  $v_E = 400$  m/s (Middle), and  $L_n = 6$  km and  $v_E = 425$  m/s (Bottom).

More examples for the magnitude of energy sources and dissipations are shown in figure (5.6) for different magnitudes of density-gradient scale-lengths ( $L_n$ ) and cross-fields drift velocity ( $v_E$ ). These plots again emphasize the fact that the increase of the  $\mathbf{E} \times \mathbf{B}$  drift velocity injects more energy into the system and drives the evolving fields to be saturated faster. A similar effect happens with the shorter density-gradient scale length but the impact is much less. This means that our dynamical system drives the Farley-Buneman instability stronger than the gradient-drift instability.

The small simulation box might be the reason for the small effect of the density-gradient scale-length in the variations of the energy contents of the plasma instabilities. This will be examined in future with larger simulation boxes. However, running the unified fluid 2-D model in a larger simulation box will require more computational resources but should be tractable for scale separations that would be potentially prohibitive for kinetic or hybrid models.

### 5.1.5 Energy Transfer Mechanisms

We made more investigation of the distribution of the energy over each term in the energy equation to study the role of those terms in achieving energy balance in the dynamical system<sup>1</sup>. Figure (5.7) shows that the major source of the energy comes from  $\dot{E}_\phi = n_e T_e v_E \delta\tilde{\phi} \partial_y \delta\tilde{n}$  which adds about 40 Joules every second to the system. This term shows the role of the electrons cross-field drift velocity along with the gradient of the fluctuating density in the horizontal direction to drive the two-stream instability, where the secondary electric field and density-gradient are anti-parallel to each other which causes the growing if the unstable modes.

Due to the electrons collisions with the background, 10 Joules are dissipating every second in diffusion of the fluctuating electric field,  $\dot{E}_\phi = n_e T_e \rho_e^2 \nu_{en} \delta\tilde{\phi} \nabla^2 \delta\tilde{\phi}$ , however, the rest of the source energy components injected into the system are dissipated in the density diffusion which couples the dynamics of the electrons and ions.

The energy that is transferred to the ions dynamic equation through  $\dot{E}_\chi = n_e T_e \delta\tilde{\phi} \nabla^2 \delta\tilde{\chi}$  dissipates into the ions collisional and viscosity terms through  $\dot{E}_\chi = n_i m_i \nu_{in} \delta\tilde{\chi} \nabla^2 \delta\tilde{\chi}$

---

<sup>1</sup>We included only the terms that add, couple, or dissipate appreciable amount of energy. Terms that add, couple, or dissipate energy of the order of  $mW$  or  $\mu W$  are dropped for their smallness.

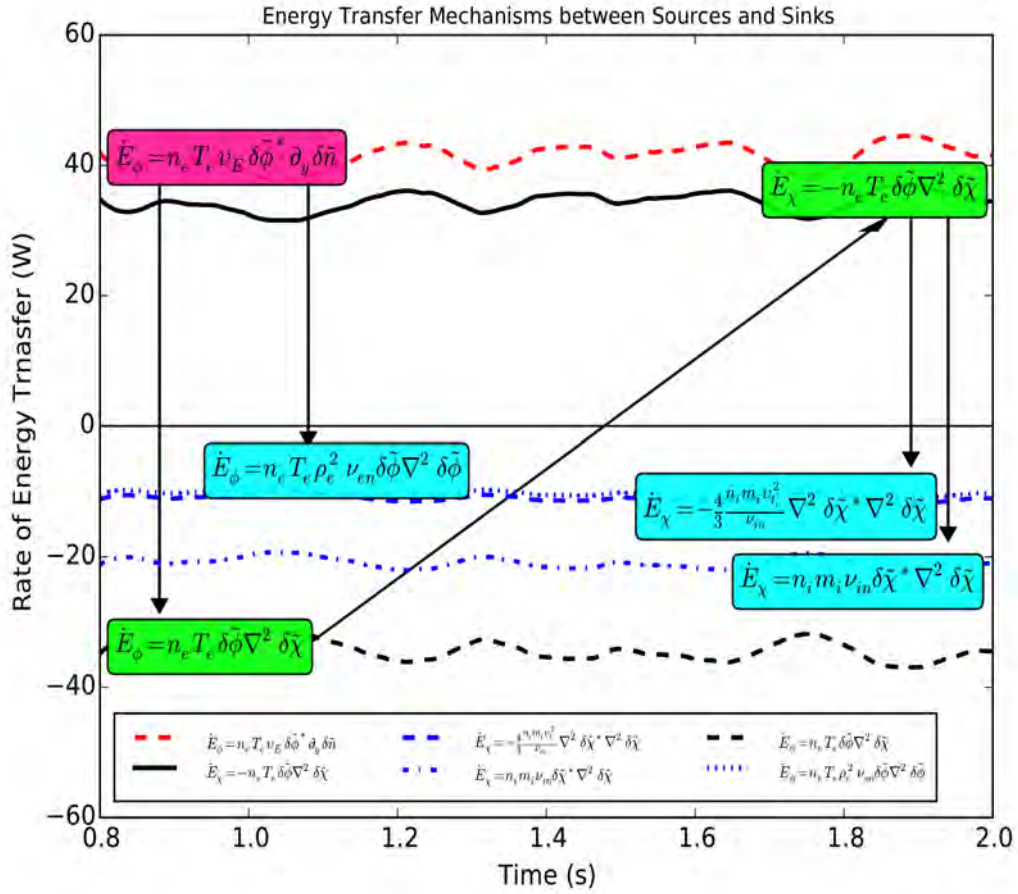


Figure 5.7: The energy transfer mechanisms and physics between the source (pink) and dissipation (cyan) terms in addition to the coupling (green) terms between the saturated evolving fields for the case of  $L_n = 6$  km and  $v_E = 400$  m/s.

and  $\dot{E}_\chi = -\frac{4}{3} \frac{n_i T_i}{\nu_{in}} \nabla^2 \delta \tilde{\chi} \nabla^2 \delta \tilde{\chi}$ , respectively. It was found that the dissipation in the collisional part is almost double the dissipation in viscosity one which explains the importance of the ions collisions with the background compared to the ions viscosity in stabilizing the unstable modes and saturating the evolving fields.

To conclude, the electron dynamics inject energy into the system and the major source of energy is coming from the cross-field drift when it exceeds the ion-acoustic speed. The injection of the energy throughout the density-gradient is small for the current simulation conditions. The collision processes of the ions and electrons with the background neutrals provide a large sink for the available energy in the dynamic system. In addition, the ions viscosity dissipates one-third of the transferred energy.

More work needs to be done to examine the input of different magnitudes of density-gradient scale-lengths to the energy sources in the dynamic system. This might need a larger simulation box close to the density scale-lengths which is in our future plan as we explained earlier.

### 5.1.6 Energy Cascades

In equation (5.19) we have two terms identified as nonlinear because their time-averaged total energy is zero. The two nonlinear terms come from the dynamic equation of the perturbed electric potential. The first nonlinear term,  $[\delta \tilde{\phi}, \delta \tilde{n}]$ , shows the variation of the electric potential along the plasma flow. However, the other nonlinear term  $[\delta \tilde{\phi}, \nabla^2 \delta \tilde{\phi}]$ , shows the variation of the electric potential along the flow of the vorticity in the plasma fluid.

The rate of change in energy content of the first term ( $\dot{E}_\phi = \frac{en_o}{B} \delta \tilde{\phi} [\delta \tilde{\phi}, \delta \tilde{n}]$ ) during the saturation phase of the simulation for  $L_n = 6$  km and  $v_E = 400$  m/s is shown in figure (5.8). The contour color plot in the top-panel shows the magnitude of this term integrated in the vertical direction as a function of time and the horizontal wavenumber ( $k_y$ ). The lower-panel shows the time-average of the magnitude of  $\dot{E}_\phi = \frac{en_o}{B} \delta \tilde{\phi} [\delta \tilde{\phi}, \delta \tilde{n}]$  as a function of  $k_y$ . From these subplots we can see a forward energy cascade where the region of small-wavenumber ( $k_y \leq 5.0 m^{-1}$ ) has a negative rate of energy change, while the rate of variation in energy is positive in the region

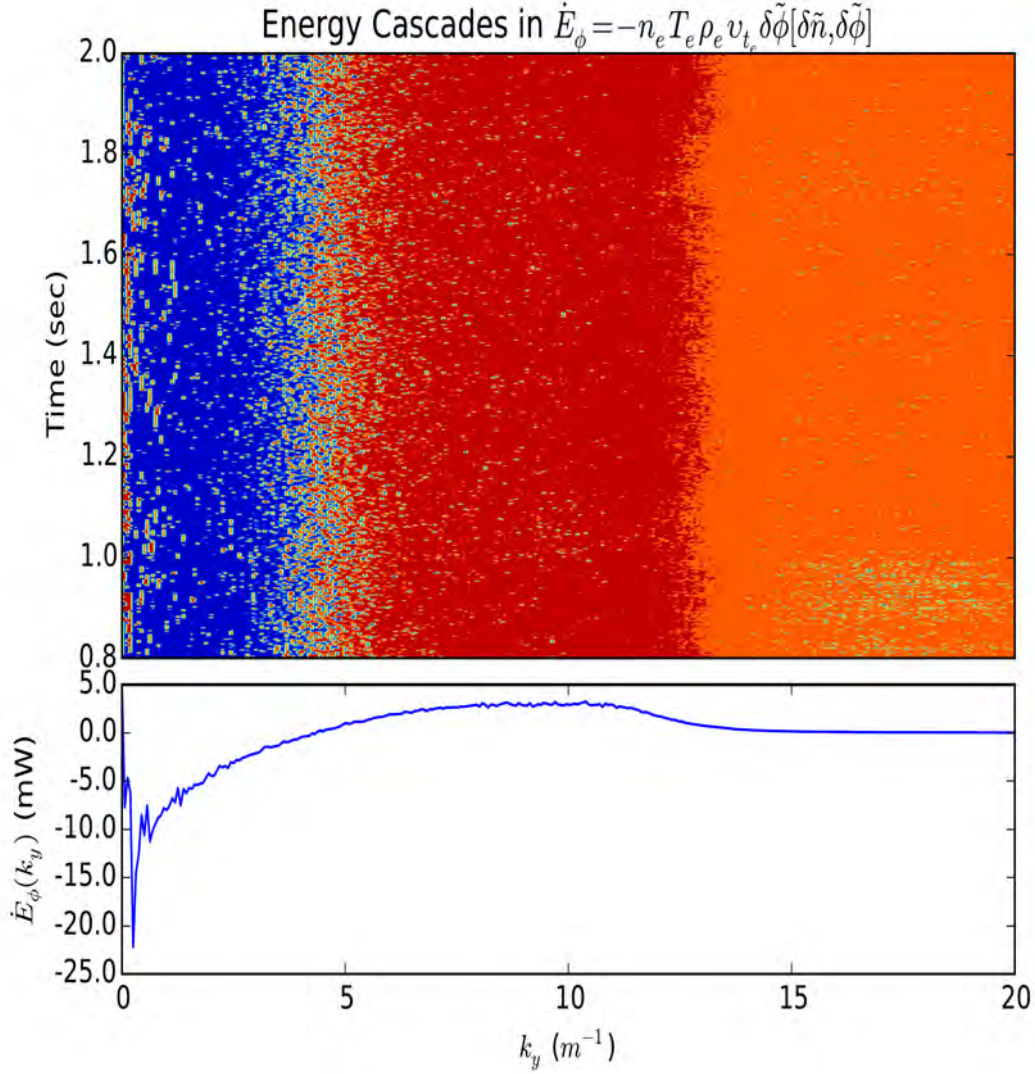


Figure 5.8: Forward energy cascade over the saturation state of the simulation for a case of  $L_n = 6$  km and  $v_E = 400$  m/s. The top panel shows the term  $\dot{E}_\phi = \frac{en_e}{B} \delta\tilde{\phi}[\delta\tilde{\phi}, \delta\tilde{n}]$  over the saturation phase of the simulation and integrated in the vertical direction. The bottom panel shows the time-average of the rate of change in energy over the saturation phase. (The color bar has removed and the bottom panel can be use as a reference for the energy level in the color coded on)

of long-wavelength structures ( $k_y \geq 5.0m^{-1}$ ).

This indicates that the Jacobi bracket of  $\delta\tilde{\phi}$  and  $\delta\tilde{n}$  is transferring the energy from large to small scale structures. The energy is transferred in a cascade process to smaller structures until it ends at structures in the scale of a meter or less with a peak in the range of  $k_y = 9.0 - 11.0m^{-1}$ . Above  $k_y = 15m^{-1}$ , the rate of change of energy is almost zero which means that there is a strong energy dissipation in this region and only low amplitude turbulent structures for the plasma can be found at such small-scales.

These results are in agreement with the radar observations that describe the presence of sub-meter structures with very small energy content to scatter the RF signal, but all structures above half a meter are expected to be seen in the radar echoes when the proper frequency is used.

The other nonlinear term that is responsible for a dual energy cascading mechanisms is shown in figure (5.9). The effect of  $\dot{E}_\phi = \frac{en_o}{B}\delta\tilde{\phi}[\delta\tilde{\phi}, \nabla^2\delta\tilde{\phi}]$  is much smaller than  $\dot{E}_\phi = \frac{en_o}{B}\delta\tilde{\phi}[\delta\tilde{\phi}, \delta\tilde{n}]$  due to the small amount of energy cascaded in forward and backward directions (notice the *milliwatts* and *microwatts* units on the y-axis of figure (5.8) and figure (5.9), respectively). The Jacobi bracket between  $\delta\tilde{\phi}$  and  $\nabla^2\delta\tilde{\phi}$  shows two overlapped regions of forward and dual energy cascading mechanisms. The first region again at  $k_y = 0.0 - 5.0 m^{-1}$  where the energy is forward-cascaded from the long-structures around the size of the simulation box at  $k_y \sim 0.15 m^{-1}$  to the smaller structures of order of 1 - 10 meters.

In the second region at  $k_y = 1 - 15 m^{-1}$  we can see a dual energy cascading mechanism. In the right half of the second region ( $k_y \leq 4\pi$ ) the energy is reverse-cascaded from the 0.75 - 1.00 meter structures to the longer-structures of order 1 - 10 meters. This emphasize on the fact that the Farley-Buneman instability itself can generate structures of long-wavelength as proposed by Kudeki *et al.* [54] and Pfaff *et al.* [81] in the region of the E-region of negative density scale-length. On the other half of the second region we can see a forward transfer of energy to irregularities of scale-length less than half a meter. Checking the peaks and the spectral spread in the second half of the second region we can see that the effect of the forward cascading in the second region is stronger than that of the reverse cascading that has smaller peak and gets

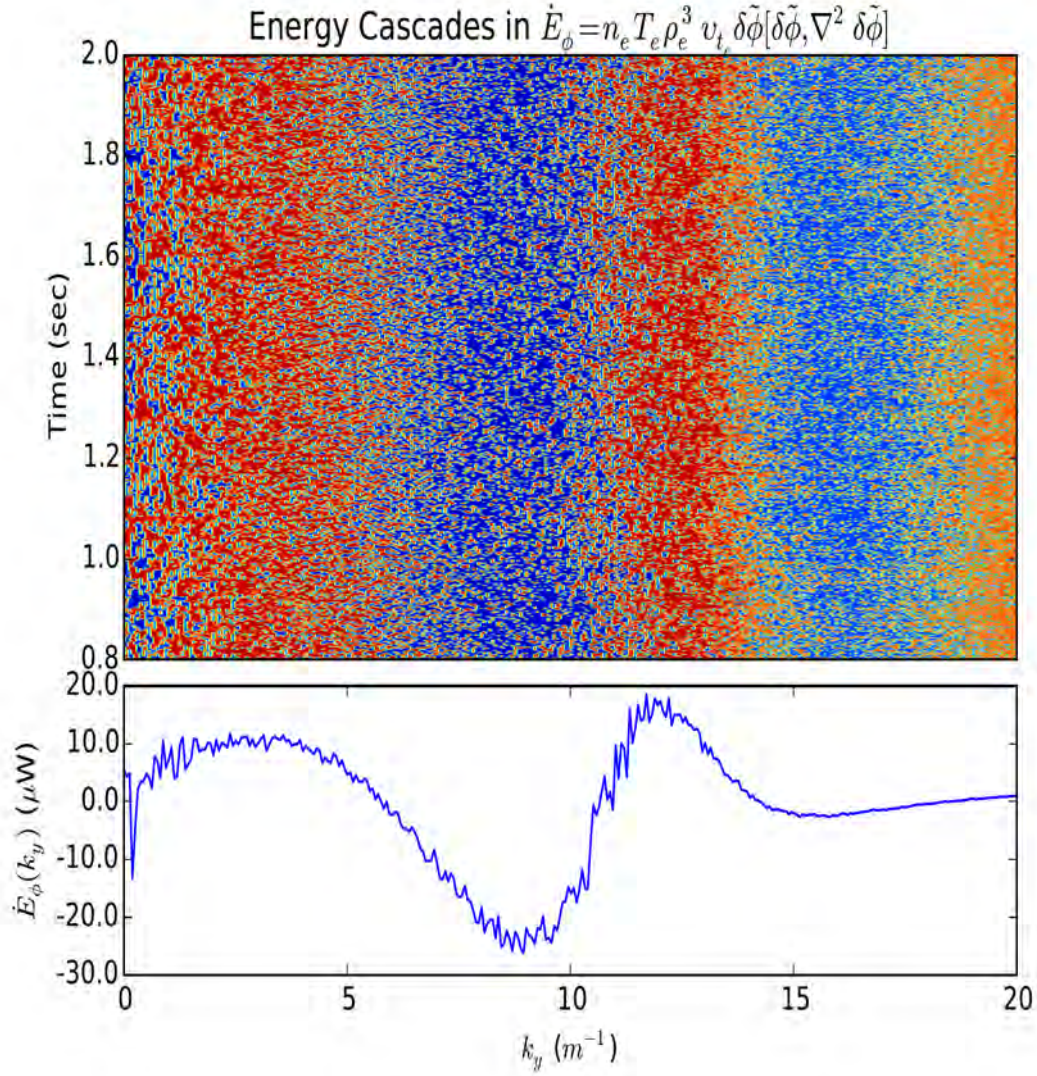


Figure 5.9: Dual energy cascades over the saturation state of the simulation for a case of  $L_n = 6$  km and  $v_E = 400$  m/s. The top panel shows the temporal variations of energy in  $\dot{E}_\phi = \frac{en_o}{B} \delta\tilde{\phi}[\delta\tilde{\phi}, \nabla^2 \delta\tilde{\phi}]$  over the saturation phase of the simulation and integrated in the vertical direction. The bottom panel shows the time-average of the rate of energy variations over the saturation phase. (The color bar has been removed and the bottom panel can be use as a reference for the energy level in the color coded on)

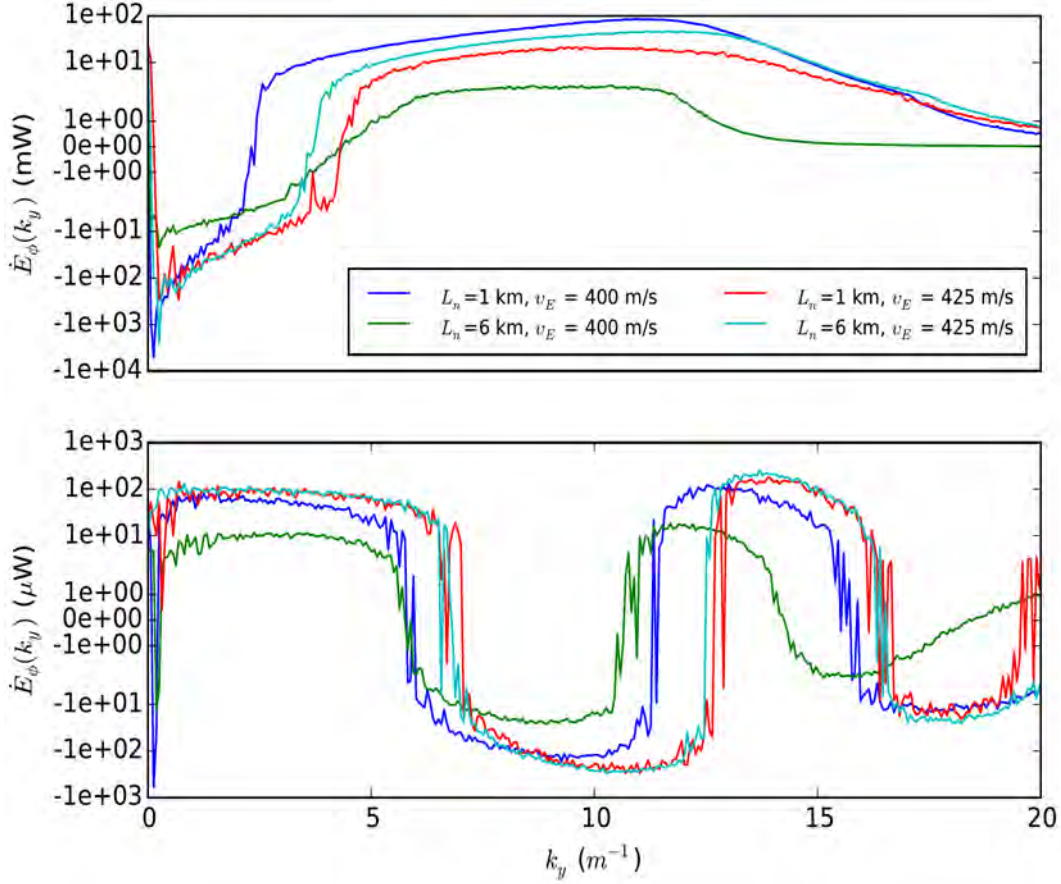


Figure 5.10: Forward (top-panel) and Dual (bottom-panel) energy cascading mechanisms over the saturation state of the simulation for different cases of density-gradient scale-length,  $L_n = 1, 6$  km, and cross-field drift velocities,  $v_E = 400, 425$  m/s.

energy from two regions in independent energy cascading processes.

An interesting comparison between the simulation results for the forward and reverse cascading of energy mechanisms is shown in figure (5.10) for different density scale-lengths ( $L_n = 1$  and  $6$  km) and electron cross-field drifts ( $v = 400$  and  $425$  m/s). The similar trend of the dual energy cascades for different magnitudes of the density scale-lengths at the same  $\delta \mathbf{E} \times \mathbf{B}$  drift ( $v_E = 425$  m/s) is the first interesting points we can notice in the upper and lower panels of figure (5.10). While the difference between the rate of energy transfer between the evolving modes in the Jacobi bracket

of  $\delta\tilde{\phi}$  and  $\delta\tilde{n}$  at  $v_E = 425$  m/s is smaller than the difference between the corresponding profiles at  $v_E = 400$  m/s, that difference is negligible in the Jacobi bracket of  $\delta\tilde{\phi}$  and  $\nabla^2\delta\tilde{\phi}$ . It is also surprising to find the rate of forward energy cascade in the top-panel of figure (5.10) is small in the case of sharp density-gradient (i.e. small density-gradient scale-length) when  $v_E = 425$  m/s in contrast with the cases of  $v_E = 400$  m/s.

Therefore, the polarization drift of the electrons helps in understanding the generation of structures of order smaller than a meter and the reverse energy cascades that allow the generation of long-wavelength structures in the absence of gradient-drift instability conditions in the ionosphere background. These simulation results can be considered a verification of the Sudan *et al.* [113] theory about the responsibility of the two-step energy cascading mechanism in generating the small-scale structures in the equatorial electrojet irregularities.

## 5.2 Non-Canonical Hamiltonian System

### 5.2.1 The System Hamiltonian Bracket

To find the Hamiltonian bracket that shows the energy dynamics of the plasma instabilities in the Equatorial Electrojet we need first to calculate the functional derivatives of the system Hamiltonian with-respect-to each evolving field  $\{\delta n, \delta\phi, \delta\chi\}$ , where for any random field  $\zeta$ , the functional derivative of the system Hamiltonian with-respect-to  $\zeta$  is  $dH = \int d^2x' \frac{\delta H}{\delta \zeta} \delta \zeta$ . In appendix(.2) we calculated the functional derivatives of the system Hamiltonian and we can write them in the following form:

For the Electric Potential

$$\frac{\delta H}{\delta \nabla^2 \phi} = -\frac{m_e n_o}{B^2} \phi \quad (5.20)$$

For the Ion Velocity Potential

$$\frac{\delta H}{\delta \chi} = -m_i \nabla \cdot (n \nabla \chi) \quad (5.21)$$

For the Electron Density

$$\frac{\delta H}{\delta n} = \frac{m_i |\nabla \chi|^2}{2} + m_i v_{t_i}^2 n \quad (5.22)$$

Now, we can use the functional derivatives of the system Hamiltonian with-respect-to the evolving fields in each partial differential equation in the dynamic system to find its corresponding bracket based on the fact that  $\partial_t f = \{f, H\}$ , where  $f \in \{\delta n, \delta \phi, \delta \chi\}$  and H is the system Hamiltonian. Hence we can combine all these brackets into one that represents the system dynamics in all of the evolving fields. Finally, we will need to check if that bracket satisfies the Jacobi Identity to ensure the dynamics in our system can be treated as a non-canonical Hamiltonian system.

**Density Continuity Equation:**  $\partial_t n = \{n, H\}$

$$\begin{aligned}
\partial_t n &= \nabla \cdot (n \nabla \chi) \\
\partial_t n &= \int d^2 x' \delta_n(x' - x) \nabla \cdot (n \nabla \chi) \\
\partial_t n &= \int d^2 x' \left( \frac{\delta n}{\delta n} \right) \left( \frac{-1}{m_i} \frac{\delta H}{\delta \chi} \right) \\
\partial_t n &= \frac{-1}{m_i} \int d^2 x' \left( \frac{\delta n}{\delta n} \frac{\delta H}{\delta \chi} \right) \\
\partial_t n &= \frac{-1}{m_i} \int d^2 x' \left( \frac{\delta n}{\delta n} \frac{\delta H}{\delta \chi} - \frac{\delta H}{\delta n} \frac{\delta n}{\delta \chi} \right) \tag{5.23}
\end{aligned}$$

So, the density continuity equation gives rise to the following bracket:

$$\{F, G\} = -\frac{1}{m_i} \int d^2 x' (F_n G_\chi - G_n F_\chi) \tag{5.24}$$

**Ion's Equation of Motion:**  $\partial_t \chi = \{\chi, H\}$

$$\begin{aligned}
\partial_t \chi &= \frac{\Omega_{ci}}{B} \phi + v_{t_i}^2 \ln n + \frac{1}{2} |\nabla \chi|^2 \\
\partial_t \chi &= \frac{\Omega_{ci}}{B} \int d^2 x' \delta_\chi(x' - x) \phi + \int d^2 x' \delta_\chi(x' - x) \left( v_{t_i}^2 \ln n + \frac{1}{2} |\nabla \chi|^2 \right) \\
\partial_t \chi &= -\frac{B \Omega_{ci}}{m_e n_o} \int d^2 x' \left( \frac{\delta \chi}{\delta \chi} \frac{\delta H}{\delta \zeta} \right) + \frac{1}{m_i} \int d^2 x' \left( \frac{\delta \chi}{\delta \chi} \frac{\delta H}{\delta n} \right) \\
\partial_t \chi &= -\frac{B \Omega_{ci}}{m_e n_o} \int d^2 x' \left( \frac{\delta \chi}{\delta \chi} \frac{\delta H}{\delta \zeta} - \frac{\delta H}{\delta \chi} \frac{\delta \chi}{\delta \zeta} \right) - \frac{1}{m_i} \int d^2 x' \left( \frac{\delta \chi}{\delta n} \frac{\delta H}{\delta \chi} - \frac{\delta H}{\delta n} \frac{\delta \chi}{\delta \chi} \right) \tag{5.25}
\end{aligned}$$

where,  $\zeta = \nabla^2 \phi$ .

So, the ions equation of motion gives rise to the following bracket:

$$\{F, G\} = -\frac{1}{m_i} \int d^2x' (F_n G_\chi - G_n F_\chi) - \frac{B\Omega_{ci}}{m_e n_o} \int d^2x' (F_\chi G_\zeta - G_\chi F_\zeta) \quad (5.26)$$

**Quasi-Neutrality Condition:**  $\partial_t \phi = \{\phi, H\}$

$$\begin{aligned} \partial_t \zeta &= \frac{\Omega_{ce}}{n_o} \int d^2x' \delta_\zeta(x' - x) [n, \phi] - \frac{1}{B} \int d^2x' \delta_\zeta(x' - x) [\phi, \zeta] \\ &\quad - \frac{B\Omega_{ce}}{n_o} \int d^2x' \delta_\zeta(x' - x) \nabla \cdot (n \nabla \chi) \\ \partial_t \zeta &= -\frac{\Omega_{ce}}{n_o} \int d^2x' n [\delta_\zeta(x' - x), \phi] - \frac{1}{B} \int d^2x' \zeta [\delta_\zeta(x' - x), \phi] \\ &\quad + \frac{B\Omega_{ce}}{m_i n_o} \int d^2x' \left( \frac{\delta \zeta}{\delta \zeta} \frac{\delta H}{\delta \chi} - \frac{\delta H}{\delta \zeta} \frac{\delta \zeta}{\delta \chi} \right) \\ \partial_t \zeta &= \frac{B^2 \Omega_{ce}}{m_e n_o^2} \int d^2x' n \left[ \frac{\delta \zeta}{\delta \zeta}, \frac{\delta H}{\delta \zeta} \right] + \frac{B}{m_e n_o} \int d^2x' \zeta \left[ \frac{\delta \zeta}{\delta \zeta}, \frac{\delta H}{\delta \zeta} \right] \\ &\quad - \frac{B\Omega_{ci}}{m_e n_o} \int d^2x' \left( \frac{\delta \zeta}{\delta \chi} \frac{\delta H}{\delta \zeta} - \frac{\delta H}{\delta \chi} \frac{\delta \zeta}{\delta \zeta} \right) \end{aligned} \quad (5.27)$$

So, the quasi-neutrality condition gives rise to the following bracket:

$$\begin{aligned} \{F, G\} &= -\frac{1}{m_i} \int d^2x' (F_n G_\chi - G_n F_\chi) - \frac{B\Omega_{ci}}{m_e n_o} \int d^2x' (F_\chi G_\zeta - G_\chi F_\zeta) + \\ &\quad \frac{B^2 \Omega_{ce}}{m_e n_o^2} \int d^2x' n [F_\zeta, G_\zeta] + \frac{B}{m_e n_o} \int d^2x' \zeta [F_\zeta, G_\zeta] \end{aligned} \quad (5.28)$$

Now, by comparing the brackets in equations (5.24, 5.26, 5.28) we find that the bracket in equation(5.28) which comes from the quasi-neutrality condition contains the dynamics in the density continuity equation and ions equation of motion. Therefore, the bracket in equation(5.28) represents all the dynamics of the plasma instabilities in the equatorial electrojet model.

To verify that our dynamic system can be considered a non-canonical Hamiltonian system we need to check its bracket against the Jacobi identity which states that:

$$\{\{F, G\}, H\} + \{\{H, F\}, G\} + \{\{G, H\}, F\} = 0 \quad (5.29)$$

where, F, G, and H are random functional variables.

The detailed calculations of the Jacobi Identity using the Hamiltonian bracket in equation (5.28) are made in appendix(.3) and we write here only the final results for each permutation of the bracket as follows:

$$\{\{F, G\}, H\} = \frac{B^3 \Omega_{ce}}{m_e^2 n_o^2} \int d^2 x' n [[F_\zeta, G_\zeta], H_\zeta] + \frac{B^2}{m_e^2 n_o^2} \int d^2 x' \zeta [[F_\zeta, G_\zeta], H_\zeta] \quad (5.30)$$

$$\{\{H, F\}, G\} = \frac{B^3 \Omega_{ce}}{m_e^2 n_o^2} \int d^2 x' n [[H_\zeta, F_\zeta], G_\zeta] + \frac{B^2}{m_e^2 n_o^2} \int d^2 x' \zeta [[H_\zeta, F_\zeta], G_\zeta] \quad (5.31)$$

$$\{\{G, H\}, F\} = \frac{B^3 \Omega_{ce}}{m_e^2 n_o^2} \int d^2 x' n [[G_\zeta, H_\zeta], F_\zeta] + \frac{B^2}{m_e^2 n_o^2} \int d^2 x' \zeta [[G_\zeta, H_\zeta], F_\zeta] \quad (5.32)$$

Thus, substituting equations (5.30, 5.31, and 5.32) in the left-hand-side of equation (5.29) we get zero, and the Jacobi identity is satisfied. This ensures that we have a non-canonical Hamiltonian system.

## 5.2.2 Casimir's Invariant

Casimirs are functionals found in a dynamical system and commute with every other functional in that system, and belong to the kernel of the Poisson bracket ( $\frac{\delta C}{\delta \mathbf{q}} \in \text{kerr}(\mathbf{J})$ ) [64]. The Poisson bracket of a Casimir (C) with any functional A satisfies the following identity:

$$[A, C] = \left\langle \frac{\delta A}{\delta \mathbf{q}}, \mathbf{J} \frac{\delta C}{\delta \mathbf{q}} \right\rangle = 0, \quad \forall A(\mathbf{q}) \quad (5.33)$$

The system Hamiltonian is considered invertible when the functional derivative  $\frac{\delta c}{\delta \mathbf{q}}$  vanishes which is satisfied when the inverse of the Jacobian ( $\mathbf{J}$ ) exists. Then the Casimirs are said to be trivial and the Jacobi has a trivial kernel. Otherwise, for example when  $\mathbf{J}^{-1}$  does not exist, the Hamiltonian is considered noninvertible and the Casimirs give a nontrivial Poisson's kernel which will have a co-rank equal to the number of independent Casimirs [64].

The vanishing of the Poisson bracket of the Casimirs with the system Hamiltonian characterizes these Casimirs to be geometric constants of motion in the phase-space, but their properties are determined by the degenerate structure of the symplectic operator ( $\mathbf{J}$ ) not the Hamiltonian (H) [97].

## Finding the Casimir's Invariant

To find the system Casimirs we choose any random functionals  $F$  and  $C$ , then we substitute them in the dynamic system bracket in equation(5.28) to get:

$$\begin{aligned}
\{F, C\} &= -\frac{1}{m_i} \int d^2x' (F_n C_\chi - C_n F_\chi) - \frac{B\Omega_{ci}}{m_e n_o} \int d^2x' (F_\chi C_\zeta - C_\chi F_\zeta) \\
&\quad + \frac{B}{m_e n_o} \int d^2x' \zeta [F_\zeta, C_\zeta] + \frac{B^2 \Omega_{ce}}{m_e n_o^2} \int d^2x' n [F_\zeta, C_\zeta] \\
\{F, C\} &= \int d^2x' F_n \left( -\frac{1}{m_i} C_\chi \right) + \int d^2x' F_\chi \left( \frac{1}{m_i} C_n - \frac{B\Omega_{ci}}{m_e n_o} C_\zeta \right) \\
&\quad + \int d^2x' F_\zeta \left( \frac{B^2 \Omega_{ce}}{m_e n_o^2} [n, C_\zeta] + \frac{B}{m_e n_o} [\zeta, C_\zeta] \right)
\end{aligned} \tag{5.34}$$

Hence, for  $C$  to be a Casimir, the bracket  $\{F, C\}$  should vanish which can take place under the following conditions:

$$C_\chi = 0 \tag{5.35}$$

$$C_n = \frac{B\Omega_{ce}}{n_o} C_\zeta \tag{5.36}$$

$$[B\Omega_{ce}n + n_o\zeta, C_\zeta] = 0 \tag{5.37}$$

Therefore, the system has infinite number of Casimirs that can be given for any arbitrary function,  $f$ , by:

$$C = \int d^2x' f(B\Omega_{ce}n + n_o\zeta) \tag{5.38}$$

From equation(5.4) and equation(5.6), we can write the time derivative for the parameter in the functional  $f$  in equation (5.38) in the following form:

$$\begin{aligned}
\partial_t (B\Omega_{ce}n + n_o\nabla^2\phi) &= \partial_t B\Omega_{ce}n + \partial_t n_o\nabla^2\phi \\
\partial_t (B\Omega_{ce}n + n_o\nabla^2\phi) &= \Omega_{ce}[n, \phi] - \frac{n_o}{B}[\phi, \nabla^2\phi] \\
\partial_t (B\Omega_{ce}n + n_o\nabla^2\phi) &= -\left[\frac{\phi}{B}, B\Omega_{ce}n\right] - \left[\frac{\phi}{B}, n_o\nabla^2\phi\right] \\
\partial_t (B\Omega_{ce}n + n_o\nabla^2\phi) + \left[\frac{\phi}{B}, B\Omega_{ce}n + n_o\nabla^2\phi\right] &= 0 \\
\partial_t Q + [F_{E \times B}, Q] &= 0
\end{aligned} \tag{5.39}$$

where,  $Q = B\Omega_{ce}n + n_o\nabla^2\phi$  and  $F_{E \times B} = \frac{\phi}{B}$ .

## Re-formulating System Dynamics in New Variables

Now we can use the new variable in equation (5.39) with any arbitrary functional  $F$  to make a change of the variable in the dynamic equation as following:

$$F[n, \zeta, \chi] = \bar{F}[n, Q, \chi]$$

$$\int d^2x' \left( \frac{\delta F}{\delta n} \delta n + \frac{\delta F}{\delta \zeta} \delta \zeta + \frac{\delta F}{\delta \chi} \delta \chi \right) = \int d^2x' \left( \frac{\delta \bar{F}}{\delta n} \delta n + \frac{\delta \bar{F}}{\delta Q} \delta Q + \frac{\delta \bar{F}}{\delta \chi} \delta \chi \right)$$

Hence we can use  $Q = B\Omega_{ce}n + n_o\zeta \rightarrow \delta Q = B\Omega_{ce}\delta n + n_o\delta\zeta$  to rewrite the previous equation in the following form:

$$\int d^2x' \left( \frac{\delta F}{\delta n} \delta n + \frac{\delta F}{\delta \zeta} \delta \zeta + \frac{\delta F}{\delta \chi} \delta \chi \right) = \int d^2x' \left( \left[ \frac{\delta \bar{F}}{\delta n} + B\Omega_{ce} \frac{\delta \bar{F}}{\delta Q} \right] \delta n + \left[ n_o \frac{\delta \bar{F}}{\delta Q} \right] \delta \zeta + \frac{\delta \bar{F}}{\delta \chi} \delta \chi \right)$$

Comparing both sides in the previous equation, we get:

$$\begin{aligned} F_n &= \bar{F}_n + B\Omega_{ce}\bar{F}_Q \\ F_\zeta &= n_o\bar{F}_Q \\ F_\chi &= \bar{F}_\chi \end{aligned} \tag{5.40}$$

Thus, we can rewrite the system Hamiltonian bracket in equation(5.28) in terms of the new variables as following:

$$\{\bar{F}, \bar{G}\} = -\frac{1}{m_i} \int d^2x' (\bar{F}_n \bar{G}_\chi - \bar{G}_n \bar{F}_\chi) + \frac{B}{m_e} \int d^2x' Q [\bar{F}_Q, \bar{G}_Q]$$

or, generally:

$$\{F, G\} = -\frac{1}{m_i} \int d^2x' (F_n G_\chi - G_n F_\chi) + \frac{B}{m_e} \int d^2x' Q [F_Q, G_Q]$$

Moreover, the dynamic equations for the equatorial electrojet instabilities can be rewritten in the following form:

$$\partial_t n = \nabla \cdot (n \nabla \chi) \tag{5.41}$$

$$\partial_t Q = [Q, \frac{\phi}{B}] \tag{5.42}$$

$$\partial_t \nabla^2 \chi = \frac{\Omega_{ci}}{n_o B} Q - \frac{\Omega_{ce} B}{n_o} n + v_{ti} \nabla^2 \ln n + \frac{1}{2} \nabla^2 |\nabla \chi|^2 \tag{5.43}$$

The new form of the dynamic equation (5.42) which is based on the quasineutrality condition of the plasma shows the dependence of plasma dynamics to drive the equatorial electrojet instabilities on the density gradient and the  $\mathbf{E} \times \mathbf{B}$  drift velocity. However, the other two dynamic equations which control the coupling and dissipation in the system do not show any change and their formulation.

# Chapter Six: Impacts of the Solar Wind on the Equatorial Electrojet

Knowing the upstream solar wind condition is essential in forecasting the variations in the geomagnetic field and the status of the Earth's ionosphere. The solar wind measurements at the magnetosphere nose can be used in many data-driven simulations for the purpose of space weather forecasting. However, there is no monitoring station at that location, and also it might not be useful to have a monitoring station that close from the Earth. The presence of a solar wind monitoring station at the first Lagrangian orbit, such as Advanced Composition Explorer (ACE), does the same job if we employed a good advection technique for the solar wind to the magnetosphere nose. We used three years of solar wind data measured at Advance Composition Explorer (ACE) and advected them to the location of the Interplanetary Monitoring Platform (IMP8) spacecraft. The concurrent records in ACE advected solar wind data and IMP8 measurements are used to establish Kernel Density Estimation the(KDE) functions. The location of the IMP8 spacecraft allows us to use these KDE functions to generate ensemble of solar wind data at the Earth's magnetopause that can be used to forecast the status of the geomagnetic field and the ionosphere. In addition, we employed a 4-categorization scheme for the incoming solar wind data to established KDE functions for each category and compared them with the uncategorized KDE functions.

## 6.1 Introduction

Space weather forecasting found its way to be a top priority research due to its great impact on the modernized technology we have nowadays [2, 17, 121]. Besides the heat flux and visible light the Sun emits, there are other active solar phenomena such as the solar flares and coronal-mass-ejections that might cause a great impact on Earth's system. The connection between the solar activities and their impacts on the Earth's system was first considered by Carrington [1859] [12] who reported observing a flare in visible light that was followed hours later by a very large geomagnetic disturbance.

This was the birth date of what we call today space weather, and since that time the scientists focused on studying different activities on our nearest star; the Sun, and record their impacts on the Earth.

One aspect of solar behavior that occurs continuously is the solar wind, which is the outflow of plasma from the area of open magnetic field lines in the solar corona [51]. Historically, the solar winds are classified according to their region of origin in the Solar corona. The fast solar winds are emerging from the coronal holes, which are always present in the solar poles and cover most of the Sun during the solar minimum. The fast solar winds are characterized by low-density plasma and speed ranges in 450-850 km/s. In contrast, the plasma density in the slow solar wind is comparatively larger, its speed typically lies in the range 250-450 km/s and its origin is still controversial [104]. According to the recent categorization scheme proposed by Xu and Borovoski [124], the slow solar wind can be subdivided into two subcategories: streamer-belt-origin and sector-reversal-region, and we discuss this categorization scheme in section(6.2). In addition, there is another kind of solar wind called ejecta which are associated with corona-mass-ejections. At times coronal mass ejections take the form of magnetic clouds carrying flux rope magnetic fields that result from the generation mechanism in the solar corona. In addition, the speed and density of these ejecta vary according to the generation mechanism.

Because the solar wind variations happen continuously and the interplanetary magnetic field for a plasma parcel is connected to the Sun, the solar winds carry lots of information about their origins on the Sun [74]. Also, the impact of the solar wind on the Earth's system varies according to bulk parameters, such as the speed, density, and the interplanetary magnetic field (IMF) vector. Therefore, measuring the upstream solar wind conditions can help in forecasting their impact on the Earth's system. As a result, numerous satellite missions have been sent upstream of Earth to continuously monitor the solar wind conditions.

The interaction between the incoming solar wind and the Earth's system first takes place at the magnetosphere nose, or what is called the bow-shock. The ram pressure<sup>1</sup> and both the orientation and magnitude of the interplanetary magnetic field

---

<sup>1</sup>The ram pressure is the force per unit area required to stop the solar wind flow.

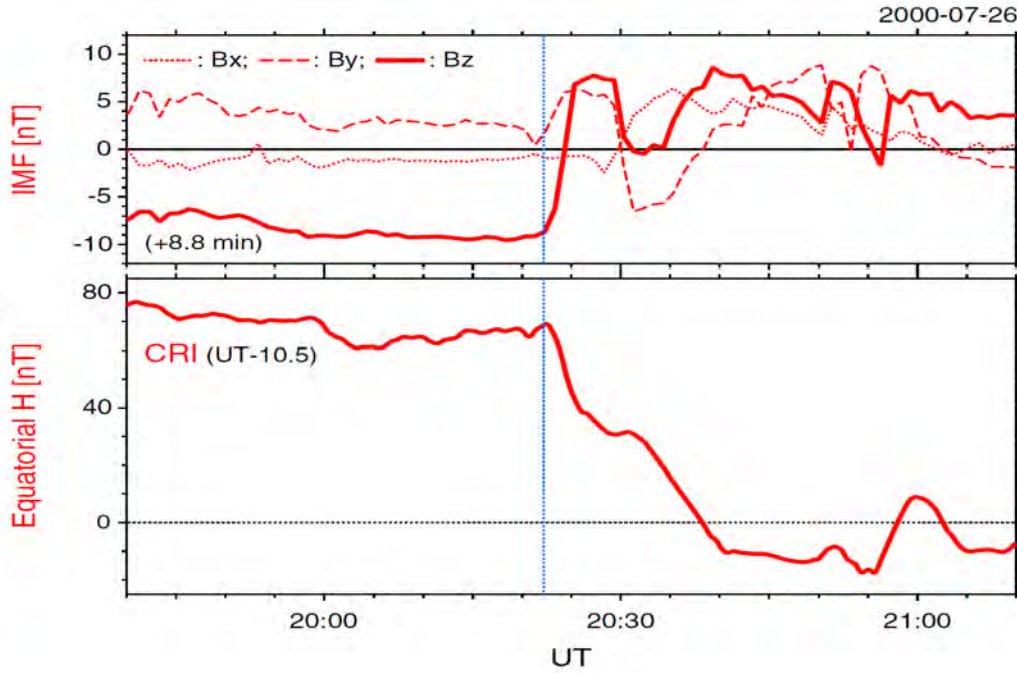


Figure 6.1: The enhancement of the horizontal component of the geomagnetic field (H) in the lower panel as a result of the tangential discontinuity of the interplanetary magnetic field (IMF) from southward to northward in the upper panel [adapted from Ohtani *et al.* [67]].

determine the severity of this interaction on the magnetosphere [18, 24]. The magnetic reconnection process that takes place at the bow-shock between the IMF and the geomagnetic field has its largest effect when the IMF is oriented southward (i.e. opposite to orientation of the Earth’s magnetic field) [61, 31]. This magnetic reconnection process, which breakdown the geomagnetic field lines on the day-side of the Earth, is mostly followed by another magnetic reconnection at the magnetotail on the night-side. These continuous magnetic reconnection processes inject a huge shower of energetic particles on the polar caps that give rise to the northern lights or the aurora borealis [62, 85].

Regarding the impact of the solar wind on the ionosphere, the effect is most pronounced in the polar caps [30]. However, it is found that the impact of the severe interaction between the solar wind and the ionosphere at high-latitudes can extend to the lower magnetic latitudes. In 2013, Ohtani *et al* [67] reported an enhancement

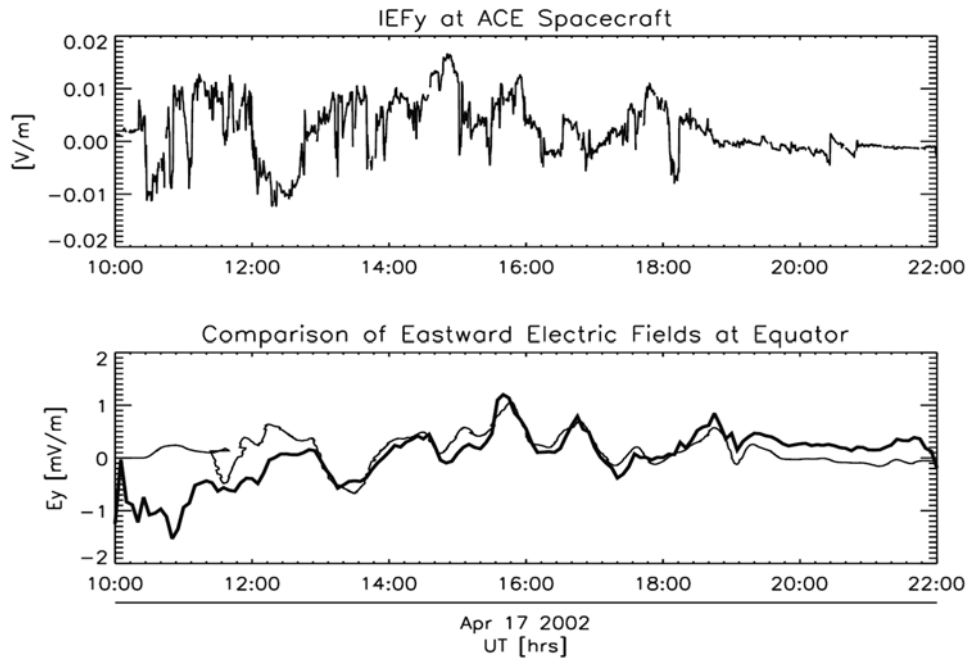


Figure 6.2: The horizontal component of the perturbed electric field measured at the magnetic equator is comparable to the east-west component of the interplanetary electric field measured at ACE spacecraft [adapted from Kelley *et al.* [47]]

in the equatorial electrojet current due to a variation in the horizontal component of the geomagnetic field during a sharp transition of IMF orientation from southward to northward direction, as shown figure(6.1). A sudden re-orientation of a northward IMF to southward does not show the same effect of the equatorial geomagnetic field [67].

On the other hand, Kelley *et al.* [47] in 2003 reported a nighttime variation in the eastward component of the electric field measured close to the magnetic equator that perfectly matches the variation in the calculated Interplanetary Electric Field (EMF) that was measured at ACE spacecraft as shown in figure(6.2).

Thus, the consequences of the interaction of solar wind with the magnetosphere, and in turn on the Earth's ionosphere, is not limited to the high latitudes but it can extend to the low-latitude and equatorial regions. These penetrating IMF and IEF to the low-latitudes might play an important role in driving different types of insta-

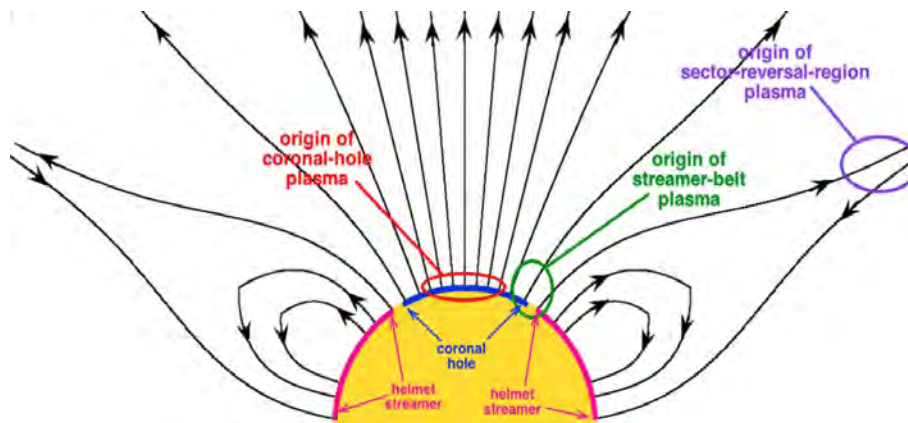


Figure 6.3: Four categories of solar wind origins in the Solar Corona. Adapted after Xu and Borovsky [124]

bilities or have influence on the established instability mechanisms on these regions. The expected enhancement of the low-latitude and equatorial instabilities provides motivation to study the dynamic variations of different types of solar winds as they propagate from the Sun to the Earth. We consider this work as a step toward forecasting the status of the ionosphere at different latitudes during storm and substorm events based on an ensemble of solar wind data generated from one upstream point measurement.

## 6.2 Solar Wind 4-Categorization Scheme

The solar winds are commonly categorized according to their origin within different regions in the solar corona. Most frequently three categories have been used: ejecta, slow solar wind, and fast solar wind [87, 88]. The slow winds release from the cusp between the close and open magnetic field lines and are characterized by their low-speed and high-proton-density, and they are called *streamer-belt-origin* winds. However, the fast solar wind release from the open magnetic field lines which are characterized their low-proton-density and high-speed, and they are called *coronal-hole-origin* winds. On the other hand, the ejecta are associated with *coronal-mass-ejections* from the Sun, which includes magnetic clouds that exhibits different shapes of magnetic ropes [95].

Based on twenty-years (1998-2008) of ACE solar wind data, Zhao *et al.* [125] used

Table 6.1: Average solar wind parameters at 1 AU during a solar minimum [105].

	Unit	Slow Wind	Fast Wind
Flow Speed	$km\ s^{-1}$	250 - 400	400 - 800
Proton Density	$cm^{-3}$	10.7	3.0
Proton Flux Density	$cm^{-3}\ s^{-1}$	$3.7 \times 10^8$	$2.0 \times 10^8$
Proton Temperature	K	$3.4 \times 10^4$	$2.3 \times 10^5$
Electron Temperature	K	$1.3 \times 10^5$	$1.0 \times 10^5$
Momentum Flux Density	$dyne\ cm^{-2}$	$2.1 \times 10^8$	$2.3 \times 10^8$
Total Energy Flux Density	$erg\ cm^{-2}\ s^{-1}$	1.55	1.43
Helium Content	%	2.5	3.6
Solar Origin	-	Streamer Belt	Coronal Holes

the ( $O^{7+}/O^{6+}$ ) density ratio and the solar wind speed to propose a scheme that categorizes the solar winds into coronal-hole, non-coronal-hole origin plasmas, and ejecta. In 2015, Xu and Borovsky proposed a 4-class categorization scheme for the solar wind plasma [124]. They added a new category based on another solar wind origin called *sector-reversal-region*, as shown in figure(6.3). The sector-reversal-region is formed within the helmet streamer which separates two coronal holes of opposite polarities and is characterized by its very low proton specific entropy [124].

In their categorization algorithm, Xu and Borovsky [124] used the proton temperature ( $T_p$ ), proton density ( $n_p$ ), proton speed ( $v_p$ ), and the interplanetary magnetic field (B) to calculate the proton specific-entropy ( $S_p$ ), proton Alfvén speed ( $v_A$ ), and the expected temperature of the proton at a given solar wind speed ( $T_{exp}$ ). A three-dimensional plot of the proton specific-entropy, the proton Alfvén speed, and the ratio between expected and proton temperatures separates data into four groups, as shown in figure(6.4). The separation planes between different groups of points were adjusted manually by eye using a three-dimensional visualization program to maximize the fractional separation between points of different groups, such that the magenta plane separates ejecta from non-ejecta plasma, the blue separates corona-hole-origin from streamer-belt-origin, and the blue plane separates streamer-belt-origin from the sector-reversal-region.

Thus, based on the orientation of these surfaces, we can use the algorithm in equation(6.1), to differentiate between solar winds from different origin according to their measurements. The ratio between the proton expected temperature ( $T_{exp}$ ) and pro-

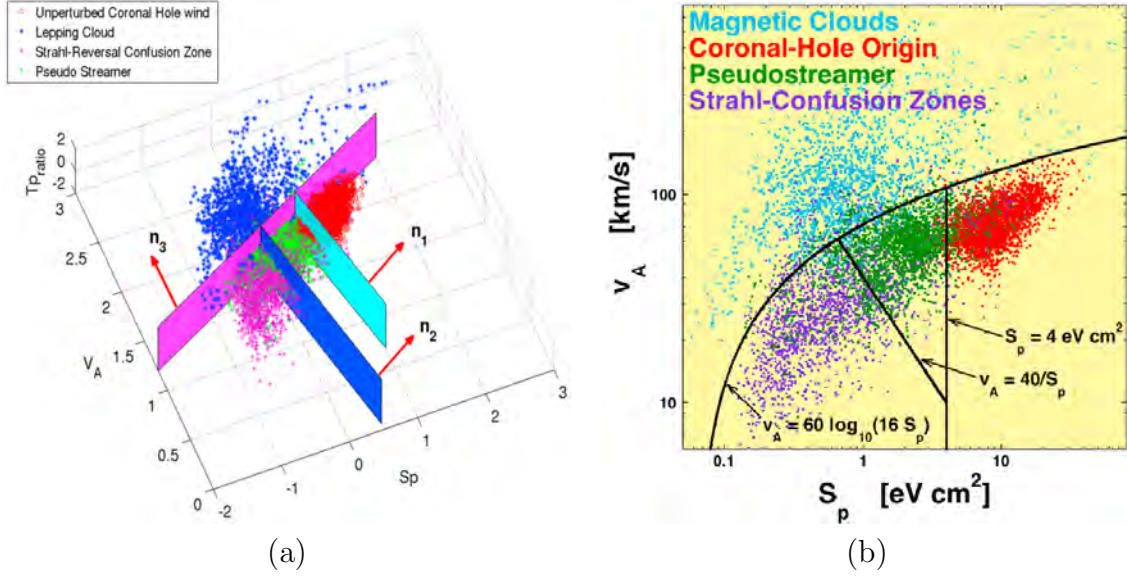


Figure 6.4: Separation of four solar wind categories in (a) 3-D plot of  $S_p$ ,  $v_A$ , and  $T_{exp}/T_p$  and (b) 2-D plot of  $S_p$  and  $v_A$ . The blue points are the ejecta, the red points are the coronal hole wind, the green points are the streamer-belt wind, and the purple points are the regions around sector reversals. Adapted after Xu and Borovsky [2015].

ton temperature ( $T_p$ ), which is verified in equation(6.1a), separates the ejecta from non-ejecta. If the solar wind is not ejecta and equation(6.1b) is verified, the solar wind is categorized as coronal-hole-origin. However the verification of equation(6.1c) for non-ejecta solar wind tells about the origin of sector-reversal-solar winds, and otherwise we have a streamer-belt-origin solar wind.

$$\log_{10}(v_A) > 0.277\log_{10}(S_p) + 0.055\log_{10}(T_{exp}/T_p) + 1.83 \quad (6.1a)$$

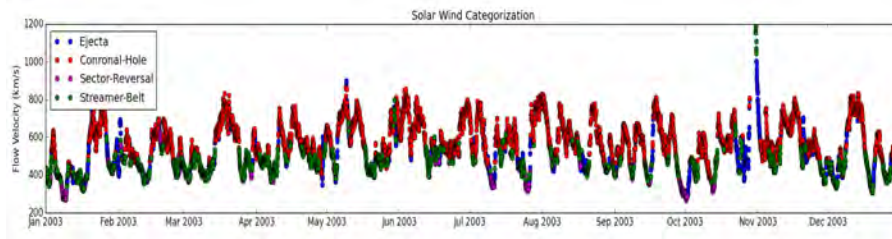
$$\log_{10}(S_p) > -0.525\log_{10}(T_{exp}/T_p) - 0.676\log_{10}(v_p) + 1.74 \quad (6.1b)$$

$$\log_{10}(S_p) < -0.658\log_{10}(v_A) - 0.125\log_{10}(T_{exp}/T_p) + 1.04 \quad (6.1c)$$

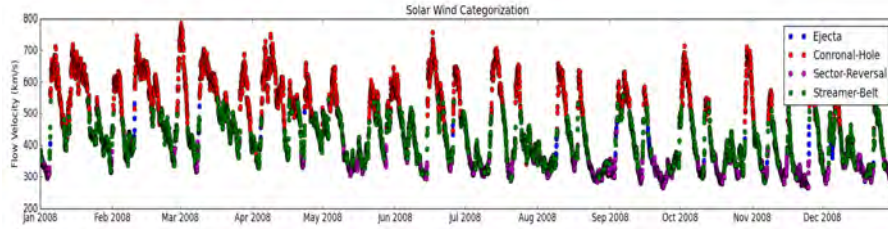
where,

$$S_p = \frac{T_p}{n_p^{2/3}}, \quad v_A = \frac{B}{(4\pi m_p n_p)^{1/2}}, \quad T_{exp} = \left(\frac{v_p}{258}\right)^{3.113}$$

We tested the solar wind data from OMNI dataset against the 4-categorization algorithm during a year around solar maximum (2003) and a year around solar minimum



(a) Solar Maximum (2003)



(b) Solar Minimum (2008)

Figure 6.5: Testing the solar wind data in OMNI dataset against 4-categorization scheme during (a) solar maximum and (b) solar minimum conditions.

(2008). The four groups of solar winds with the proton speed as an example are shown in figure(6.5). In the solar maximum year, we see the release of the ejecta from the Sun multiple times over the year, especially at the end of October and beginning of November where some unusual extreme storms were recorded [3, 56]. In March 2008, which is considered as one of the deepest minimum recorded [96, 123, 8], the coronal-hole-origin solar wind type dominates the categorization. On the other hand, the observed speed of the coronal-hole-origin and streamer-belt-origin solar winds are in good agreement with the expected values. Moreover, the solar winds originating from sector-reversal-region are characterized by low speed (around 300 km/s) in years of both solar maximum and minimum.

### 6.3 Solar Wind Advection

In 1958, Parker [75] proposed the spiral model for the solar wind interplanetary magnetic field (IMF) propagation into the heliosphere based on the radial outflow of parcels of plasma from the surface of the corona in the sun, as shown in figure(6.6-a). The arrival angle of the IMF at 1 AU, which is the angle between the orientation of the IMF and the radial direction, according to Parker spiral model should be ap-

proximately  $45^\circ$ . However, the probability distribution function (PDF) of the arrival angle at 1 AU, figure(6.6-b), elucidates the dependence of the arrival angle on the solar wind speed. The occurrence of the  $45^\circ$  arrival angle is found to be the most probable for solar wind speeds in the [350 - 450] km/s interval. However, there are always probabilities for other angles of arrival depending on the structural variation of the interplanetary magnetic field.

To test the advection or propagation model, it is preferable to have a distinct event that can be seen by the two monitoring stations we do the advection between them. A discontinuity in the IMF has been used by Horbury *et al.* [40] in 2001 to uniquely identify the same structure at two monitoring stations, and it is defined as a sudden change in the orientation or magnitude of the interplanetary magnetic field.

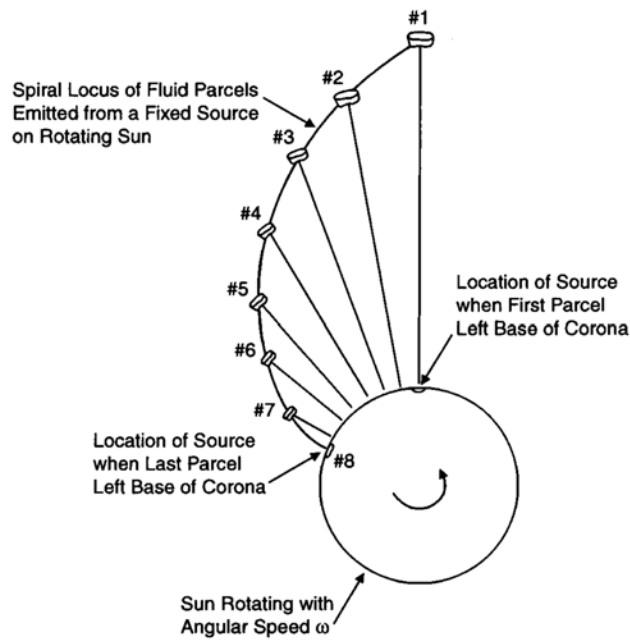
Based on Parker spiral model and assuming that the parcel of magnetized plasma is advected with constant velocity along the Sun-Earth line. Therefore, we can use the simplest law of kinematic for constant speed ( $v_x = x/t$ ) to find the travel time of the solar wind plasma with the embedded magnetic field between two spacecraft. However, the advection of the solar wind as a flat surface ignores the variation in the phase front of the IMF which is tilted at arbitrary angles with-respect-to the Sun-Earth line [118, 119, 117, 89]. Also, it ignores the relative location between the spacecraft, and their locations with respect to the Sun-Earth line.

To include the orientation of the magnetic field phase front, we need to calculate the normal to the surface of minimum variations in the interplanetary magnetic field. Then we can estimate the propagation time between two points in the space using equation(6.2):

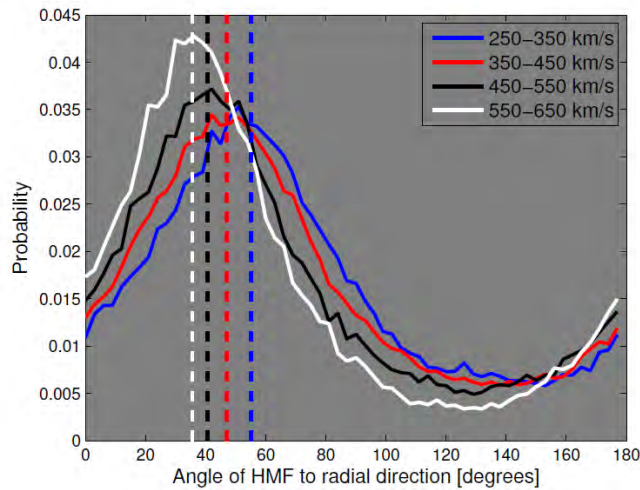
$$t_{adv} = \frac{(\mathbf{r}_{s_2} - \mathbf{r}_{s_1}) \cdot \hat{\mathbf{n}}}{\mathbf{v}_{sw} \cdot \hat{\mathbf{n}}} \quad (6.2)$$

where,  $\mathbf{r}_{s_1}$  and  $\mathbf{r}_{s_2}$  are the locations of the two upstream monitoring stations,  $\hat{\mathbf{n}}$  is the normal to the IMF surface of minimum variations, and  $\mathbf{v}_{sw}$  is the solar wind velocity.

Weimer and his colleagues [118, 119] used the minimum variance of the magnetic field (MVAB) method by constructing a covariance matrix from the IMF measurements, and then seek the eigenvector that corresponds to the smallest non-negative eigenvalue to use it to estimate the orthogonal to the surface of minimum variations in the



(a) Parker Spiral Model of the interplanetary magnetic field with the emission of magnetized plasma from the rotating sun. [Adapted from Hundhausen [42]].



(b) Probability distribution function of the solar wind arrival angle at 1 AU as a function of its speed. [Adapted from Owens and Forsyth [74]].

Figure 6.6: (a) Parker spiral model for the advection of magnetized plasma parcels in the solar wind, and (b) the probability distribution function of the solar wind speed dependence on arrival angle at 1 AU.

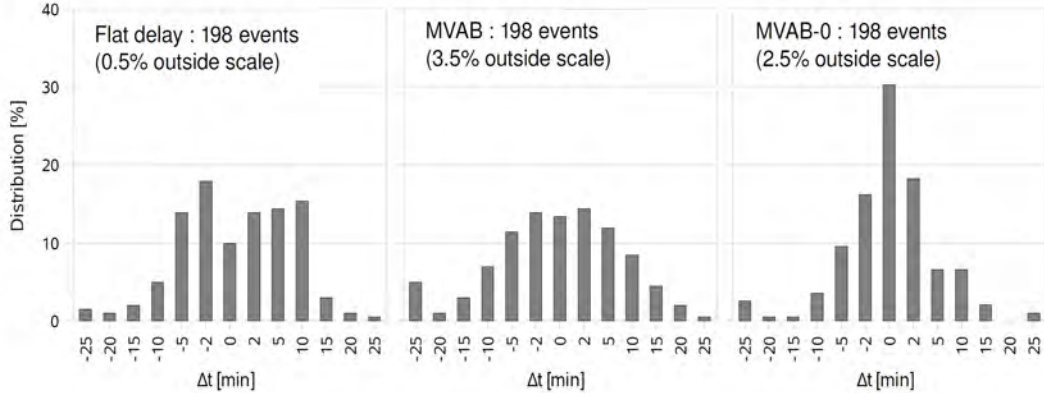


Figure 6.7: A comparison of the error in the arrival time between different methods (flat delay, MVAB, and MVAB-0) for calculating the solar wind time delay [adapted from Mailyan *et al.* [59]].

magnetic field. Another improvement to the MVAB method was made by Weimer *et al.* [117] in 2008 when they added a constraint in the magnitude of the magnetic field along the normal, and they called this method MVAB-0. They considered all events they studies are characterized as *tangential-discontinuity* which makes the component of the magnetic field along the normal the surface of minimum variations vanishes.

Mailyan *et al.* [59] estimated the propagation time of the solar wind between ACE and Cluster for 198 events using the “Flat Delay”, “MVAB”, and “MVAB-0” methods. Then, they calculated the relative distribution of the timing errors from these methods using the difference between the estimated and observed arrival time, as shown in figure(6.7). They found that the error in the arrival time for “flat-delay” and “MVAB” for most of the events are within  $\pm 10$  minutes, however, more than two-third of the events arrived in the limit of  $\pm 5$  minutes using “MVAB-0” method. Thus, a difference of only  $\pm 5$  minutes was only found between the best estimation method for the arrival time and the worst one. Because the solar wind does not change in 5 minutes, we employed the “flat-delay” in calculating the time shift due to it easiness.

## 6.4 Data Sources, Limitations, and Conditioning

To generate an ensemble for the solar wind parameters, such as velocity, density, and z-component of the IMF, we need to use the measurements from at least two monitoring stations or spacecraft in the heliosphere. The more upstream spacecraft is used as a reference for the solar wind measurements and the closest spacecraft is used as a target to generate the Kernel Density Estimation (KDE) function. The two monitoring stations should have concurrent and continuous measurements of the solar wind parameters over appreciable time slots to allow the establishment of good and reliable KDE functions.

The presence of the Advanced Composition Explorer (ACE) satellite in its halo orbit at the first Lagrangian point<sup>2</sup> ( $L_1$ ) gives it an advantage over other solar wind mission satellites to be the reference point [1, 110]. For the target monitoring station we found the Interplanetary Monitoring Platform-8 (IMP8) spacecraft spends most of its circular orbit around the Earth outside the magnetopause (i.e. it is immersed in the solar wind in the heliosphere before it starts its interaction with the nose of the magnetosphere at the bow shock) [77]. Also, having IMP8 very close to the magnetopause gives it an advantage over other solar wind missions because the ensemble that will be generated from its measurements will be very close to that at the magnetosphere nose.

Although choosing ACE and IMP8 to generate the ensemble is good regarding their locations and orbits, there are two limitations in choosing this couple of spacecraft. The first limitation is that there is only three years (1998, 1999, 2000) of overlap between ACE and IMP8, which makes the concurrent measurements of the solar wind parameters from these spacecraft very limited for deriving Kernel Density Estimation (KDE) functions. The second limitation is that the IMP8, that was about to be decommissioned, solar wind data has many large gaps due to non-continuous telemetry as well orbits that are partially inside Earth's bow shock. Moreover, the different rates of recording the measured data in ACE and IMP8, and even between the measurements of the plasma parameters and magnetic field components in the same spacecraft is a factor that should be considered. Moreover, the different rates of

---

<sup>2</sup>At the Lagrangian points the gravitational forces on the spacecraft from the Earth and the Sun cancel out because they are equal to each other in magnitude but opposite in direction.

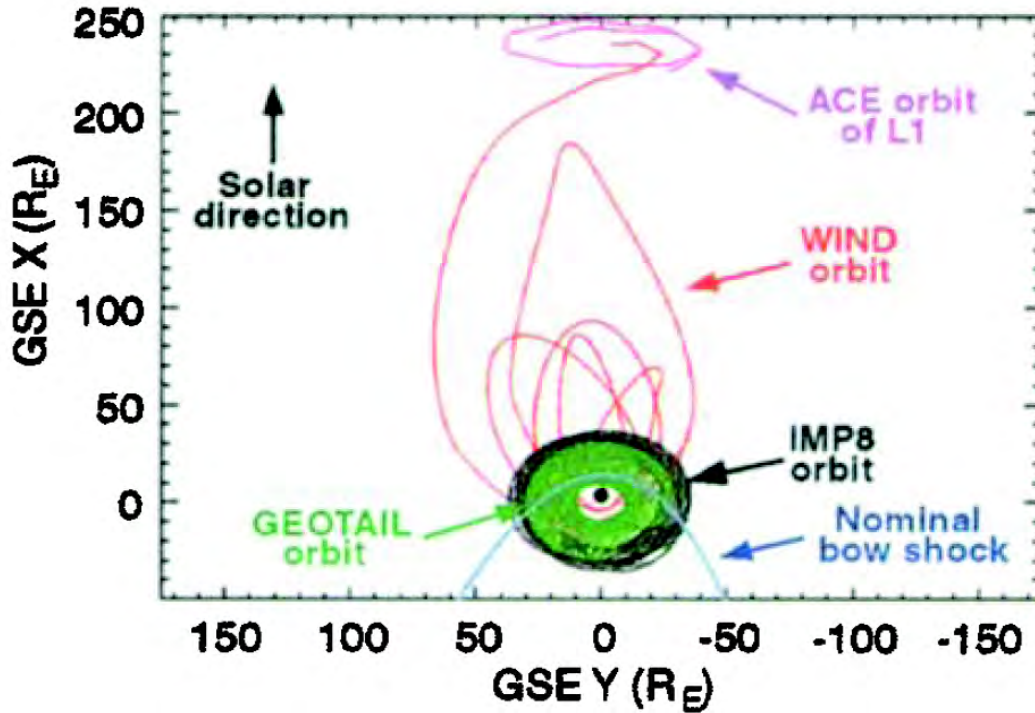


Figure 6.8: Comparison of the location of ACE and IMP8 in the heliosphere to other spacecraft such as WIND and Geotail. ACE stays in its halo orbit at the first Lagrangian point and IMP8 orbits the Earth and stays outside the nominal bow shock location most of its orbital time. [Adapted after Haggerty *et al.* [33]]

recording the measured data in ACE and IMP8, and even between the measurements of the plasma parameters and magnetic field components in the same spacecraft is a factor that should be considered.

Because our current plan includes only the use of ACE and IMP8 spacecraft, the three years limitation has no solution which requires the use of measurements from other solar wind missions. On the other hand, to overcome the large gaps in data found in IMP8 measurements, we divided the three years of data into time-slots of four hours length<sup>3</sup>. Then, we employed a 15 minutes gap-length restriction in the contiguous data in both ACE and IMP8 in each time-slot. The gap-length restriction helps in minimizing the inaccuracy that might arise while using the linear interpolation method which is used to fill the gaps in measured data in both spacecraft.

<sup>3</sup>The number of time-slots available to generate the solar wind ensembles of four hours length are found to be much more than those of six hours length.

Finally, we tested that all the solar wind parameters we use in categorizing the solar wind and generating their ensembles are found in the corresponding time-slots in both spacecraft, and we filtered-out all the time-slots that do not pass this test.

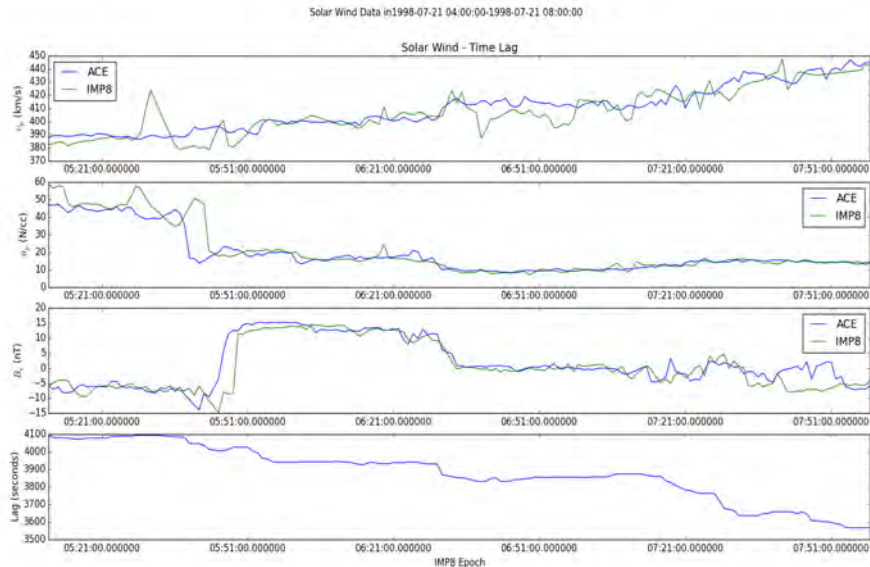
## 6.5 Advected Solar Wind Parameters

To calculate the advection time, we used the simplest method which based the first law-of-kinematic,  $t = x/v_{sw,x}$ , for a constant solar wind velocity over the interval  $[t_1, t_2]$ , where  $t = t_2 - t_1$ . This method does not consider the relative positions of ACE and IMP8 spacecraft in their orbits or the spatial variations of the interplanetary magnetic field components in the solar wind. These two factors will add some error to our method, but as we mentioned earlier while discussing Mailyan *et al.* [59] work, this error will not exceed 5 - 10 minutes which is acceptable in the current phase of the work and will be considered for improvement in future.

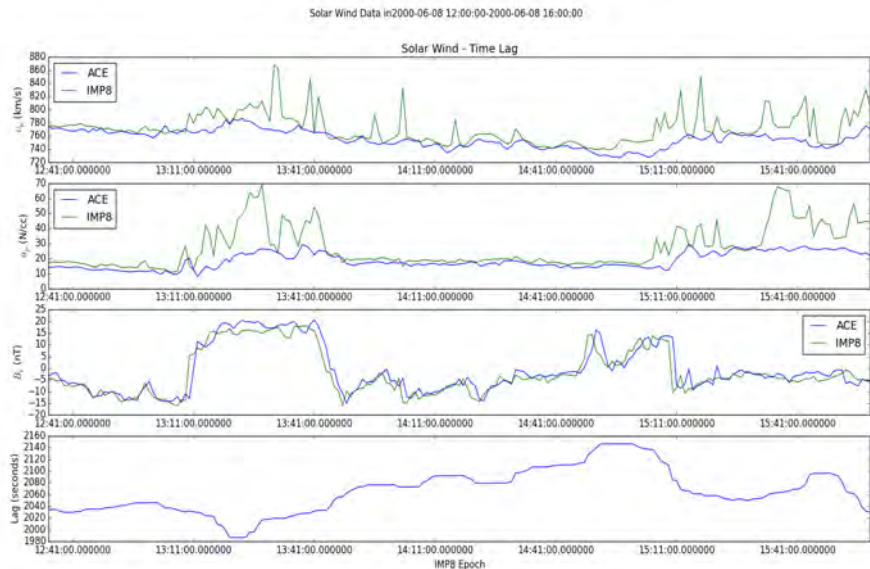
To have all the measured solar wind data in matched time-scale, we divided the available dataset into time-slots of (fixed) 4-hour length and then we shifted all measured parameters in time to have them in the same time-scale. We calculated the advection time at each point measurement of solar wind parameters in ACE and IMP8 at each time-slot, and to avoid any non-realistic variations or noise in these measurements, we employed a 15 - 20 minute spatial median-filter to smoothing the measured data. We chose the median-filter because of its superiority over the mean-filter in preserving all the useful details in the dataset.

In figure(6.9), we show a comparison between the measured solar wind parameters at ACE and IMP8, with ACE measurements advected in time to be compared with the measurements at IMP8. The panels in subfigures(6.9-a,b) presents the solar wind speed, density, interplanetary magnetic field, and pointwise lag-time between ACE and IMP8, respectively. We can see a sharp transition in the magnitude and orientation of the interplanetary magnetic field in the two time-slots. This discontinuity in the magnetic field helps in matching this feature or event in the distant monitoring stations, and it is called “tangential discontinuity” [59].

Although, the measurements in subfigures(6.9-a,b) had been taken in Summer of



(a) Data measured on July 21, 1998.



(b) Data measured on June 8, 2000.

Figure 6.9: Two comparisons between the solar wind speed (first-panel), density (second-panel), and magnetic field (third-panel) measured at IMP8 spacecraft to those measured at ACE spacecraft and are the advected to IMP8 location. The calculated pointwise advection time (time-lag) is shown in the fourth-panel. The comparisons are made between these solar wind parameters that are measured in Summer 1998 (a) and Summer 2000 (b) that show different solar wind status.

1998 and 2000, respectively, the solar wind parameters in subfigure(6.9-a) shows a low-speed and high-proton-density solar wind compared to the high-speed and low-proton-density solar wind in subfigure(6.9-b). So, the 4-categorization scheme tells us that we have “streamer-belt-origin” and “coronal-hole-origin” solar winds in Summer of 1998 and 2000, respectively.

Comparing the trend and the fine details in the advected ACE measurements and the corresponding measured data in IMP8, we found that the IMF measurements match very nicely in both spacecraft datasets in 1998 and 2000. On the other hand, the IMP8 measurements for the solar wind speed and proton density in Summer of 2000 show many spikes all over the time-slot but they have a similar trend to the ACE advected measurements. Thus, we can rely on the flat-delay advection method for generating an ensemble for the solar wind measured parameters on IMP8, especially in the presence of tangential discontinuity in the IMF measurements.

## 6.6 Solar Wind Ensemble

To generate the solar wind ensemble ( $p(V_{IMP}-V_{ACE})$ ) for the measurements of the solar wind speed at IMP8 based on the advected measurements of the speed at ACE, we grouped solar wind speed measurements into 25 km/s wide bins, and for every measured speed at the ACE spacecraft found to fall into that bin we recorded the concurrent speed at IMP8 in a corresponding interval. We therefore have approximated our conditional probability distributions by using data within the neighborhood of the exact value, i.e.  $p(V_{IMP}-V \in \mathcal{N}(V_{ACE}))$ . Then we used all the intervals of IMP8 recorded solar wind speed to establish a Kernel Density Estimation (KDE) function for each interval. Basically, we establish a *conditional probability distribution (CPD)* for IMP8 solar wind measurements based on the corresponding recorded data advected from the ACE spacecraft. We in turn used this CPD to establish the KDE functions for IMP8 solar wind parameters [106, 122].

The Kernel Density Estimation (KDE) does not use a specific parametric variable to estimate the parameters of a probability density. Instead, the KDE produces a smooth continuous density curve with its bandwidth is adapted to the sample data and its shape is related to the Probability Density Function (PDF) generator. Al-

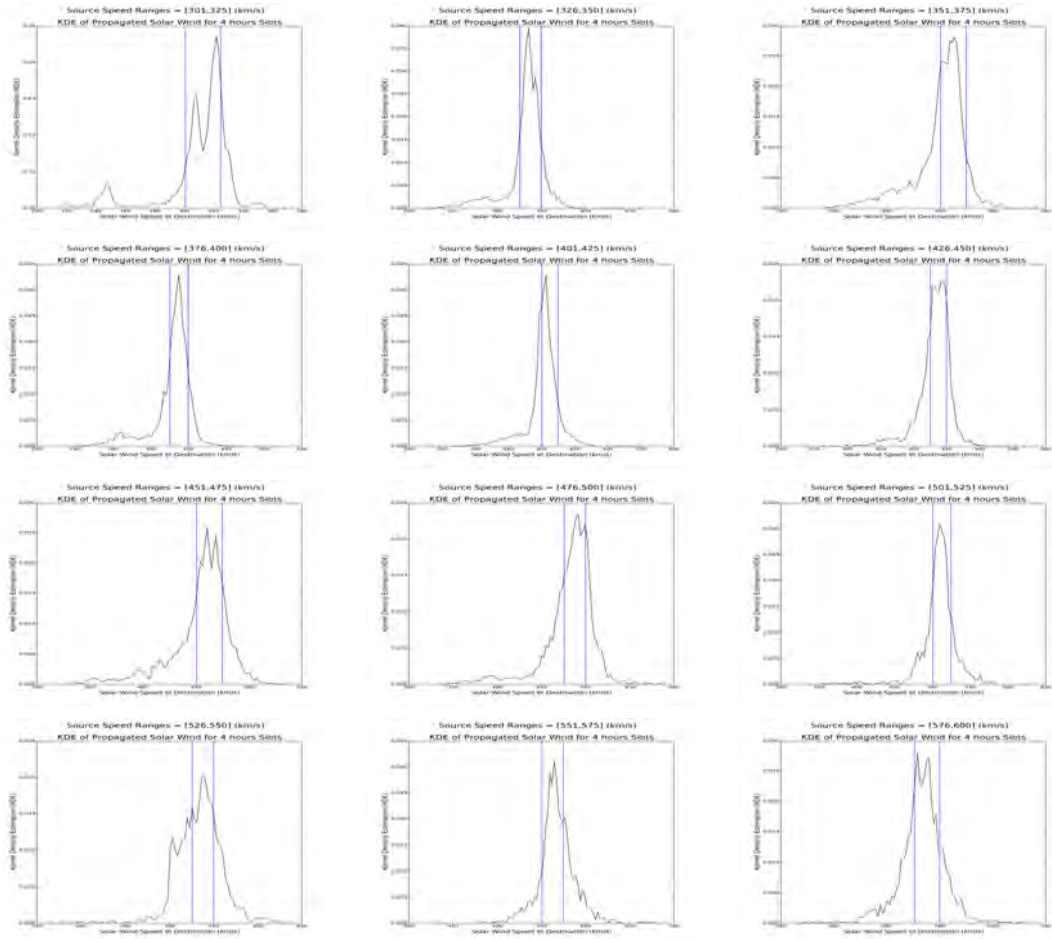


Figure 6.10: Uncategorized Kernel Density Estimation (KDE) functions of solar wind that are measured at IMP8 spacecraft based on three years of advected measurements from ACE spacecraft to the IMP8 location using the flat-delay method. The vertical blue lines represent the interval of solar wind speeds measured at ACE.

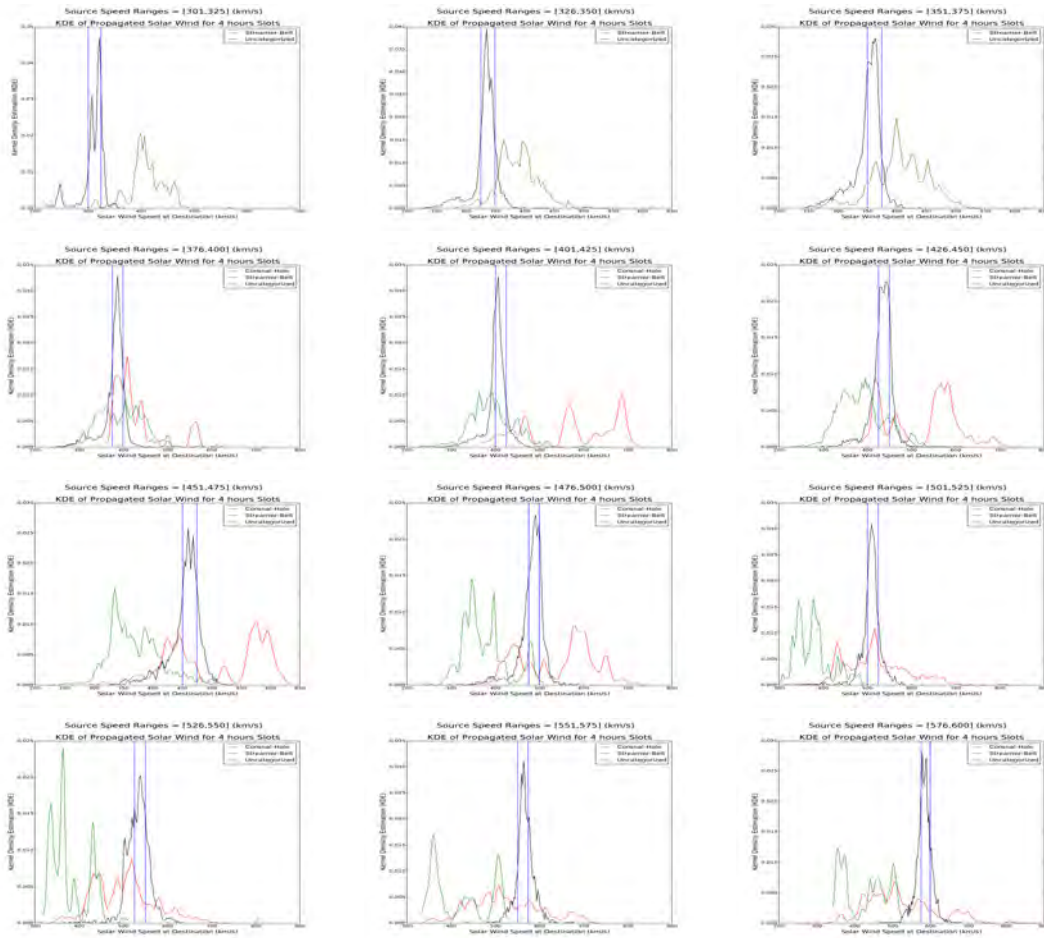


Figure 6.11: Categorized Kernel Density Estimation (KDE) functions (streamer-belt-origin in green and coronal-hole-origin in red) of solar wind speed at IMP8 spacecraft based on three years of advected measurements from ACE spacecraft, compared to the unclassified KDE functions (solid black line). The vertical blue lines represent the corresponding interval of solar wind speed at ACE.

though the histogram is similar to the KDE in building a function to represent the probability distribution, it distributes the sample data into discrete bins in such a way that can not be used to generate random numbers from the density distribution which requires a continuous probability density function. Because we need to draw random samples from the PDF functions, the kernel density estimation is superior over the histogram to do this job.

Figure(6.10) shows the KDE functions (solid black line) of the solar wind speed at

IMP8 based on three years measurements. The two vertical lines represent the limits of the interval of solar wind speed at ACE. We found that in some cases about 65% of the solar wind speeds that are measured at IMP8 fall inside this interval. The lack of sufficient qualified measurements over the three years of overlap between ACE and IMP8 influenced the power of the established KDE functions. especially for the less frequently sampled solar wind speeds over that specific period of time in the solar cycle. This becomes more clear when we discuss the categorized KDE functions for different solar wind origins.

Based on the 4-categorization algorithm for the solar wind [Xu and Borovoski 2015], we used the solar wind measured speeds at ACE to establish a Kernel Density Estimation (KDE) functions for the “coronal-hole-origin” and “streamer-belt-origin” categories of the solar wind. Figure(6.11) shows the KDE functions of the speed in the uncategorized solar wind (black solid line) and the categorized solar winds, coronal-hole-origin in red solid line and streamer-belt-origin in green solid line. The subplots in figure(6.11) shows the tendency of the uncategorized KDE of the solar wind speed toward the KDE of solar wind speed in the streamer-belt-origin category in the interval of slow solar winds, and this tendency shifts with the solar wind speed to be completely toward the KDE of solar wind speed in the coronal-hole-origin category.

Definitely, we can employ the KDE functions to generate an ensemble of the solar wind speed at IMP8 location in the upstream using one-point measurement at ACE. The ensemble of solar wind data can be generated by any number of random samples using the KDE functions for each measurement at ACE spacecraft. Then we can calculate any statistical quantity from these random samples depending on the calculations we want to use for. In figure(6.12) we used the established KDE functions to generate an ensemble of the solar wind speed to use it to calculate the range of speeds that is expected to be measured at IMP8 based on the measurement at ACE spacecraft. The interval of time we calculated the expected range of solar wind speed at IMP8 is Jan-Mar 2003 which is different from the interval we used to establish those KDE functions. This ensemble can be used to forecast the status of the solar wind right before it interacts with the bow-shock, which helps in forecasting the status of the magnetosphere and ionosphere about one hour in advance. Also, using the

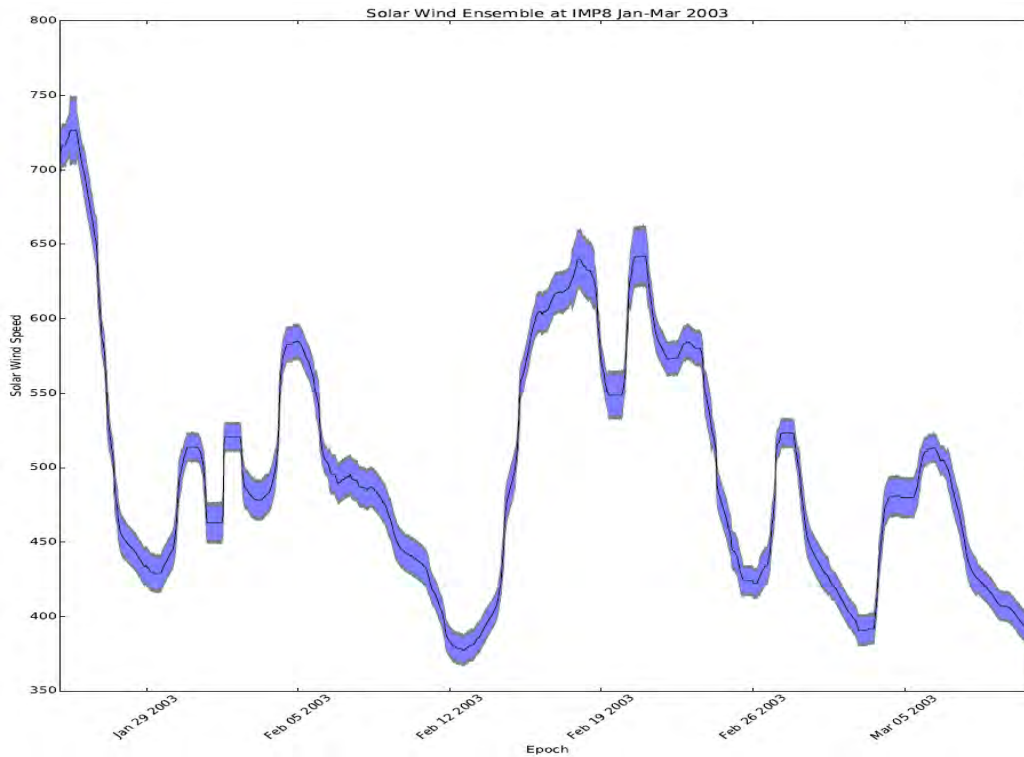


Figure 6.12: An ensemble of solar wind speed at IMP8 location based on one-point of measurements at ACE spacecraft on Jan-Mar 2003 by using the KDE functions generated for the solar wind data in 1998 - 2000.

categorized KDE functions helps in forecasting the probability of the incoming solar wind to be fast or slow solar wind according to the historical events we studied.

The three years of solar wind data availability limited our ability to establish better KDE functions for the categorized and uncategorized solar wind speed. This can be seen in the large bins which will give rise to random ensemble values that might lead to faster rate of variability in the solar wind parameters than observed. Because of the previous points “surrogate” time series of the solar wind should not be expected to preserve all properties of the solar wind, but should primarily be regarded as a first estimate of the uncertainty in the estimate of solar wind parameters impacting the magnetosphere. The results we showed for the categorized and uncategorized KDE functions give us a good sign for the applicability of this method to predict the solar wind status under certain limitations.

## 6.7 Conclusions

We introduced the new 4-categorization scheme proposed by Xu and Borovoski [124] for the type of the solar wind. Then we employed categorization empirical algorithm on solar wind data from OMNI dataset during solar maximum and solar minimum conditions to get the sense of the model applicability. Also, we employed that categorization algorithm on the measured solar wind data at both ACE and IMP8 to check the matching between findings in both missions which supposed to be the same in a four-hours time slot.

After we studied the comparison made by Mailyan *et al.* [59] between different advection techniques (flat-delay, MVAB, and MVAB-0), we decided to accept the 5-10 minutes error and use the flat-delay method in the current phase of the work. We presented a comparison between the measured solar wind parameters, such as solar wind speed, proton density, and interplanetary magnetic field (IMF), at IMP8 with the advected solar wind measurements from ACE to IMP8 location. The comparison has been made for many time slots over three years, but we only presented the comparison between the summer of 1998 and 2000 to show the applicability of the technique under two different solar wind conditions. The comparison between the recorded solar wind measurements at IMP8 and the advected ones from ACE show a good agreement both in the overall trend and the fine details, especially when there is a sharp transition in the vertical component of the interplanetary magnetic field.

After checking the robustness of our advection model, we used the measured data at ACE and IMP8 to establish a Kernel Density Estimation (KDE) functions for the solar wind speed using intervals of 25 km/s. The KDE functions of the solar wind speed at IMP8 show a good fit inside the corresponding intervals of solar wind speed that measured at ACE and advected to IMP8. In some cases we found 65% of the IMP8 measurements fall inside the 25 km/s bin of solar wind speed at ACE while the other cases have their measurements fall outside those intervals. We attributed the falling of large percentage of measurements outside the expected interval to the lack of available and qualified measurements over the three years, especially after employing the 15-minutes gap restrictions on all time slots.

A comparison between the KDE functions of the uncategorized and categorized solar winds was made and showed a tendency of the uncategorized solar wind toward the expected category based on the solar wind speed. The KDE functions can be used to generate an ensemble of solar wind data which helps in forecasting the nature of interaction between the solar wind and the bow-shock and the status of the magnetosphere and ionosphere about two hours in advance. However, to acquire KDE functions that generate reliable ensembles of the solar wind data we need to have more measurements which can be achieved by including more missions in the upstream.

## Chapter Seven: Summary and Conclusions

The equatorial electrojet region in the Earth's ionosphere is characterized by its large conductivity due to the large ratio between the Hall and Pedersen conductivities. This large (Cowling) conductivity is attributed to the different drift mechanisms of the ions and electrons in this region. The large ratio between the ions collision frequency with the background neutral particles and their gyrofrequency ( $\nu_{in} \gg \Omega_{ci}$ ) makes the ions unmagnetized and their mobility depends on the Pedersen conductivity. However, the same ratio is small ( $\nu_{en} \ll \Omega_{ce}$ ) in case of the electrons which are considered magnetized and their mobility depends on the Hall and Pedersen conductivities. This gives rise to a large relative speed between the ions and electrons in the electrojet region. The two-stream or Farley-Buneman instability is excited inside the equatorial electrojet region when the relative speed between ions and electrons exceeds the ion-acoustic speed. In addition, the presence of a sharp density-gradient in the E-region at 90 - 120 km altitude is another driver for the gradient-drift or cross-field instability.

A series of radar observations and sounding rocket measurements has been done over seventy years to study the spectral and spatial characteristics of the Farley-Buneman and gradient-drift instabilities in the equatorial electrojet region. These observations and measurements provided appreciable details for the status of the irregularities in the plasma density under different solar conditions. This detailed picture of the plasma turbulence in the equatorial electrojet triggered many research groups to focus on finding the physical mechanisms for the evolution, coupling, and saturation of these instabilities. Therefore, different models have been proposed to simulate the evolution and saturation of type-I and type-II instabilities in the equatorial electrojet.

In this work we show our contribution in modeling and simulating the plasma turbulence in the equatorial electrojet due to the Farley-Buneman and gradient-drift instabilities. We proposed a unified fluid model that has the capability to resolve both types of instabilities in the fluid regime. While this model is based on the same physics like the standard two-stream model of the equatorial electrojet instabilities, it

considers the contribution of the ion viscosity moments from the Vlasov equation and the electrons polarization drift which arises from the electrons inertia term that used to be ignored for its smallness. These two terms play important roles in stabilizing the unstable growing modes in the linear domain and saturating the evolving fields in the nonlinear regime.

The temporal and spatial evolution of the plasma density, electric potential, and ion velocity potential are studied linearly and nonlinearly in a two-dimensional fluid model. Our unified fluid model considers both ion viscosity and electron polarization drift. The dominant nonlinear terms,  $[\delta\tilde{\varphi}, \delta\tilde{n}]$  and  $[\delta\tilde{\varphi}, \nabla^2\delta\tilde{\varphi}]$ , are responsible for the coupling between type-I and type-II instabilities and the driving of the dynamic system into a statistically steady state.

In our unified model, the electron inertia, which has been ignored in the earlier models, adds the polarization drift to the dynamic system which is found important for the nonlinear coupling between different modes and the saturation of growing modes of small-scale structures. The ion viscosity plays a similar role to the ions Landau damping in dissipating the energy content of the unstable modes of very small structures, which, in contrast to kinetic models, is not included in fluid treatments.

The linear results show that the ion viscosity and electron polarization drift are important for stabilizing the large wavenumbers of 1 - 5 meter scale sizes in the vertical direction and less than a meter in the horizontal direction. The unified fluid model linear growth rate is comparable to the growth rate calculated with a kinetic model by Schmidt and Gary [100] and a hybrid model by Oppenheim *et al.* [69] for the Farley-Buneman (type-I) instability. However, the unified model shows also the growth rate of type-II instability at the small-wavenumbers and the coupling between both instabilities in the linear and nonlinear regimes though the density-gradient scale-length.

On the other hand, the linear phase velocity predicted from our unified model is smaller than that obtained from the standard two-stream fluid model in such a way that is generally consistent with the observed values of the phase velocity and close to the ion-acoustic speed. But the magnitude of the phase velocity in the linear regime is still larger than the ion-acoustic speed which is considered, according to the radar observations [54], an upper limiting speed for the E-region irregularities.

The effects of the density gradient scale-length and  $\mathbf{E} \times \mathbf{B}$  drift velocity on the evolution of the instabilities are examined in different cases in the linear and nonlinear domains. The results show that the shorter the density-gradient scale-length, the stronger the driven instability in the system which is indicated by a large growth-rate. In the linear domain, it was found that the peak of gradient-drift instability at the small-wavenumbers and the peak of the Farley-Buneman one at the large-wavenumbers depends on the density-gradient scale-length. However, the large values of  $\mathbf{E} \times \mathbf{B}$  drift velocity influence only the unstable modes of small-structures in the plasma due to type-I instability.

The altitude-dependence of the growth rate profile shows the role of type-I and type-II instabilities in exciting the irregularities in the E-region between 90 - 120 km as suggested from the rocket measurements reported by Pffaf *et al.* [80, 81]. Type-II instability dominates between 90 - 103 km where the plasma is very collisional and electron drifts are too small to excite type-I instability. However, type-I instability dominates at 110 - 115 km where the negative density-gradients (which is parallel to the background electric field) can not excite type-II instability. Moreover, the coupling between type-I and type-II instabilities takes place at the core of the electrojet region between 103 - 110 km where the maximum growth rate is extending over a wide range of wavenumbers.

The time-series of the spectrum of the density perturbation shows the back and forth exchange of energy between plasma irregularities of different scales. This exchange of energy can be considered to be a verification of the Sudan *et al.* [113] theory of two-step energy cascading to structures of order of a meter scale in the vertical direction. The perturbed density spectrum exhibits a coupling between type-I and type-II instabilities and shows the generation of long-scale structures in the vertical direction. It also demonstrates how the energy is transferred from the large-scale perturbed density structures excited by type-II modes to the small-scale irregularities exhibiting type-I features. The plasma density spectrum shows an even distribution of energy between the large-scale structures (small wavenumbers) that produced type-I modes and the small-scale structures (large wavenumbers) that produced by type-II modes. The energy content of the irregularities of scale-length less than a meter in the vertical direction is small, which explains the difficulties to detect them by coherent scattered

radars [22]. In addition, the embedding of the small-scale structures in the large-scale structures demonstrates the difficulty to observe the long-scale structures of type-II while type-I instabilities are excited.

Our nonlinear model is able to reproduce a number of features of the sounding rocket measurements and radar observations under different solar conditions such as: (1) a saturation of the density perturbation between 7 - 15%, (2) root-mean-square values of the horizontal component ( $\delta E_y = 8.7 - 15$  (mV/m)) and vertical component ( $\delta E_z = 1.7 - 3$  (mV/m)) of the perturbed electric field, (3) a linear and nonlinear reduction of the phase velocity of the horizontal westward irregularities to values less than or equal the ion-acoustic speed, (4) an asymmetry in the plasma fluxes in the vertical direction as a result of an asymmetry of the perturbed zonal electric field components, (5) an asymmetry in the plasma drifts in the horizontal direction as a result of an asymmetry of the perturbed vertical electric field components, (6) a break-up of the large-scale vertical plasma structures into small-scale structures of 3 meters and less in the saturation state, (7) an inclination of the small structures drift toward the corners of the simulation box as a result of the vertical up (down) drifts of the depletion (enhanced) density regions due to type-II instability.

From the simulation results under solar minimum conditions, the low-level of fluctuations of the electron density and the small eastward zonal perturbed electric field are attributed to the solar quiet (Sq) and unusual minimum conditions with low total solar irradiance on March 2008. However, the simulation results of the electron density and electric field components under solar maximum conditions agree very well with the measurements that were made in the CONDOR campaign.

The energy evolution of the system was also examined in detail. The energy is injected into the dynamic system through the gradients of the background electron density and electric potential. The electrons and ions viscosity as a result of their collisions with the background neutral particles are considered sinks for the energy. The density continuity equation plays the coupling role between the evolving fields. The coupling terms transfer the energy from the source in the evolution of electric potential to be dissipated in the strong collisions of the ions with the neutrals. The two nonlinear terms are responsible for the forward and reverse energy cascading in

the system. The forward energy cascade generates the small-structures of plasma density that can not be explained in the linear regime. The strength of the forward and reverse energy cascading depend on the density-gradient scale-length,  $L_n$ , and the cross-field drift speed,  $v_E$ . In the case of large drift,  $v_E = 425$  m/s, the influence of the density-gradient scale-length is negligible. This explains the strong driving of Farley-Buneman instability over the gradient-drift one. Different density-gradient scale-length with the smaller drift,  $v_E = 400$  m/s, shows a considerable difference in the forward and reverse energy cascaded between the unstable modes of different length. The effect of a small simulation box compared to the density-gradient scale-length on the reverse energy cascading should be considered for further study in the future.

The dynamic system of the plasma turbulence in the equatorial electrojet is found to be a non-canonical Hamiltonian system, where the bracket the governs the plasma dynamics in the system and proved to satisfy the Jacobi identity. Also we found that the system has a Casimir invariant which identifies that the system has a nontrivial kernel of the symplectic operator. We used the characteristic of the Casimir to reformulate the system in terms of a new variable that shows the dependence of the system dynamics on the fluctuating density and vorticities.

Finally, we studied the influence of the discontinuities in the Interplanetary Magnetic Field (IMF) of the solar wind on the variation of the horizontal component of the geomagnetic field at the equator. We presented the observations that show the penetration of the IMF and IEF to the equatorial region those are reported by Ohtani *et al.* [67] and Kelley *et al.* [47], respectively. The aim is to generate a solar wind ensemble for these parameters based on a large set of data that can be used to drive our physics-based model for the purpose of space weather forecasting.

We used three years of measured solar wind data at two spacecraft to establish *Kernel Density Estimation (KDE)* functions that can be used to generate ensembles of the solar wind parameters. These ensembles can be used for forecasting the status of the solar wind and in driving our future model of the E-region electrojet both in the equatorial and high-latitudinal regions. This will provide more understanding of the status of the ionosphere during storm and substorm events. Forecasting the status of

the local ionosphere is important in expecting any loss of GPS signals that are used in the navigation for the flights that cross the north or south poles.

In conclusion, the unified fluid model is able to reproduce comparable results in the linear regime to the kinetic theory for both the growth rate stabilization and the reduction in phase velocity. It also exhibits quantitatively the coupling between type-I and type-II instabilities excited in the equatorial electrojet region and the energy cascading to the small structures as proposed by Sudan [1973]. The excitation of secondary type-I instabilities from type-II is verified and seen from the spectrum of the perturbed density at 105 km altitude. Finally, the nonlinear results show very good agreement with most of the radar observations and rocket measurements and the model proves its stability and conservation of energy.

As a future plan, we are going to employ advanced parallel computing techniques such as *Message Passing Interface (MPI)* with this 2-D fluid model to ensure the retrieval of all the E-region features with a large-scale simulation that covers electrojet layer in the equatorial and high-latitude regions. Also, we are going to include the ion thermal flux that causes stronger damping of the stable modes at 3 meter scales by extending our simulation into the third dimension along the geomagnetic field. The fluctuation of the geomagnetic field due to the discontinuities in the solar wind interplanetary magnetic field will be considered in future data-driven simulations based on the forecasting of the status of the ionosphere at low- and high-latitudes.

Further, the work we have done using the Kernel Density Estimation (KDE) functions will be extended in two ways. First we will include the calculation of the KDE functions for more solar wind parameters such as the proton-density and interplanetary magnetic field components in addition to the solar wind speed. The establishment of the KDE functions for these three parameters will allow us to use the Burton's empirical equation [Burton *et al.* 1975] to estimate the Dst magnetic index and compare it to the measurements at the ground stations. This will show the confidence level of using this method as a reliable tool for forecasting. Next we will include the solar wind measurements from more missions such as Clusters and Wind to be able to cover longer time period, which will result in establishing better KDE functions.

# Appendices

## .1 Appendix A: Vector Identities

- $\int \nabla \cdot \mathbf{A} dV = 0$
- $\int \phi [\phi, \chi] dV = 0$
- $(n \nabla \chi) \cdot \nabla \phi = \nabla \cdot [\phi (n \nabla \chi)] - \phi \nabla \cdot (n \nabla \chi)$
- $\int \partial_t |\nabla \phi|^2 dV = 2 \int \nabla \phi \cdot \partial_t \nabla \phi dV = 2 \int [\nabla \cdot (\phi \partial_t \nabla \phi) - (\phi \partial_t \nabla^2 \phi)] dV = -2 \int [(\phi \partial_t \nabla^2 \phi)] dV$   
where,  $\int [\nabla \cdot (\phi \partial_t \nabla \phi)] dV = 0$
- $n \partial_x n = \frac{1}{2} \partial_x n^2$
- $n \nabla^2 n = \frac{1}{2} \nabla^2 n^2 - \nabla n \cdot \nabla n$
- $n \nabla^4 n = \frac{1}{2} \nabla^4 n^2 - 2 \nabla n \cdot \nabla \nabla^2 n + (\nabla^2 n)^2 + \nabla^2 (\nabla n)^2$
- $n \nabla^2 (\nabla n \cdot \nabla n) = \nabla^2 [n (\nabla n \cdot \nabla n)] - \nabla^2 (\nabla n \cdot \nabla n) - 2 \nabla n \cdot \nabla (\nabla n \cdot \nabla n)$
- $n (\nabla n \cdot \nabla n) = \frac{1}{2} \nabla n^2 \cdot \nabla n$
- $n \partial_y \nabla^2 n = \frac{1}{2} \partial_y \nabla^2 n^2 - \partial_y (\nabla n \cdot \nabla n) - \nabla^2 n \partial_y n$
- $n [n, \phi] = \frac{1}{2} [n^2, \phi]$
- $\phi [n, \nabla^2 \phi] = [n, \phi \nabla^2 \phi] - \nabla^2 \phi [n, \phi] = \frac{1}{2} [n, \nabla^2 \phi] - [n, \nabla \phi \cdot \nabla \phi] - \nabla^2 \phi [n, \phi]$
- $n \partial_t \nabla^2 n = \frac{1}{2} \partial_t \nabla^2 n^2 - \nabla^2 n \partial_t n - 2 \nabla n \cdot \partial_t \nabla n = \frac{1}{2} \partial_t \nabla^2 n^2 - \nabla^2 n \partial_t n - \partial_t (\nabla n)^2$
- $\hat{\mathbf{e}}_z \times \nabla n \cdot \nabla \phi = [n, \phi]$
- $\hat{\mathbf{e}}_z \times \nabla \chi \cdot \nabla \nabla \chi = [\chi, \nabla \chi]$

## .2 Appendix B: Functional Derivative for the Electric Potential

$$\begin{aligned}
H(\phi) &= \int d^2x' \left( n_o \frac{m_e}{2B^2} |\nabla\phi|^2 \right) \\
H(\phi + \delta\phi) &= \frac{m_e n_o}{2B^2} \int d^2x' (|\nabla(\phi + \delta\phi)|^2) \\
H(\phi + \delta\phi) &= \frac{m_e n_o}{2B^2} \int d^2x' (|\nabla\phi + \nabla\delta\phi|^2) \\
H(\phi + \delta\phi) &= \frac{m_e n_o}{2B^2} \int d^2x' (|\nabla\phi|^2 + 2\nabla\phi \cdot \nabla\delta\phi + |\nabla\delta\phi|^2) \\
H(\phi + \delta\phi) &= \frac{m_e n_o}{2B^2} \int d^2x' (|\nabla\phi|^2) + \frac{m_e n_o}{B^2} \int d^2x' (\nabla\phi \cdot \nabla\delta\phi) + \frac{m_e n_o}{2B^2} \int d^2x' (|\nabla\delta\phi|^2) \\
H(\phi + \delta\phi) &= H(\phi) - \frac{m_e n_o}{B^2} \int d^2x' \phi \delta\nabla^2\phi
\end{aligned}$$

where, we can drop the second-order term in the right-hand side for its very small value.

$$\begin{aligned}
H(\phi + \delta\phi) - H(\phi) &= \int d^2x' \left( -\frac{m_e n_o}{B^2} \phi \right) \delta\nabla^2\phi \\
dH(\phi) &= \int d^2x' \left( -\frac{m_e n_o}{B^2} \phi \right) \delta\nabla^2\phi \\
\frac{\delta H}{\delta\nabla^2\phi} &= -\frac{m_e n_o}{B^2} \phi
\end{aligned} \tag{.1}$$

Functional Derivative for the Ion Velocity Potential

$$\begin{aligned}
H(\chi) &= \int d^2x' \left( n \frac{m_i}{2} |\nabla\chi|^2 \right) \\
H(\chi + \delta\chi) &= \frac{m_i}{2} \int d^2x' n (|\nabla(\chi + \delta\chi)|^2) \\
H(\chi + \delta\chi) &= \frac{m_i}{2} \int d^2x' n (|\nabla\chi + \nabla\delta\chi|^2) \\
H(\chi + \delta\chi) &= \frac{m_i}{2} \int d^2x' n (|\nabla\chi|^2 + 2\nabla\chi \cdot \nabla\delta\chi + |\nabla\delta\chi|^2) \\
H(\chi + \delta\chi) &= \frac{m_i}{2} \int d^2x' n (|\nabla\chi|^2) + m_i \int d^2x' n (\nabla\chi \cdot \nabla\delta\chi) + \frac{m_i}{2} \int d^2x' n (|\nabla\delta\chi|^2) \\
H(\chi + \delta\chi) &= H(\chi) - m_i n \int d^2x' \nabla \cdot (n \nabla\chi) \delta\chi
\end{aligned}$$

where, we can drop the second-order term in the right-hand side for its very small value.

$$\begin{aligned}
H(\chi + \delta\chi) - H(\chi) &= \int d^2x' -m_i \nabla \cdot (n \nabla \chi) \delta\chi \\
dH(\chi) &= \int d^2x' -m_i \nabla \cdot (n \nabla \chi) \delta\chi \\
\frac{\delta H}{\delta \chi} &= -m_i \nabla \cdot (n \nabla \chi) \tag{.2}
\end{aligned}$$

Functional Derivative for the Electron Density

$$\begin{aligned}
H(n) &= \int d^2x' \left( n \frac{m_i}{2} |\nabla \chi|^2 + \frac{m_i}{2} v_{t_i}^2 n^2 \right) \\
H(n + \delta n) &= \int d^2x' \left( \frac{m_i |\nabla \chi|^2}{2} (n + \delta n) + \frac{m_i}{2} v_{t_i}^2 (n + \delta n)^2 \right) \\
H(n + \delta n) &= \int d^2x' \left( \frac{m_i |\nabla \chi|^2}{2} (n + \delta n) + \frac{m_i}{2} v_{t_i}^2 (n^2 + 2n\delta n + \delta n^2) \right) \\
H(n + \delta n) &= \int d^2x' \left( n \frac{m_i}{2} |\nabla \chi|^2 + \frac{m_i}{2} v_{t_i}^2 n^2 \right) + \int d^2x' \left( \frac{m_i |\nabla \chi|^2}{2} + m_i v_{t_i}^2 n \right) \delta n \\
H(n + \delta n) &= H(n) + \int d^2x' \left( \frac{m_i |\nabla \chi|^2}{2} + m_i v_{t_i}^2 n \right) \delta n
\end{aligned}$$

where, we can drop the second-order term in the right-hand side for its very small value.

$$\begin{aligned}
H(n + \delta n) - H(n) &= \int d^2x' \left( \frac{m_i |\nabla \chi|^2}{2} + m_i v_{t_i}^2 n \right) \delta n \\
dH(n) &= \int d^2x' \left( \frac{m_i |\nabla \chi|^2}{2} + m_i v_{t_i}^2 n \right) \delta n \\
\frac{\delta H}{\delta n} &= \frac{m_i |\nabla \chi|^2}{2} + m_i v_{t_i}^2 n \tag{.3}
\end{aligned}$$

### .3 Appendix C: Verifying Jacobi Identity For Hamiltonian Bracket

The Jacobi identity says:

$$\{\{A, B\}, C\} + \{\{C, A\}, B\} + \{\{B, C\}, A\} = 0 \quad (.4)$$

where, A, B, and C are random functional variables.

**The first bracket:**

$$\begin{aligned} \{\{A, B\}, C\} = & -\frac{1}{m_i} \int d^2x' (\{A, B\}_n C_\chi - C_n \{A, B\}_\chi) \\ & - \frac{B\Omega_{ci}}{m_e n_o} \int d^2x' (\{A, B\}_\chi C_\zeta - C_\chi \{A, B\}_\zeta) \\ & + \frac{B^2\Omega_{ce}}{m_e n_o} \int d^2x' n [\{A, B\}_\zeta, C_\zeta] \\ & + \frac{B}{m_e n_o} \int d^2x' \zeta [\{A, B\}_\zeta, C_\zeta] \end{aligned}$$

$$\begin{aligned} \{A, B\}_n = & \frac{\delta}{\delta n} \left[ -\frac{1}{m_i} \int d^2x' (A_n B_\chi - B_n A_\chi) - \frac{B\Omega_{ci}}{m_e n_o} \int d^2x' (A_\chi B_\zeta - B_\chi A_\zeta) \right] + \\ & \frac{\delta}{\delta n} \left[ \frac{B}{m_e n_o} \int d^2x' \zeta [A_\zeta, B_\zeta] + \frac{B^2\Omega_{ce}}{m_e n_o^2} \int d^2x' n [A_\zeta, B_\zeta] \right] \end{aligned}$$

$$\{A, B\}_n = \frac{B^2\Omega_{ce}}{m_e n_o} [A_\zeta, B_\zeta]$$

$$\begin{aligned} \{A, B\}_\chi = & \frac{\delta}{\delta \chi} \left[ -\frac{1}{m_i} \int d^2x' (A_n B_\chi - B_n A_\chi) - \frac{B\Omega_{ci}}{m_e n_o} \int d^2x' (A_\chi B_\zeta - B_\chi A_\zeta) \right] + \\ & \frac{\delta}{\delta \chi} \left[ \frac{B}{m_e n_o} \int d^2x' \zeta [A_\zeta, B_\zeta] + \frac{B^2\Omega_{ce}}{m_e n_o^2} \int d^2x' n [A_\zeta, B_\zeta] \right] \end{aligned}$$

$$\{A, B\}_\chi = 0$$

$$\begin{aligned} \{A, B\}_\zeta = & \frac{\delta}{\delta \zeta} \left[ -\frac{1}{m_i} \int d^2x' (A_n B_\chi - B_n A_\chi) - \frac{B\Omega_{ci}}{m_e n_o} \int d^2x' (A_\chi B_\zeta - B_\chi A_\zeta) \right] + \\ & \frac{\delta}{\delta \zeta} \left[ \frac{B}{m_e n_o} \int d^2x' \zeta [A_\zeta, B_\zeta] + \frac{B^2\Omega_{ce}}{m_e n_o^2} \int d^2x' n [A_\zeta, B_\zeta] \right] \end{aligned}$$

$$\{A, B\}_\zeta = \frac{B}{m_e n_o} [A_\zeta, B_\zeta]$$

$$\begin{aligned}
\{\{A, B\}, C\} &= -\frac{B^2\Omega_{ci}}{m_e^2n_o^2} \int d^2x' [A_\zeta, B_\zeta] C_\chi + \frac{B^2\Omega_{ci}}{m_e^2n_o^2} \int d^2x' [A_\zeta, B_\zeta] C_\chi \\
&\quad + \frac{B^3\Omega_{ce}}{m_e^2n_o^2} \int d^2x'n [[A_\zeta, B_\zeta], C_\zeta] + \frac{B^2}{m_e^2n_o^2} \int d^2x'\zeta [[A_\zeta, B_\zeta], C_\zeta] \\
\{\{A, B\}, C\} &= \frac{B^3\Omega_{ce}}{m_e^2n_o^2} \int d^2x'n [[A_\zeta, B_\zeta], C_\zeta] + \frac{B^2}{m_e^2n_o^2} \int d^2x'\zeta [[A_\zeta, B_\zeta], C_\zeta] \quad (.5)
\end{aligned}$$

**The second bracket:**

$$\begin{aligned}
\{\{C, A\}, B\} &= -\frac{1}{m_i} \int d^2x' (\{C, A\}_n B_\chi - B_n \{C, A\}_\chi) \\
&\quad - \frac{B\Omega_{ci}}{m_e n_o} \int d^2x' (\{C, A\}_\chi B_\zeta - B_\chi \{C, A\}_\zeta) \\
&\quad + \frac{B^2\Omega_{ce}}{m_e n_o} \int d^2x'n [\{C, A\}_\zeta, B_\zeta] + \frac{B}{m_e n_o} \int d^2x'\zeta [\{C, A\}_\zeta, B_\zeta] \\
\{C, A\}_n &= \frac{\delta}{\delta n} \left[ -\frac{1}{m_i} \int d^2x' (C_n A_\chi - C_n A_\chi) - \frac{B\Omega_{ci}}{m_e n_o} \int d^2x' (C_\chi A_\zeta - A_\chi C_\zeta) \right] + \\
&\quad \frac{\delta}{\delta n} \left[ \frac{B}{m_e n_o} \int d^2x'\zeta [C_\zeta, A_\zeta] + \frac{B^2\Omega_{ce}}{m_e n_o^2} \int d^2x'n [C_\zeta, A_\zeta] \right] \\
\{C, A\}_n &= \frac{B^2\Omega_{ce}}{m_e n_o} [C_\zeta, A_\zeta] \\
\{C, A\}_\chi &= \frac{\delta}{\delta \chi} \left[ -\frac{1}{m_i} \int d^2x' (C_n A_\chi - A_n C_\chi) - \frac{B\Omega_{ci}}{m_e n_o} \int d^2x' (C_\chi A_\zeta - A_\chi C_\zeta) \right] + \\
&\quad \frac{\delta}{\delta \chi} \left[ \frac{B}{m_e n_o} \int d^2x'\zeta [C_\zeta, A_\zeta] + \frac{B^2\Omega_{ce}}{m_e n_o^2} \int d^2x'n [C_\zeta, A_\zeta] \right] \\
\{C, A\}_\chi &= 0 \\
\{C, A\}_\zeta &= \frac{\delta}{\delta \zeta} \left[ -\frac{1}{m_i} \int d^2x' (C_n A_\chi - A_n C_\chi) - \frac{B\Omega_{ci}}{m_e n_o} \int d^2x' (C_\chi A_\zeta - A_\chi C_\zeta) \right] + \\
&\quad \frac{\delta}{\delta \zeta} \left[ \frac{B}{m_e n_o} \int d^2x'\zeta [C_\zeta, A_\zeta] + \frac{B^2\Omega_{ce}}{m_e n_o^2} \int d^2x'n [C_\zeta, A_\zeta] \right] \\
\{C, A\}_\zeta &= \frac{B}{m_e n_o} [C_\zeta, A_\zeta]
\end{aligned}$$

$$\begin{aligned}
\{\{C, A\}, B\} &= -\frac{B^2\Omega_{ci}}{m_e^2n_o^2} \int d^2x' [C_\zeta, A_\zeta] B_\chi + \frac{B^2\Omega_{ci}}{m_e^2n_o^2} \int d^2x' [C_\zeta, A_\zeta] B_\chi \\
&\quad + \frac{B^3\Omega_{ce}}{m_e^2n_o^2} \int d^2x' n [[C_\zeta, A_\zeta], B_\zeta] + \frac{B^2}{m_e^2n_o^2} \int d^2x' \zeta [[C_\zeta, A_\zeta], B_\zeta] \\
\{\{C, A\}, B\} &= \frac{B^3\Omega_{ce}}{m_e^2n_o^2} \int d^2x' n [[C_\zeta, A_\zeta], B_\zeta] + \frac{B^2}{m_e^2n_o^2} \int d^2x' \zeta [[C_\zeta, A_\zeta], B_\zeta] \quad (.6)
\end{aligned}$$

**The third bracket:**

$$\begin{aligned}
\{\{B, C\}, A\} &= -\frac{1}{m_i} \int d^2x' (\{B, C\}_n A_\chi - A_n \{B, C\}_\chi) \\
&\quad - \frac{B\Omega_{ci}}{m_e n_o} \int d^2x' (\{B, C\}_\chi A_\zeta - A_\chi \{B, C\}_\zeta) \\
&\quad + \frac{B^2\Omega_{ce}}{m_e n_o} \int d^2x' n [\{B, C\}_\zeta, A_\zeta] + \frac{B}{m_e n_o} \int d^2x' \zeta [\{B, C\}_\zeta, A_\zeta] \\
\{B, C\}_n &= \frac{\delta}{\delta n} \left[ -\frac{1}{m_i} \int d^2x' (B_n C_\chi - C_n B_\chi) - \frac{B\Omega_{ci}}{m_e n_o} \int d^2x' (B_\chi C_\zeta - C_\chi B_\zeta) \right] + \\
&\quad \frac{\delta}{\delta n} \left[ \frac{B}{m_e n_o} \int d^2x' \zeta [B_\zeta, C_\zeta] + \frac{B^2\Omega_{ce}}{m_e n_o^2} \int d^2x' n [B_\zeta, C_\zeta] \right] \\
\{B, C\}_n &= \frac{B^2\Omega_{ce}}{m_e n_o} [B_\zeta, C_\zeta] \\
\{B, C\}_\chi &= \frac{\delta}{\delta \chi} \left[ -\frac{1}{m_i} \int d^2x' (B_n C_\chi - C_n B_\chi) - \frac{B\Omega_{ci}}{m_e n_o} \int d^2x' (B_\chi C_\zeta - C_\chi B_\zeta) \right] + \\
&\quad \frac{\delta}{\delta \chi} \left[ \frac{B}{m_e n_o} \int d^2x' \zeta [B_\zeta, C_\zeta] + \frac{B^2\Omega_{ce}}{m_e n_o^2} \int d^2x' n [B_\zeta, C_\zeta] \right] \\
\{B, C\}_\chi &= 0 \\
\{B, C\}_\zeta &= \frac{\delta}{\delta \zeta} \left[ -\frac{1}{m_i} \int d^2x' (B_n C_\chi - C_n B_\chi) - \frac{B\Omega_{ci}}{m_e n_o} \int d^2x' (B_\chi C_\zeta - C_\chi B_\zeta) \right] + \\
&\quad \frac{\delta}{\delta \zeta} \left[ \frac{B}{m_e n_o} \int d^2x' \zeta [B_\zeta, C_\zeta] + \frac{B^2\Omega_{ce}}{m_e n_o^2} \int d^2x' n [B_\zeta, C_\zeta] \right] \\
\{B, C\}_\zeta &= \frac{B}{m_e n_o} [B_\zeta, C_\zeta]
\end{aligned}$$

$$\begin{aligned}
\{\{B, C\}, A\} &= -\frac{B^2\Omega_{ci}}{m_e^2n_o^2} \int d^2x' [B_\zeta, C_\zeta] A_\chi + \frac{B^2\Omega_{ci}}{m_e^2n_o^2} \int d^2x' [B_\zeta, C_\zeta] A_\chi \\
&\quad + \frac{B^3\Omega_{ce}}{m_e^2n_o^2} \int d^2x' n [[B_\zeta, C_\zeta], A_\zeta] + \frac{B^2}{m_e^2n_o^2} \int d^2x' \zeta [[B_\zeta, C_\zeta], A_\zeta] \\
\{\{B, C\}, A\} &= \frac{B^3\Omega_{ce}}{m_e^2n_o^2} \int d^2x' n [[B_\zeta, C_\zeta], A_\zeta] + \frac{B^2}{m_e^2n_o^2} \int d^2x' \zeta [[B_\zeta, C_\zeta], A_\zeta] \quad (.7)
\end{aligned}$$

Add (.5-.7), we get:

$$\begin{aligned}
&\{\{A, B\}, C\} + \{\{C, A\}, B\} + \{\{B, C\}, A\} = \\
&\frac{B^3\Omega_{ce}}{m_e^2n_o^2} \int d^2x' n ([[A_\zeta, B_\zeta], C_\zeta] + [[C_\zeta, A_\zeta], B_\zeta] + [[B_\zeta, C_\zeta], A_\zeta]) + \\
&\frac{B^2}{m_e^2n_o^2} \int d^2x' \zeta ([[A_\zeta, B_\zeta], C_\zeta] + [[C_\zeta, A_\zeta], B_\zeta] + [[B_\zeta, C_\zeta], A_\zeta]) \quad (.8)
\end{aligned}$$

Therefore,

$$\{\{A, B\}, C\} + \{\{C, A\}, B\} + \{\{B, C\}, A\} = 0 \quad (.9)$$

where, ([[A<sub>ζ</sub>, B<sub>ζ</sub>], C<sub>ζ</sub>] + [[C<sub>ζ</sub>, A<sub>ζ</sub>], B<sub>ζ</sub>] + [[B<sub>ζ</sub>, C<sub>ζ</sub>], A<sub>ζ</sub>]) = 0

## Bibliography

- [1] MH Acuña, KW Ogilvie, DN Baker, SA Curtis, DH Fairfield, and WH Mish. The global geospace science program and its investigations. *Space Science Reviews*, 71(1-4):5–21, 1995. 110
- [2] Daniel N Baker. The occurrence of operational anomalies in spacecraft and their relationship to space weather. *Plasma Science, IEEE Transactions on*, 28(6):2007–2016, 2000. 99
- [3] C Balch, B Murtagh, D Zezula, L Combs, G Nelson, K Tegnell, M Crown, and B McGehan. Service assessment: Intense space weather storms october 19–november 07, 2003. *NOAA Silver Spring, Md*, 2004. 106
- [4] BB Balsley and DT Farley. Radar studies of the equatorial electrojet at three frequencies. *Journal of Geophysical Research*, 76(34):8341–8351, 1971. xiii, 14, 15, 16, 17, 63
- [5] BB Balsley and DT Farley. Radar observations of two-dimensional turbulence in the equatorial electrojet. *Journal of Geophysical Research*, 78(31):7471–7479, 1973. 14
- [6] Ben B Balsley. Some characteristics of non-two-stream irregularities in the equatorial electrojet. In *Low-Frequency Waves and Irregularities in the Ionosphere*, pages 152–172. Springer, 1969. xii, 14, 15, 25
- [7] Peter M Banks and Gaston Kockarts. *Aeronomy*. Elsevier, 2013. 2
- [8] EE Benevolenskaya and IG Kostuchenko. The total solar irradiance, uv emission and magnetic flux during the last solar cycle minimum. *Journal of Astrophysics*, 2013, 2013. 54, 63, 106
- [9] KL Bowles, BB Balsley, and Robert Cohen. Field-aligned e-region irregularities identified with acoustic plasma waves. *Journal of Geophysical Research*, 68(9):2485–2501, 1963. 13, 15, 27

- [10] O Buneman. Excitation of field aligned sound waves by electron streams. *Physical Review Letters*, 10(7):285, 1963. 27
- [11] RK Burton, RL McPherron, and CT Russell. An empirical relationship between interplanetary conditions and dst. *Journal of geophysical research*, 80(31):4204–4214, 1975.
- [12] Richard C Carrington. Description of a singular appearance seen in the sun on september 1, 1859. *Monthly Notices of the Royal Astronomical Society*, 20:13–15, 1859. 99
- [13] S Chapman. The solar and lunar diurnal variations of terrestrial magnetism. *Philosophical Transactions of the Royal Society of London. Series A, Containing Papers of a Mathematical or Physical Character*, pages 1–118, 1919. 9
- [14] S Chapman and RS Lindzen. Atmospheric tides, 200 pp. *D. Reidel, Dordrecht, Netherlands*, 1970. 10
- [15] Sydney Chapman. The equatorial electrojet as detected from the abnormal electric current distribution above huancayo, peru, and elsewhere. *Archiv Fuer Meteorologie, Geophysik und Bioklimatologie, Serie A*, 4(1):368–390, 1951. 9
- [16] Robert Cohen and Kenneth L Bowles. Secondary irregularities in the equatorial electrojet. *Journal of Geophysical Research*, 72(3):885–894, 1967. xii, 13, 14
- [17] Anthea Coster, John Foster, and Philip Erickson. Innovation-monitoring the ionosphere with gps-space weather-large gradients in the ionospheric and plasmapheric total electron content affects gps observations and measurements. gps data. *GPS World*, 14(5):42–49, 2003. 1, 99
- [18] James W Dungey. Interplanetary magnetic field and the auroral zones. *Physical Review Letters*, 6(2):47, 1961. 101
- [19] J Egedal. Daily variation of the horizontal magnetic force at the magnetic equator. *Nature*, 161(4090):443, 1948. 9
- [20] DT Farley. A plasma instability resulting in field-aligned irregularities in the ionosphere. *Journal of Geophysical Research*, 68(22):6083–6097, 1963. 27

- [21] DT Farley. The equatorial e-region and its plasma instabilities: a tutorial. *Ann. Geophys.*, 27(4):1509–1520, 2009. 10, 11, 19
- [22] DT Farley and BB Balsley. Instabilities in the equatorial electrojet. *Journal of Geophysical Research*, 78(1):227–239, 1973. 14, 15, 25, 44, 68, 124
- [23] DT Farley, Bela G Fejer, and BB Balsley. Radar observations of two-dimensional turbulence in the equatorial electrojet, 3. nighttime observations of type 1 waves. *Journal of Geophysical Research: Space Physics (1978–2012)*, 83(A12):5625–5632, 1978. 14, 68
- [24] CJ Farrugia, FT Gratton, VK Jordanova, H Matsui, S Mühlbachler, RB Torbert, KW Ogilvie, and HJ Singer. Tenuous solar winds: Insights on solar wind–magnetosphere interactions. *Journal of Atmospheric and Solar-Terrestrial Physics*, 70(2):371–376, 2008. 101
- [25] Bela G Fejer, DT Farley, BB Balsley, and RF Woodman. Vertical structure of the vhf backscattering region in the equatorial electrojet and the gradient drift instability. *Journal of Geophysical Research*, 80(10):1313–1324, 1975. xiii, 14, 15, 16, 43, 44
- [26] Bela G Fejer, DT Farley, BB Balsley, and RF Woodman. Radar observations of two dimensional turbulence in the equatorial electrojet, 2. *Journal of Geophysical Research*, 81(1):130–134, 1976. 14, 68
- [27] Bela G Fejer and MC Kelley. Ionospheric irregularities. *Reviews of Geophysics*, 18(2):401–454, 1980. 2
- [28] Richard Fitzpatrick. Introduction to plasma physics. *The University of Texas at Austin: sn*, page 242, 2008. 36
- [29] JM Forbes and RS Lindzen. Atmospheric solar tides and their electrodynamic effects—ii. the equatorial electrojet. *Journal of Atmospheric and Terrestrial Physics*, 38:911–920, 1976. xii, 10
- [30] HU Frey, TD Phan, SA Fuselier, and SB Mende. Continuous magnetic reconnection at earth’s magnetopause. *Nature*, 426(6966):533–537, 2003. 101

- [31] SA Fuselier, KJ Trattner, and SM Petrinec. Antiparallel and component reconnection at the dayside magnetopause. *Journal of Geophysical Research: Space Physics (1978–2012)*, 116(A10), 2011. 101
- [32] George Graham. An account of observations made of the variation of the horizontal needle at london, in the latter part of the year 1722, and beginning of 1723. by mr. george graham, watchmaker, frs. *Philosophical Transactions*, 33(381-391):96–107, 1724. 9
- [33] DK Haggerty, EC Roelof, CW Smith, NF Ness, RL Tokar, and RM Skoug. Interplanetary magnetic field connection to the l1 lagrangian orbit during upstream energetic ion events. *Journal of Geophysical Research: Space Physics (1978–2012)*, 105(A11):25123–25131, 2000. xix, 111
- [34] C Hanuise and M Crochet. 5-to 50-m wavelength plasma instabilities in the equatorial electrojet 3. counter-electrojet conditions. *Journal of Geophysical Research: Space Physics (1978–2012)*, 86(A9):7761–7766, 1981. 15, 25
- [35] E Hassan, W Horton, SK Litt, A Smolyakov, and S Benkadda. Transitions in ionospheric turbulence from farley-buneman to drift gradient regimes. In *APS Meeting Abstracts*, volume 1, page 9086P, 2011. xiv, 53
- [36] Ehab Hassan, W Horton, AI Smolyakov, DR Hatch, and SK Litt. Multiscale equatorial electrojet turbulence: Baseline 2-d model. *Journal of Geophysical Research: Space Physics*, 120(2):1460–1477, 2015. xiv, xv, xvi, 27, 42, 43, 45, 56, 58, 59, 60, 61, 62, 65, 67, 69
- [37] Ehab Hassan, Wendell Horton, Andrei Smolyakov, and David Hatch. Equatorial electrojet instabilities-new fluid model approach. In *APS Meeting Abstracts*, volume 1, page 5012, 2014. xvi, 64
- [38] Oliver Heaviside. On the theory of the electric telegraph. *Encyclopedia Britannica*, 33:213, 1902. 4
- [39] FC Hoh. Instability of penning-type discharges. *Physics of Fluids (1958-1988)*, 6(8):1184–1191, 1963. 15, 27

- [40] TS Horbury, D Burgess, M Fränz, and CJ Owen. Prediction of earth arrival times of interplanetary southward magnetic field turnings. *Journal of Geophysical Research: Space Physics (1978–2012)*, 106(A12):30001–30009, 2001. 107
- [41] Todd E Humphreys, Mark L Psiaki, Brent M Ledvina, Alessandro P Cerruti, and Paul M Kintner Jr. Data-driven testbed for evaluating gps carrier tracking loops in ionospheric scintillation. *Aerospace and Electronic Systems, IEEE Transactions on*, 46(4):1609–1623, 2010. 7
- [42] AJ Hundhausen. The solar wind. *Introduction to space physics*, pages 91–128, 1995. 108
- [43] DL Hysell, J Drexler, EB Shume, JL Chau, DE Scipion, M Vlasov, R Cuevas, and C Heinselman. Combined radar observations of equatorial electrojet irregularities at jicamarca. In *Annales Geophysicae*, volume 25, pages 457–473, 2007. xiii, 18, 63, 68
- [44] G Kh Kamenetskaya. Quasi-linear theory of formation of inhomogeneities in the equatorial electrojet. Technical report, Gorky State Univ., USSR, 1971. 25
- [45] Predhiman K Kaw. Wave propagation effects on observation of irregularities in the equatorial electrojet. *Journal of Geophysical Research*, 77(7):1323–1326, 1972. 26
- [46] Michael C Kelley. *The Earth’s Ionosphere: Plasma Physics & Electrodynamics*, volume 96. Academic press, 2009. xii, 5, 7, 10, 11
- [47] Michael C Kelley, Jonathan J Makela, Jorge L Chau, and Michael J Nicolls. Penetration of the solar wind electric field into the magnetosphere/ionosphere system. *Geophysical Research Letters*, 30(4), 2003. xviii, 102, 125
- [48] Michael C Kelley, Jonathan J Makela, Jorge L Chau, and Michael J Nicolls. Penetration of the solar wind electric field into the magnetosphere/ionosphere system. *Geophysical Research Letters*, 30(4), 2003.
- [49] Arthur E Kennelly. On the elevation of the electrically-conducting strata of the earth’s atmosphere. *Electrical world and engineer*, 39(11):473, 1902. 4

- [50] Paul M Kintner and Brent M Ledvina. The ionosphere, radio navigation, and global navigation satellite systems. *Advances in Space Research*, 35(5):788–811, 2005. 1, 7
- [51] Margaret G Kivelson and Christopher T Russell. *Introduction to space physics*. Cambridge university press, 1995. 3, 100
- [52] FB Knox. A contribution to the theory of the production of field-aligned ionisation irregularities in the equatorial electrojet. *Journal of Atmospheric and Terrestrial Physics*, 26(2):239–249, 1964. 15
- [53] Erhan Kudeki, Donald T Farley, and Bela G Fejer. Theory of spectral asymmetries and nonlinear currents in the equatorial electrojet. *Journal of Geophysical Research: Space Physics (1978–2012)*, 90(A1):429–436, 1985. 68
- [54] Erhan Kudeki, Bela G Fejer, Donald T Farley, and Christian Hanuise. The condor equatorial electrojet campaign: Radar results. *Journal of Geophysical Research: Space Physics (1978–2012)*, 92(A12):13561–13577, 1987. 15, 20, 63, 68, 82, 90, 122
- [55] SK Litt, AI Smolyakov, Ehab Hassan, and Wendell Horton. Ion thermal and dispersion effects in farley-buneman instabilities. *Physics of Plasmas (1994-present)*, 22(8):082112, 2015. xiv, 46, 49
- [56] Jeffrey J Love. Magnetic monitoring of earth and space. *Physics Today*, 61(2):31, 2008. 106
- [57] S Machida and CK Goertz. Computer simulation of the farley-buneman instability and anomalous electron heating in the auroral ionosphere. *Journal of Geophysical Research: Space Physics (1978–2012)*, 93(A9):9993–10000, 1988. 28
- [58] K Maeda, T Tsuda, and H Maeda. Theoretical interpretation of the equatorial sporadic e layers. *Physical Review Letters*, 11(9):406, 1963. 15
- [59] B Mailyan, C Munteanu, and S Haaland. What is the best method to calculate the solar wind propagation delay? In *Annales Geophysicae*, volume 26, pages 2383–2394. Copernicus GmbH, 2008. xix, 109, 112, 119

- [60] Motonori Matuyama. On the direction of magnetisation of basalt in japan, tyosen and manchuria. *Proceedings of the Imperial Academy*, 5(5):203–205, 1929. 8
- [61] Robert L McPherron, James M Weygand, and Tung-Shin Hsu. Response of the earth’s magnetosphere to changes in the solar wind. *Journal of Atmospheric and Solar-Terrestrial Physics*, 70(2):303–315, 2008. 101
- [62] SE Milan, G Provan, and Benoît Hubert. Magnetic flux transport in the dungey cycle: A survey of dayside and nightside reconnection rates. *Journal of Geophysical Research: Space Physics (1978–2012)*, 112(A1), 2007. 101
- [63] Pratap Misra and Per Enge. *Global Positioning System: Signals, Measurements and Performance Second Edition*. Lincoln, MA: Ganga-Jamuna Press, 2006. 7
- [64] Philip J Morrison. Hamiltonian description of the ideal fluid. *Reviews of modern physics*, 70(2):467, 1998. 96
- [65] Alice L Newman and Edward Ott. Nonlinear simulations of type 1 irregularities in the equatorial electrojet. *Journal of Geophysical Research: Space Physics (1978–2012)*, 86(A8):6879–6891, 1981. 28
- [66] Keith W Ogilvie, A Durney, and TT von Rosenvinge. Description of experimental investigations and instruments for the isee spacecraft. *IEEE Transactions on Geoscience Electronics*, 16:151–153, 1978.
- [67] Shinichi Ohtani, Teiji Uozumi, Hideaki Kawano, Akimasa Yoshikawa, Hisashi Utada, Tsutomu Nagatsuma, and Kiyohumi Yumoto. The response of the day-side equatorial electrojet to step-like changes of imf bz. *Journal of Geophysical Research: Space Physics*, 118(6):3637–3646, 2013. xviii, 101, 102, 125
- [68] Meers Oppenheim and Niels Otani. Spectral characteristics of the farley-buneman instability: Simulations versus observations. *Journal of Geophysical Research: Space Physics (1978–2012)*, 101(A11):24573–24582, 1996. 28, 62
- [69] Meers Oppenheim, Niels Otani, and Corrado Ronchi. Saturation of the farley-buneman instability via nonlinear electron  $e \times b$  drifts. *Journal of Geophysical Research: Space Physics (1978–2012)*, 101(A8):17273–17286, 1996. 28, 44, 122

- [70] MM Oppenheim, Y Dimant, and LP Dyrud. Large-scale simulations of 2-d fully kinetic farley-buneman turbulence. In *Annales geophysicae: atmospheres, hydrospheres and space sciences*, volume 26, page 543, 2008. 29
- [71] MM Oppenheim and Ya S Dimant. Kinetic simulations of 3-d farley-buneman turbulence and anomalous electron heating. *Journal of Geophysical Research: Space Physics*, 118(3):1306–1318, 2013. 29
- [72] Niels F Otani and Meers Oppenheim. A saturation mechanism for the farley-buneman instability. *Geophysical research letters*, 25(11):1833–1836, 1998. 29
- [73] Niels F Otani and Meers Oppenheim. Saturation of the farley-buneman instability via three-mode coupling. *Journal of Geophysical Research: Space Physics (1978–2012)*, 111(A3), 2006. 29
- [74] Matt J Owens and Robert J Forsyth. The heliospheric magnetic field. *Living Reviews in Solar Physics*, 10(5), 2013. 4, 100, 108
- [75] Eugene N Parker. Dynamics of the interplanetary gas and magnetic fields. *The Astrophysical Journal*, 128:664, 1958. 106
- [76] AK Patra, D Tiwari, CV Devasia, TK Pant, and R Sridharan. East-west asymmetries of the equatorial electrojet 8.3 m type-2 echoes observed over trivandrum and a possible explanation. *Journal of Geophysical Research: Space Physics (1978–2012)*, 110(A11), 2005. 67
- [77] KI Paularena and JH King. Nasas imp 8 spacecraft. In *Interball in the ISTP Program*, pages 145–154. Springer, 1999. 110
- [78] RF Pfaff, MC Kelley, Bela G Fejer, NC Maynard, and KD Baker. In-situ measurements of wave electric fields in the equatorial electrojet. *Geophysical Research Letters*, page 688, 1982. 19
- [79] RF Pfaff, MC Kelley, BG Fejer, NC Maynard, LH Brace, BG Ledley, LG Smith, and RF Woodman. Comparative in situ studies of the unstable day-time equatorial e-region. *Journal of atmospheric and terrestrial physics*, 47(8):791–811, 1985. 19

- [80] RF Pfaff, MC Kelley, E Kudeki, Bela G Fejer, and KD Baker. Electric field and plasma density measurements in the strongly driven daytime equatorial electrojet: 1. the unstable layer and gradient drift waves. *Journal of Geophysical Research: Space Physics (1978–2012)*, 92(A12):13578–13596, 1987. xiii, 20, 21, 46, 63, 123
- [81] RF Pfaff, MC Kelley, E Kudeki, Bela G Fejer, and KD Baker. Electric field and plasmadensity measurements in the strongly-driven daytime equatorial electrojet: 2. two-streamwaves. *Journal of Geophysical Research*, 92(A12):13597–13612, 1987. xiii, 20, 22, 23, 24, 63, 82, 90, 123
- [82] RF Pfaff, J Sahr, JF Providakes, WE Swartz, DT Farley, PM Klntner, I HaÈggstroÈm, Ake Hedberg, H Opgenoorth, G Holmgren, et al. The e-region rocket/radar instability study (errris): Scientific objectives and campaign overview. *Journal of atmospheric and terrestrial physics*, 54(6):779–808, 1992. 19
- [83] Robert F Pfaff, Mario H Acuña, Paul A Marionni, and Nalin B Trivedi. Dc polarization electric field, current density, and plasma density measurements in the daytime equatorial electrojet. *Geophysical Research Letters*, 24(13):1667–1670, 1997. xiii, 24, 25, 63
- [84] Satya Prakash, BH Subbaraya, and SP Gupta. Rocket measurements of ionization irregularities in the equatorial ionosphere at thumba and identification of plasma instabilities. *Indian J. Radio Space Phys*, 1:72–80, 1972. xiii, 19, 20
- [85] TI Pulkkinen, M Palmroth, EI Tanskanen, N Yu Ganushkina, MA Shukhtina, and NP Dmitrieva. Solar windmagnetosphere coupling: a review of recent results. *Journal of Atmospheric and Solar-Terrestrial Physics*, 69(3):256–264, 2007. 101
- [86] George C Reid. The formation of small-scale irregularities in the ionosphere. *Journal of Geophysical Research*, 73(5):1627–1640, 1968. 15
- [87] IG Richardson, EW Cliver, and HV Cane. Sources of geomagnetic activity over the solar cycle: Relative importance of coronal mass ejections, high-speed streams, and slow solar wind. *JOURNAL OF GEOPHYSICAL RESEARCH-ALL SERIES-*, 105(A8):18–203, 2000. 103

- [88] IG Richardson, EW Cliver, and HV Cane. Sources of geomagnetic storms for solar minimum and maximum conditions during 1972–2000. *Geophys. Res. Lett.*, 28(13):2569–2572, 2001. 103
- [89] AJ Ridley. Estimations of the uncertainty in timing the relationship between magnetospheric and solar wind processes. *Journal of Atmospheric and Solar-Terrestrial Physics*, 62(9):757–771, 2000. 107
- [90] André Rogister. Nonlinear theory of cross-field instability with application to the equatorial electrojet. *Journal of Geophysical Research*, 77(16):2975–2981, 1972. 25, 28
- [91] André Rogister and Nicola D’Angelo. On the origin of small-scale type ii irregularities in the equatorial electrojet. *Journal of Geophysical Research*, 77(31):6298–6299, 1972. 15
- [92] C Ronchi, PL Similon, and RN Sudan. A nonlocal linear theory of the gradient drift instability in the equatorial electrojet. *Journal of Geophysical Research: Space Physics (1978–2012)*, 94(A2):1317–1326, 1989. 40
- [93] C Ronchi, RN Sudan, and PL Similon. Effect of short-scale turbulence on kilometer wavelength irregularities in the equatorial electrojet. *Journal of Geophysical Research: Space Physics (1978–2012)*, 95(A1):189–200, 1990. 28
- [94] Corrado Ronchi, RN Sudan, and Donald T Farley. Numerical simulations of large-scale plasma turbulence in the daytime equatorial electrojet. *Journal of Geophysical Research: Space Physics (1978–2012)*, 96(A12):21263–21279, 1991. 28
- [95] CT Russell. Solar wind and interplanetary magnetic field: A tutorial. *Space Weather*, pages 73–89, 2001. 4, 103
- [96] CT Russell, JG Luhmann, and LK Jian. How unprecedented a solar minimum? *Reviews of Geophysics*, 48(2), 2010. 106
- [97] Rick Salmon. *Lectures on geophysical fluid dynamics*. Oxford University Press, 1998. 96

- [98] Tetsuya Sato. Stabilization of the two-stream instability in the equatorial electrojet. *Physical Review Letters*, 28(12):732, 1972. 26
- [99] Tetsuya Sato and Takao Tsuda. Computer study of nonlinear cross-field instability. *Physics of Fluids (1958-1988)*, 10(6):1262–1268, 1967. 28
- [100] Michael J Schmidt and S Peter Gary. Density gradients and the farley-buneman instability. *Journal of Geophysical Research*, 78(34):8261–8265, 1973. 34, 44, 122
- [101] Robert Schunk and Andrew Nagy. *Ionospheres: physics, plasma physics, and chemistry*. Cambridge university press, 2009. 7
- [102] Arthur Schuster. The diurnal variation of terrestrial magnetism. *Philosophical Transactions of the Royal Society of London. A*, 180:467–518, 1889. 4, 9
- [103] Arthur Schuster. The diurnal variation of terrestrial magnetism. *Philosophical Transactions of the Royal Society of London. A*, 208:163–204, 1908. 4, 9
- [104] R Schwenn. Solar wind sources and their variations over the solar cycle. In *Solar Dynamics and Its Effects on the Heliosphere and Earth*, pages 51–76. Springer, 2007. 100
- [105] Rainer Schwenn and P Murdin. Solar wind: Global properties. *Encyclopedia of Astronomy and Astrophysics (ed. P. Murdin)*, Institute of Physics and Macmillan Publishing, Bristol, pages 1–9, 2001. xx, 104
- [106] David J Sheskin. *Handbook of parametric and nonparametric statistical procedures*. crc Press, 2003. 114
- [107] Albert Simon. Instability of a partially ionized plasma in crossed electric and magnetic fields. *Physics of Fluids (1958-1988)*, 6(3):382–388, 1963. 15, 27
- [108] G Skadron and Jerome Weinstock. Nonlinear stabilization of a two-stream plasma instability in the ionosphere. *Journal of Geophysical Research*, 74(21):5113–5126, 1969. 26
- [109] B. Stewart. Hypothetical views regarding the connection between the state of the sun and terrestrial magnetism. *Encyclopedia Britannica*, 16:181–184, 1882. 4, 9

- [110] EC Stone, AM Frandsen, RA Mewaldt, ER Christian, D Margolies, JF Ormes, and F Snow. The advanced composition explorer. In *The Advanced Composition Explorer Mission*, pages 1–22. Springer, 1998. 110
- [111] RN Sudan. Nonlinear theory of type i irregularities in the equatorial electrojet. *Geophysical research letters*, 10(10):983–986, 1983. 15, 25, 26
- [112] RN Sudan. Unified theory of type i and type ii irregularities in the equatorial electrojet. *Journal of Geophysical Research: Space Physics (1978–2012)*, 88(A6):4853–4860, 1983. 26
- [113] RN Sudan, J Akinrimisi, and DT Farley. Generation of small-scale irregularities in the equatorial electrojet. *Journal of Geophysical Research*, 78(1):240–248, 1973. 15, 25, 28, 44, 57, 93, 123
- [114] RN Sudan, AV Gruzinov, W Horton, and N Kukharkin. Convective turbulence in weakly ionized plasma. *Physics reports*, 283(1):95–119, 1997. 52
- [115] William Thomson. On the theory of the electric telegraph. *Proceedings of the Royal Society of London*, 7:382–399, 1854.
- [116] George W Walker. The diurnal variation of terrestrial magnetism. *Proceedings of the Royal Society of London. Series A, Containing Papers of a Mathematical and Physical Character*, pages 379–392, 1914.
- [117] Daniel R Weimer and Joseph H King. Improved calculations of interplanetary magnetic field phase front angles and propagation time delays. *Journal of Geophysical Research: Space Physics (1978–2012)*, 113(A1), 2008. 107, 109
- [118] DR Weimer, DM Ober, NC Maynard, WJ Burke, MR Collier, DJ McComas, NF Ness, and CW Smith. Variable time delays in the propagation of the interplanetary magnetic field. *Journal of Geophysical Research: Space Physics (1978–2012)*, 107(A8):SMP–29, 2002. 107
- [119] DR Weimer, DM Ober, NC Maynard, MR Collier, DJ McComas, NF Ness, CW Smith, and J Watermann. Predicting interplanetary magnetic field (imf) propagation delay times using the minimum variance technique. *Journal of Geophysical Research: Space Physics (1978–2012)*, 108(A1), 2003. 107

- [120] Jerome Weinstock and Arthur Sleeper. Nonlinear saturation of type irregularities in the equatorial electrojet. *Journal of Geophysical Research*, 77(19):3621–3624, 1972. 26
- [121] DT Welling. The long-term effects of space weather on satellite operations. In *Annales Geophysicae*, volume 28, pages 1361–1367. Copernicus GmbH, 2010. 99
- [122] Daniel S Wilks. *Statistical methods in the atmospheric sciences*, volume 100. Academic press, 2011. 114
- [123] Thomas N Woods. Irradiance variations during this solar cycle minimum. *arXiv preprint arXiv:1003.4524*, 2010. 54, 63, 106
- [124] Fei Xu and Joseph E Borovsky. A new four-plasma categorization scheme for the solar wind. *Journal of Geophysical Research: Space Physics*, 120(1):70–100, 2015. xviii, 100, 103, 104, 119
- [125] L Zhao, TH Zurbuchen, and LA Fisk. Global distribution of the solar wind during solar cycle 23: Ace observations. *Geophysical Research Letters*, 36(14), 2009. 103